Institute for Materials Research
SCHOOL OF PROCESS, ENVIRONMENTAL
& MATERIALS ENGINEERING

UNIVERSITY OF LEEDS

Development of bismuth ferrite derived piezoelectric ceramics for high temperature applications

James Thomas Bennett

Submitted in accordance with the requirements for the degree of
Doctor of Philosophy

Institute for Materials Research
School of Chemical and Process Engineering
The University of Leeds

October 2014

The candidate confirms that the work submitted is his own and that appropriate credit has been given where reference has been made to the work of others.

The candidate confirms that the work submitted is his own, except where work which has formed part of jointly-authored publications has been included. The contribution of the candidate and the other authors to this work has been explicitly indicated below. The candidate confirms that appropriate credit has been given within the thesis where reference has been made to the work of others.

All synchrotron and neutron experiments were completed with Dr. Tim Comyn as the principal investigator. The work herein is the author's own analysis of the data, except where explicitly highlighted in the text;
Chapter 4.4.1. Neutron diffraction refinements by Dr. T.P. Comyn
Chapter 6.7.1. Diffraction data collected by Dr. T.P. Comyn

Acknowledgements

~~"It was all down to me and hard work"~~

I would like to express my deepest gratitude to my supervisors, Professor Andrew Bell and Dr Tim Comyn who have been unwavering in their support throughout my studies, from undergraduate to postgraduate. Their ability to inspire, listen, advise and support is unparalleled. My pseudo-supervisor, Dr Tim Stevenson has provided me with much needed academic and social guidance over the past 4 years, Prost! Elsewhere in the department I must thank Anton Goetzee-Balls, Laura Stoica, Heather Owston, Adam Royles, Diane, Rob Simpson* and Faye Bygrave/Esat* (*The Pasty Crew).

Without financial support I would not have had the opportunity to fulfil my ambitions, for this I must thank EPSRC, STFC, IoM^3, IEEE and Ionix Advanced Technologies for granting me a PhD top-up award, which allowed me to travel to Anfield and the rest of England to watch the Reds many more times than I could afford. The World Universities Network funded a 4-month trip to the Pennsylvania State University and my gratitude must be extended to Professors Thomas Shrout and Shujun Zhang for making me feel so welcome and Jeff Long for his help in the lab. Colleen and all of the Wyckoff family took me in and showed me the wonders of the chicken wing festival on Tussey mountain, American beer and (especially) Bruce Springsteen, We are…..Penn State!. Andy has enabled me to visit amazing places that would not have been possible without his financial support and encouragement. The jagerbombs in Edinburgh, Vancouver, Les Arcs, Sestiere, and State College were much appreciated!

My friends in St.Helens and Leeds must be thanked for steering me off the straight and narrow wherever possible, Dre, Lev, Latham, Adam, Swebs, Daz, Bulman, Ric, Cozzy, Marco, Dillon and Mat. My family and girlfriend have been supportive throughout, Mum, Dad, Kate, Nanna Sue, Hazel. Whether it is the moaning that Mum and Hazel have had to put up with or the graft that my Dad has put in over the years to support us, thank you.

Abstract

The foundations of this project lay in the authors research into the xBiFeO$_3$-(1-x)(K$_{0.5}$Bi$_{0.5}$)TiO$_3$ ceramic system. A broad pseudocubic region was identified where x = 0.4-0.3, these compositions produced large electric-field induced strains (>0.3%) due to the presence of polar nanoregions that are easily switched by an applied electric field, however, these return to a random order upon removal of the field. Positive-up negative-down (PUND) showed that ferroelectric switching was reduced in the pseudocubic region and synchrotron studies with an applied electric-field *in-situ* demonstrated predominantly reversible domain switching.

Solid-solutions based upon the (1-x-y)BiFeO$_3$-x(K$_{0.5}$Bi$_{0.5}$)TiO$_3$-yPbTiO$_3$ ternary system have been fabricated by conventional mixed oxide processing, this system is the primary focus of this thesis. Structural analysis using XRD established that long-range crystallographic order was present above a critical PbTiO$_3$ concentration, in addition a broad mixed symmetry region was identified comprised of tetragonal and rhombohedral symmetries. The ferroelectric Curie temperature was between 410-590 ºC. Conventional ferroelectric and piezoelectric ordering was observed with the use of strain and polarization-field measurements. Rayleigh analysis was used to quantify the intrinsic and extrinsic contributions, a critical c/a ratio was identified at 1.045 with domain switching limited above this. Synchrotron x-rays with *ex-situ* electric-fields allowed for a more detailed structural analysis, selected compositions demonstrated significant phase changing behaviour. The room temperature tetragonal c/a ratio across the mixed symmetry region, Curie temperature, and piezoelectric d_{33} were found to correlate strongly with the PbTiO$_3$ concentration in a number of compositions.

This work demonstrates a number of important results that have wider implications. Ternary and pseudo-quaternary systems have recently been subject to large amounts of research as many of the possible binary systems have been exhausted. This has led to a raft of materials with reported high electric-field induced strains, these are often electrostrictive or have limited operating temperatures. The partial substitution of PbTiO$_3$ promotes long-range non-centrosymmetric order, which leads to increased piezoelectric activity and T_C.

Contents

1. BACKGROUND 3

1.1 CHAPTER OVERVIEW 3
1.2 STRUCTURE 3
1.2.1 CRYSTAL STRUCTURE 3
1.2.2 SYMMETRY AND SPACE GROUPS 5
1.2.3 LATTICE POINTS, PLANES AND DIRECTIONS 6
1.2.4 PEROVSKITE STRUCTURE 6
1.2.5 TILTING 10
1.3 ELECTRICAL PROPERTIES 11
1.3.1 DIELECTRICS 11
1.3.2 POLARIZATION MECHANISMS 14
1.3.3 DIELECTRIC BREAKDOWN 15
1.4 FERROELECTRICITY 16
1.4.1 FERROELECTRIC CURIE POINT AND CURIE TEMPERATURE 16
1.4.2 FERROELECTRIC PHASE TRANSITIONS 17
1.4.3 DOMAINS 18
1.4.4 HYSTERESIS 19
1.4.5 RELAXOR FERROELECTRICS 20
1.4.5.1 Polar Nanoregions 22
1.5 PIEZOELECTRICITY 25
1.5.1 ELECTROSTRICTION 25
1.5.2 PIEZOELECTRICITY PHENOMENON 25
1.5.3 PIEZOELECTRIC MODES 27
1.5.4 TEMPERATURE STABILITY 28
1.5.5. ELECTROMECHANICAL COUPLING 29
1.5.6 MPB 30
1.5.6.1 PZT 30
1.5.7 DOPING 34
1.5.8 APPLICATIONS 35
1.5.8.1 Actuators 35
1.5.8.2 Sensors 36
1.6 FERROELECTRIC AND PIEZOELECTRIC MATERIALS 37
1.6.1 LEAD-FREE PIEZOELECTRIC CERAMICS 37
1.6.1.1 $(K_{0.5}Bi_{0.5})TiO_3$-$(Na_{0.5}Bi_{0.5})TiO_3$ 38
1.6.1.2 $(K_{0.5}Na_{0.5})NbO_3$ 39
1.6.2 $Bi(Me)O_3$ BASED PEROVSKITES 40
1.6.2.1 $BiFeO_3$-$PbTiO_3$ 42
1.6.2.2 $BiFeO_3$-$(K_{0.5}Bi_{0.5})TiO_3$ 47
1.6.2.3 $BiScO_3$-$PbTiO_3$ 49
1.6.2.4 $BiMe^{3+}O_3$-$PbTiO_3$ 51
1.6.3 HIGH TEMPERATURE ABO_3 ALTERNATIVES 52
1.6.3.1 Tungsten Bronze Structures 52
1.6.3.2 Bismuth Layer Structure Ferroelectrics 53
1.6.3.3 Perovskite Layer Ferroelectrics 53
1.6.3.4 Piezoelectric Single Crystals 53

2. CHARACTERISATION TECHNIQUES 56

2.1 CHAPTER OVERVIEW **56**
2.2 ROOM TEMPERATURE CHARACTERISATION **56**
2.2.1 LABORATORY X-RAY DIFFRACTION 56
2.2.2 SYNCHROTRON X-RAY DIFFRACTION 63
2.2.3 STRAIN-ELECTRIC FIELD 64
2.2.4 POLARIZATION- ELECTRIC FIELD 65
2.2.5 POSITIVE UP NEGATIVE DOWN (PUND) 67
2.3 HIGH TEMPERATURE CHARACTERISATION **68**
2.3.1 STRAIN-ELECTRIC FIELD AND POLARIZATION-ELECTRIC FIELD 68
2.3.1.1 Rayleigh Analysis 69
2.3.2 PERMITTIVITY-TEMPERATURE 71
2.3.3 IMPEDANCE ANALYSIS 71
2.4 IMAGING TECHNIQUES **72**
2.4.1 SCANNING ELECTRON MICROSCOPY 72
2.4.2 PIEZORESPONSE FORCE MICROSCOPY 74

3. EXPERIMENTAL TECHNIQUES 75

3.1 CHAPTER OVERVIEW **75**
3.2 SYNTHESIS OF POWDERS **75**
3.3 SYNTHESIS OF PELLETS **76**
3.4 ROOM TEMPERATURE EXPERIMENTAL TECHNIQUES **77**
3.4.1 X-RAY DIFFRACTION 77
3.4.1.1 Data Refinement 78
3.4.2 SYNCHROTRON 79
3.4.2.1 Data Reduction 80
3.4.3 STRAIN-ELECTRIC FIELD 80
3.4.4 POLARIZATION-ELECTRIC FIELD 81
3.4.5 PUND 82
3.5 HIGH TEMPERATURE EXPERIMENTAL TECHNIQUES **82**
3.5.1 STRAIN-ELECTRIC FIELD 82
3.5.1.1 Rayleigh Analysis 83
3.5.2 POLARIZATION-ELECTRIC FIELD 83
3.5.3 PERMITTIVITY-TEMPERATURE 84
3.5.4 PRAP 84
3.6 IMAGING TECHNIQUES **85**
3.6.1 SCANNING ELECTRON MICROSCOPY 87
3.6.2 PIEZORESPONSE FORCE MICROSCOPY 87

4. PREPARATION AND CHARACTERISATION OF $BiFeO_3$-$(K_{0.5}Bi_{0.5})TiO_3$ 88

4.1 CHAPTER OVERVIEW **88**
4.2 BACKGROUND **88**
4.3 SAMPLE PREPARATION **89**
4.4 STRUCTURAL PHASE ANALYSIS **90**
4.4.1 NEUTRON DIFFRACTION 92
4.5 ELECTRICAL PROPERTIES **93**
4.6 CONCLUSIONS **102**

5. DEVELOPMENT OF $BiFeO_3$-$(K_{0.5}Bi_{0.5})TiO_3$-$PbTiO_3$ PIEZOELECTRIC CERAMIC SYSTEM 104

5.1 Sample Appearance and Density **106**
5.2 Microstructure Analysis **106**
5.2.1 EDX Analysis 108
5.3 Phase Analysis **109**
5.3.1 Sample Form 109
5.3.2 Compositional Space 111
5.4 Basic Electrical Characterisation **118**
5.4.1 Electric-field Induced Polarization and Strain 118
5.4.2 Poling Study 120
5.6 Conclusions **123**

6. ORIGINS OF THE PIEZOELECTRIC BEHAVIOUR AND HIGH TEMPERATURE CHARACTERISATION 125

6.1 Narrowing the Compositional Space **125**
6.2 High Temperature X-ray Diffraction **131**
6.3 Permittivity-Temperature **133**
6.4 High Temperature Piezoelectric Coefficients **136**
6.5 Piezoelectric Nonlinearity **139**
6.5.1 The Effect of Tetragonal Distortion on the Room-Temperature Intrinsic/Extrinsic Effects 142
6.5.2 The Intrinsic/Extrinsic Response at Elevated Temperatures 146
6.5.3 Reconstructing the Temperature Dependence of the Intrinsic/Extrinsic Effects 148
6.6 PUND **153**
6.7 Structural Analysis **157**
6.7.1 Synchrotron Study **159**
6.8 Scanning Electron Microscopy **165**
6.7 Piezoresponse Force Microscopy **171**
6.8 Summary and Discussion **180**

7. CONCLUDING REMARKS 184

8. FUTURE WORK 188

9. REFERENCES 191

10. APPENDIX 218

10.1 Supplementary Data **218**
10.2 Electrical and Resonance Measurements **218**
10.3 SEM **222**
10.4 PFM **224**

11. PUBLICATIONS 228

11.1 Conference Proceedings **229**

12. CONFERENCES AND TRAVEL 230

List of Figures

Figure 1-1. A unit cell highlighting the cell axes and angles [2]..... 4
Figure 1-2. The 14 Bravais Lattices [1] 4
Figure 1-3. Unit cell with point A, direction B and plane C 6
Figure 1-4. The perovskite structure, ABO_3, of La-doped $Pb(Zr,Ti)O_3$ in the paraelectric cubic phase [7] 7
Figure 1-5. Curie temperature of various PbTiO3 based MPBs versus end member tolerance factor [15] 9
Figure 1-6. Untilted oxygen octahedra [16] 10
Figure 1-7. The unit cell of rhombohedral PZT. The B-site cation is located at the centre of the oxygen cage [17]..... 11
Figure 1-8. Phasor diagram of the current-voltage lag in (a) an ideal dielectric and (b) a real dielectric material..... 13
Figure 1-9. The four polarization mechanisms [18] 14
Figure 1-10. Variation of $\varepsilon r'$ and $\varepsilon r''$ with frequency [18] 15
Figure 1-11. Spontaneous polarization and permittivity in (a) first-order and (b) second-order phase transitions [9] 17
Figure 1-12. The temperature dependent phase changes of $BaTiO_3$ [25] 17
Figure 1-13. Formation of 90° and 180° domain walls in $PbTiO_3$ [9]..... 18
Figure 1-14. A typical hysteresis loop for a ferroelectric material [25]..... 19
Figure 1-15. Relative permittivity as a function of temperature and frequency in lead magnesium niobate [29] 21
Figure 1-16. (a) Polar structures in $PbTiO_3$ at room temperature and (b) PLZT below the transition temperature with (c) and (d) showing PNRs in Barium-based single crystal and ceramic respectively [41]..... 22
Figure 1-17. The effect of temperature and pressure upon the permittivity, loss and the correlation length, of the PNRs in PMN [47] 24
Figure 1-18. Direct and Converse Piezoelectric effect [18] 26
Figure 1-19. Operational modes of piezoelectric elements in actuator and sensor modes with corresponding formulas where V=voltage, x=strain, F=force, P=poling direction, t=thickness, w=width and l=length [55]..... 27
Figure 1-20. Dielectric constant and electromechanical coupling factor across the morphotropic phase boundary for PZT [76] 31

Figure 1-21. Phase diagram of the $Pb(Zr_{1-x}Ti_x)O_3$ system from 1971 [25] 32
Figure 1-22. Phase diagram proposed in 2005 by Woodward et al [79] .. 33
Figure 1-23. Blocking force (F) versus free stroke (S) [93] 36
Figure 1-24. Piezoelectric activity versus the Curie temperature for various perovskite and non-perovskite families [95] 37
Figure 1-25. Low-signal and high-signal piezoelectric coefficient as a function of composition [100] 38
Figure 1-26. Phase diagram for the $KNbO_3$-$NaNbO_3$ system [25]..... 39
Figure 1-27. Magnetic and ferroelectric phase diagram for BFPT across the compositional space [130]..... 42
Figure 1-28. Lattice parameters for BFPT [139]..... 44
Figure 1-29. Polarization field and strain field data for x = 0.7 ((a) and (b) respectively) and x = 0.8 ((c) and (d) respectively) [141] 45
Figure 1-30. Polarization-electric field loops for La-doped BFPT [138].... 46
Figure 1-31. Effect of c/a ratio on the d_{33} for La-BFPT [138]..... 46
Figure 1-32. (a) The dielectric constant at room temperature (b) temperature dependence of k_{33} coupling coefficient and (c) dielectric constant and (d) loss as a function of temperature for x = 0.4 [144] 48
Figure 1-33. x-E and P-E loops for BF-KBT ceramics [145] N.B. The stoichiometric ratios above are contrary to those in the text 48
Figure 1-34. (a) Lattice parameters highlighting the MPB and (b) the phase diagram highlighting the paraelectric phase transition [15] 49
Figure 1-35. Enhancement of d_{33} at the MPB in BSPT ceramics [14]..... 50
Figure 2-1. Derivation of the Bragg equation (Modified from Cullity)..... 57
Figure 2-2. Schematic Diagram of an X-ray Tube [160]..... 58
Figure 2-3. Characteristic X-ray spectrum at varying voltages for Mo target [159]..... 60
Figure 2-4. Schematic of the Bragg-Brentano geometry used during XRD (Modified from Cullity [159]) 61
Figure 2-5. Representation of the stress effect upon diffraction patterns for (a) a perfect lattice, (b) a uniformly strained lattice and (c) non-uniformly strained lattice..... 62
Figure 2-6. Schematic diagram of an optical probe (Courtesy of MTI Instruments [167]) 65

Figure 2-7. Sawyer-Tower circuit used to determine P-E loops [169] 66
Figure 2-8. A typical Voltage profile during a PUND measurement [175] 68
Figure 2-9. Impedance spectra of BSPT single crystal in longitudinal mode [187] 72
Figure 2-10. Schematic diagram of a SEM microscope column [190]..... 73
Figure 2-11. Schematic diagram of the (a) vertical and (b) lateral PFM imaging modes [194] 74
Figure 3-1. Diagram representing the calcining regime 76
Figure 3-2. Diagram representing the sintering regime 77
Figure 3-3. Experimental set-up used at Diamond I15 [207] 79
Figure 3-4. 1 µm polishing stage, 50x magnification 86
Figure 3-5. 0.02 µm polishing stage, 50x magnification 86
Figure 4-1. Geometrically measured density across the compositional space 89
Figure 4-2. X-ray diffraction patterns taken from crushed annealed ceramics of $BiFeO_3$-$(K_{0.5}Bi_{0.5})TiO_3$ 91
Figure 4-3. X-ray diffraction patterns of the 111 family $x$$BiFeO_3$-(1-$x$)$(K_{0.5}Bi_{0.5})TiO_3$ from 38 to 41° 91
Figure 4-4. X-ray diffraction patterns of the 200 family belonging to $x$$BiFeO_3$-(1-$x$)$(K_{0.5}Bi_{0.5})TiO_3$ from 44 to 47° 92
Figure 4-5. Neutron diffraction patterns with the associated structural and magnetic refinements for bulk ceramics collected at 296 K. The residual is shown underneath each scan. 93
Figure 4-6. Bipolar electric field induced strain values for $x$$BiFeO_3$-$(K_{0.5}Bi_{0.5})TiO3$ at 8.5 kV/mm and a frequency of 0.1 Hz 95
Figure 4-7. Unipolar electric field induced strain values for $x$$BiFeO_3$-$(K_{0.5}Bi_{0.5})TiO_3$ where x = 0.4 at 0.1 Hz 95
Figure 4-8. Piezoelectric coefficient obtained from a Berlincourt meter (110 Hz) and the effective d_{33} obtained from bipolar strain-field loops (0.1 Hz) across the compositional range 96
Figure 4-9. Bipolar electric-field induced polarization values for $x$$BiFeO_3$-(1-$x$)$(K_{0.5}Bi_{0.5})TiO_3$ at 8.5 kV/mm and a frequency of 10Hz 98
Figure 4-10. Saturation and remanent polarization values at 8.5 kV/mm across the compositional space 98

Figure 4-11. PUND data showing the switchable polarization of 6040 $BiFeO_3$-$(K_{0.5}Bi_{0.5})TiO_3$ normalised to both P_{SAT} and P_R at 8.5 kV/mm 99
Figure 4-12. PUND data showing the switchable polarization of 40 $BiFeO_3$-$(K_{0.5}Bi_{0.5})TiO_3$ normalised to both P_{SAT} and P_R at 8.5 kV/mm 100
Figure 4-13. Leakage current density as a function of applied electric field strength for 8020, 6040 and 4060 $BiFeO_3$-$(K_{0.5}Bi_{0.5})TiO_3$ at ambient temperature 101
Figure 4-14. Leakage current density at 1kV/mm and 8.5 kV/mm for 8020, 6040 and 4060 $BiFeO_3$-$(K_{0.5}Bi_{0.5})TiO_3$ polycrystalline ceramics 101
Figure 4-15. Phase diagram of the $BiFeO_3$-$(K_{0.5}Bi_{0.5})TiO_3$ system highlighting the low-field and high-field piezoelectric charge coefficients across the compositional space as well as the Curie temperature. The dashed lines represent the phase boundaries identified by Kim (blue), Matsuo (green) Morozov (pink) and Bennett (red), those at x = 0.1 (red and blue) represent the transition from pseudocubic to tetragonal. 103
Figure 5-1. The ternary phase diagram of the $BiFeO_3$-$(K_{0.5}Bi_{0.5})TiO_3$-$PbTiO_3$ system with the strarting MPB end members highlighted and the iterations taken during the development of these ceramics. The first iteration of materials were ball milled, however, all subsequent compositions were attrition milled 104
Figure 5-2. Flow-diagram of the typical procedure used when characterising the $BiFeO_3$-$(K_{0.5}Bi_{0.5})TiO_3$-$PbTiO_3$ system 105
Figure 5-3. Scanning electron micrographs of (a) the starting reagents, (b) attrition milled powders pre-calcination, (c) calcined powders and (d) a fracture surface from a ceramic pellet of the composition where x = 0.15 and y = 0.3. 107
Figure 5-4. EDX image of a polished surface highlighting (a) the mapped area (b-g) and individual elemental maps 108
Figure 5-5.(a-f) Diffraction data collected using different sample forms and detection methods 109
Figure 5-6. Ternary diagram highlighting the mixed symmetry region with selected compositions presented 114
Figure 5-7. X-ray diffraction patterns of BF-KBT-PT ceramics in the 2θ range of 18°–60° and (b) from 41° to 48.5° 115

Figure 5-8. Lattice parameters and c/a ratio as a function of $PbTiO_3$ content 116
Figure 5-9. Diffraction patterns of poled and unpoled samples for the {111} peak (a) and (c) and the {200} peak (b) and (d) using lab x-rays 117
Figure 5-10. Electrical-field induced strains for compositions where (a) x = 0.45 and y = 0.075, (b) x = 0.375 and y = 0.1125, (c) x = 0.225 and y = 0.1875 and (d) x = 0.15 and y = 0.25 118
Figure 5-11. Electrical-field induced polarization for compositions where (a) x = 0.45 and y = 0.075, (b) x = 0.375 and y = 0.1125, (c) x = 0.225 and y = 0.1875 and (d) x = 0.15 and y = 0.25 120
Figure 5-12. Contour plot showing the low-signal piezoelectric coefficient d_{33} as a function of composition, the colour of the markers corresponding those represented in Figure 5-1. Values from the literature have also been included (indicated by the yellow markers) where possible in order to map a greater compositional space 122
Figure 6-1. This region of the ternary phase diagram was characterised in detail due to the correlation between structural properties and $PbTiO_3$ concentration 125
Figure 6-2. Electric field induced strains for Compositions A-E2 as a function of temperature 126
Figure 6-3. Temperature dependence of the coercive field for Compositions A-E2, taken from high-field x-E measurements 128
Figure 6-4. Electric field induced polarization values for compositions A-E2 as a function of temperature 129
Figure 6-5. P_{SAT} and P_R as a function of the tetragonal distortion across the MSR 130
Figure 6-6. Temperature dependence of the {200} lattice parameters for Composition A 132
Figure 6-7. Temperature dependence of the {200} lattice parameters for Composition E1 132
Figure 6-8. Permittivity and loss as a function of temperature for Compositions A - E2 highlighting the transition to the paraelectric phase 134

Figure 6-9. The relationship between the $PbTiO_3$ content and T_C & the room temperature low-field piezoelectric coefficient d_{33}..... 135
Figure 6-10. $-d_{31}$ as a function of temperature for Compositions A-E2 .. 137
Figure 6-11. Temperature dependence of the electromechanical planar coupling coefficient, k_p, for Compositions A-E2..... 138
Figure 6-12. The c/a ratio, Curie temperature and piezoelectric charge coefficient of the compositions examined in this section..... 140
Figure 6-13. (a-f) d_{33} vs. E_0 at varying temperatures for various compositions belonging to the $BiFeO_3$-$(K_{0.5}Bi_{0.5})TiO_3$-$PbTiO_3$ system ... 141
Figure 6-14. (a-f) Measured and calculated electric-field induced strain loops using the Rayleigh model at 25 °C and 150 °C at 1 kV/mm 142
Figure 6-15. Room temperature values of the (a) d_{init}, (b) Rayleigh coefficient, α_d and (c) extrinsic contributions as a function of the tetragonal distortion. The lines are drawn as a guide for the eye..... 143
Figure 6-16. The red triangles show the experimentally observed c/a-1 correlated with the calculated P^2 values (Following Qi [227])..... 145
Figure 6-17.(a-f) d_{init}, α_d and (g-l) extrinsic contributions as a function of temperature for various compositions..... 147
Figure 6-18.(a) Relative permittivity, (b) polarization and (c) lattice parameters of a poled sample of composition D1..... 150
Figure 6-19. The measured d_{init}, calculated d_{init} values and the reversible extrinsic component as a function of temperature for composition D1... 152
Figure 6-20. P-E loops measured pre-PUND analysis..... 154
Figure 6-21. $\Delta P/P_{SAT}$ for selected compositions..... 155
Figure 6-22. Leakage Current as a function of electric field..... 156
Figure 6-23. {200} Lattice Parameters, c/a ratio and tetragonal intensity ratio as a function of $PbTiO_3$ content 159
Figure 6-24. *In-situ* synchrotron diffraction patterns of the 111 family where φ = 0° (a) and 90° (c) and the 200 family where φ = 0° (b) and 90° (d) for BF-KBT 4060 before, during and after application of 6 kV/mm..... 161
Figure 6-25.(a-n) Diffraction patterns of unpoled and *ex-situ* poled samples from the same pellet at φ = 0° and 90° for BF-KBT-PT..... 164
Figure 6-26.(a-d) Scanning electron micrographs of Composition D1 as a function of etching time in a HF and HCl based solution..... 167

Figure 6-27. Scanning electron micrograph of Composition A that has been optically polished and chemically etched. The inset image is of a highly magnified grain belonging to a different region 169
Figure 6-28. Scanning electron micrograph of 4060 $BiFeO_3$-$(K_{0.5}Bi_{0.5})TiO_3$, sample prepared as above 170
Figure 6-29. PFM images of a 400 μm^2 area of a polished sample of Composition A with (a)topography, (b)deflection error, (c)vertical amplitude, (d)vertical phase, (e)lateral amplitude and (f)lateral phase... 172
Figure 6-30. PFM images of a 25 μm^2 area of a polished sample of Composition A..... 172
Figure 6-31. PFM images of a 400 μm^2 area of a polished sample of (1-*x*-*y*)$BiFeO_3$-*x*$(K_{0.5}Bi_{0.5})TiO_3$-*y*$PbTiO_3$ where *x* = 0.3 and *y* = 0.15 174
Figure 6-32. PFM images of a 36 μm^2 area of a polished ceramic disc of (1-*x*-*y*)$BiFeO_3$-*x*$(K_{0.5}Bi_{0.5})TiO_3$-*y*$PbTiO_3$ where *x* = 0.3 and *y* = 0.15..... 174
Figure 6-33. PFM images of a 400 μm^2 area of a polished ceramic disc of *x*$BiFeO_3$-(1-*x*)$(K_{0.5}Bi_{0.5})TiO_3$ where *x* = 0.8..... 176
Figure 6-34. PFM images of a 25 μm^2 area of a polished ceramic disc of *x*$BiFeO_3$-(1-*x*)$(K_{0.5}Bi_{0.5})TiO_3$ where *x* = 0.8..... 176
Figure 6-35. PFM images of a 400 μm^2 area of a polished ceramic disc of *x*$BiFeO_3$-(1-*x*)$(K_{0.5}Bi_{0.5})TiO_3$ where *x* = 0.6..... 177
Figure 6-36. PFM images of a 25 μm^2 area of a polished ceramic disc of *x*$BiFeO_3$-(1-*x*)$(K_{0.5}Bi_{0.5})TiO_3$ where *x* = 0.6..... 177
Figure 6-37. PFM images of a 400 μm^2 area of a polished ceramic disc of *x*$BiFeO_3$-(1-*x*)$(K_{0.5}Bi_{0.5})TiO_3$ where *x* = 0.4..... 178
Figure 6-38. PFM images of a 25 μm^2 area of a polished ceramic disc of *x*$BiFeO_3$-(1-*x*)$(K_{0.5}Bi_{0.5})TiO_3$ where *x* = 0.4..... 179
Figure 7-1. d_{33} as a function of T_C for a range of piezoelectric compounds with the purple rectangle highlighting the mixed symmetry region of the BF-KBT-PT system [95]. 187
Figure 10-1. P-E loop for (1-*x*-*y*)$BiFeO_3$-*x*$(K_{0.5}Bi_{0.5})TiO_3$-*y*$PbTiO_3$ where *x* = 0.375 and *y* = 0.075 at 8 kV/mm and 13 kV/mm 218
Figure 10-2. (a) Electric-field induced strain, (b) coercive-field and (c) S_{MAX}/E_{MAX} as a function of temperature for composition C 219

Figure 10-3. Permittivity and loss as a function of temperature for 1-*x*-*y*)$BiFeO_3$-*x*($K_{0.5}Bi_{0.5}$)TiO_3-*y*$PbTiO_3$ where *x* = 0.375 and *y* = 0.075 219
Figure 10-4. Elastic compliance as a function of temperature for Compositions A-E2 220
Figure 10-5. Room temperature (a) d_{init}, (b) α_d and (c) extrinsic contributions as a function of the $PbTiO_3$ concentration across the MSR 221
Figure 10-6. Scanning electron micrograph of Composition B 222
Figure 10-7. Scanning electron micrograph of Composition D1 222
Figure 10-8. Scanning electron micrograph of Composition D2 223
Figure 10-9. Scanning electron micrograph of Composition E1 223
Figure 10-10. PFM images of a 400 μm^2 area of a polished sample of Composition B 224
Figure 10-11. PFM images of a 400 μm^2 area of a polished sample of Composition C 224
Figure 10-12. PFM images of a 400 μm^2 area of a polished sample of Composition D1 225
Figure 10-13. PFM images of a 400 μm^2 area of a polished sample of Composition D2 225
Figure 10-14. PFM images of a 400 μm^2 area of a polished sample of Composition E1 226
Figure 10-15. PFM images of a 400 μm^2 area of a polished sample of Composition E2 226
Figure 10-16. PFM images of a 6.25 μm^2 area of a polished ceramic disc of *x*$BiFeO_3$-(1-*x*)($K_{0.5}Bi_{0.5}$)TiO_3 where *x* = 0.4 227
Figure 10-17. Thermal degradation study of composition B at 470 ºC ... 227

List of Tables

Table 1-1. Key properties of undoped MPB PZT ceramics [77] 32
Table 1-2. Applications of piezoelectrics 35
Table 1-3. Summary of crystallographic data available for BFPT 44
Table 1-4. Summary of T_C, c/a ratio and d_{33} in the Bi*Me*O_3-$PbTiO_3$ family 51
Table 1-5. Electromechanical properties of selected non-ABO_3 perovskite materials, the data were collated from Refs. [94] and [95] 55
Table 2-1. Mean characteristic wavelengths of target materials 59
Table 3-1. Polshing routine used for BF-KBT-PT ceramics (Supplied by Buehler) 86
Table 5-1. Typical poling study data obtained for this family, the data shown below belongs to Composition D1 121
Table 6-1. Summary of electrical properties and Rayleigh parameters at room temperature for BF-KBT-PT, La-BFPT [137] and PZT ceramics [25] [166], d_{33} values were measured with a Berlincourt meter, E_C was taken from x-E data at 7 kV/mm. 153
Table 6-2. Summary of structural and electrical properties across the BF-KBT and BF-KBT-PT compositional space 183
Table 10-1. Key of the labelling system and the corresponding stoichiometric ratios 218

Abbreviations

AFE – Antiferroelectric

AFM – Atomic Force Microscope

BF-KBT – Bismuth Ferrite - Potassium Bismuth Titanate, $BiFeO_3$–$(K_{0.5}Bi_{0.5})TiO_3$

BF-KBT-PT – Bismuth Ferrite - Potassium Bismuth Titanate - Lead Titanate, $BiFeO_3$–$(K_{0.5}Bi_{0.5})TiO_3$-$PbTiO_3$

BFPT – Bismuth Ferrite Lead Titanate, $BiFeO_3$ – $PbTiO_3$

BSPT - Bismuth Scandate Lead Titanate, $BiScO_3$ – $PbTiO_3$

EDX –Energy dispersive x-ray spectroscopy

FE – Ferroelectric

KBT – Potassium Bismuth Titanate, $(K_{0.5}Bi_{0.5})TiO_3$

MPB – Morphotropic Phase Boundary

MSR – Mixed Symmetry Region

P-E – Polarization-Electric field

PFM – Piezoresponse Force Microscopy

PLZT – Pb,La$(Zr,Ti)O_3$

PNR – Polar nanoregions

PRAP – Piezoelectric Resonance Analysis Program

PUND – Positive Up Negative Down

PZT – Lead Zirconate Titanate, $Pb(Zr_{1-x}Ti_x)O_3$

SEM – Scanning Electron Microscopy

TEM – Transmission electron microscopy

TSDC – Thermally stimulated depolarization current

XRD – X-ray Diffraction

x-E – Strain- Electric field

Introduction

Piezoelectric ceramics belong to a broader class of engineering materials known as electroceramics which are exploited in a far-reaching number of applications due to their electronic response. The performance of electroceramics is often related to microstructure and processing techniques. Piezoelectrics have been used commercially for over 50 years with applications including medical ultrasound, piezoelectric sonar systems, ultrasonic motors and diesel fuel injectors in the automotive industry. Higher temperature piezoceramics are required in a number of sectors. The application demands cannot be satisfied by $Pb(Zr_{1-x}Ti_x)O_3$ (x~0.48) (PZT) as the paraelectric phase transition temperature, T_C, is in the region of 386 °C. Discovered in 1952, it is still commercially dominant as no suitable alternative has been found.

One of the vital steps in the understanding of piezoelectric materials was the discovery of $BaTiO_3$ which has a perovskite structure that belongs to the general formula ABO_3 and is key to commercial ferroelectric and piezoelectric materials. PZT also belongs to this family, its enhanced electrical properties are due to a morphotropic phase boundary (MPB) between the $PbZrO_3$-rich rhombohedral and the $PbTiO_3$-rich tetragonal phases. Many binary systems belonging to the general formula $(1-x)BiMeO_3$-$xPbTiO_3$ and $(1-x)Bi(Me',Me'')O_3$-$xPbTiO_3$ have attempted to replicate the MPB but no fiscally viable, high temperature piezoelectric ceramic has been identified.

The exhaustion of possible binary systems has led to the recent development in $PbTiO_3$-based ternary and pseudo-quaternary systems. High temperature alternatives include non-perovskite crystal structures such as; lead-niobate ($PbNbO_6$) which has a tungsten-bronze structure, bismuth titanate (Bi_4TiO_{12}) which belongs to the bismuth structure layer ferroelectrics family and lithium niobate ($LiNbO_3$) which has a corundum structure, these materials all suffer from low piezoelectric coefficients (>85 pm/V). It is apparent that there is a demand from both industry and academia for novel high-temperature piezoceramics.

Aims and Objectives

The overall aim of this work is to develop and characterise (1-*x*-*y*)$BiFeO_3$-*x*$(K_{0.5}Bi_{0.5})TiO_3$-*y*$PbTiO_3$ ceramics with the intent of identifying a new family of piezoelectric ceramics. This contribution follows on from research into the $BiFeO_3$-$PbTiO_3$ and $BiFeO_3$-$(K_{0.5}Bi_{0.5})TiO_3$ systems, both of which will be presented throughout this study for useful comparison and are well known to the research group at Leeds, the former being a traditional ferroelectric and the latter exhibiting relaxor-like properties. Therefore, a transition traversing these quite contradictory behaviours could exist and its origin and mechanisms may be explored.

This project will be split into three main branches; the first being an overview of the lead-free $BiFeO_3$-$(K_{0.5}Bi_{0.5})TiO_3$ system in terms of structural and electrical ordering. The second branch introduces the development of the (1-*x*-*y*)$BiFeO_3$-*x*$(K_{0.5}Bi_{0.5})TiO_3$-*y*$PbTiO_3$ system, beginning with phase and microstructural analysis, and the optimisation of processing also being included in this section. X-ray diffraction studies will be discussed and correlated with basic electrical measurements such as poling studies and electric-field induced strain and polarization measurements. The third branch of this work includes characterisation of the structural and electrical properties, often as a function of temperature. The mechanisms governing the electrical behaviour observed will be investigated. Electrical results will be correlated with phase and microstructural analysis. This methodology will be compared to other well researched systems such as PZT and the (1-*x*)$BiMeO_3$-*x*$PbTiO_3$ family.

1. Background

1.1 Chapter Overview

This chapter aims to cover the basic principles governing the behaviour of piezoelectric ceramics, primarily dealing with structure-property relationships. The applications of piezoelectric materials will be discussed and the structure and properties of commercial materials such as PZT and barium titanate will be outlined. Piezoelectric compounds that are of importance to this investigation will also be reviewed.

1.2 Structure

1.2.1 Crystal Structure

A fundamental principle of materials science is that a close association is found between the structure and properties exhibited. Materials science as a field aims to exploit favourable properties via the choreography of atoms in a structure. A crystalline solid is said to have a highly regular repeating arrangement of atoms in three dimensions. This differs from liquids or glasses which often possess only short range order, are extensively disordered and no long range periodicity exists.

A polycrystalline material is not infinite but rather made up of many crystallites, each of which, contains enough atoms to satisfy approximations. The repeating array of atoms form a lattice, that is, the environment of each point is identical [1]. The smallest repeating entity of the lattice is known as the unit cell, or the motif, and this can be categorised by one of the seven lattice systems. The varying parameters can be explained using the three axial distances a, b, c and the angles between them α, β, γ highlighted in Figure 1-1 and whether there are any additional lattice points on the faces or body of the unit cell. The cell edges lengths and angles combined to produce; cubic, tetragonal, orthorhombic, rhombohedral, hexagonal, monoclinic and triclinic lattice systems. When these lattice systems are combined with the various possible lattice centres, this leads to the possibility of fourteen different ‘Bravais lattices’, as initially demonstrated by Auguste Bravais [1], shown in Figure 1-2.

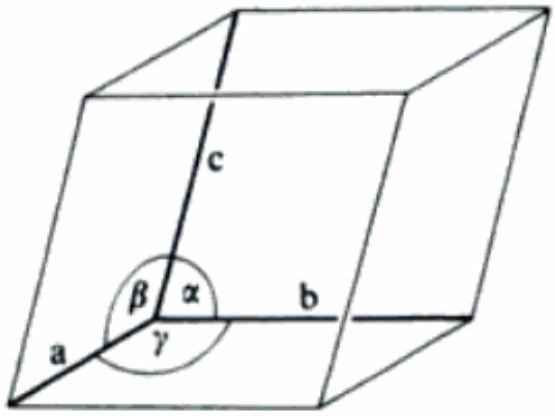

Figure 1-1. A unit cell highlighting the cell axes and angles [2]

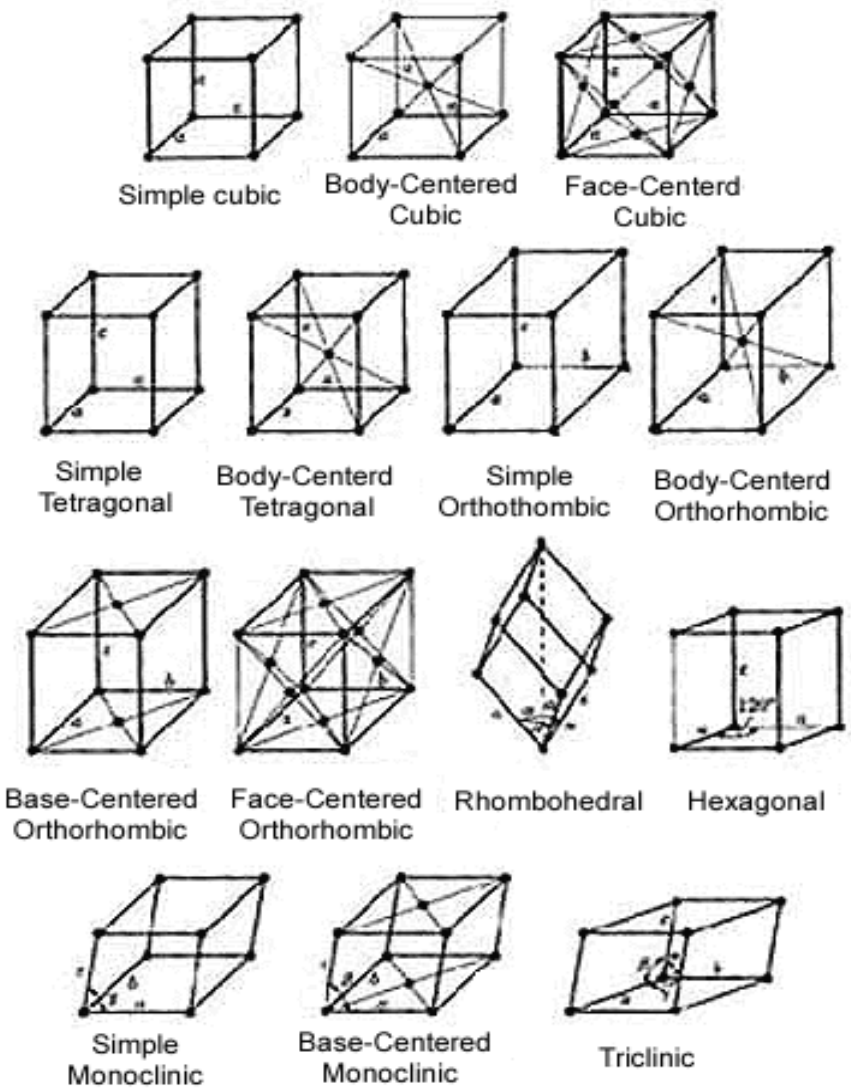

Figure 1-2. The 14 Bravais Lattices [1]

1.2.2 Symmetry and Space Groups

In order to further define a crystal, greater understanding of its symmetry elements are required so that it is known how it will appear after a point or translational symmetry element. The point symmetry elements are mirror, rotation and inversion. A combination of these symmetry and translation elements in addition to the crystal structure of the unit cell renders a detailed description of the structure and allows us to define the term space group. The identification of the possible space groups was carried out individually by Fedorov and Schoenflies [3]. As more symmetry operations are possible in three dimensions as opposed to two, the number of unique space groups increases from 17 to 230.

Although Schoenflies was a pioneer in this field, his notation system has been overlooked here in favour of Hermann-Maguin notation. Another commonly used system is that of the International Union of Crystallography whereby all space groups have been allocated a number with 1 having the least symmetry, triclinic crystals, and 230 belonging to cubic crystals with the highest symmetry. Hermann-Maguin notation consists of three or four symbols, the first of which is the lattice centering type denoted by the letter *P*, *I*, *F*, *C* or *R*, which refer to primitive, body-centred, face-centred, centred or base-centred and rhombohedral primitive respectively. The symmetry is then detailed, the examples of P4mm and R3c shall be used as examples due to their importance in this study. P4mm consists of a primitive centering with a 4 fold rotation and two mirror planes, and R3c consists of a rhombohedral unit cell with 3 fold rotation and a glide plane along the c-axis.

Of the 32 crystallographic point groups into which crystalline materials can be divided into, 11 are centrosymmetric and cannot support piezoelectricity. The cubic class 432 although non-centrosymmetric cannot exhibit piezoelectricity. 20 classes are therefore piezoelectric and of those, 10 have a unique polar axis and a spontaneous dipole moment along the polar axis, these are termed pyroelectric. Further sub-division can lead to crystal structures that exhibit ferroelectricity as this must possess a reversible unique polar axis that can exhibit a reversible spontaneous polarization in the absence of an electric field.

1.2.3 Lattice Points, Planes and Directions

Lattice points can be given in terms of its Cartesian axis co-ordinates as demonstrated in Figure 1-3. These relate to the origin, O, in terms of fractions of the lengths along x, y and z, and expressed as whole numbers, thus A is 011. Directions use the same system but brackets [uvw] are used to denote a direction, the direction B is [210]. Planes in the Bravais lattices are indexed using a system known as Miller indices where the reciprocal of the intersection of the plane is used. These are placed in parentheses, plane C is (010), although, multiple planes also belonging to this family can be unified within brackets [4].

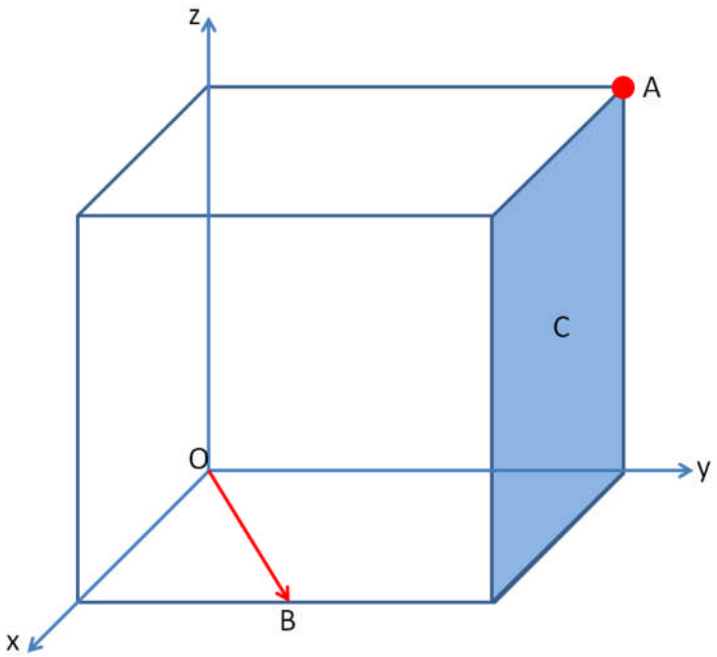

Figure 1-3. Unit cell with point A, direction B and plane C

1.2.4 Perovskite Structure

Most piezoelectric and ferroelectric materials of commercial interest belong to the family of crystalline ceramics known as perovskites [5]. Perovskites are the most abundant minerals on earth and were identified as far back as the 1830s by Gustav Rose and named in honour of the mineralogist Count Lev Aleksevich von Perovskji [6]. The work of von Hippel and his contemporaries led to the discovery of ferroelectricity in $BaTiO_3$, the prototype ferroelectric, in the 1940s. This was a major breakthrough and led to the unearthing of a new family of ferroelectric and piezoelectric ceramics [6].

The perovskite structure is of the form ABX_3, where large cations (A site) are located at the corners, and the body centre is occupied by the smaller cations (B site) while X is commonly occupied by oxygen anions which lie on the face centres to form an oxygen cage as shown in Figure 1-4 in La-doped PZT. The unit cell can also be represented with the small cations on the corners, the anions at the midpoint of each edge and the large cation at the body centre of the unit cell.

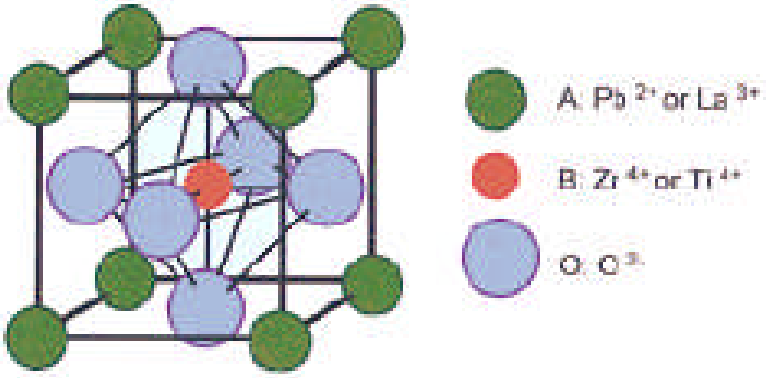

Figure 1-4. The perovskite structure, ABO_3, of La-doped $Pb(Zr,Ti)O_3$ in the paraelectric cubic phase [7]

As the central atom is not 'touching' it is in direct violation of Pauling's first rule which states that "A coordinated polyhedron of anions is formed about each cation, the cation-anion distance is determined by the sum of ionic radii and the coordination number by the radius ratio" [8]. This rule means that for stability to occur the atoms must be tightly packed and must not "rattle", and this can only occur if cations are in contact with each neighbour [8]. There are few ionic compounds that satisfy this criterion, only $SrTiO_3$, alternative combinations of A and B cations lead to distorted central atoms and thus "rattling".

The origin of ferroelectric behaviour and phase stability in perovskites is still not fully understood and has been widely deliberated for some time. Structurally, in general this can be simplified as displacements of the B-site and O ions in relation to the large A-site cation [9]. Varying properties in similar perovskites has been proposed by Kinase to be due to the polarizability of the A-site ion, which influences the local fields acting upon the B-site ion, thus causing

a displacement [10] whereas other studies have focussed upon the electronic state and phase behaviour of the A-site cations such as Pb and Ba [5].

The perovskite family is extremely accommodating of ions of differing valence, with the A-site cation permitting monovalent, divalent or trivalent ions and the B-site permitting trivalent, tetravalent and pentavalent ions provided that the total valence is 6+. A fractional combination of cations is also permitted such as in $(K^{+}_{1/2}Bi^{3+}_{1/2})Ti^{4+}O_3$. It would be reasonable to assume that a large amount of disorder would occur in binary, ternary and pseudo-quarternary systems with varying A and B-site cations, although it has been suggested that this is not the case due to local valency balance effects [11]. This is extremely useful when fabricating new morphotropic phase boundary (MPB) piezoelectric ceramics as many symmetry variant end members can be incorporated, often with the $PbTiO_3$ end member.

Not all ABO_3 compounds crystallise as a perovskite, Goldschmidt proposed the tolerance factor equation in 1926 which uses ionic radii to assess the suitability of varying ions in forming the perovskite family [12] given by the following equation.

$$t = \frac{R_A + R_O}{\sqrt{2(R_B + R_O)}}$$

Equation 1-1

where t is the tolerance factor, R_A, R_B and R_O represent the ionic radii of the A, B and oxygen ions.

A cubic structure would result in a tolerance factor of ~1 such as in $SrTiO_3$. Using octahedral ionic radii results suggested that a perovskite would be expected in the range of 0.77-0.99, while a co-ordination number 12 for the A-site cation suggested a tolerance factor in the region of 0.88-1.09 [6]. $LiNbO_3$ has a tolerance factor of 0.86 and crystallises with the ilmenite structure.

Empirical evidence shows that in general low symmetry distortions occur, with rhombohedral or monoclinic structures forming <1, whereas t>1 usually results in tetragonal or hexagonal distortions. It must be stated that the existence of ferroelectricity cannot be elucidated from this calculation. This method has its limitations as the ionic radius is not disclosed for Bi^{3+} and many other ions, work thus far has been based upon extrapolated data from Shannon. An assumption is made that all bonds are totally ionic whereas it has been shown that this is often not the case, an example being $PbTiO_3$ which has been shown to demonstrate considerable covalence [13], it also does not apply to perovskites with extensive A-site ionic vacancies.

Eitel utilised this method as a practical technique in the development of novel high temperature piezoelectric perovskites belonging to the $BiMeO_3$-$PbTiO_3$ family, postulating a link between the tolerance factor and T_C. Shown in Figure 1-5, the T_C was projected to increase linearly with decreasing tolerance factor, such that $BiScO_3$, $BiInO_3$ and $BiYbO_3$ exhibited tolerance factors of 0.907, 0.884 and 0.857 along with an estimated T_C of 450°C, ~550°C and ~650°C respectively, these values were confirmed by experimental methods [14-15]. Notable exceptions to this rule are cations that change valence such as Fe, W and Co, with $BiFeO_3$-$PbTiO_3$ exhibiting a much greater T_C than expected.

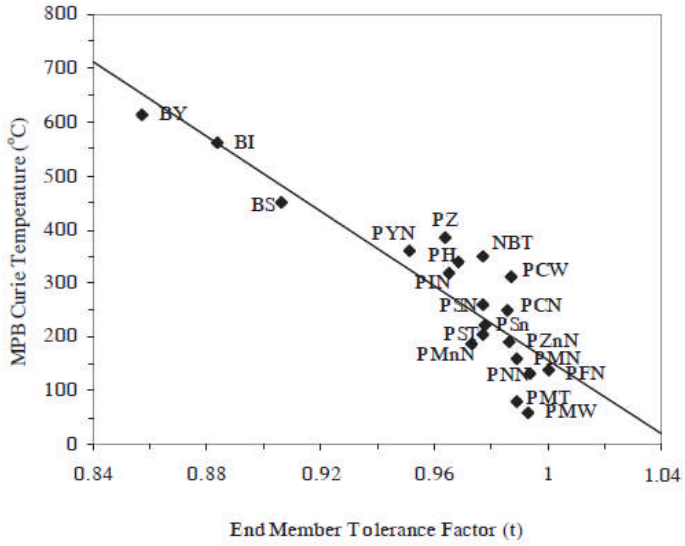

Figure 1-5. Curie temperature of various PbTiO3 based MPBs versus end member tolerance factor [15]

1.2.5 Tilting

As discussed previously, the displacement of the cations can generate ferroelectric and piezoelectric behaviour in the perovskite structure. The interaction between the oxygen anions and the cations can lead to discrete variations of the unit cell. Glazer observed that the role of the oxygen octahedral tilt, such as in $CaTiO_3$ can have a far greater effect on the lattice parameters than cation displacements [16]. The oxygen cage of a perovskite material is illustrated in Figure 1-6. It can be envisaged from this that when one octahedron tilts, this leads to the neighbour tilting also in a contrary manner and this propagates throughout the lattice.

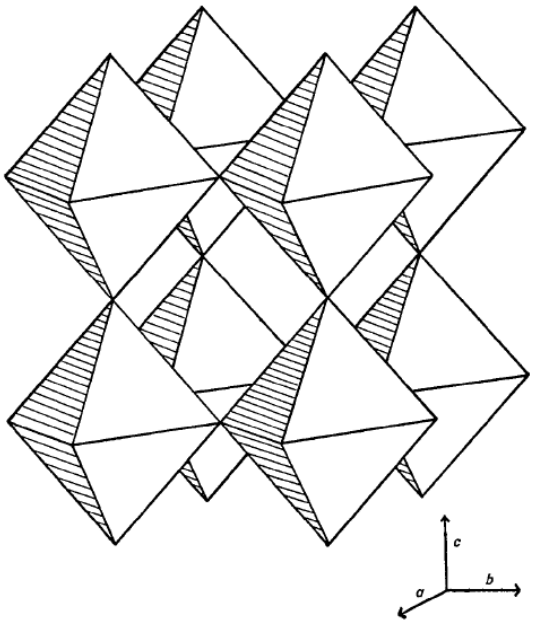

Figure 1-6. Untilted oxygen octahedra [16]

The accommodating nature of the perovskite family has already been discussed, and a number of different tilting systems are permissible. Tilting can also have a profound effect upon properties, as witnessed in rhombohedral PZT, leading to a suppression of the piezoelectric properties at low temperatures [17]. At room temperature the oxygen octahedra are in an irregular clockwise-anticlockwise order rotated around the [111] direction as demonstrated in Figure 1-7. Oxygen tilts were found to suppress the extrinsic effect, therefore limiting a significant contribution to the total piezoelectric response [17]. The origin of this is due to the

presence of additional pinning sites in the tilted phase. An understanding of these tilt systems is important when developing novel MPB materials.

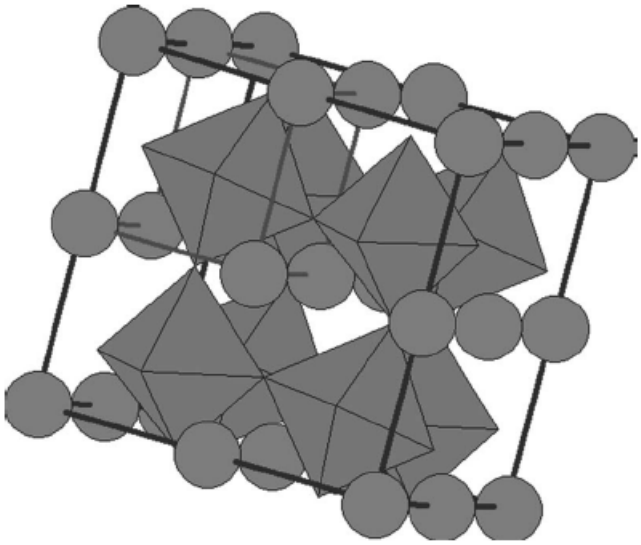

Figure 1-7. The unit cell of rhombohedral PZT. The B-site cation is located at the centre of the oxygen cage [17]

Glazer defined a notation system for the many different types of tilts that exist [16]. Figure 1-7 is defined as ($a^-a^-a^-$) as the rotations are of equal scale (a) and alternating in the direction ($^-$).

1.3 Electrical Properties

1.3.1 Dielectrics

A dielectric material is broadly said to be an insulating or non-conductive material that exhibits or can be made to exhibit a polar structure. The initial development of these materials was a result of the practical need for insulators and early experiments were based upon the isolation of electrostatic charge by dielectric materials which would not conduct the charge away [18]. When exposed to an electric field, it is possible for a dielectric to be polarized due to the balancing of fixed charges. This is between positive and negative charges which lead to a distortion in the unit cell upon application of an electric field [19], this can be envisaged with a positive charge at one end of a ceramic plate and negative

charge at the other. This symbolises the surface charges as a result of the internal dipole moments and is representative of a polarized material. This transport of charge cannot happen via long range transport but it is instead via short range order, this can be imagined by long chains of dipoles extending from surface to surface [20]. The field of dielectrics was revolutionised as a result of the semiconductor boom as wide band gap materials with high permittivity were required in order to store charge and prevent breakdown of components.

The dipole moment per unit volume of a dielectric material is known as the polarization, P, which is proportional to the applied electric field, E.

$$P = \chi \varepsilon_0 E$$

Equation 1-2

where χ is the dielectric susceptibility and ε_0 is the permittivity of free space and has the value 8.854×10^{-12} F/m. Permittivity is the extent to which a material can support an electrostatic field and quantifies the amount that a material can separate charges of opposing polarity. The permittivity in a dielectric can be denoted as ε, while the relative permittivity, ε_r, is relative to the permittivity of free space, ε_0. It can be defined that;

$$\varepsilon = \varepsilon_0(1 + \chi)$$

Equation 1-3

where

$$\frac{\varepsilon}{\varepsilon_0} = 1 + \chi = \varepsilon_r$$

Equation 1-4

In an ideal dielectric under an alternating field, the current is 90° out of phase with voltage, as the capacitor is charged up by the voltage, the current reduces to zero and when reversed the voltage drops to zero and the stored charge is released as the current reaches the maximum. In real dielectrics, when an

alternating current is applied to a dielectric, the current induced is not at 90º with the voltage as it does not reach maxima and minima at the same time [21]. Losses are prevalent such as those due to conduction and the flow of charge across a material or dielectric losses due to the rotation of atoms or molecules. This phase lag between the voltage and current can be represented using a phasor diagram, Figure 1-8, as it can demonstrate the real and imaginary parts.

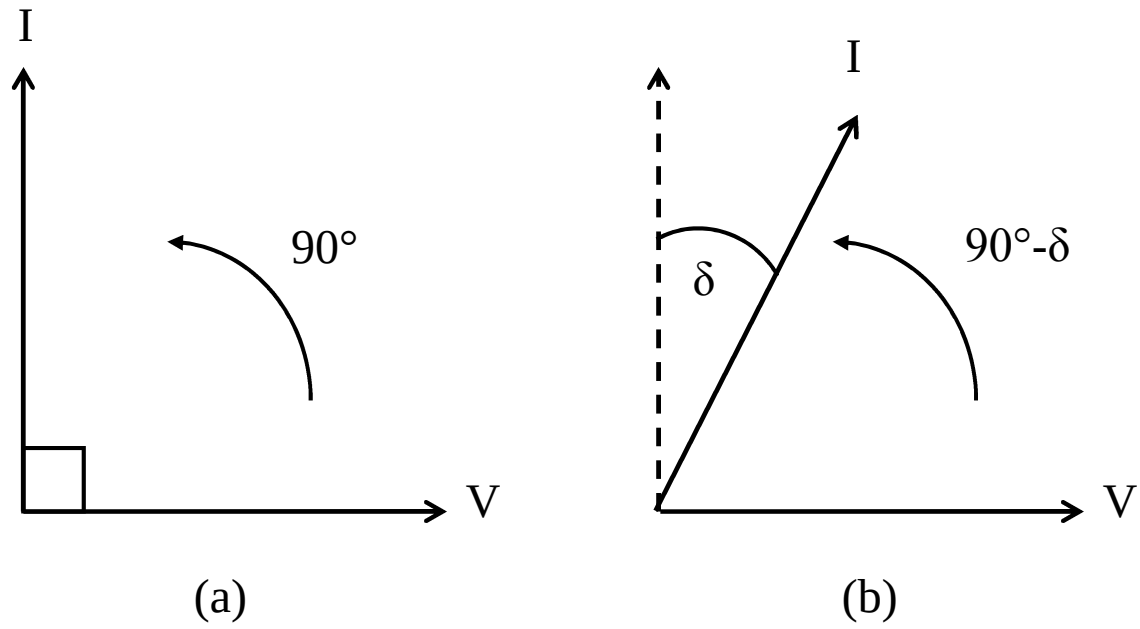

Figure 1-8. Phasor diagram of the current-voltage lag in (a) an ideal dielectric and (b) a real dielectric material

The complex permittivity can be expressed with real, ε_r' and imaginary components, ε_r'', and dielectric losses, tan δ, can be defined as the ratio between these, using the equations below.

$$\varepsilon_r^* = \varepsilon_r' + \varepsilon_r''$$

Equation 1-5

$$\frac{\varepsilon_r''}{\varepsilon_r'} = tan\delta$$

Equation 1-6

1.3.2 Polarization Mechanisms

We have so far considered the polarization of dielectric materials but not the mechanisms by which these materials become polarized. There are four commonly found mechanisms, as shown below in Figure 1-9, these are; atomic (electronic), ionic, dipolar (or molecular and orientation) and space charge (diffusional).

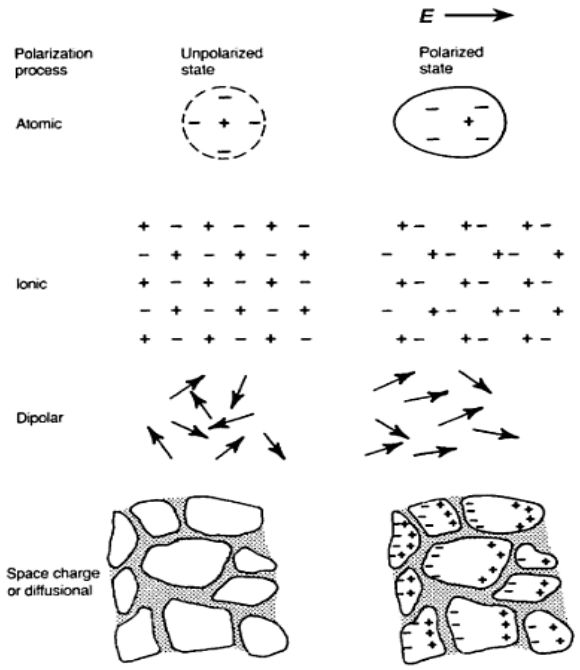

Figure 1-9. The four polarization mechanisms [18]

Atomic polarization is the most prevalent polarization mechanism as an electrical field will always displace the centre of positive charges with respect to negative charges in an atom or ion [18]. Ionic polarization inherently occurs in materials that are ionic, these have dipoles of sorts already at a localised level but there is no net dipole moment as they are balanced. Upon the application of a field, displacement of the ions from their equilibrium positions can lead to a distortion in the parameters of the dipole. Orientation polarization is common in free flowing materials such as liquids or gases as natural dipoles that can freely rotate are required. These dipoles will be randomly oriented and like the ionic mechanism carries no net polarization until the application of an external field at which point some alignment occurs, this can be the result of thermal activation also. Space charge is a mechanism that occurs at surfaces, grain boundaries,

lattice vacancies, dislocations etc whereby free charge carriers travelling through a material under an applied field become lodged on one of the previously mentioned defects and this leads to a local accumulation of charge which allows for a dipole moment to occur [18].

The real and imaginary parts of the permittivity are frequency dependent in a dielectric material. There are well distinguished relaxation frequencies, Figure 1-10, for each polarization mechanism and the Debye formulated the relaxation model to explain this.

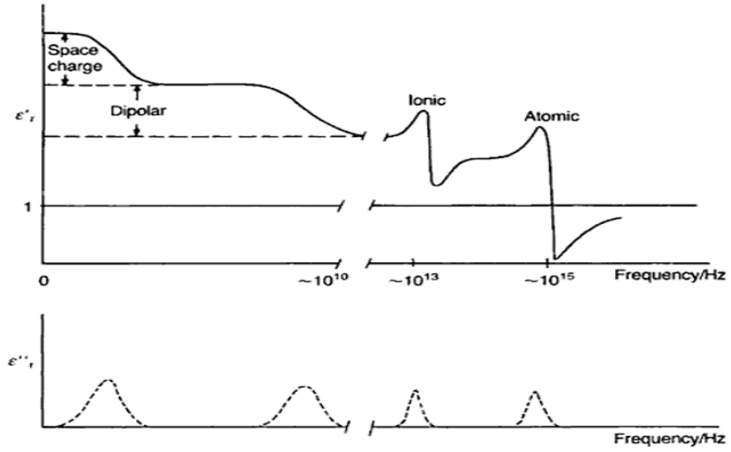

Figure 1-10. Variation of ε'_r and ε''_r with frequency [18]

1.3.3 Dielectric Breakdown

Under an applied electric field, a dielectric is subject to a limited amount of current flow. If the voltage is increased in excess of the maximum voltage that the dielectric can be subjected to then large currents will pass through the dielectric, which is known as dielectric breakdown. When this occurs, the insulating behaviour of the dielectric is altered as a conduction path has been produced. There are many mechanisms by which dielectric breakdown can occur, these include; intrinsic, thermal and discharge [18]. The breakdown strength of air is ~3 kV/mm, this means that the use of dielectric oil may be permitted in order to prevent breakdown across the sample edges. Contributing factors that affect the dielectric breakdown field includes; applied field frequency and duration, impurities, structural defects, sample geometry and thickness, electrode material, and ambient temperature, pressure and humidity [22].

1.4 Ferroelectricity

A ferroelectric is defined as a material that has two or more equilibrium orientations of the spontaneous polarization that are reversible in the absence of an electric-field [23]. These orientation states are crystallographically identical and only the polarization vector differs. This phenomenon was initially discovered in naturally occurring minerals such as Rochelle salt in 1921, during the "pre-perovskite era" [24].

1.4.1 Ferroelectric Curie Point and Curie Temperature

Ferroelectricity is only present in limited number of low symmetry non-centrosymmetric phases and this is usually across a finite temperature range. The temperature at which the transition from a ferroelectric phase to a high symmetry paraelectric phase occurs is known as the Curie point, T_C, at this temperature the thermal vibrations in the lattice provide enough energy to cause a transformation into an alternative energetically favourable state. This lower energy paraelectric state is always of higher symmetry than the ferroelectric phase. Spontaneous polarization falls to zero beyond this point.

The Curie temperature (T_0) is a different quantity from the Curie point (T_c) and is a material constant. The Curie temperature is not usually equal to the Curie point [18]. Dielectric permittivity reaches a peak at the Curie point and decreases at higher temperatures in accordance with the Curie-Weiss law.

$$\varepsilon_r = \frac{C}{T - T_0}$$

Equation 1-7

where C is the Curie constant, T_0 ($T_0 < T_C$) is the Curie-Weiss temperature.

Not all paraelectric phase transitions are governed by the same behaviour, although two common types occur, 1st and 2nd order, named as such due to the changes in the order parameter during the transition. A first order transition is common in tetragonal materials and is described as a sharp discontinuity in the order parameter. A second order transition demonstrates a continual shift of the

order parameter while the first derivative demonstrates a discontinuity, this is common in materials with rhombohedral symmetry.

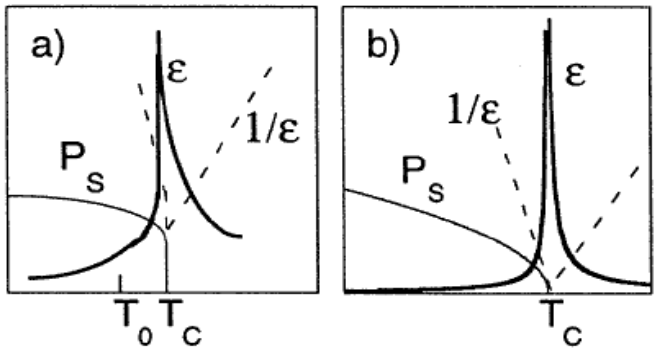

Figure 1-11. Spontaneous polarization and permittivity in (a) first-order and (b) second-order phase transitions [9]

1.4.2 Ferroelectric Phase Transitions

It is possible for changes in the crystal structure at lower temperatures that do not result in a loss of ferroelectric behaviour and these are known as ferroelectric-ferroelectric phase transitions. The T_C is still defined as the transition into the first ferroelectric phase and barium titanate, $BaTiO_3$, demonstrates a transition from cubic symmetry to the tetragonally distorted ferroelectric phase when cooled below ~130°C. However, a series of transitions occur below the T_C, such as from tetragonal to orthorhombic distortion at 0°C and from orthorhombic to rhombohedral symmetry at -90°C.

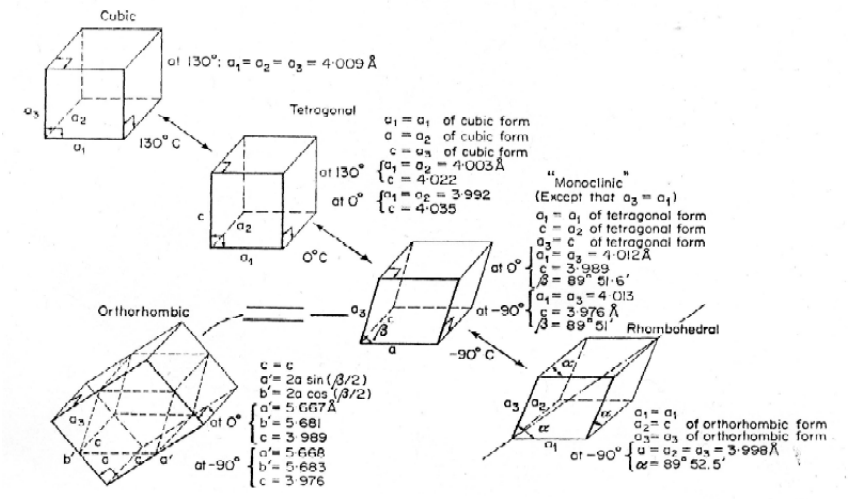

Figure 1-12. The temperature dependent phase changes of $BaTiO_3$ [25]

1.4.3 Domains

As previously discussed, when a material is cooled below the T_C, a phase transition from the paraelectric to the ferroelectric phase occurs. This leads to the onset of a spontaneous polarization which is a result of the alignment of electric dipoles. Regions with an aligned spontaneous polarization are known as domains [18]. Domain walls separate regions with differing polarization vectors and domains form in order to minimize the energy associated with depolarization fields and mechanical strains. They form with random polarization vectors leading to a zero net polarization. Domain walls reduce the overall energy of the system, and have an energy associated with their formation as they deviate from a perfect crystal, this means that a finite number of domain walls can be created. This situation arises when the energy associated with domain wall formation exceeds the energy reduction achieved by their formation. Lines *et al* discussed the variables affecting the observed domain pattern, these include; crystal symmetry, electrical conductivity, defect structure, the magnitude of the spontaneous polarization, sample geometry and the history of sample preparation [23].

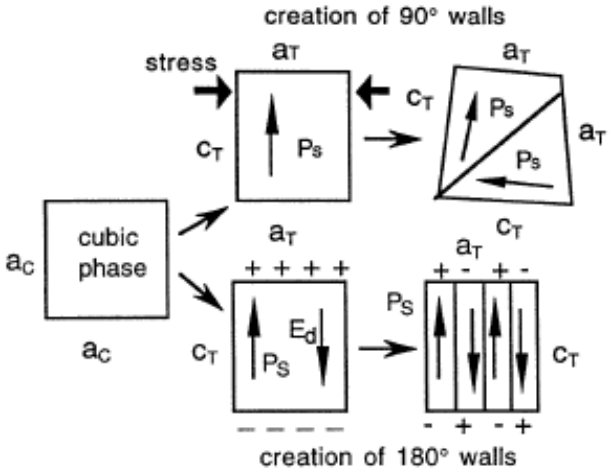

Figure 1-13. Formation of 90° and 180° domain walls in $PbTiO_3$ [9]

The formation of 180° domains occurs in an effort to reduce the energy associated with the spontaneous polarization formation and accompanying depolarizing field, E_d, in a process known as twinning [18]. The energy associated with the depolarization field can be greater than the energy associated with ferroelectric ordering, thus inhibiting ferroelectricity. In addition to 180° domains

in both tetragonal and rhombohedral crystals, the formation of 90° and 71°/109° domain walls are observed respectively. These non-180° domain walls aim to minimise the elastic energy in the ceramic, showcased in Figure 1-13, whereby the c_T axis will form perpendicular to the stress and the unstressed element, a_T, that is perpendicular to the stress polarization remains parallel [9].

A polycrystalline ferroelectric behaves macroscopically as a non-polar material even though the crystals comprising it are polar. In order to bring these materials into a polar state a static electric field is applied in a process known as poling, usually at elevated temperatures in order to 'soften' the lattice and increase domain wall motion. This process is applied to most piezoelectric materials with a few notable exceptions such as Rochelle salt [26]. Poling leads to a net remanent polarization.

1.4.4 Hysteresis

The most commonly used technique for investigating the degree of ferroelectricity is via polarization-electric field (P-E) loops, Figure 1-14, it is a graphical way of presenting domain wall switching in a ferroelectric material. It can be observed using a Sawyer-Tower circuit which is discussed in Section 2.2.4.

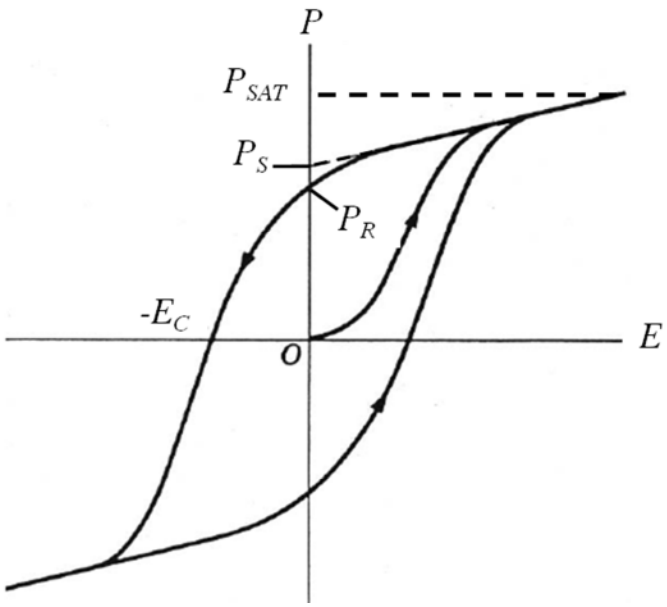

Figure 1-14. A typical hysteresis loop for a ferroelectric material [25]

As the electric field is increased from the origin, the polarization vector of domains with an unfavourable orientation will switch in the direction of the applied field. Once all the domains are aligned it will behave linearly until the saturation point, P_{SAT}, is reached, this is a field dependent term and in polycrystalline ceramics can greatly deviate from the achieved remanent polarization, P_R, which is the degree of polarization upon removal of the field where $E = 0$. The spontaneous polarization, P_S, is determined by extrapolating the P_{SAT} back to zero-field along a tangent. The electric field required for the polarization to diminish to zero is defined as the coercive field, E_C. When the field polarity is reversed and the coercive field is surpassed, domain reorientation in the opposite direction begins to occur. This is reversed once again and positive polarity is applied and the loop is complete. Hysteresis loops are electric field, temperature, and frequency dependent.

1.4.5 Relaxor Ferroelectrics

Professor Smolenskii and his contemporaries first discovered relaxor ferroelectrics in the 1950s. These are a distinct class of ferroelectric materials, typically perovskites although not exclusively, that can maintain multiple ionic species on the same crystallographic site [27]. Lead magnesium niobate, Figure 1-15, is regarded as the model relaxor ferroelectric although behaviour is not limited to lead-based ferroelectrics and it can also occur in compositions with multiple ions on the A-site. Characteristic properties of a relaxor ferroelectric include [28-29];

(1) A diffuseness of the temperature dependent properties related to the polarization. An example being a broad maximum in the permittivity accompanied with a shift in the T_{MAX} toward higher temperatures and the suppression of permittivity with increasing frequency.

(2) No obvious macroscopic phase transition to a polar phase in the region of T_{MAX} as probed by X-ray diffraction or optical techniques in the absence of an electric field.

(3) Spontaneous polarization appears at temperatures far beyond the permittivity maximum, T_{MAX}. Above the T_{MAX}, relaxors do not adhere to the Curie–Weiss law.

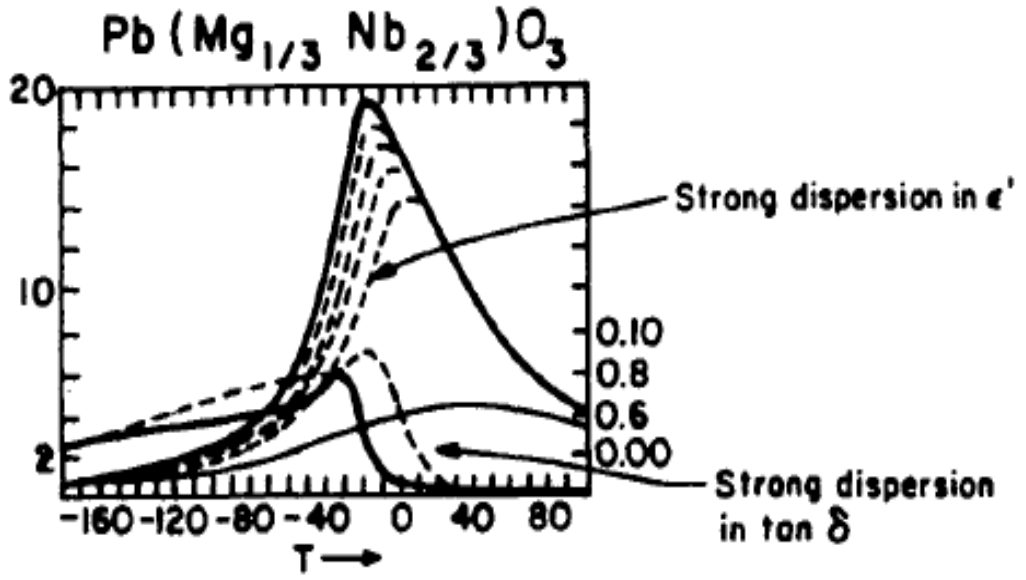

Figure 1-15. Relative permittivity as a function of temperature and frequency in lead magnesium niobate [29]

Several models have been proposed to describe relaxor behaviour, such as the compositional fluctuation model proposed by Smolenskii *et al* [30–33] whereby compositional variances of the B-site species with disordered 'B_1' and 'B_2' ions leads to fluctuations in the local ferroelectric Curie temperature, thus leading to a diffuse rather than sharp loss of spontaneous polarization and the T_{MAX} represented a mean Curie temperature [27].

Cross proposed the polar region size effect model based on an analogy with the superparamagnetic state, that the broad transition is due to the nucleation of polar nanoregions (PNR's) as the material cools through the T_C. The PNR's are believed to form due to multiple species on the same site which frustrates long range ferroelectric order [34]. As these PNR's can exist over a range of sizes, albeit relatively small, they are associated with a characteristic frequency.

1.4.5.1 Polar Nanoregions

The precise nature of polar nanoregions is still subject to intense debate and is far from understood. Liu suggested that when multiple ions appear on the same site, these create local strain fields frustrating long-range strain distortion of the unit cell which frustrates long range ferroelectric order [35]. This is often difficult to observe experimentally, however, long-range order and PNR's are highlighted below in Figure 1-16 with the use of PFM.

It is agreed that PNR's are lower-symmetry structural regions embedded in a higher symmetry matrix [27, 36]. The lower symmetry regions with correlations over nanometer-length scales that when arranged in random orientations do not lead to the destruction of the unit cell and will average to mimic the higher symmetry structure in which it is embedded such as cubic as observed using conventional x-ray diffraction techniques [27]. In order to investigate PNR's, alternative experimental techniques are required that probe the local structure such as TEM [37], PFM [38], and the atomic pair distribution function (PDF) technique can be employed with the use of high intensity X-rays, synchrotron or neutron diffraction facilities for the bulk structure [39-40]. The PDF approach has been used for some years on glasses and liquids.

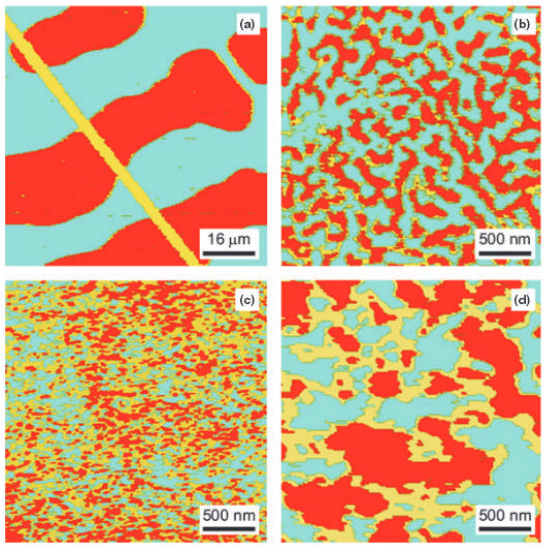

Figure 1-16. Piezoresponse Force Microscopy of (a) Polar structures in $PbTiO_3$ at room temperature and (b) PLZT below the transition temperature with (c-d) showing PNRs in $Sr_{0.61}Ba_{0.49}Nb_2O_6$ single crystal and $BaTi_{0.85}Sn_{0.15}O_3$ ceramic [41]

A number of questions remain unanswered regarding polar nanoregions especially with regard to how and when do they form, are they static or dynamic, and how are they measured, this section will attempt to address these issues. At high temperatures exceeding the Curie temperature, a non-polar paraelectric state can be observed in both ferroelectrics and relaxors. Upon cooling the ferroelectric ceramics will form a non-centrosymmetric phase that supports long-range ferroelectricity, while relaxors undergo a transition at the Burns temperature in which an ergodic relaxor forms with dynamic PNRs that house random dipole moment directions [42]. It is said that they are then frozen out as the temperature decreases and a nonergodic state is formed that resembles a glassy state with the absence of long-range non-centrosymmetric order [43].

As stated previously, the directions of the PNR dipole moments are said to be random over a mesoscopic scale when conventional structural analysis techniques are used (i.e. x-rays) [43]. This compositional disorder, which results in the formation of PNRs, is prevalent in both lead-based and lead-free materials. PFM is a useful technique when probing these structures as it is a highly localised technique that scan over nanometre-length areas and can be time-resolved allowing structures to be observed over a short time-scale [43].

Time-resolved PFM spectroscopic studies have suggested the existence of two distinct types of PNR's, static and dynamic [44]. These are proposed to exist over different temperature ranges, with the static PNRs deemed the precursor to long-range ferroelectric ordering [45]. Upon cooling from above the Burns temperature, dynamic PNRs coalesce and their size/volume gradually increase leading to a transformation to static PNRs [44]. Using PFM, 'Labyrinth'-like domain configurations have been observed and these are proposed to be due to static PNRs while the local relaxation in the piezoresponse has been owed to dynamic PNRs, this may account for the macroscopic aging effect observed.

The coherence length of the polarization is limited to a dimension at which thermal fluctuations dominate, this effect has been observed in bismuth ferrite based materials [46]. Generally, as a class of materials they can be described as

being electrically soft and have locally ordered domains and at sufficiently high electric fields the orientation of the nanodomains will align with the field which can lead to a large polarization and strain response. Upon removal of the field, the domains revert to short range ordering and a small remanent polarization is observed [46]. One technique used is to apply a sufficiently large electric field upon cooling, this can lead to the growth of large domains that promote the onset of long-range order and normal ferroelectric behaviour [47].

The effect of pressure and temperature upon the correlation length of the PNR's is not well understood although some evidence exists to show that the application of even moderate pressures in $Pb(Mg_{1/3}Nb_{2/3})O_3$ (PMN) can reduce the correlation length and therefore long-range order as shown in Figure 1-17. Samara *et al* found that pressure increases the soft-mode frequency which reduces the polarizability of the host lattice, and the correlation length, this correlation length is expected to be comparable to the PNRs [47].

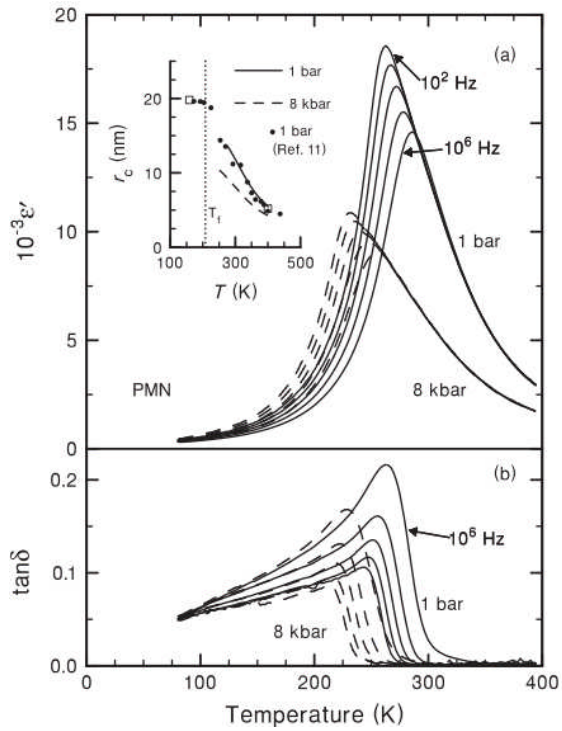

Figure 1-17. The effect of temperature and pressure upon the permittivity, loss and the correlation length, of the PNRs in PMN [47]

1.5 Piezoelectricity

1.5.1 Electrostriction

Before piezoelectricity can be defined, a distinction between electrostriction and piezoelectricity needs to be made. All dielectric materials subjected to the application of an electric field exhibits a small alteration in dimensions, this is known as electrostriction. This response is due to the displacement of charge and the effect is normally minimal and only appreciable in high permittivity materials or at elevated temperatures. Cady stated that during electrostriction, "the sign of the deformation which occurs with an applied field is independent of polarity of the field and proportional to the square of the field" [48], expressed as;

$$x = QP^2$$

Equation 1-8

where x is the strain and Q is the electrostriction coefficient.

1.5.2 Piezoelectricity Phenomenon

The term 'piezo' comes from the Greek translation for pressure, and can be literally translated as pressure electricity. Piezoelectricity is the property of some materials to develop electric charge on their surfaces when exposed to a mechanical stress, known as the direct effect, and due to the coupling between mechanical and electrical parameters the application of an electric field can produce a strain in the crystal, known as the converse effect as shown in Figure 1-18 [49]. Distinguished from electrostriction, the piezoelectric effect exhibits a linear coupling between the electrical and mechanical parameters [25], this can be observed in a change in sign of the deformation with varying electrical polarity.

Piezoelectricity was first discovered in 1880 by the brothers Curie [50] in zinc-blende, sodium chlorate, boracites, tourmaline, quartz, calamine, topaz, tartaric acid, cane sugar and Rochelle salt. It was some time before piezoelectric materials were used in practical applications, the onset of World War 1 accelerated research into piezoelectric crystals and the piezoelectric properties of quartz were utilised in the detection of submerged vessels [51]. Initial research led

to the belief that piezoelectricity was limited to single crystals due to the isotropic nature of bulk polycrystalline ceramics. The discovery of $BaTiO_3$ as a useful piezoelectric transducer [52–54] in 1945 introduced the beginning of the "perovskite" era and hundreds of piezoelectric materials have since been discovered [7]. A mathematical expression can be used to describe these relations, the direct effect is given as;

$$P_i = d_{ijk} X_{jk}$$

Equation 1-9

where X is a mechanical stress and d is a third rank tensor of the piezoelectric charge coefficient (C N^{-1}). The converse effect can be given as;

$$x_{ij} = d_{kij} E_k$$

Equation 1-10

where the units of the converse piezoelectric are (mV^{-1}).

The piezoelectric charge coefficients for the direct and converse effect are thermodynamically identical, although the sign of the response is dependent upon the vector of the mechanical or electric field. Piezoelectric properties are anisotropic so relevent tensor notation is used to define directions and coefficients.

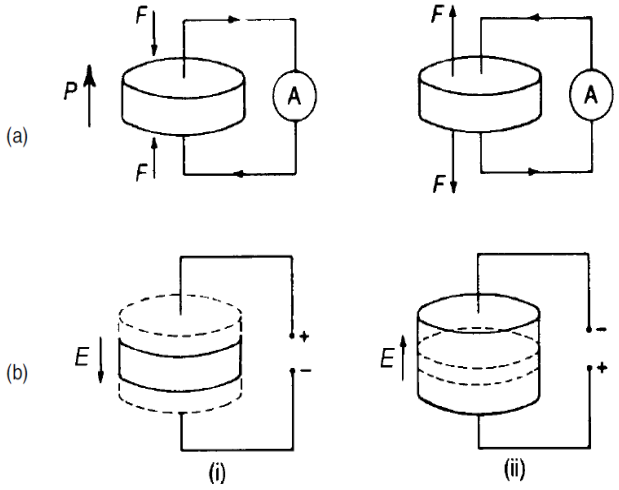

Figure 1-18. Direct and Converse Piezoelectric effect [18]

1.5.3 Piezoelectric Modes

The tensor notation can be quite complex but due to symmetry constraints in most piezoelectric systems these can be simplified with reduced notation. When considering the converse effect, d_{ij}, the first subscript gives the direction of the electric field. The second subscript gives the axis of the mechanical stress or strain. The polar axis is taken as parallel to the poling direction and is denoted 3. Indices 4,5 and 6 refer to shear planes about axes 1,2 and 3 respectively, due to symmetry many of the combinations cancel to 0. The two main piezoelectric coefficients, the piezoelectric charge coefficient (d_{ij}) and the piezoelectric voltage coefficient (g_{ij}) are used when evaluating the properties relevant to actuators and sensing applications. The modes of operation that are commonly used are shown in Figure 1-19, along with the governing equations.

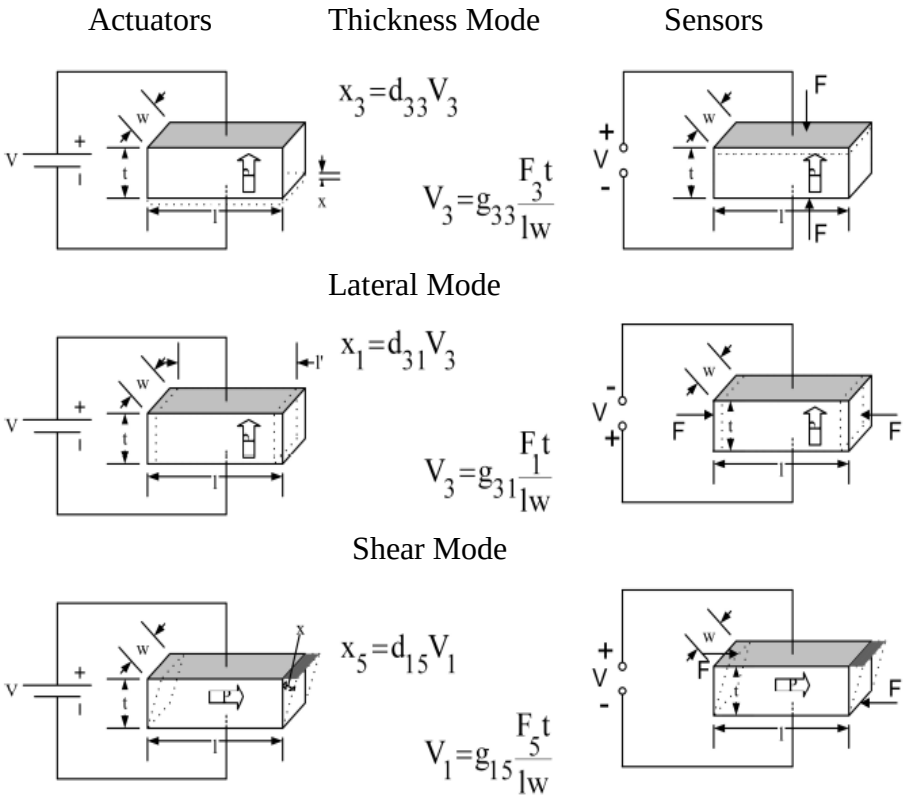

Figure 1-19. Operational modes of piezoelectric elements in actuator and sensor modes with corresponding formulas where V = Electric-field, x = strain, F = force, P = poling direction, t = thickness, w = width and l = length [55]

1.5.4 Temperature Stability

The temperature dependence piezoelectric coefficients are extremely important when designing novel piezoelectric ceramics. Zhang *et al* has discussed in a number of publications that in order to obtain high T_C ceramics, piezoelectric properties may have to be sacrificed [49, 56–58]. High T_C ceramics are more likely to offer improved temperature stability in their electrical performance and higher Q_M values (the mechanical quality factor) [59]. The thermal stability of the piezoelectric coefficients are linked to a number of factors, namely the intrinsic and extrinsic contributions.

The intrinsic effect is dominated by distortions of the lattice and domain wall vibrations, these are reversible and non-lossy [60]. The temperature dependence of the intrinsic piezoelectric response can be approximated using Landau theory [49], to give the following equation;

$$d = 2\varepsilon_r \varepsilon_0 Q P_S$$

Equation 1-11

The polarization and permittivity demonstrate strong temperature dependence. The electrostriction coefficient is largely temperature independent [61–63], although this is disputed [64]. It is therefore apparent that the type of phase transition the material undergoes when exceeding the Curie temperature will have a significant impact upon the temperature stability of the piezoelectric properties.

Extrinsic contributions are often described as having the most profound effect upon piezoelectric properties, Eitel suggested that they could account for up to 70% of the total piezoelectric response in high-performance ceramics [17] as the efficiency of the poling process is largely related to domain structure. The extrinsic effect is due to the domain structure, particularly the density and mobility of the domain walls. These are frequency, field, time dependent, non-linear (as are the majority of ferroelectrics at significant fields) and lossy [60]. An understanding and ability to control the domain structure has been shown to be

important across a range of systems. Comyn reported low extrinsic contributions in the high temperature $BiFeO_3$-$PbTiO_3$ (BFPT) system, proposed to be due to the clamping of ferroelastic domain walls resulting in low piezoelectric charge coefficients. The extrinsic effect was shown to increase with temperature, in the tilted and untilted phases in rhombohedral PZT [65], as domain wall motion is a thermally activated process [66]. Dopants can be utilised in an effort to control these effects, this will be discussed in more detail in Chapter 1.5.7.

1.5.5. Electromechanical Coupling

Jaffe defined the electromechanical coupling factor, *k*, as "possibly the best single measurement of the strength of the piezoelectric effect" [25]. This provides an indication as to the efficiency of material during the conversion of electrical to mechanical energy when a material is subject to an applied electric field, or vice versa when a mechanical stress is applied. The relationship is given in terms of k^2:

$$k^2 = \frac{electrical\ energy\ converted\ to\ mechanical\ energy}{input\ electrical\ energy}$$

Equation 1-12

$$k^2 = \frac{mechanical\ energy\ converted\ to\ electrical\ energy}{input\ mechanical\ energy}$$

Equation 1-13

Values of the electromechanical coupling are always <1, the highest values can be found in single crystal and relaxor materials. Analogous to the subscripts used to describe the piezoelectric charge and voltage coefficients a similar notation system is used to describe the electromechanical coupling. This report will often refer to k_p values as these can easily be determined in the laboratory, this represents the planar coupling of a thin disc, and illustrates the coupling between

an electric field parallel to the poling vector (direction 3) and the radial response perpendicular to the poling vector (direction 1 and 2).

1.5.6 MPB

A morphotropic phase boundary (MPB) is a practically temperature independent phase boundary between differing symmetries although in reality there is some divergence from the original definition [67]. Ahart discussed how the definition has evolved over time, the original use meaning “phase transitions due to compositional changes”, now the common parlance amongst researchers refers to a region that “separates tetragonal symmetry from rhombohedral symmetry by varying the composition in ferroelectrics” [68]. MPBs are commonly found in perovskite solid solutions, and are the basis of the majority of commercial electroceramics. A significant increase in the dielectric and piezoelectric properties can be observed in this region, due to the increased polarizability from the coupling between two varying crystallographic symmetries. During poling, when subject to large static electric fields, the increased number of thermodynamically equivalent states allows for a large degree of alignment between the ferroelectric dipoles, with 6 and 8 polarization vectors existing for the tetragonal and rhombohedral phases respectively allowing a total of 14 possible polarization vectors thus increasing the polarizability and piezoelectric properties. The commercially dominant $PbZrO_3$-$PbTiO_3$ (PZT) utilises an MPB and this will be considered in further detail below.

1.5.6.1 PZT

After the discovery and early success of $BaTiO_3$ much research centred on alternative ferroelectric perovskite systems. Pure $PbTiO_3$ is tetragonally distorted and belongs to the P4*mm* space group, the c/a lattice vector ratio is 1.063 [69] which leads to high anisotropy of its piezoelectric properties [70] that are maintained up to 490 °C, and is postulated to be the result of covalence of the Pb-O bond [13]. A direct result of this anisotropy of the unit cell is the difficulty in synthesising the bulk ceramic form when the grain size exceeds 1 μm [71]. The enhancement of piezoelectric properties in $PbTiO_3$ compared to $BaTiO_3$ and

$SrTiO_3$ was proposed to be owed to the deformable and polarizable nature of Pb [69].

$PbZrO_3$ was also discovered and the relatively modest Curie temperature was established, belonging to the orthorhombic space group up to 234 °C. It has antiferroelectric ordering whereby the cations adopt an antiparallel arrangement along $[110]_p/[-1-10]_p$ directions, thus leading to a net spontaneous polarization of zero.

$Pb(Zr_{1-x}Ti_x)O_3$ is formed as a result of the solid solution between $PbTiO_3$ and $PbZrO_3$ with the MPB located where x = 0.48. Work carried out in Japan by Shirane, Takeda and Sawaguchi outlined the phase diagram of solid solutions between $PbTiO_3$ and $PbZrO_3$ [72–74] but was largely centred away from the MPB, ultimately it was work by Jaffe that lead to the realisation of PZT's exceptional piezoelectric properties at the MPB [75] as highlighted in Figure 1-20. Since this time, PZT has been the mainstay for high performance actuators and transducers owed to its outstanding piezoelectric properties shown in Table 1-1. It is the most widely used commercial piezoelectric ceramic as it is extremely versatile and can be fabricated into many shapes and sizes with relatively low cost processing techniques. Despite its widespread use the electromechanical response is still not fully understood.

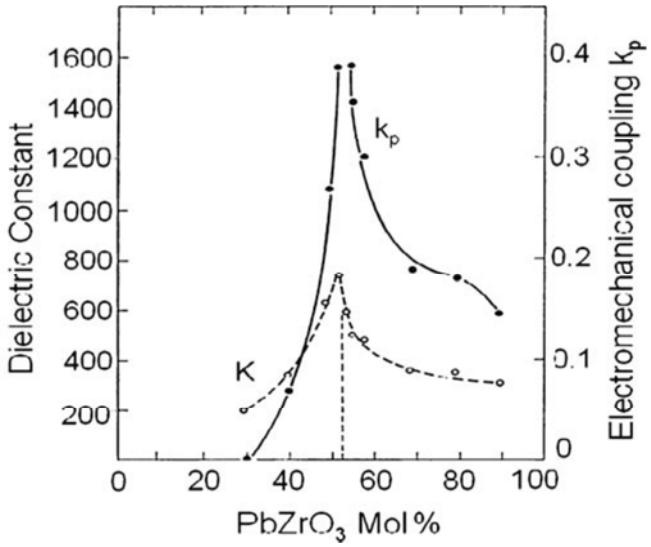

Figure 1-20. Dielectric constant and electromechanical coupling factor across the morphotropic phase boundary for PZT [76]

Table 1-1. Key properties of undoped MPB PZT ceramics [77]

d_{33}	d_{31}	d_{15}	k_p	ε_r	T_C (°C)
223	93.5	494	0.529	800	386

In order to explain the enhancement of electrical properties at the MPB it is imperative to explain its structural origin. At ambient temperatures small additions of lead titanate to lead zirconate generate a transition from orthorhombic symmetry to rhombohedral symmetry where the antiferroelectric ordering diminishes and ferroelectric ordering is induced. Since its discovery the accepted view of the MPB was that it was temperature independent and separated regions of rhombohedral and tetragonal symmetry as shown in Figure 1-21 and that the enhanced polarizability was a result of the coupling between two equivalent energy states in an almost 'schizophrenic' form.

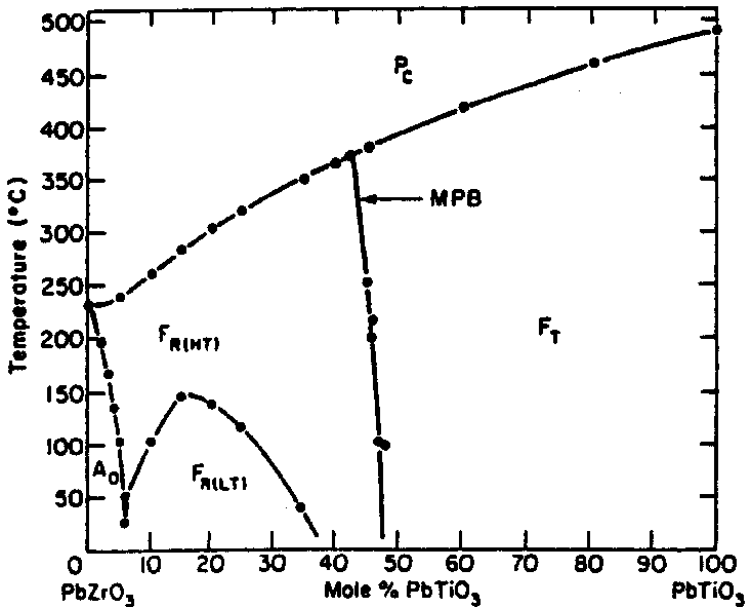

Figure 1-21. Phase diagram of the $Pb(Zr_{1-x}Ti_x)O_3$ system from 1971 [25]

However, since the late 1990s many publications have presented data revealing lower symmetry intermediary monoclinic phases separating the tetragonal and rhombohedral symmetries using synchrotron x-ray diffraction to probe the bulk structure [78] as confirmed by Woodward in 2005, Figure 1-22,

based upon electron diffraction data which is a localised technique [79]. First-principle calculations support the existence of the monoclinic phase [80]. The nature of the MPB is still a matter of contention for researchers, with a number of publications illustrating this [81–85]. In response to the evidence suggesting the existence of a monoclinic phase a number of publications discussed its role in generating the favourable piezoelectric coefficients in PZT. Guo used high resolution x-ray powder diffraction to confirm that piezoelectric strains observed in PZT [86] were found to be along directions associated with the monoclinic phase and concluded that the origin of the exceptional piezoelectric properties were due to polarization rotation as the polar axis of the monoclinic phase lies in the [110] direction and is flanked by the tetragonal [001] and rhombohedral [111] polar axes which allows polarization rotation without symmetry changing phase transitions [85–87], although the effect of internal stress in generating lattice strain as a result of domain switching was overlooked.

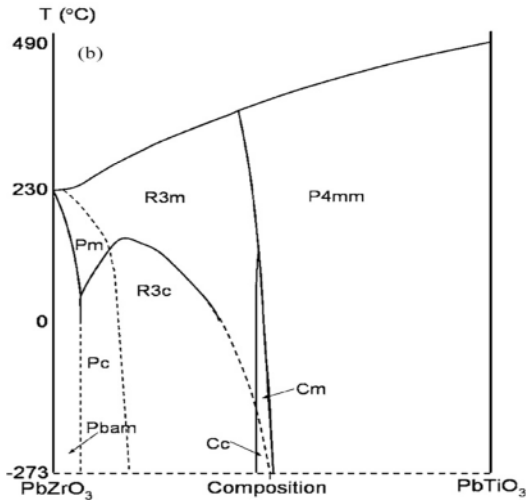

Figure 1-22. Phase diagram proposed in 2005 by Woodward et al [79]

PZT is also favoured as it can accommodate a number of dopant ions and allow for further modification of the structural and piezoelectric properties that can be tailored for specific applications, this has led to a wide assortment of commercially available PZT piezoceramics. Substitutional doping of PZT on the A or B site, while providing favourable electrical properties, often results in the reduction of the Curie point and operating ceiling [88].

1.5.7 Doping

Substitutional doping is used in a wide range of materials but will be discussed here in the context of PZT for clarity and brevity. The modification of PZT is often centered near to the MPB with substitution of small but significant amounts of cations (0.05-5 mol%) on either the A-site or B-site [18]. Doping of PZT often falls in to one of the two main classes, donor or acceptor and these are said to result in “soft” and “hard” PZT ceramics respectively. Donor dopants have a higher charge than those of the ions they replace while acceptor dopants have a lower charge than those of the ions they replace.

Donor doping of PZT generally reduces the concentration of oxygen vacancies which also reduces the amount of domain stabilising defect pairs [18], thus increasing domain wall mobility thus “softening” the material, both electrically and mechanically. The increase in wall mobility increases dielectric and piezoelectric properties as well as decreasing the coercive field [89]. Typical donor dopants include La^{3+} on the Pb^{2+} A-site and Nb^{5+}/Sb^{5+} on the B-site. As there are fewer vacancies in the oxygen cage and increased Pb vacancies the energy barrier required for electronic/ionic transport is reduced and dielectric loss can increase, due to friction between domain walls under excitation.

Acceptor doping i.e. K^{+} on the A-site or Fe^{3+} substituting for Ti^{4+}/Zr^{4+} on the B–site results in increased oxygen vacancies. The oxygen vacancies are created as it maintains electroneutrality, as two lower valence dopant ions lead to the creation of one oxygen vacancy. When subjected to local or applied fields thermally activated re-orientation of the dipoles occurs which align with the polarization vector, these create internal bias fields that stabilize the domains and reduce wall mobility by the mechanism of pinning and/or clamping, ergo “hardening” the material. This internal bias field can be observed in polarization-field loops in the form of asymmetry in PZT and lead-free materials [90-91]. In general, acceptor doped materials offer a lower permittivity, lower dielectric loss, lower piezoelectric coefficients and a higher coercive field.

1.5.8 Applications

The applications that exploit piezoelectric devices range from the sophisticated to the relatively simple with an ever-increasing number. As a result Table 1-2 aims to collate the main uses of piezoelectric devices.

Table 1-2. Applications of piezoelectrics

Operating Mode	Uses
Actuators	Micropositioning
	Diesel fuel injection
	Inkjet printer heads
	Motors
Sensors	Flow meters
	Engine ignition knock sensors
	Air bag sensors
	NDT Testing
Voltage Generators	Gas and cigarette lighters
	Camera flashes
Ultrasonic Generators	SONAR
	Ultrasonic Cleaning

1.5.8.1 Actuators

When considering a material for actuator applications the free stroke and blocking force at the maximum applied electric-field are two of the most important materials parameters. The free stroke is the displacement achieved by the actuator for a given applied field while the blocking force can be defined as the required force to return a fully extended actuator to its zero-position. A piezoelectric can only be used as an actuator in the region of a stroke versus force graph that intersects the axes as shown in Figure 1-23. The electric fields that actuators operate at are typically 0.5 kV/mm and largely in the unipolar mode to limit the degradation of the properties in the piezoceramic component [92].

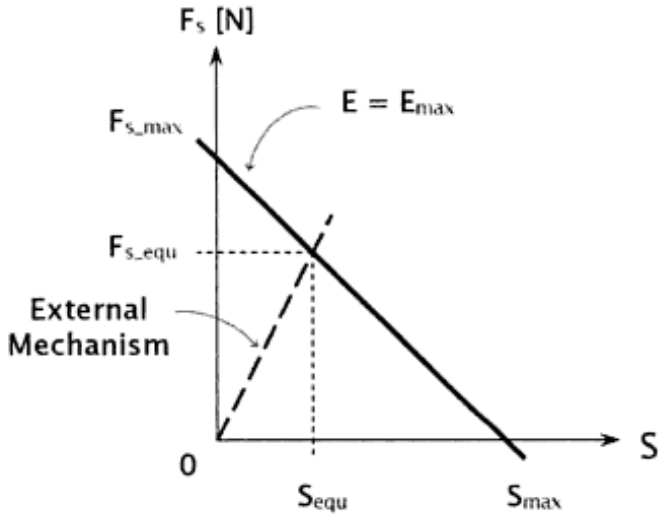

Figure 1-23. Blocking force (F) versus free stroke (S) [93]

1.5.8.2 Sensors

Sensors not only require high piezoelectric coefficients but a high resistivity and time constant, a high resistivity is also favourable for poling. The larger this value is then the longer a device can maintain the charge associated with an applied stress or strain [59]. The longer the charge is maintained then the longer the electronic processing system has to detect it. The RC time constant reduces with increased temperature which reduces sensitivity. The minimum useful frequency of a sensor can be defined by the lower limit frequency which is inversely proportional to the RC time constant, it is given as;

$$f_{ll} = \frac{1}{2\pi RC}$$

Equation 1-14

where R is resistance and C is capacitance

Below this frequency the charge will dissipate before detection so a low f_{ll} is desired to allow a large sensing bandwidth [94].

1.6 Ferroelectric and Piezoelectric Materials

This section aims to outline currently available materials, some of which are commercially available while some are of purely academic interest. The motivation for this work has previously been outlined, it was stated that there is a demand for high temperature piezoelectric ceramics as evidenced in Figure 1-24. While PZT can satisfy the demand for many applications there remains a need for operating temperatures exceeding those of PZT, the leading candidate is $BiScO_3$-$PbTiO_3$ (BSPT) as it fulfils the performance requirements, however, it is prohibitively expensive.

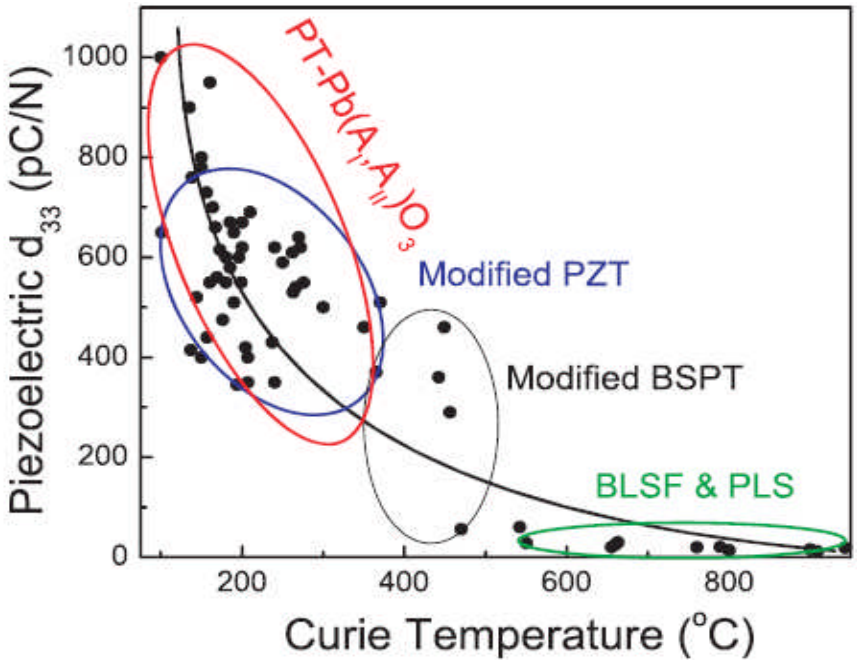

Figure 1-24. Piezoelectric activity versus the Curie temperature for various perovskite and non-perovskite families [95]

1.6.1 Lead-free Piezoelectric Ceramics

There has recently been an impetus towards lead-free piezoelectrics in light of EU environmental legislation, with directives encapsulating waste from electrical and electronic equipment (WEEE), restriction of hazardous substances (RoHS) and end of life vehicles (ELV) [96]. A number of excellent review articles have been published in this field [76, 95] that are far-reaching, however, this section will focus on two of the principal families of materials.

1.6.1.1 $(K_{0.5}Bi_{0.5})TiO_3$-$(Na_{0.5}Bi_{0.5})TiO_3$

$x(K_{0.5}Bi_{0.5})TiO_3$-$(1-x)(Na_{0.5}Bi_{0.5})TiO_3$ (KNBT) is formed as the result of a solid solution between the rhombohedral (R3c) $(Na_{0.5}Bi_{0.5})TiO_3$ (NBT) and the tetragonal (P4mm) $(K_{0.5}Bi_{0.5})TiO_3$ (KBT) end members which was first reported by Buhrer in 1962 [97]. An MPB exists at x = 0.18 - 0.2 and an increase in dielectric and piezoelectric properties is associated with this region. The crystallography underpinning this system is still lacking clarity with recent publications offering alternative views with over four differing phase diagrams proposed as summarised by Carroll [98]. The structure of the respective end members is agreed upon and both have proved difficult to fabricate in pure form due to the volatilisation of the K^+, Na^+ and Bi^{3+} ions which are partially stabilised in a solid solution although the importance of sintering conditions cannot be overstated as a modification of the sintering temperature by 40 °C resulted in an increase in the d_{33} from 155 to 192 pm/V [99].

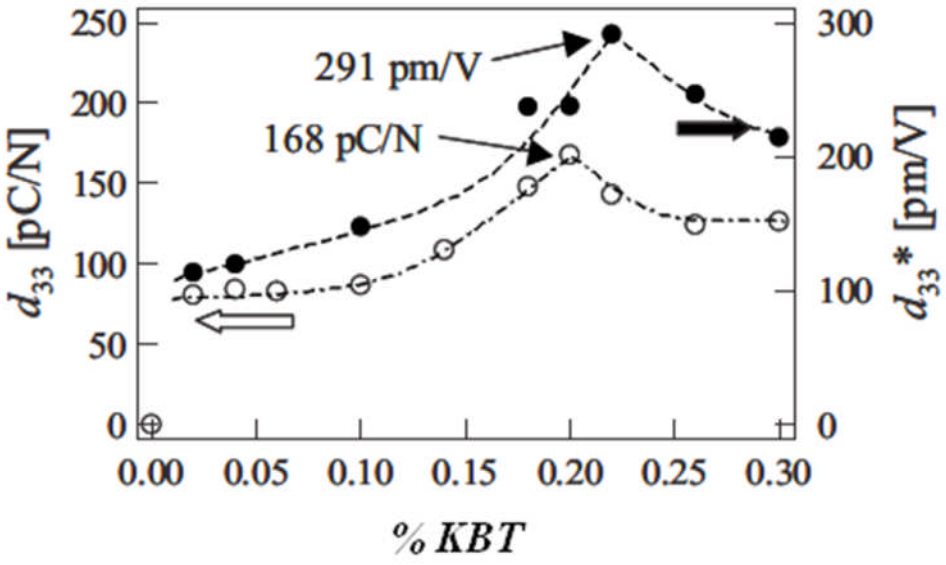

Figure 1-25. Low-signal and high-signal piezoelectric coefficient as a function of composition [100]

KNBT as with many lead-free piezoelectric ceramics suffers from depolarization temperatures that are much lower than the Curie temperature and the peak in permittivity. Where x = 0.2 the Curie temperature is at 320 °C while the depolarization temperature is extremely modest at 130 °C [101], thus limiting the potential applications.

1.6.1.2 $(K_{0.5}Na_{0.5})NbO_3$

The solid solution of xNaNbO$_3$-(1-x)KNbO$_3$ (KNN) was first reported in 1955. An enhancement of electrical properties was reported between the two orthorhombic end members where x = 0.5, sodium niobate (NaNbO$_3$) is antiferroelectric (AFE) and potassium niobate (KNbO$_3$) is ferroelectric [89]. Despite the enhancement of electrical properties where x = 0.5 it cannot be defined as an MPB as there is no modification in crystal symmetry, the enhanced properties are owed to a polymorphic phase transition whereby an increased polarizability is linked to a temperature induced transition. The phase diagram is presented in Figure 1-26. The Curie temperature of this system is above that of PZT at 420 °C with an intermediate phase transition from orthorhombic to tetragonal at 200 °C. Initial efforts produced moderate electrical properties with piezoelectric charge coefficients of 80 pm/V [102] until more sophisticated processing methods were utilised such as hot pressing and spark plasma sintering which produced much improved piezoelectric coefficients [103-104]. The modest piezoelectric properties from conventional processing are due to extreme sensitivity to non-stoichiometry and air-fired ceramics suffer from poor densification and volatility of the alkali species above 1140 °C [105], as such repeatability is an issue [106]. It is also proposed that the relatively low electromechanical properties are owed to the phase boundary between the two orthorhombic phases. These processing issues coupled with its modest electrical properties do not currently make it a suitable replacement for PZT [106].

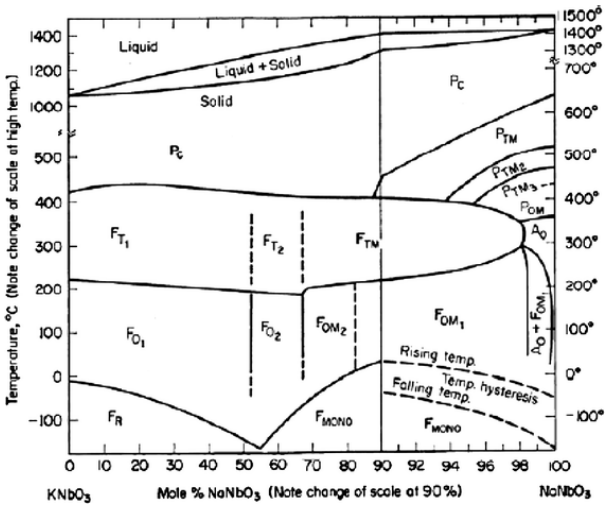

Figure 1-26. Phase diagram for the $KNbO_3$-$NaNbO_3$ system [25]

A large body of work exists focussed on doping, sintering aids and texturing in an attempt to increase the piezoelectric properties of KNN ceramics. Saito *et al* reported piezoelectric coefficients in excess of 400 pm/V by doping with $LiTaO_3$ and crystallographic texturing in <001> oriented ceramics [107], subsequently many other dopants were considered such as $LiNbO_3$, $LiSbO_3$, and $(Li_{0.5}Ag_{0.5})NbO_3$ amongst others [105, 108-109]. Many of these compositional studies have attempted to displace the orthorhombic-tetragonal polymorphic phase transition (T_{O-T}) to near ambient temperatures, however, the increase in piezoelectric properties is often at the expense of the temperature stability of the piezoelectric response [105].

1.6.2 $Bi(Me)O_3$ Based Perovskites

Research into new piezoelectric materials is broad and far reaching so it is not feasible to review the entire field. This section aims to discuss high temperature $Bi(Me)O_3$ perovskite systems with a valence of 3+ that are used in conjunction with alternate symmetry end members in order to engineer an MPB. The tetragonal end member is usually $PbTiO_3$ although a lead-free alternative has been included in order to elucidate the motivation behind this current work.

$BiFeO_3$ was first discovered in 1957 by Royen [110], it is unique among the $Bi(Me^{3+})O_3$ family as the compound can be formed at ambient pressures using conventional processing techniques [111], while a limited number of multiple cation B-site compounds have been fabricated. Since its discovery, a great deal of research has centred upon its multiferroic properties, Smolenskii *et al* confirmed its antiferromagnetic ordering [112] and ferroelectricity was subsequently established in 1970 by Teague [113]. The structure of $BiFeO_3$ is rhombohedrally distorted belonging to the R3c space group as determined by Michel in 1969 [114], which differs from earlier interpretations as belonging to the R3m space group. The $BiFeO_3$ compound has a Neel temperature, T_N, of 370 °C and ferroelectric T_C of 825 °C which has led to its wide use in binary compounds.

A limiting factor of bulk $BiFeO_3$ ceramics is conductivity owed to the difficulty in fabricating single-phase materials, and problems associated with; the

thermodynamic stability of $BiFeO_3$, the reaction kinetics between Bi_2O_3 and Fe_2O_3, purity of the starting powders, cooling rates and the furnace atmosphere [115-116]. The level of conductivity is so problematic that it is not simply application limiting but the characterisation of the basic ferroelectric and piezoelectric properties is difficult.

The magnetic structure of $BiFeO_3$ was initially determined by neutron diffraction, from a simplistic approach the magnetic order can be described as G-type with each Fe^{3+} cation surrounded by six Fe^{3+} cations with antiparallel spins [117]. Current thinking suggests that the magnetic moment is incommensurate, with chiral canting of the spins over a distance of 620 Å [118] which cancel out to zero. This may explain the weak ferromagnetism observed in previous studies [114].

In an attempt to assuage the problems of conductivity and the incommensurate magnetic ordering a number of approaches have been attempted. A large number of transition metal ions have been doped on the A and B-site, including though not exclusively– Co, Ni, Nb, W, Ti, Pb and Mn [119–122]. Mn doping in $Bi(Mn_xFe_{1-x})$ leads to the collapse of the magnetic spiral and a collinear antiferromagnetic structure for $x > 0.2$ [123]. Rare earth dopants, i.e., Dy, La, Gd, Nd, Sm [124–128] have also been doped on the A-site to modify the electric and magnetic properties. $BiFeO_3$ has also been used to form solid solutions with satellite tetragonal end members in order to engineer an MPB to increase ferroelectric and piezoelectric properties. The formation of secondary phases, such as $Bi_2Fe_4O_9$, is inhibited by the formation of solid solutions with other stable members of the perovskite family.

1.6.2.1 $BiFeO_3$-$PbTiO_3$

The xBiFeO$_3$-(1-x)PbTiO$_3$ (BFPT) system has been well studied since its discovery in the 1960s [129]. A solid solution is formed across the entire compositional space between the previously discussed rhombohedral $BiFeO_3$ (R3c) end member, which has a T_C of 825 °C and exhibits a tilted oxygen octahedral, a pre-requisite for anti-ferromagnetism, and the tetragonally distorted lead titanate (P4mm) which has a T_C of 490 °C [25]. Figure 1-27 shows the magnetic and ferroelectric phase diagram where *I* is the tetragonal phase, *II* is the MPB consisting of rhombohedral and tetragonal phase and *III* is the rhombohedral phase, Fedulov *et al* located the MPB at x = 0.66-0.73 and reported a T_C of ~700°C although this has since been widely accepted as being at 632 °C.

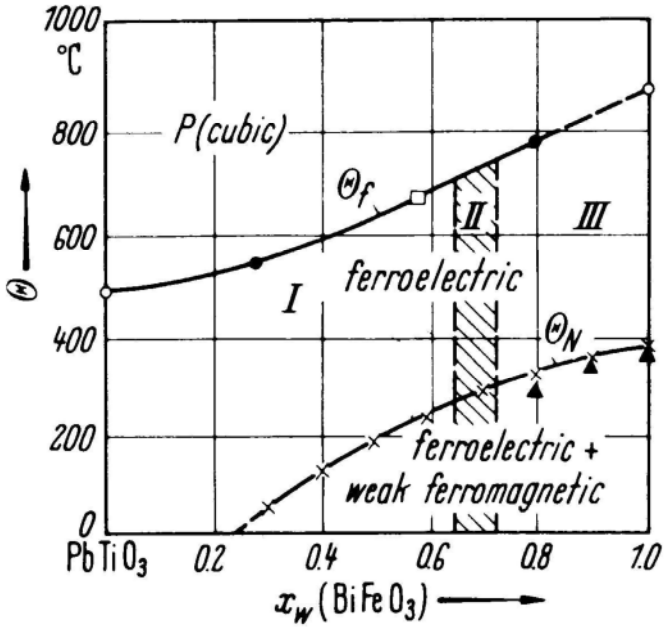

Figure 1-27. Magnetic and ferroelectric phase diagram for BFPT across the compositional space [130]

Researchers have debated the location and breadth of the MPB vehemently ever since the initial mapping of the phase diagram. The existence of an orthorhombic phase has also recently been proposed by Zhu *et al* [131] who reported the MPB existed where x = 0.6-0.8, Woodward *et al* located the MPB at x = 0.6-0.7 [132] and Bhattacharjee *et al* suggested that the MPB exists over a much narrower range where x = 0.67-0.71 [133]. Much of the disagreement is a result of the sample form or experimental techniques used, this is summarised in

Table 1-3. All of the previously mentioned studies have used powder XRD, while it is a powerful technique it cannot be readily used for identifying the location of the oxygen ions due to their low scattering factor (related to the atomic number, Z), this is also true for synchrotron x-rays and only neutron diffraction can analyse the average bulk structure. The penetration depth of laboratory x-rays is relatively small, of the order of a handful of grains, and the surface can have contradictory symmetry to the bulk material, whereas neutrons can penetrate large samples which enables analysis of the entire sample. The conflicting sample forms, processing and post-processing treatment results in differing stress arrangements thus yielding reproducible results can be problematic.

Another structural phenomenon observed in the BFPT system is the enhanced tetragonal c/a ratio with increased $BiFeO_3$, shown in Figure 1-28. The increased tetragonality observed with substitution of the $PbTiO_3$ end member is almost exclusive with a limited number of systems reporting a similar manifestation [134]. The tetragonal distortion increases from 1.063 in pure $PbTiO_3$ to ~1.187 at the MPB, as a result of the huge tetragonal strain much of the early work into BFPT was conducted on powders as bulk ceramics were prone to intergranular fracture upon cooling. BFPT also possesses a broad mixed symmetry region (MSR) at $0.4 < 0.7$ between the P4mm and R3c phases whereby both phases coexist simultaneously, associated with the relief of internal stresses whereby the material transforms into the rhombohedral phase [57, 135]. The hybridisation between the (Bi,Pb)(6s,6p) and O(2p) orbitals has been reported to be the origin of the large c/a ratio and strong ferroelectric ordering [136], Pb-O hybridisation was calculated to be driving force behind the larger ferroelectric response in $PbTiO_3$ compared to $BaTiO_3$ [5]. As with PZT and other MPB systems the dielectric and piezoelectric properties are enhanced in this region. Due to the increased lattice strain, it would follow that the highest achievable spontaneous polarization would be in the composition exhibiting the highest spontaneous strain, x_S. It has been observed in La-doped BFPT that the domain reorientation is often suppressed [137-138], Leist *et* al concluded that nucleation of new domains is inhibited due to extremely high stress levels generated upon cooling through the paraelectric phase transition, thus the creation of domain

walls induced via an electric field is energetically unfavourable which also suggests that the domain wall density is low for materials with high c/a ratios compared to those with low c/a ratios [138]. Large poling fields are required in order to exceed the coercive field in BFPT, this value can be an order of magnitude greater than those of commercial PZT ceramics.

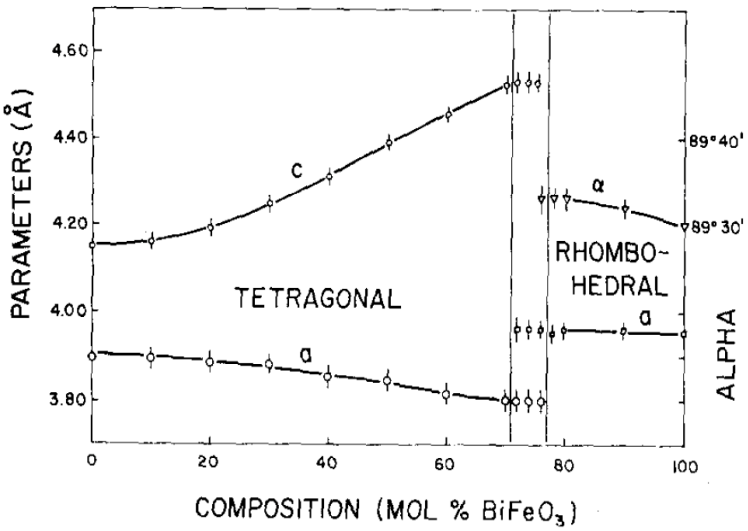

Figure 1-28. Lattice parameters for BFPT [139]

Table 1-3. Summary of crystallographic data available for BFPT

Author	Sample	Experimental Technique	MPB Location	Max c/a Ratio	Max c/a Location
Fedulov (1964)	Undisclosed	Powder XRD	0.66 < x< 0.73	1.17	0.66
Sai Sunder (1995)	Crushed pellets	Powder XRD	0.7 < x < 0.8	1.187	0.7
Woodward (2003)	Annealed crushed pellets	Powder XRD	0.6 < x < 0.7	1.15	0.7
Bhattacharjee (2007)	Undisclosed	Powder XRD	0.67 < x < 0.71	1.187	0.69
Zhu (2008)	Ceramic pellets	Powder XRD	0.6 < x < 0.8	1.187	0.69

A high resistivity is therefore paramount in order to pole the materials with the large electric fields required, this occurs above room temperature in order to reduce the abnormally high coercive field. In BFPT, the resistivity was found to be sensitive to compositional changes with a value of ~150 MΩ.m observed at 100 °C with an applied field of 1 kV/mm at x = 0.7, however, this was less than half of this value where x = 0.6 and 0.8 [140]. Comyn and Stevenson carried out electrical measurements across the entire compositional range for BFPT in bulk polycrystalline ceramics. Polarization-field (P-E) measurements did not confirm the existence of ferroelectricity as hysteretic loops that were saturated could not be obtained even at fields in excess of 10 kV/mm, the composition where x = 0.8 showed "pinching" which is evidence of a hard material. Strain-field (x-E) measurements of BFPT while appearing largely electrostrictive did confirm the existence of piezoelectricity (as indicated by the negative strain values), ferroelectricity is often inferred from these results although it cannot be confirmed. Substantial electric fields in excess of 18 kV/mm were used at x = 0.7 in order to obtain a large-signal d_{33}^* value of 160 pm/V although this has never been achieved in low-signal measurements, thus making it unviable for use in actuator applications.

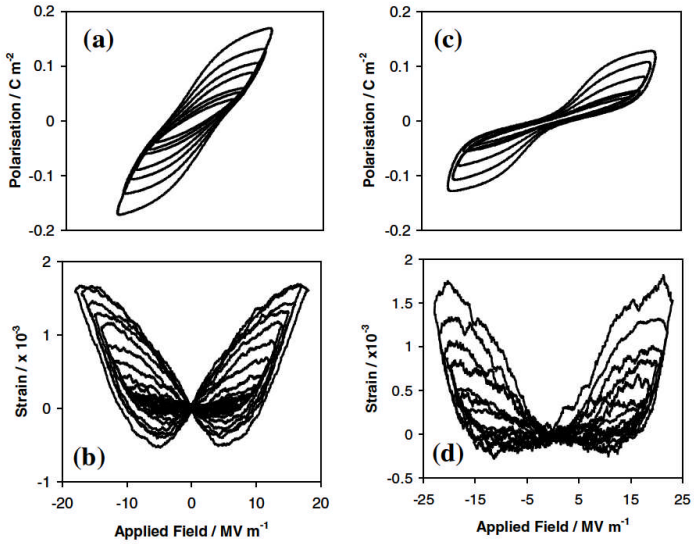

Figure 1-29. Polarization field and strain field data for x = 0.7 ((a) and (b) respectively) and x = 0.8 ((c) and (d) respectively) [141]

The properties of BFPT can be drastically altered with the addition of suitable dopants on the A or B-site, however, this is often at the expense of operating temperature, two exemplar dopants will be briefly introduced. La doping on the A-site proved successful in improving the ferroelectric and piezoelectric properties, Figures 1-30 and 1-31, as ferroelectric loops could be obtained as well as reasonable low-signal piezoelectric charge coefficients [138]. An increase in electrical properties was at the expense of the operating temperature. In a separate study the resistivity increased by approximately two orders of magnitude with the addition of 3% Lanthanum [142]. Manganese doping on the B-site has also been utilised in order to increase resistivity analogous to its success in pure $BiFeO_3$. Doping with up to 0.75 at% on the Fe^{3+} B-site produced an increase in resistivity, also by two orders of magnitude. Piezoelectric and ferroelectric characterisation has not been presented in the Mn-doped materials.

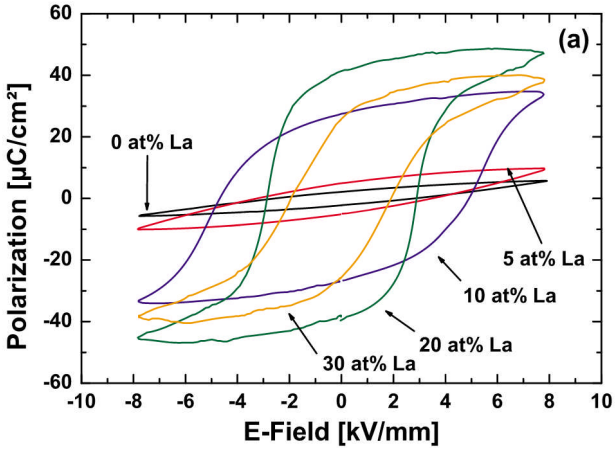

Figure 1-30. Polarization-electric field loops for La-doped BFPT [138]

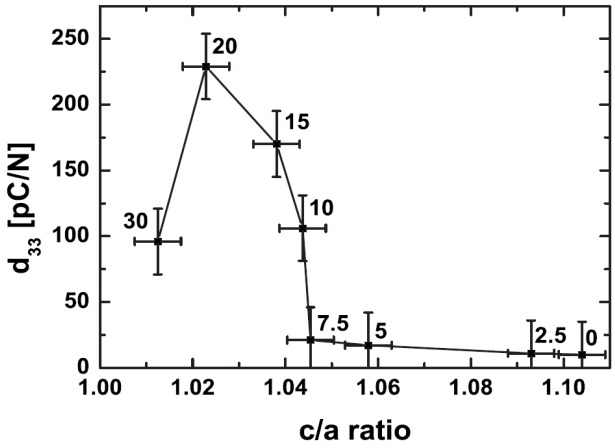

Figure 1-31. Effect of c/a ratio on the d_{33} for La-BFPT [138]

1.6.2.2 $BiFeO_3$-$(K_{0.5}Bi_{0.5})TiO_3$

The search for both a high temperature piezoelectric and lead-free material recently lead to the discovery of the (1-*x*)$BiFeO_3$-(*x*)$(K_{0.5}Bi_{0.5})TiO_3$ system by a number of research groups [143–147]. $(K_{0.5}Bi_{0.5})TiO_3$ is a perovskite ferroelectric material that is tetragonally distorted (a = 3.913, c = 3.990) belonging to the P4mm space group. It has received some attention recently due to its relatively high Curie temperature of 380 °C although it adopts a pseudo-cubic symmetry at 270 °C. Similar to NBT it can be difficult to produce dense samples with the correct stoichiometry as weight loss of the volatile elements is apparent, beginning at temperatures as low as 530 °C [148].

Kim first published a contribution into the structural and electrical properties of KBT rich compositions at $0.6 < x < 1$. Ball milled powders were prepared with secondary phases observed in the XRD scans. The c/a ratio reduced with increased $BiFeO_3$. The piezoelectric charge coefficient peaked at 64 pm/V where $x = 0.94$, broad dielectric constant plots were observed as a function of temperature [143]. This was swiftly followed by Matsuo who investigated the $BiFeO_3$ rich region of the phase diagram at $0.2 < x < 0.6$. During their initial investigation, samples with a relative density exceeding 90% could not be achieved using conventional techniques which led to the use of the flash creation method to produce nanosized powders, this produced samples with densities exceeding 95% [144]. With the use of x-ray and neutron powder diffraction an MPB between the rhombohedral (ferroelectric) and pseudocubic (ferroelectric) symmetries was identified at $0.4 < x < 0.43$ ceramics. An enhancement of ferroelectric properties was observed with hysteretic P-E loops observed with a P_r of 52 $\mu C/cm^2$ and a k_{33} of 0.36 at $x = 0.4$, however, the S_{MAX}/E_{MAX} and dielectric constant peaked with additional $(K_{0.5}Bi_{0.5})TiO_3$ at $x = 0.6$ [144]. This work was supported by Ozaki who utilised transmission electron microscopy (TEM) at $0.2 < x < 0.5$ on the same samples. The microstructure at the MPB consisted of polar domains, with a rhombohedral distortion of the order of 10 nanometres. XRD revealed a pseudocubic structure but TEM revealed a coexistence between rhombohedral and cubic structures, the domain size on the rhombohedral rich side of the phase diagram increased to ~200 nm [147].

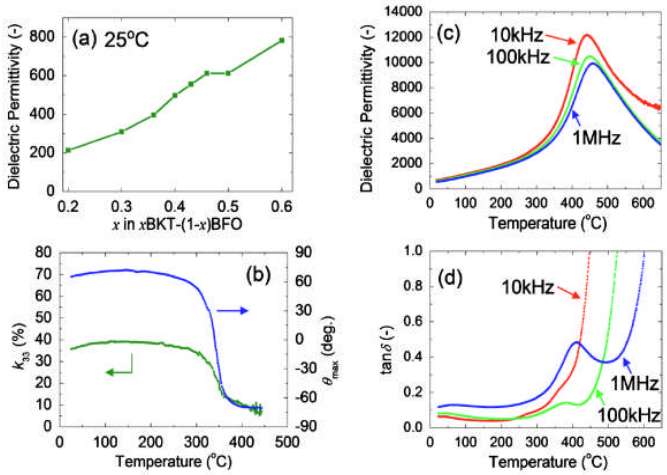

Figure 1-32. (a) The dielectric constant at room temperature (b) temperature dependence of k_{33} coupling coefficient and (c) dielectric constant and (d) loss as a function of temperature for x = 0.4 [144]

Morozov recently published a number of contributions relating to this system, the entire compositional space was investigated between $0.1 < x < 0.9$, in contrast to Matsuo conventional solid state processing was utilised, a high density of 97-98% was achieved by optimisation of the preparation route. The structural data correlated well with the previous contributions with a broad pseudocubic region observed, Morozov also examined the tetragonal rich side of the phase diagram where tetragonal splitting was observed at $x = 0.75 – 0.9$ [145].

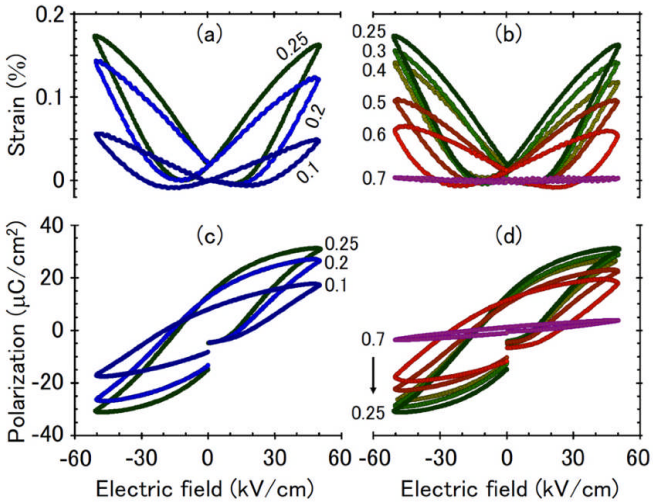

Figure 1-33. x-E and P-E loops for BF-KBT ceramics [145] N.B. The stoichiometric ratios above are contrary to those in the text

The level of hysteresis observed in the P-E loops is much reduced for the same compositions, although lower fields were used. Relatively large electric field induced strains were observed by Morozov and Matsuo, they are proposed to be due to the presence of PNRs which are easily switched by an applied electric field during the measurement, however, the PNRs return to a random order upon removal of the field, hence the electromechanical properties are dominated by electrostriction and it cannot be used as a high temperature piezoelectric [145].

1.6.2.3 $BiScO_3$-$PbTiO_3$

The (1-x)$BiScO_3$-(x)$PbTiO_3$ system was first predicted and fabricated by Eitel in 2001 based upon end member tolerance factor calculations [15]. Not much is known about pure $BiScO_3$ as it can only be synthesised under extremely large pressures, > 6 GPa, where neutron diffraction confirmed a monoclinic distortion. Scandium is also prohibitively expensive for widespread uptake, 5 grams of 99.9% purity Sc_2O_3 is £157.50 at the time of writing (Sigma-Aldrich) [149]. $PbTiO_3$ stabilises the $BiScO_3$ compound for compositions with greater than 50 mol% $PbTiO_3$ and secondary phases were observed for compositions below this. An MPB exists at x = 0.64 and piezoelectric properties were enhanced in this region, Figure 1-34, the piezoelectric coefficient d_{33} reached up to 450 pm/V coupled with a transition temperature of 450 °C [14] which is unrivalled in any other system.

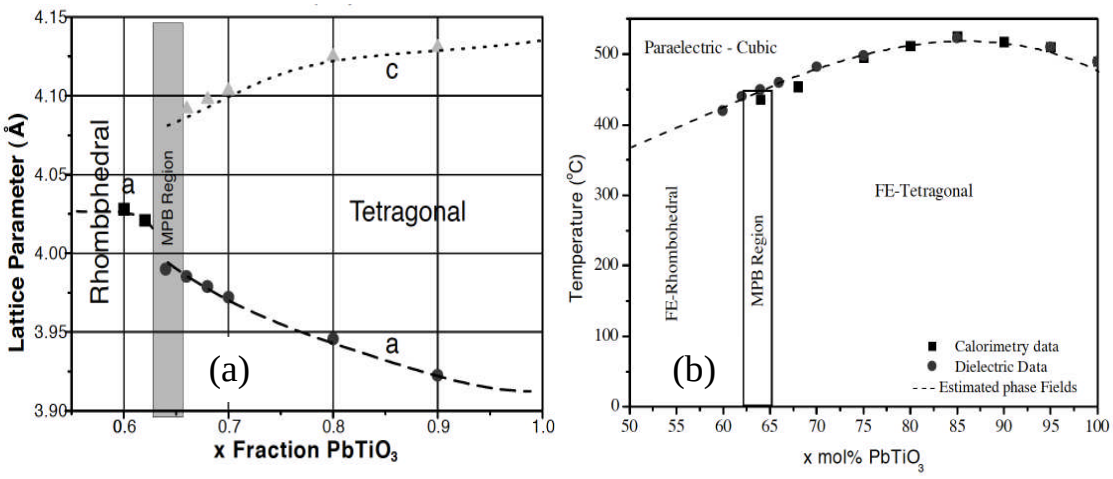

Figure 1-34. (a) Lattice parameters highlighting the MPB and (b) the phase diagram highlighting the paraelectric phase transition [15]

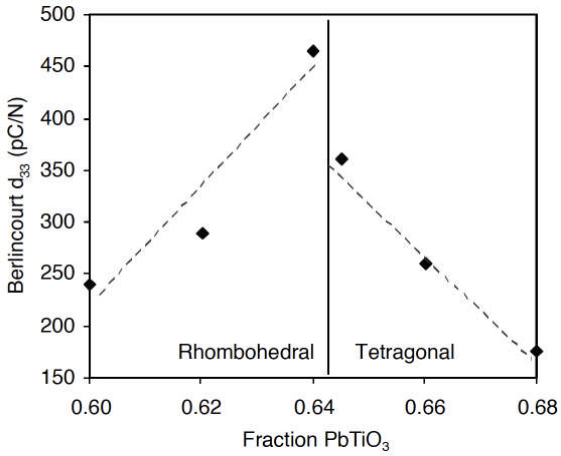

Figure 1-35. Enhancement of d_{33} at the MPB in BSPT ceramics [14]

Unlike in the BFPT system there is no significant increase in the c/a ratio when the $PbTiO_3$ end member is diluted with $BiScO_3$ and instead a gradual decrease in both the *c* and *a*-lattice parameter occurs, although the Curie temperature does increase above that of the $PbTiO_3$ end member where $x = 0.85$.

In order to determine the mechanisms contributing to the large piezoelectric coefficients the modified Rayleigh law was utilised to characterise the extrinsic contributions to the piezoelectric effect in MPB ($x = 0.64$), rhombohedral ($x = 0.62$) and tetragonal ($x = 0.7$) BSPT ceramics [150]. This technique will be discussed in more detail in Chapter 2.3.1.1. The MPB composition had a Rayleigh coefficient, α_d, of 334 x 10^{-18} m^2/V^2, this was higher than in the non-MPB compositions and TRS 200 PZT ceramic specimens (equivalent to Navy Type II). The tetragonal composition showed a reduced d_{33} coefficient as well as Rayleigh coefficient highlighting the role of the crystal structure in domain wall mechanics [150].

Mn-doping was also employed to increase the resistivity to enable use as a high temperature sensor. The resistivity increased by two orders of magnitude compared to unmodified BSPT samples which was also slightly greater than that of PZT Navy Type V, although this was the expense of piezoelectric d_{33} coefficient which decreased to 390 pm/V [59]. The resistivity and RC time constant at 450 °C was measured using a 100 V source to be 1.9x10^7 Ω.cm and 0.05 seconds in the Mn-doped MPB composition [59].

1.6.2.4 $BiMe^{3+}O_3$-$PbTiO_3$

Alternative $BiMe^{3+}O_3$ perovskite compounds have also been used in solid solution with $PbTiO_3$ based upon tolerance factor calculations as a method of predicting T_C. Much of this research has stemmed from Shrout, Zhang and Randall *et al* at Penn State over the past decade.

Table 1-4. Summary of T_C, c/a ratio and d_{33} in the $BiMeO_3$-$PbTiO_3$ family

Composition $(1-x)BiMeO_3$-$xPbTiO_3$	x	T_C (°C)	c/a	d_{33} (pm/V)	Summary	Author, Reference
$BiYbO_3$	0.7	620	1.10	-	-	Eitel, [15]
$BiYbO_3$	0.95	530	-	28	Pyrochlore phases in all compositions	Feng, [151]
	0.9	590	-	18		
	0.85	575	-	17		
	0.8	570	-	12		
$BiInO_3$	0.7	570	1.08	-	Stabilised with 1-3% $BaTiO_3$ for $x \leq$	Eitel, [15]
$BiInO_3$	0.95	540	1.07	-	No MPB observed	Duan, [152]
	0.9	568	1.077	-		
	0.85	576	1.08	-		
	0.8	582	1.082	-		
	0.75	580	1.081	-		
$BiInO_3$	0.8	570	-	18	1% Nb modified	Zhang, [56]
	0.8	550	-	36	2% Nb modified	
	0.8	531	-	30	3% Nb modified	
	0.85	542	1.067	60	1.5% Nb modified	
$BiGaO_3$	0.9	-	~1.08	-	No MPB observed	Cheng, [153]
	0.8	495	~1.055	-		
	0.6	-	~1.05	-		
$BiAlO_3$	0.95	460	1.053	-	Non perovskite where $x < 85\%$	Yu, [154]
	0.9	455	1.052	-		
	0.85	450	1.051	-		

Eitel discovered that the stabilisation of the perovskite phase was problematic in $BiInO_3$ for $x \geq 0.9$, thus the addition of 1-3 mol% barium was substituted on the Pb site to stabilize the perovskite phase, similar difficulties

were observed in $BiYbO_3$ with the generation of the pyrochlore phase. The Curie temperature of both systems exceeds that of BSPT, although neither could be poled due to low resistivity and the high coercive field stemming from the large c/a ratio. Zhang modified a number of $BiInO_3$-$PbTiO_3$ compositions with Nb, this allowed poling of the ceramic specimens at 12.5 kV/mm, a piezoelectric coefficient d_{33} of 60 pm/V was achieved albeit with a reduction in the Curie temperature as expected. Variants of the $BiMeO_3$-$PbTiO_3$ family include Ga and Al, these are summarised in Table 1-4, the key compositions are included along with the Curie temperature, c/a ratio and low signal d_{33}.

1.6.3 High Temperature ABO_3 Alternatives

This section aims to summarise alternatives to ABO_3 perovskite polycrystalline ceramics, while they are relatively cheap to fabricate and offer high piezoelectric coefficients they are temperature limited which has previously been discussed in some detail, illustrated in Figure 1-24. A range of materials with various crystal structures will be discussed, many are polycrystalline bulk ceramics while some are single crystals. Many non-ABO_3 perovskite materials maintain piezoelectric properties up to extremely high temperatures, far exceeding typical Curie temperatures of conventional perovskite materials, however, the piezoelectric response can be extremely low, the advantages and disadvantages of a select few will be discussed. The discourse will mainly be centred on sensing applications as this sector is where ultrahigh temperature piezoelectrics are most likely to be employed.

1.6.3.1 Tungsten Bronze Structures

Lead meta-niobate ($PbNb_2O_6$)(PN) belongs to the tungsten bronze family, it has found some commercial success in transducers in NDT and medical ultrasound imaging on account of its low Q_M ~20 which allows for a wide bandwidth and its high d_{33} to d_{31} ratio [95]. A commonly used composition is doped with 10% Ba (PBN) which has a T_C of 400 °C, although the low resistivity above 300 °C limits its operating window, issues around densification and low mechanical strength have also prevented its widespread application [94].

1.6.3.2 Bismuth Layer Structure Ferroelectrics

Bismuth layer (aurivillius) structure ferroelectric (BLSF) consist of repeating slabs of perovskite-like layers with bismuth oxide layers. They are characterised by low dielectric constants, high Curie temperatures (>600 °C), large electromechanical anisotropy, high mechanical quality factors and low aging rates [95]. Low resistivity is problematic as the orientation with the largest piezoelectric response is also the most conductive, thus poling is difficult and low d_{33} values are achieved. $Bi_4Ti_3O_{12}$ (BIT) is well known and the most understood of the BLSF family due to its relatively simple structure. The anisotropy of BIT as demonstrated in single crystals is profound with a spontaneous polarization of 50 and 4 $\mu C/cm^2$ found along the a- and c- axes respectively [96]. Doping with Nb helps to increase the resistivity and d_{33}. $Na_{0.5}Bi_{4.5}Ti_4O_{15}$ also belong to the BLSF structure and is more resistive and exhibits larger piezoelectric coefficients than BIT whilst maintaining its high Curie temperature.

1.6.3.3 Perovskite Layer Ferroelectrics

Perovskite layer ferroelectrics (PLS) are similar to BLSF in that they have an anisotropic layered structure, belonging to the general formula $A_2B_2O_7$. $La_2Ti_2O_7$ compound has a Curie temperature of ~1500 °C and resistivity is acceptable at elevated temperatures. Non-conventional processing techniques such as spark plasma sintering are also employed to improve the electrical properties by texturing samples a d_{33} of 2.6 pm/V was achieved, the predicted maximum operating temperature of these ceramics is in the region of 900 °C [95].

1.6.3.4 Piezoelectric Single Crystals

Generally piezoelectric crystals are employed rather than polycrystalline ceramics as their domain stability is superior and aging is reduced and resistivity is increased. Despite the significant cost to the user, a wide range of single crystals are available and currently under development. These are summarised in Table 1-5.

$LiNbO_3$ is currently used in electro-optic applications which requires extremely high quality single crystals [155], these are grown using the Czochralski pulling method and poled *in-situ* with a field of 1 V/mm at temperatures just below the T_C, exhibiting piezoelectric coefficients d_{33} of ~ 6 pm/V. Resistivity is the limiting factor which reduces the operating temperature to ~650 °C [94].

Quartz, SiO_2, is a widely used piezoelectric material, initially natural quartz crystals were used although they have now been replaced by hydrothermally-grown quartz. The resistivity is extremely high ($>10^{17}$ Ω.cm), and mechanical loss is low, however, the piezoelectric and electromechanical coefficients are low (d_{11} ~2.3 pm/V), the operating temperature is limited by the displacive α-β phase transition at 573 °C [156].

It has been intimated that a new generation of piezoelectric crystals are required as there is a lack of candidates with the appropriate properties for high temperature sensing that can be produced on a mass scale [156]. The first system of the latest generation to be discussed is a quartz analogue, simplified as ABO_4, with the same crystallographic symmetry, the gallium orthophosphate ($GaPO_4$) family shares many of the same favourable properties as quartz, notably the high resistivity and low mechanical loss while the piezoelectric and electromechanical coupling is improved. In contrast to quartz the β phase transition occurs at a much higher temperature which allows for potential operation up to ~950 °C [156], although the Q_M decreases significantly at temperatures above 700 °C. These are produced by the hydrothermal growth method which offers low yields.

Langasites crystals are produced by the Czochralski pulling or Bridgman growth routes. The langasites family have the general formula $A_3BC_3D_2O_{14}$ and belong to the trigonal system, the composition of interest in this discussion is the eponymous langasite compound, $La_3Ga_5SiO_{14}$. Langasite unlike quartz does not undergo a phase transition until the melting temperature at 1470 °C [157]. The limit to the operating temperature appears to be due to device packaging such as housing and wiring rather than the material itself, although mechanical strength

may be a limiting factor at high pressures. The piezoelectric coefficient d_{11} is 6.15 pm/V and the k_{12} is 0.16 [158].

Oxyborate crystals with the general formula $ReCa_4O(BO_3)_3$ where Re = rare earth element, exhibit a monoclinic *m* distortion. They were first reported in 1992 and can be readily grown using the Czochralski pulling or Bridgman growth methods. No phase transitions occur prior to the melting temperature(s), allowing for high temperature operation. They are favoured due to their extreme resistivity at high temperatures [95]. The d_{26} exhibited across the range of possible systems is between 7.6 – 15.8 pm/V.

Table 1-5. Electromechanical properties of selected non-ABO_3 perovskite materials, the data were collated from Refs. [94] and [95]

Material	Structure	Curie point (°C)	d_{33} (pm/V)	k_{33}	Q_M	Resistivity ($10^{12}\Omega$.cm)
$(Pb,Ba)Nb_2O_6$ (PBN)	Tungsten bronze	400	85	0.3	20	1
$Bi_4Ti_3O_{12}$-Nb	BLSF	655	20	-	-	-
$Na_{0.5}Bi_{4.5}Ti_4O_{15}$ + 0.3 wt% CoO	BLSF	663	30	0.05 (k_p)	3800	1000
$La_2Ti_2O_7$	PLS	1461	2.6	-	-	-
$LiNbO_3$	Corundum	1150	6	0.23	10,000	1
SiO_2 (single crystal)	α-Quartz	573	2 (d_{11})	-	10^5	1000
$La_3Ge_5SiO_{15}$	Langasite	1470	6.15 (d_{11})	0.16 (k_{12})	-	-
$GaPO_4$	Quartz Analogue	970	4.5 (d_{11})	0.16 (k_{eff})	-	-

2. Characterisation Techniques

2.1 Chapter Overview

The role of this chapter is to introduce the various techniques used to analyse the structure and electrical properties of the (1-*x*)$BiFeO_3$-(*x*)$(K_{0.5}Bi_{0.5})TiO_3$ and (1-*x*-*y*)$BiFeO_3$-*x*$(K_{0.5}Bi_{0.5})TiO_3$-*y*$PbTiO_3$ system.

2.2 Room Temperature Characterisation

2.2.1 Laboratory X-ray Diffraction

X-ray diffraction (XRD) is one of the most commonly used characterisation techniques in materials science and was used for phase identification during this study [159]. X-rays are a form of electromagnetic (EM) radiation although with much smaller (0.1-100 Å) wavelengths than visible light. The wavelength of x-rays is important as they are similarly matched to the interatomic distances in a crystal, in the region of 1-5 Å while visible light (3000-7000 Å) will not interact with the lattice in the same manner. The technique uses EM radiation to interact with the lattice and detectable 'reflections' in characteristic directions form the basis of X-ray diffraction.

X-rays are produced by electrically charged particles that are rapidly decelerated upon striking a metallic surface, upon impact a large amount of energy is released due to the change in momentum and X-rays are released. High-energy electrons are the most commonly used form of particle.

Research undertaken at the University of Leeds almost 100 years ago by William Henry Bragg and William Lawrence Bragg also resulted in the Nobel prize for "their services in the analysis of crystal structure by means of X-rays". The Braggs' formulated the essential condition required for diffraction to occur based upon the existence of phase relations between two or more EM waves, where the path length is an integer number of wavelengths. The Bragg's also viewed crystals as sets of planes that would 'reflect' X-rays at certain angles of incidence. It must be stated X-rays are not actually 'reflected' by the planes of atoms and that diffraction and reflection are quite different although reflection of

x-rays is possible at angles < 1°. Reflection of visible light is almost 100% efficient whereas the diffracted beam intensity is small relative to the incident beam. Reflection only occurs on a very thin surface whereas diffraction is built up from many layers in the path of the incident beam and reflection occurs at all angles whereas diffraction only occurs once the Bragg condition has been satisfied.

Bragg's law derived a relationship between the X-ray wavelength, the spacing between planes of atoms and the angle of the incident X-ray radiation, a diagram demonstrating the derivation of Bragg's law is included underneath along with a description.

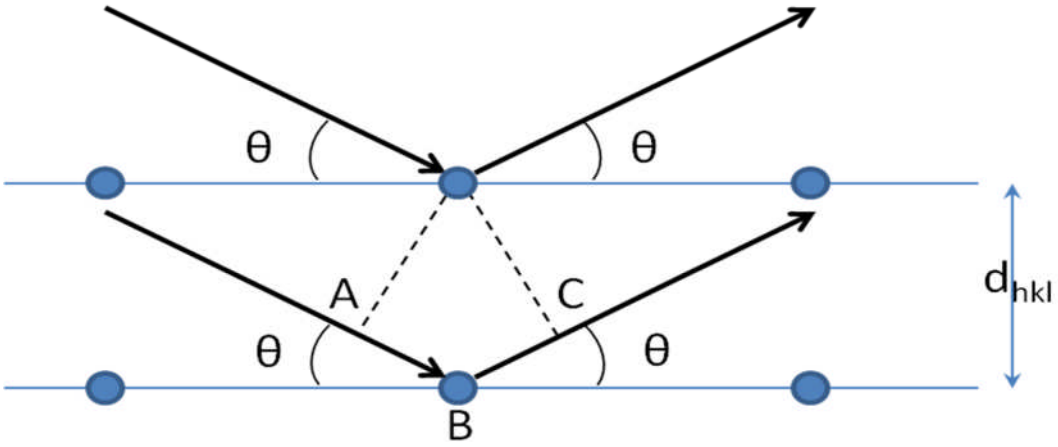

Figure 2-1. Derivation of the Bragg equation (Modified from Cullity)

For constructive interference to occur the two wavelengths must be in-phase. The beams are parallel upon scattering from the top atom by the first beam. The second beam continues until it reaches the bottom atom. The second beam must therefore travel the extra distance AB + BC if the two beams are to continue traveling parallel to each other and in-phase. This extra distance must therefore be an integer number of wavelengths greater than the first beam for the scattering to be constructive. Using trigonometry, we can determine *d* as the hypotenuse of a right angle triangle; *d* and *θ* are related to the distance (AB + BC) as the distance AB is opposite to angle *θ*. Therefore, AB = *d*sinθ, as AB = BC it becomes true that nλ = 2AB. Therefore Braggs law can be given as;

$$n\lambda = 2d_{hkl}\sin\theta$$

Equation 2-1

where n is labeled the order of diffraction, λ is the wavelength, d is the distance between two planes and θ is the Bragg angle.

X-rays are commonly produced using sealed high-vacuum X-ray tubes. An X-ray tube, shown in Figure 2-2, has 3 essential components namely (a) source of electrons, (b) metal target and (c) large accelerating voltage. Beams of focused electrons are generated with applied voltages of the order 30 – 60 kV [160]. These electrons strike the target anode, this is a flat plate of extremely pure metal, X-rays are produced in all directions but are only useful in the directions containing the beryllium windows. It is water cooled as it must sustain a power input of up to 3 kW for prolonged periods.

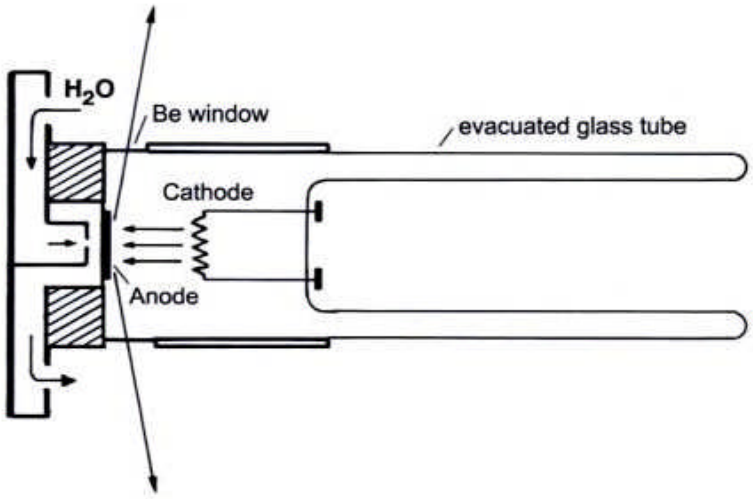

Figure 2-2. Schematic Diagram of an X-ray Tube [160]

Upon striking the anode, some of the energy resulting from the deceleration of the electrons is converted into radiation that produces a continuous energy spectrum which consists of a mixture of x-ray wavelengths. The characteristic radiation is produced above a critical voltage given in the equation 2-2 that is specific to the target anode.

$$I_{Kline} = Bi(V - V_K)^n$$

Equation 2-2

where I_{Kline} is the intensity of the characteristic wavelength, *i* is the current carried in the X-ray tube, *V* is the accelerating voltage, V_K is the characteristic voltage, and *B* and *n* are constants.

The x-rays arise as a result of electrons being expelled from the target material, these characteristic lines are referred to as K, L, M-shells. When an electron from a higher energy level replaces a vacancy in the K-shell, X-rays of specific wavelengths are emitted as shown in Figure 2-3 for a Molybdenum target which gives rise to Kα and Kβ lines. Common target materials include Cu, Mo, Cr, Ag, Fe and Au, characteristic wavelengths are unique to each anode. 'Harder' X-rays have much shorter wavelengths and can be used to probe deeper into samples or can be used to identify pair distribution functions at higher angles and probe smaller features. Table 2-1 summarizes commonly used target materials and their associated characteristic wavelengths. A Cu target was used throughout this study, this can lead to difficulties with Co, Ni and Fe containing materials due to fluorescent radiation being emitted by the sample whereby some of the atoms absorb the incident X-rays and upon interaction fluoresce, and the resultant diffracted X-ray has a different wavelength and is therefore out of phase. This occurs because the characteristic wavelength of Cu is shorter than the K absorption edge of the specimen [159]. A monochromator was used to reduce the intensity of this background radiation as it can lead to a weakened intensity of the reflections and the signal to noise ratio can be substantial.

Table 2-1. Mean characteristic wavelengths of target materials

Metal	Wavelength (Å)
Cr	2.2909
Fe	1.9373
Co	1.7902
Cu	1.5418
Mo	0.7107
Ag	0.5594
Au	0.1801

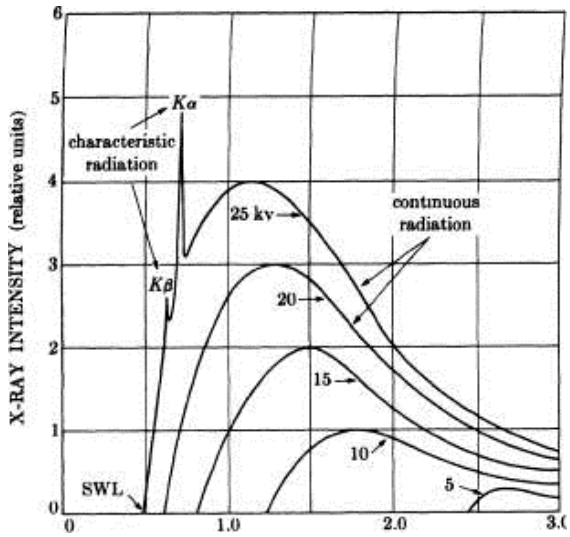

Figure 2-3. Characteristic X-ray spectrum at varying voltages for Mo target [159]

The most commonly used powder diffractometers are operated using the Bragg-Brentano geometry, shown in Figure 2-4. This geometry operates using a focussing circle where the x-ray source and the detector are positioned about the sample at a constant distance. Using this geometry the diffraction vector is always normal to the surface of the sample. A series of slits are used to reduce divergence in the incident beam and scattered beam. These slits influence the peak intensity and shape. Narrow divergence slits can reduce the intensity of the incident beam but can produce sharper peaks. As the angle of the beam varies the irradiated area penetrates deeper into the sample thus keeping the sample volume measured constant. This allows for detailed structural analysis as accurate peak intensity quantification is vital.

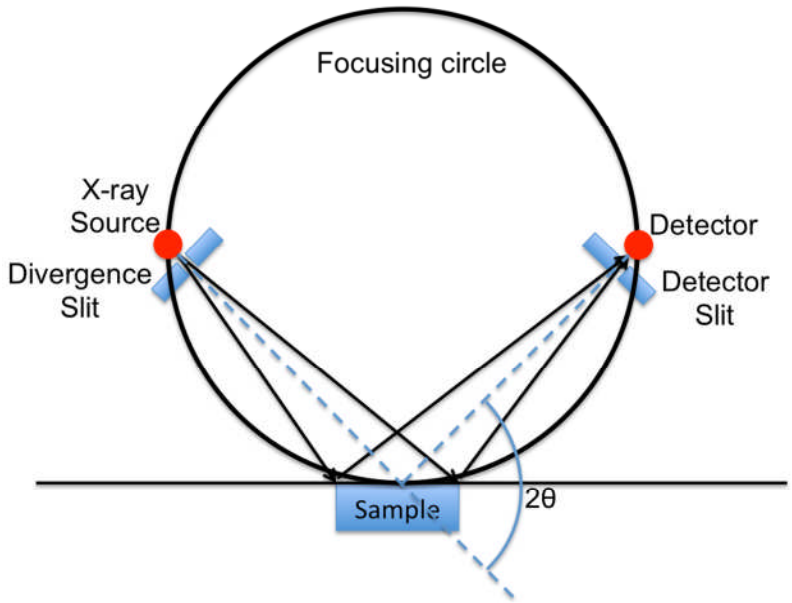

Figure 2-4. Schematic of the Bragg-Brentano geometry used during XRD (Modified from Cullity [159])

Upon interaction with matter, X-rays are largely scattered through an interaction between the EM field of the X-rays and the electron cloud of the specimen. The electrons in the sample oscillate with the period of the incident x-ray, emitting their own EM field that is constructive and of the same wavelength as the original X-ray [161]. The nucleus has a relatively large mass compared to that of the electron and cannot oscillate to any practical extent. Thus the scattering is dependent upon the amount of electrons in the electron cloud and this is weak for low-Z materials such as polymers and biological tissue. Scattering for bismuth and lead is strong but elements such as oxygen and hydrogen partake in weak scattering due to the smaller electron cloud.

The intensity of the diffraction peaks is a result of the arrangement of the atoms within the structure. The structure factor (F_{hkl}) describes the total scattering intensity and is the summation of scattering from all of the atoms in the unit cell to form a diffraction peak in the hkl reflection. The amplitude of the scattering is dependent upon the atoms positions and what atoms exist on these planes. The structure factor can be described as;

$$F_{hkl} = \sum_{1}^{N} f_n e^{2\pi i(hu_n + kv_n + lw_n)}$$

Equation 2-3

where f_n is the scattering factor for atom n and is related to its atomic number and u_n, v_n and w_n are its fractional co-ordinates.

In a perfect crystal lattice the peaks where Braggs law is satisfied will appear as sharp lines. In a real sample, the arrangement of atoms is far from ideal with distortions as a result of the crystallite size, internal strain and point defects. With a uniformly strained structure a relatively sharp peak is still observed although its location is shifted as the unit cell dimensions have been modified. In a material with non-uniform internal strain, the structure is distorted and a wide distribution of unit cell dimensions can be found that satisfy the Bragg condition hence the substantial peak broadening observed.

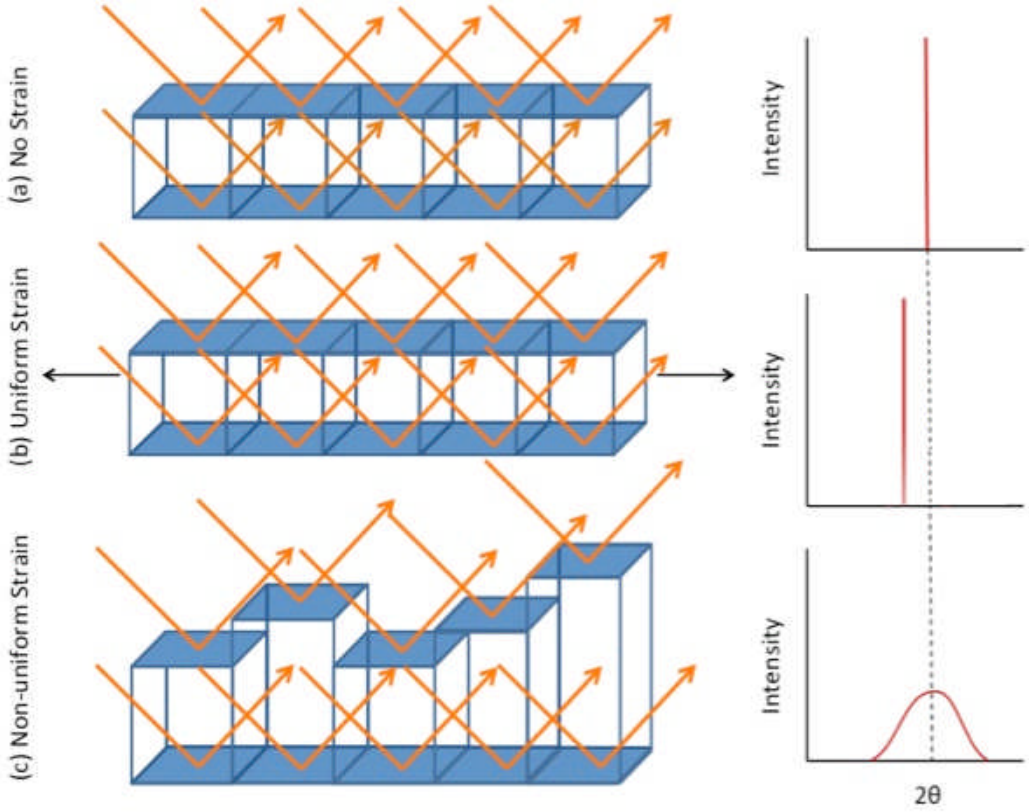

Figure 2-5. Representation of the stress effect upon diffraction patterns for (a) a perfect lattice, (b) a uniformly strained lattice and (c) non-uniformly strained lattice

A decrease in the crystallite size causes peak broadening to increase due to smaller crystallites having fewer successive planes of atoms where constructive interference occurs.

2.2.2 Synchrotron X-ray Diffraction

A synchrotron is a particle accelerator that accelerates electrons up to relativistic high speeds that produces very bright light (electromagnetic waves) in the region from infrared through to X-rays, allowing the characterisation of extremely small structures. The origins of synchrotron radiation can be traced back to Maxwell in 1873 who proposed that changing charge densities and electric currents would result in electro-magnetic fields that would radiate outward and in 1887 Hertz demonstrated these waves [162]. The first synchrotron is often reported as being General Electric Laboratory's 70 MeV machine in Schenectady, USA. While it was the first dedicated synchrotron, the machine that first demonstrated synchrotron acceleration was by Goward and Barnes using a converted betatron at Woolwich Arsenal, UK [162]. We are now entering the fourth generation of synchrotron radiation facilities and over 70 exist across the globe with a wide variation in sizes and energies.

The operation of a particle accelerator begins with an electron gun which fires low energy electrons in the same way to laboratory XRD. Here, a high voltage cathode is heated in an evacuated atmosphere and electrons are stripped and then accelerated in a process known as thermionic emission [163]. The electrons then enter a bunching cavity which uses an AC field in order to group the electrons. The linac (linear accelerator) then accelerates the electrons to close to the speed of light into a booster synchrotron which accelerates the electrons even more. The booster synchrotron uses bending magnets to curve the electrons around the bends, once the electrons reach 3 GeV it can be transferred into the main storage ring [164]. All of these processes occur under a vacuum in order to avoid collisions with atoms and molecules.

The storage ring is actually made up of many small straight sections connected at a constant offset angle, these are directed with the use of bending

magnets where direction is controlled by the magnetic field strength. Diamond Light Source, Harwell, UK has a circumference of 562 m and 24 straight sections [163]. Electrons remain in the storage ring for approximately 20 hours before they are “topped-up”.

As the electron beam passes through the bending magnets electromagnetic radiation is emitted tangentially with a broad spectrum of photon energies. At Diamond a smaller number of beamlines use bending magnets as the source, denoted with the prefix B while the majority use an insertion device which is an array of magnets that are inserted into straight section that produce a much brighter and intense X-ray and allows for tunability, these are known as wigglers and undulators, denoted with the prefix I [163].

Synchrotron radiation offers a significant number of advantages over laboratory XRD sources. The intensity of the x-rays is far greater, coupled with the high collimation of the beam and the small angular divergence this allows for much higher resolutions to be achieved. Extremely short wavelengths can be achieved allowing for the total structure of a sample to be probed as opposed to the surface, this also enables the application of an electric field, temperature or stress *in-situ*. The broad spectrum of electromagnetic waves emitted allows for high tunability in conjunction with monochromators. Other advantages are the highly polarized nature of the x-rays and the short emittance. Synchrotron radiation allows the user to observe phase changes in piezoelectric ceramics and also the domain switching as a function of electric field across the whole sample [165-166].

2.2.3 Strain-Electric Field

The strain-electric field (x-E) measurement is a vital experiment in the field of piezoelectric materials. It is especially important in the arena of actuator design, as the high-field d_{33}, obtained from the slope of the x-E measurement is one of the key figures of merit when designing an actuator. The measurement utilises the converse effect as an electric field is applied and the displacement of the material is measured. The polarization can also be measured simultaneously as

described in Chapter 2.2.4. Hysteretic behaviour is ideally at a minimum in applications that require extremely accurate displacements such as in precision positioning devices [156].

The displacement probe functions with the use of multiple fibre optic strands arranged in a random configuration. The sample chamber is sealed and filled with dielectric oil to prevent the sample from the arcing that may occur in "open air". The displacement is calculated from the reflected light intensity of an unclamped copper body that is connected to the sample. The copper body is free to move allowing for various geometries and for the displacement of the sample under an applied field to be accurately gauged. The fibre optic probe is calibrated before testing each sample by reaching the optical peak, the equipment then adjusts the output level. This method of measuring displacement is advantageous as it is non-contact, it has high sensitivity and the frequency bandwidth range is more than capable for this study (0.1 -100 Hz).

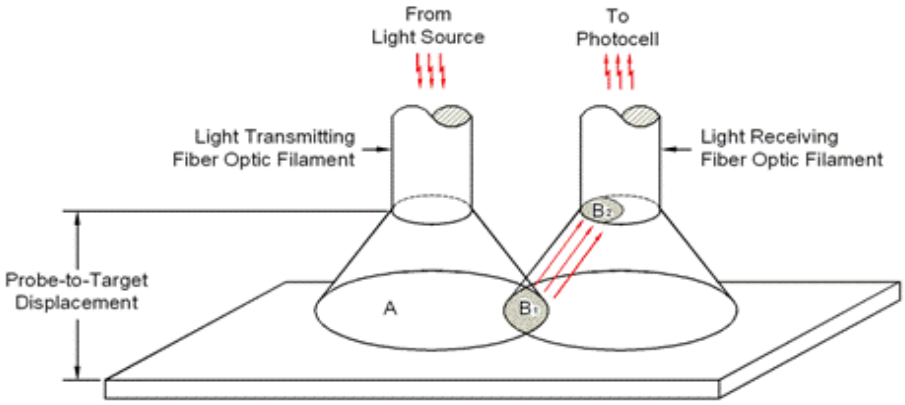

Figure 2-6. Schematic diagram of an optical probe (Courtesy of MTI Instruments [167])

2.2.4 Polarization- Electric Field

The Polarization-electric field (P-E) measurement is a fundamental technique in the field of ferroelectrics as a defining property is the ability to switch between two metastable states with the application of an external electric field. The apparatus has been improved through the years with the introduction of

computer based data acquisition. The technique used is based upon a modified Sawyer-Tower circuit [168], shown in Figure 2-7.

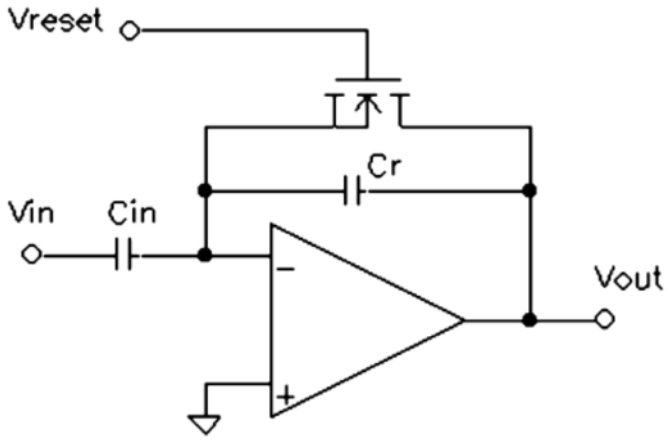

Figure 2-7. Sawyer-Tower circuit used to determine P-E loops [169]

It is possible to obtain a P-E loop by virtue of the V_{IN} and V_{OUT} readings. The geometric parameters of the sample must be known in order to generate accurate data. The following equations express the relationship between the input/output signals of the circuit and the polarization- field.

$$E = \frac{V_{IN}}{d}$$

Equation 2-4

where d is the thickness of the sample and V_{IN} is the input voltage.

$$P = \frac{Q}{A} = \frac{C_R V_{OUT}}{A}$$

Equation 2-5

where Q is charge across the sample, A is area, C_R is the reference capacitor and V_{OUT} is the voltage across the capacitor.

The measurement of charge across an unknown sample can be determined by multiplying the value of the reference capacitor with the voltage across the reference capacitor.

The simplicity in this approach can cause problems as the leakage current and other parasitic components are not accounted for, thus making characterisation of ‘real’ ferroelectric ordering more complicated than it might first appear. In an ideal ferroelectric, a P-E loop will be symmetric and have clearly defined hysteretic behaviour, coercive field and remnant polarization, however, a number of material and measurement errors can mimic behaviour which resemble that of ferroelectric behaviour. A number of articles have passionately argued that ferroelectric hysteresis loops are often misinterpreted and misrepresented as exhibiting ferroelectric behaviour [170], due to having open P-E loops, going as far as to compare bananas to the ferroelectric $Ba_2NaNb_5O_{15}$ system (often labeled ‘bananas’) [171]. Contributions to P-E loops may arise from the electrodes, dielectric permittivity, electrical conductivity and PNRs. The sample may also only appear ferroelectric across a small frequency bandwidth which may also suggest that it is not ferroelectric. PUND measurements can therefore be used to quantify the switchable polarization [172].

2.2.5 Positive Up Negative Down (PUND)

Positive-up-negative-down (PUND) measurements were employed to confirm the time stability of the remanence, in which a series of voltage pulses were applied and the current during the pulses integrated to determine the switchable polarization. It has largely been applied in the area of thin films but has recently garnered interest in bismuth-ferrite based ceramics [46, 173–175].

A typical pulse profile is shown in Figure 2-8, although the order of the pulses presented is contrary to the description below. The test consists of five pulses in which the pulse width, delay time and voltage can be varied. The first pulse presets the sample to a known polarization state. The next pulse (P) is applied with positive polarity, one at the maximum applied voltage to switch the sample, the next pulse is up (U) in the same direction which does not result in switching, this is repeated with the sample switched using a negative (N) pulse and then down (D) in the same direction. The current obtained during the U pulse can be subtracted from that of the P pulse so that only the switchable polarization

current is obtained. This in then integrated over the switching time. The N and D pulses complete the measurement.

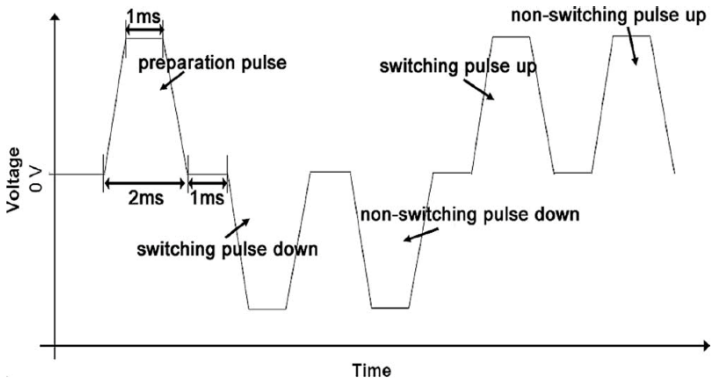

Figure 2-8. A typical profile during a PUND measurement [175]

2.3 High temperature characterisation

In order to determine the suitability of the BF-KBT-PT system for high temperature applications it was appropriate to characterise the materials over a wide temperature range. The structure-property relationship is significant in this process, as the piezoelectric properties such as d_{33} often increase at high temperatures due to a softening of intrinsic and extrinsic contributions. The Curie temperature can also be preferentially controlled with greater use of the structure-property relationship.

2.3.1 Strain-Electric Field and Polarization-Electric Field

This technique has previously been outlined in Chapter 2.2.3 and 2.2.4, however, for high temperature characterisation small alterations were made to the measurement techniques used as they were performed at Pennsylvania State University during a 4-month secondment. The P-E component functions as previously outlined with the use of a modified Sawyer-Tower circuit that measures the charge of the sample.

The x-E measurement can also be performed simultaneously but a linear variable differential transducer (LVDT) is used in contact with the sample rather than a non-contact optical probe. The strain was converted to an AC voltage by

the LVDT and the AC voltage was converted to a DC voltage by a lock-in amplifier and a displacement value was generated.

2.3.1.1 Rayleigh Analysis

Ferroelectric ceramics exhibit both an intrinsic and extrinsic contribution to the piezoelectric effect [176]. The Rayleigh law was first used to describe induced magnetisation and magnetic permeability for low field levels below the coercive magnetic field (H_C) [177]. The analogy between ferromagnetic and ferroelectric behaviour has led to its application in describing non-linear dielectric, ferroelectric and piezoelectric responses [60], [178]. The intrinsic contribution is a result of the atomic displacements of the unit cell under an applied field, whilst the extrinsic contribution is a result of domain wall motion [17] and is generally associated with irreversible and lossy processes and can greatly affect the electromechanical response. Therefore, as the intrinsic and extrinsic contributions vary with composition and temperature [179], Rayleigh analysis is an effective method in analysing new materials. Piezoelectric ceramics are often characterised from electrical impedance at low voltage (0.5-1 V) frequency sweeps in conjunction with the sample geometry and density [180] while transducers and actuators are typically driven at much higher excitation levels (1-2 kV/mm) [181], this technique therefore allows the possibility of simulated studies of real applications (assuming that the ceramics will not be driven by bipolar switching electric-fields).

The technique has been applied to $BaTiO_3$, PZT, $BiScO_3$-$PbTiO_3$, lanthanum doped BFPT and lead-free materials [60, 150, 178, 179, 182–184]. Hall expanded upon the use of the Rayleigh model in ferroelectrics to describe the linear dependence of the converse piezoelectric coefficient upon application of an AC electric field. The intrinsic response is generally assumed to be independent of the electric-field at low-field amplitudes while non-180^o domain wall motion increases the volume fraction to the vector most closely associated with the applied electric-field creating a strain response, thus allowing this behaviour to be quantified. The Rayleigh region is limited to electric field amplitudes that do not cause the reorientation or nucleation of domains, these are typically limited to

between one-half to one-third of the coercive field [150]. The principal difficulty with this technique is attaining accurate displacement measurements due to the relatively low fields applied. The piezoelectric Rayleigh coefficient (a_d) can be obtained experimentally with relatively few terms from a plot of d_{33} as a function of maximum field strength.

$$d_{33} = d_{\text{init}} + \alpha_d E_o$$

Equation 2-6

where d_{init} is a field independent term and represents the contribution from the reversible intrinsic response along with reversible domain wall motion, and E_0 is the maximum field strength. The term $\alpha_d E_o$ represents contributions to d_{33} from irreversible domain wall translation processes.

The value of the Rayleigh coefficient is a gauge as to the extent of extrinsic domain wall contributions. We obtain the values of the above terms experimentally using the gradient and its extrapolation back to zero field of the d_{33} as a function of E_o from sub-switching x-E loops. An additional relationship can be used to describe the strain behaviour at any given field amplitude.

$$x = (d_{init} + \alpha_d . E_0)E \pm \frac{\alpha_d}{2}(E_0^2 - E^2)$$

Equation 2-7

where x is the strain and E is the instantaneous electric field. This can be used to confirm that the experimental results adhere to the Rayleigh law.

The fractional contribution to the piezoelectric effect from irreversible extrinsic contributions at E_0 = 1 kV/mm was estimated using the following;

Extrinsic contribution =

$$\frac{d_{extrinsic}}{d_{intrinsic} + d_{extrinsic}} = \frac{\alpha_d . E_0}{d_{init} + \alpha_d . E_0}$$

Equation 2-8

2.3.2 Permittivity-Temperature

Relative permittivity plotted as a function of temperature is an important tool in determining the Curie point of material. It can also indicate any structural transformations below the T_C. The high temperature permittivity rig uses parallel plates made of silver or platinum wire to calculate capacitance (C). The dielectric loss is also measured simultaneously. The broad range of the frequencies applied can aid in identifying electronic features that exist in the sample such as relaxor behaviour. The relative permittivity can be found using the equation;

$$\varepsilon_r = \frac{C.d}{\varepsilon_0.A}$$

Equation 2-9

2.3.3 Impedance Analysis

Relatively simple measurements can be used to determine the resonant and antiresonant frequencies of a ceramic body which allows the evaluation of a number of piezoelectric figures of merit. The piezoelectric effect allows the observation of the coupling between the mechanical resonance and electrical behaviour [25]. Poled ceramics are used for this technique, this distorts the lattice structure and manipulates the speed of sound through the ceramic body. A piezoelectric material has characteristic frequencies at which its mechanical resonance is at a maximum and minimum, when at the resonant frequency, f_r, the body will resonate freely, at the anti-resonant frequency, f_a, the impedance will be at a maximum and the mechanical oscillation at a minimum [25].

Different modes of resonance of the piezoelectric ceramic body give insight into the different constants associated with that resonance mode such as thickness, shear or radial. A ceramic disc will be used to exemplify this, if the diameter is significantly different to the thickness then a series of distinct resonances are observed, relevant to the reflections in the ceramic body. The resonance at low frequencies corresponds to the mechanical response in the largest dimension of the ceramic body which is in the radial direction, while the

resonance peak at higher frequencies belongs to the thickness mode [185]. Harmonics will be seen at much higher frequencies also. An impedance spectra in longitudinal mode is shown in Figure 2-9. The ceramic body needs to remain unclamped so that it can vibrate freely during the application of the AC voltage. This technique can also be used at high temperatures to determine the depolarization temperature, T_d, to an acceptable level of accuracy and offers information relating to important piezoelectric coefficients [186].

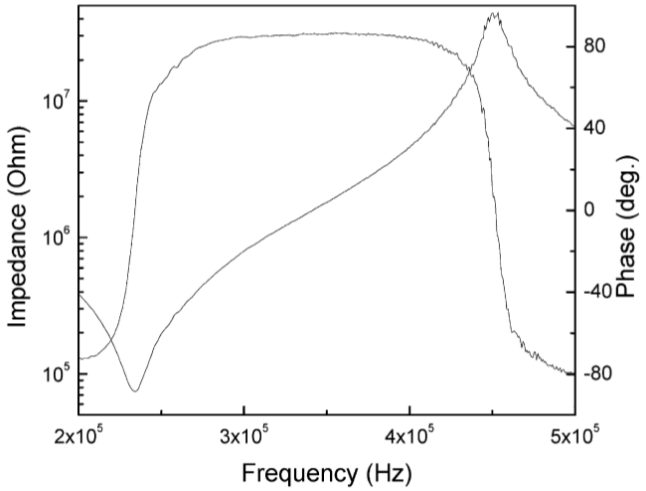

Figure 2-9. Impedance spectra of BSPT single crystal in longitudinal mode [187]

2.4 Imaging Techniques

2.4.1 Scanning Electron Microscopy

The first proposed idea for a scanning electron microscope was in 1927 by Stinzing while the first capable of producing an image was developed by Knoll in 1935 [188]. SEM is a technique used for attaining high-resolution images of surface microstructure and topography. It is similar technique to optical microscopy but differs in the obtainable resolution as electrons have a much shorter wavelength than light in accordance to the Rayleigh criterion [189]. The Rayleigh criterion describes the relationship between the wavelength (λ) and the smallest distance between two points that can be resolved. The resolution limit for optical microscopy (λ =400-700 nm) is in the range of 0.4 μm for blue light and 0.2 μm for UV light. In the SEM a potential difference is used to accelerate the

electrons, and the wavelength of an electron can be calculated using de Broglie's formula. The use of electrons allows for sub-nanometre imaging, however, in reality the resolution is determined by the working distance, accelerating voltage, stigmation, aperture size and imaging conditions.

There are two main components of an SEM, the microscope column and the electronics module. The microscope column typically consists of an electron gun which uses a tungsten filament heated to ~2700K. Condenser lenses and deflection coils are used to focus the beam of electrons onto the target. Finally an objective lens and apertures are used. This column is evacuated so that interaction of the electrons is minimised. The SEM emits electrons from the tungsten filament (cathode) at a voltage of 0.5-30kV toward the anode. The condenser lenses reduce the spot size of the electrons [188].

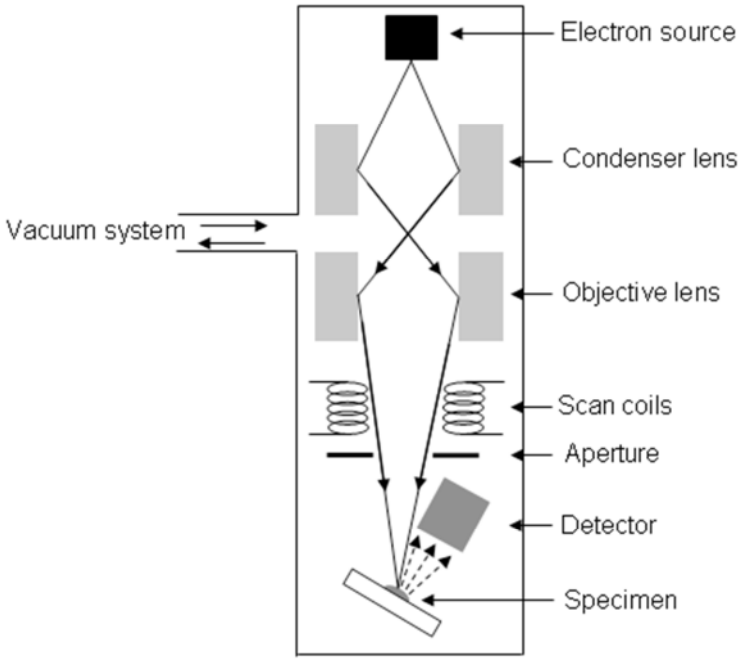

Figure 2-10. Schematic diagram of a SEM microscope column [190]

Standard operation would involve the SEM continuously scanning across the surface of the sample with the electron beam. Various detectors can be fitted in the sample chamber but the most common identify either back scattered or secondary electrons [190], these are emitted upon interaction with the sample. Secondary electrons arise from the top surface of the sample and tend to be low

energy and used mainly for topographical imaging while back-scattered electrons are high energy and used for phase identification as the level of back-scattering varies greatly with the atomic number, *Z*. The image forms by mapping the signal intensity to the scanned site [190].

2.4.2 Piezoresponse Force Microscopy

Piezoresponse force microscopy (PFM) is an imaging technique that utilises the contact mode atomic force microscope (AFM) technique, and was introduced relatively recently in 1992 [191]. A laser is directed at a reflecting surface on top of the cantilever that houses the tip and a four-quadrant photodiode can determine the sample topography with the aid of a function generator and lock-in amplifiers in order to measure the sample height variation. The converse piezoelectric effect is utilised, with the application of an electrical bias from the conductive probing tip results in variations in the surface displacements [192], albeit relatively small (of the order of 100 pm). The signal-to-noise ratio of the displacements can be improved with the use of a lock-in-amplifier. It has recently been exploited for use in thin films, bulk ceramics, single crystals and ferroelectric polymers [193]. This technique is useful as many factors controlling the ferroelectric stability are the consequence of depolarization field effects arising from the termination of polarization at surfaces which determine domain formation and are influenced by surface chemistry, grain size effects and strain effects [193]. Grain size effects also lead to variations in the Curie temperature.

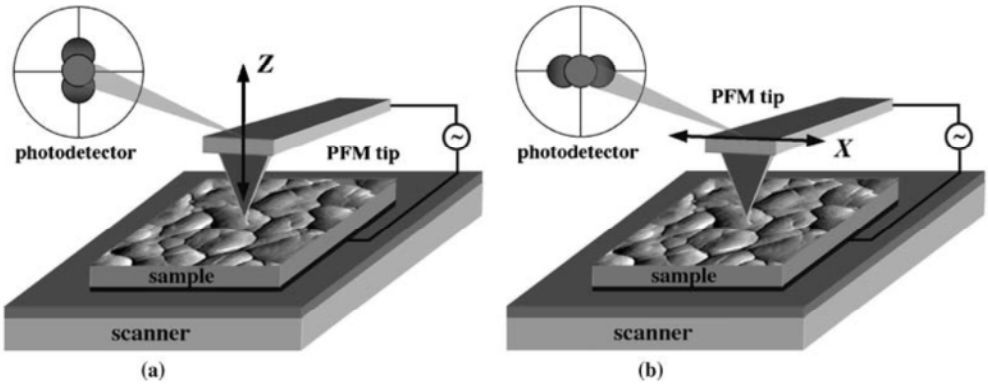

Figure 2-11. Schematic diagram of the (a) vertical and (b) lateral PFM imaging modes [194]

3. Experimental Techniques

3.1 Chapter Overview

This chapter explains in detail the procedures followed during the synthesis of the BF-KBT-PT system, final sample preparation, experimental apparatus and testing parameters used. This begins with the preparation of the powders and subsequently the processing route necessary to form a bulk polycrystalline ceramic. The techniques used often required vastly different sample preparation routes so this will be detailed robustly.

3.2 Synthesis of Powders

The characteristics of starting powders such as particle size, shape and size distribution have a profound effect upon densification, microstructure development and electrical properties including breakdown strength [195]. Conventional mixed oxide processing routes have been the mainstay for powder preparation within the research group at Leeds for a number of years as outlined in previous studies [57, 101, 135, 140, 141, 196–201].

Reagent powders of the commercially available Bi_2O_3, (99.9%), PbO (99.9%), Fe_2O_3 (99+%), TiO_2 (99.9%) and K_2CO_3 (99+%) (Sigma-Aldrich) were dried at 130 °C to remove moisture and enable accurate weighing. Stoichiometric mixtures of the starting reagents were attrition milled using a Dyno-mill KDL Type-A (Willy A. Bachofen, Switzerland) with yttria-stabilised zirconia (YSZ) (Tosoh, Japan) beads in propan-2-ol for 1 hour to ensure homogeneity. This attrition milling step applies to most of the compositions discussed belonging to the $BiFeO_3$-$(K_{0.5}Bi_{0.5})TiO_3$-$PbTiO_3$ system except where clearly stated in the text, however, all of the lead-free $BiFeO_3$-$(K_{0.5}Bi_{0.5})TiO_3$ compositions were produced instead using ball milling. Dried and sieved powders were then calcined at 800 °C for 4 hours in air, shown in Figure 3-1. These were again sieved and 1 wt% Glascol HA-40 binder (Allied Colloids, UK) and propan-2-ol was added and mixed. The resultant slurry was then dried under heat lamps with the aid of a magnetically stirred hot plate at 80 °C for 24 hours and then dried for >2 hours in an oven at 130°C. Ensuring temperatures were not reached that would lead to the ‘burning off’ of the binder. These powders were then sieved through a 300 µm

mesh. Fine primary particle sized powders were desired as the large surface area aids in driving densification upon sintering.

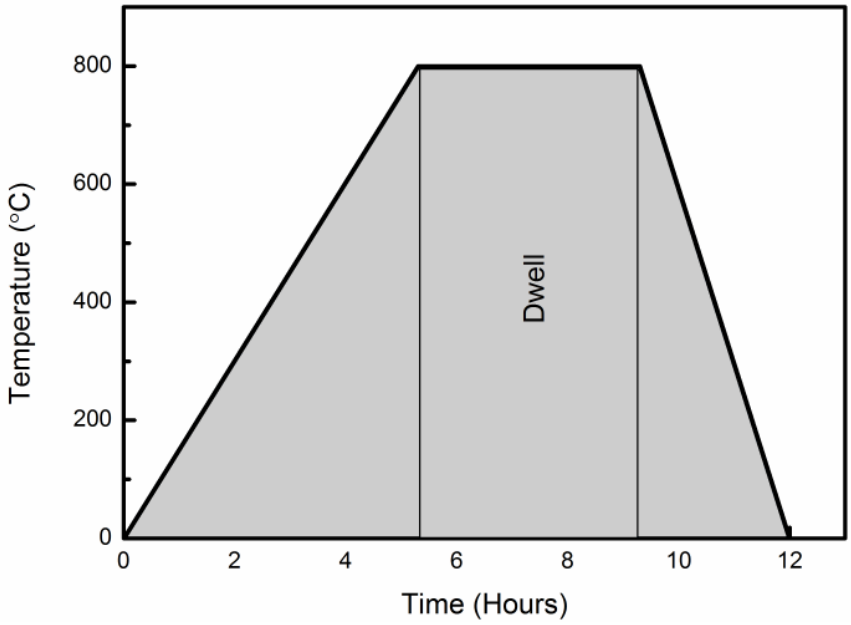

Figure 3-1. Diagram representing the calcining regime

3.3 Synthesis of Pellets

Powders were then uniaxially pressed at 50 MPa in order to form cylindrical pellets with a number of different geometries used, followed by cold isostatic pressing at 300 MPa for 10 minutes so that the density of the unsintered pellets was increased and higher densification could be achieved, also reducing the loss of volatile elements such as bismuth and potassium due to the reduction in sintering temperatures [202–205]. Pellets were sintered in a bed of calcined powders of the same composition in a covered alumina crucible to minimize the loss of volatile elements due to the creation of a positive partial pressure of volatiles. The binder was burnt out by slow heating to 600 °C, followed by sintering at 1000-1065 °C for 2 hours. During the dwell stage, porosity was further reduced with the diffusion of vacancies along grain boundaries. The pellets were then cooled to 600 °C at 150 °C/hour so that thermal shock was reduced and internal stresses minimised. Finally the temperature was reduced to room temperature at a rate of 300 °C/hour. Figure 3-2 demonstrates the sintering regime employed. Sintered pellets would show a significant increase in density ranging

between 15 and 20 %. Sintered pellets also suffered from a deleterious layer approximately ~50 µm thick that would be depleted of Bi and K oxides due to evaporation, this was misrepresentative of the bulk material and was therefore always removed [203, 206] before sample preparation by mechanical lapping with silicon carbide papers (Buehler, Germany).

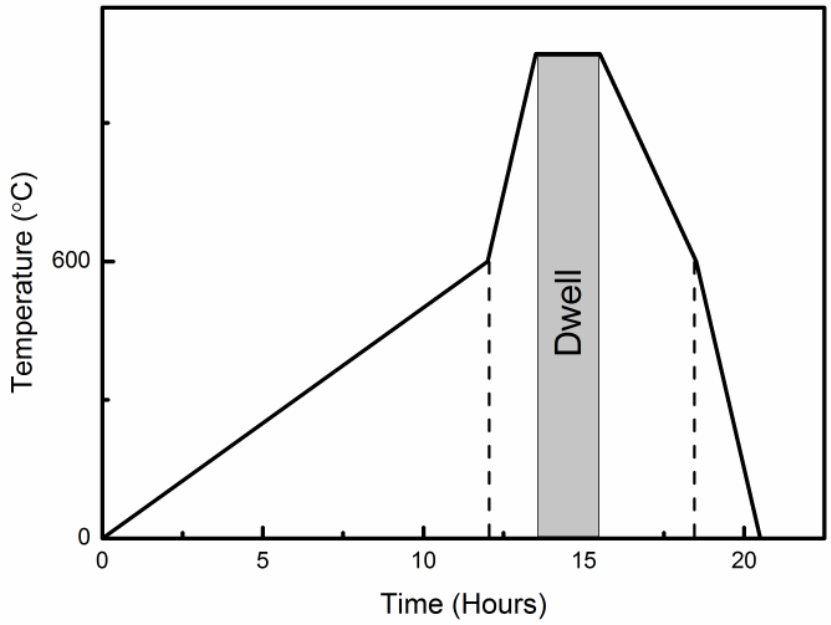

Figure 3-2. Diagram representing the sintering regime

3.4 Room Temperature Experimental Techniques

3.4.1 X-ray Diffraction

The equipment used during this study was a PANalytical X'Pert Diffractometer (Phillips, The Netherlands) using a theta-theta goniometer so that the sample remains flat at all times. This equipment allows rapid interchange between bulk ceramic samples and powders and is also capable of operating up to 1200 ºC with the use of a specialist fixture (Anton-Paar HTK 1200).

X-rays were produced at 40 kV and 40 mA throughout. A mask was used to control the area illuminated with x-rays as this would vary depending upon the sample stage. The scanning time varied depending upon the materials being examined as chemical makeup and crystallographic structure can significantly

affect the ability to analyse diffraction patterns. A standard step size of 0.033° and a scan time of 30 minutes from 18 ° to 60 ° 2-theta was used for most scans.

Pellets were made by mechanically lapping the sintered pellets with silicon carbide papers to the desired thickness which was ~1mm. The lapping routine used would involve using increasingly fine silicon carbide papers. Mechanical polishing can introduce significant residual stresses in the surface morphology that can cause a significant variation from the true structure. The samples would then be mounted using modelling clay into a sample stage. Care was taken to ensure the sample geometry was 'flat' to the surrounding fixture.

Powders were made from crushed sintered pellets which were subsequently annealed. Powders were useful in determining the structure of pellets with large internal stresses that satisfied Braggs law over a wide range of angles as discussed previously. The annealing regime used in all samples unless stated involved a ramp up rate of 200 °C/hr up to 650 °C followed by a cooling rate of 50°C/hr. Powders were also used with the hot stage so that the phase transition associated with the Curie point could be observed more clearly. When loading powders into the sample fixture it was important to avoid imparting any texture.

3.4.1.1 Data Refinement

XRD patterns were analysed using PANalytical Highscore Plus, peak profile fit was utilised to determine the different lattice parameters, unit cell volume and phases present in each composition. This is different to a Rietveld refinement in that a model of the unit cell is not generated, although a least squares method is used to generate the fit, the agreement of this fit is provided as R_{wp} values. Peak-fitting was also performed using pseudo-Voigt profiles with the program Winplotr, part of the Fullprof suite, for high temperature characterisation due to the difficulties in distinguishing peak positions with very similar d-spacing such as in materials close to the Curie temperature.

3.4.2 Synchrotron

The I15 extreme conditions beamline at Diamond was used during this study. A custom sample stage was built to allow for the application of a DC electric-field *in-situ* using an experimental set-up similar to that shown in Figure 3-3 controlled by a customised LabVIEW program.

Diffraction patterns were using a monochromatic beam of x-rays and the results presented in this thesis were obtained during two separate Diamond experiments, albeit on the same beamline. The first experiment allowed for samples to be measured *in-situ* with an applied electric-field, this was applied gradually in 0.5 kV/mm steps with the samples were contained in silicone oil to prevent dielectric breakdown through the air. A MAR 345 image plate detector, the detector distance was 988 mm from the sample with a spot size of 100 μm x 100 μm and a wavelength of 0.26 Å. The second experiment was carried out on poled and unpoled samples *ex-situ* due to time constraints. A Perkin Elmer flat panel 1621 EN detector also 988 mm from the sample with a spot size of 200 μm x 200 μm and a wavelength of 0.1839 Å.

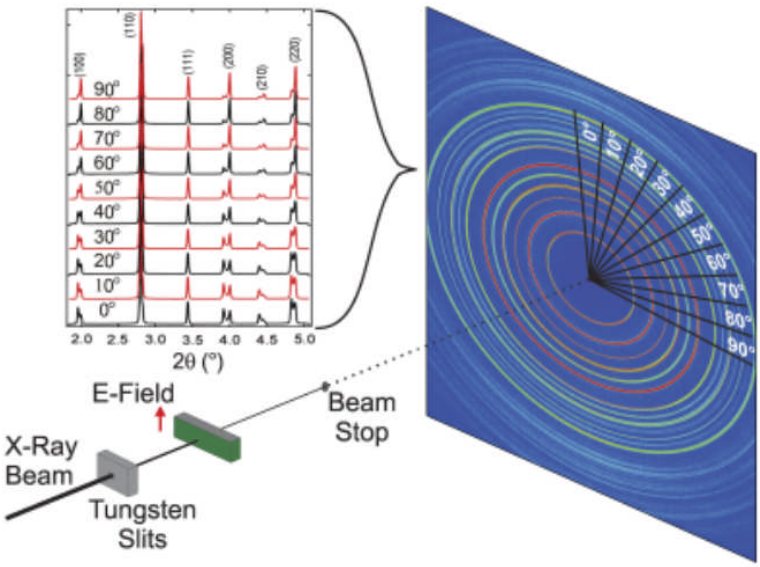

Figure 3-3. Experimental set-up used at Diamond I15 [207]

Consistent sample preparation was used throughout and samples measured were prepared from the same pellet to ensure consistency. Sintered pellets with diameters of 30 mm were first prepared, followed by a coarse mechanical lapping

stage to ~1.5 mm using a semi-automatic Motopol 2000 grinding wheel (Buehler, Germany) and magnetic diamond embedded grinding discs (Struers, Denmark). Lapping further reduced the thickness to 1 mm whilst maintaining that the sample was flat across the entire surface. The samples were then electroded with a fire on (550 °C) conductive silver paste (Gwent Group, UK). Electroded pellets were cut into bars using a diamond wafer cut-off saw (Loadpoint, UK). The bars used measured 1 x 1 x 4 mm and were polished with fine grit (P2500) silicon carbide papers on all surfaces except that of the electrode face to remove any damaged areas generated during the cutting process.

3.4.2.1 Data Reduction

The Fit2D software package was used to convert the Debye rings recorded on the image plate into a diffraction pattern in the familiar intensity vs. 2θ plots. The 2D Debye rings were caked into 36 azimuthal sectors with a width of 10° allowing for orientation dependent features to be observed. An average of the Debye rings can be easily calculated in an unpoled sample, assuming that it is not textured, however, when an electric field is applied or poled samples are introduced then the texturing in relation to 0° and 90° with respect to the applied field vector is significant in a piezoelectric ceramic body.

3.4.3 Strain-Electric Field

x-E loops were measured using a TREK (5/80) high voltage amplifier used in conjunction with a MTI-2100 Fotonic sensor (MTI Instruments, USA), with the electric-field and data collection controlled by a Precision LC (Radiant Technologies, USA) ferroelectric tester.

The electric-field applied was ramped up in 0.5 kV/mm steps from 1 kV/mm until electrical breakdown of the sample occurred. Triangular waveforms were used so that the sample did not suffer from significant self-heating and a greater accuracy in the applied field could be achieved therefore reducing the likelihood of a breakdown event. Samples were tested across a wide range of frequencies.

Much of the high electric-field experiments required similar sample preparation which will be outlined here and referred back to in future sections if necessary. The standard routine for electrical characterisation typically involved mechanically lapping the pellet(s), the thickness dependent upon the measurement, with a series of silicon carbide papers as previously outlined. These would then be electroded using a fire on conductive silver paste, chosen over a dry-on silver paste due to its thermal and chemical stability. The sides of the sample would then be lapped to remove any of the remaining sintered layer and also any excess silver paste so that an electrical contact could not be made across the sample surfaces. Thin samples <500 μm would be used in high voltage experiments such as x-E, P-E and PUND measurements in order for the experiment to be completed within the given amplification range of the apparatus (+/- 5 kV) and to reduce the likelihood of dielectric breakdown. Samples produced were relatively flat, a variation of less than 20 μm was required so that a uniform field was applied and the optical probe could measure the displacement accurately.

3.4.4 Polarization-Electric Field

P-E loops were carried out using a modified Sawyer-Tower circuit built in to the Radiant Precision LC Ferroelectric Tester and a TREK (5/80) high voltage amplifier and the manufacturer supplied High Voltage Displacement Meter (HVDM). A PTFE sample chamber with high voltage wire connections and a small well for submerging the sample in dielectric oil was used.

The P-E measurements were performed simultaneously with the x-E measurements, thus allowing for the same electric-fields and ramp to be used. Polarization-field loops can be frequency dependent so a wide frequency range was measured between 0.1-100 Hz. Samples were prepared as outlined in Chapter 3.4.3

3.4.5 PUND

The Radiant Precision LC Ferroelectric tester in conjunction with a TREK (5/80) was also used to obtain the PUND measurements. All samples were tested with a pulse delay time of 1 second and a pulse width of 1 second, these measurement parameters led to frequent dielectric breakdown events due to the rapid onset of the switching field which shocks the ceramic body. A delay of 1000 ms was chosen for the polarization to reverse in the absence of an electric-field, replicating a study by Dolgos [46], it was suggested that this was a reasonable amount of time for polarization reversal to be observed. Samples were prepared as outlined in Chapter 3.4.3.

3.5 High Temperature Experimental Techniques

3.5.1 Strain-Electric Field

The facilities at Pennsylvania State University were used during my secondment to record electric-field induced strain, polarization and Rayleigh analysis at high temperature and were not available for the entire duration this study. A linear variable differential transducer (LVDT) was used in line with a DSP SR830 lock-in amplifier (Stanford Research, USA) and a high voltage TREK 610C power supply (TREK, USA). A National instruments data acquisition card was used to record the experimental data. Samples were placed in the sample fixture between two metal electrodes and suspended in an oil bath. This fixture was then placed in a convection furnace that was also connected to a liquid nitrogen tank allowing a working range between -50 °and +150 °C. The operating limit of the equipment was due to the dielectric oil as fluoropolymers can emit toxic vapours above a critical temperature. The temperature was recorded at the sample using a thermocouple and the lock-in amplifier was calibrated to within a pre-determined voltage range that could be measured by the LVDT.

Samples were held at the set temperature for 10 minutes before measurements were recorded. Low temperature measurements were carried out before high temperature measurements. Strain-field data was recorded between

0.1 - 10 Hz in 1kV/mm steps from 1 kV/mm. Although substantial (>8 kV/mm) electric-fields could be maintained at low temperatures this was often not the case at high temperatures which was accounted for by limiting the maximum applied field to a level that would allow meaningful comparisons at low and high temperature. Samples were prepared as outlined in Chapter 3.4.3.

3.5.1.1 Rayleigh Analysis

Rayleigh analysis was carried out using the equipment discussed in Chapter 3.5.1. The applied voltage, E_0, was applied using a triangular waveform and increased for each successive measurement. The electric-field was applied in 0.1 kV/mm steps from 0.2 kV/mm to 1 kV/mm. Much lower electric-fields, between one-third to one-half of the coercive field were utilised than for a standard room temperature measurement as the coercive field often reduces with increased temperature and much lower fields would be required to nucleate new domains. Low temperature measurements were undertaken before high temperature measurements. Samples were measured at 1 Hz which allowed small displacements to be observed. Samples were prepared as stated in the corresponding low temperature measurement in Chapter 3.4.3. Experimental values were compared to the calculated Rayleigh model, if the calculated and measured values differ greatly then Rayleigh analysis may not be appropriate.

Poled samples were required for Rayleigh analysis and prepared as per the strain-electric field measurements, this would occur >24 hours before testing to allow the samples to age and the domains to stabilise. The optimal poling conditions were used for each composition and are discussed in Chapter 5.4.2.

3.5.2 Polarization-Electric Field

P-E loops were carried out simultaneously with the x-E loops using a modified Sawyer-Tower circuit. Limited to a relatively small bandwidth, in the region of 0.1 to 3.3 Hz, due to conductivity at high temperatures, a maximum applied field and frequency range were used that would allow meaningful comparisons at low and high temperature between the measured data. This

technique worked in a similar manner to the Radiant ferroelectric tester, although one of seven reference capacitors was manually selected as saturation occurred. A delay function was also used to remove the initial rise from zero so that closed loops could be obtained. Samples were prepared as outlined in 3.4.3.

3.5.3 Permittivity-Temperature

The sample capacitance was collected across a range of frequencies using an Agilent 4292A (Agilent, USA), with a non-inductively wound Pyrotherm tube furnace and a GPIB (IEEE) interface was used along with computerised data acquisition. The sample was housed in the tube furnace that was heated up to the desired temperature at 3 °C/min, a K-type thermocouple was located at the sample and the temperature was recorded using a National Instruments USB-TC01 device. The temperature range measured was changed according to the sample. Permittivity-temperature samples had a thickness of 1 mm to enable easy manipulation of the sample when fixing into the sample holder.

3.5.4 PRAP

Small signal dielectric, elastic and piezoelectric characterisation was undertaken using an Agilent 4192A (Agilent, USA) to determine the resonance spectra of the compositions of interest. These were examined at temperature with the aid of a non-inductively wound tube furnace. The resonance spectra were subsequently analysed with a commercially available package, Piezoelectric Resonance Analysis Program (PRAP)(TASI Technical Software, Canada), which fits a model to the experimentally collected values and subsequently determines the electromechanical coefficients [208], the depolarization temperatures were identified as being when a model could no longer be fitted.

By using different geometry specimens tested in different resonant frequency modes, the entire piezoelectric matrix of that material can be constructed, however, this study focused on discs as sample preparation time was minimised. As with the Rayleigh analysis, measurements were carried out on fully poled samples, first at low temperature and subsequently heated with a dwell time

of 10 minutes in order to allow thermal stabilisation of the sample. The voltage applied to the sample (<1 V) is not able to cause irreversible domain switching.

3.6 Imaging Techniques

The majority of samples analysed using SEM and PFM required extremely high levels of polishing. The main purpose of this process was not to remove large swathes of material such as in the mechanical lapping process but to remove scratches and to ensure the surface was flat and damage was limited. This was achieved either by loading ceramic samples into a cold-setting resin (Struers, Denmark) and curing for >24 hours or by attaching them to the semi-automatic grinding platen with laboratory grade bees wax. Resin mounted samples allow a greater degree of control when fixing samples into the automatic polishing wheel head. The polishing routine used is detailed in Table 3-1 and was provided by Buehler and replicated at Leeds.

Once the sample was mounted to the polishing head it would not be removed until the polishing process was complete so that flatness was kept to an optimum and all the samples were planar relative to each other. Step 1 removes material until the samples are planar and subsequent steps provide a high level of polishing. Diamond suspensions were sprayed onto the polishing cloths before and during each step, these also acted as a lubricant; these were required to minimise heat generation so that wear was limited, smearing across the sample also occurs with insufficient lubrication. The diamond spray was reapplied every 30 seconds. Each step was followed by a cleaning route of detergent, water, methanol and sonication so that the polishing material from the previous route was removed from the polishing head and sample surface. This routine was relatively non-aggressive, by using napped cloths, so that damage to the sample was minimal. The use of hard cloths is favoured so that flatness can be well controlled. The images below (courtesy of Buehler customer service laboratory) show the final two polishing stages, images were captured using a 3 MP UEye digital microscopy camera attached to a Nikon LV100 microscope. Scratches can be observed in Figure 3-4.

Table 3-1. Polishing routine used for BF-KBT-PT ceramics (Supplied by Buehler)

Step	Surface	Abrasive	Lubricant	Time (min:sec)	Platen Speed (rpm)	Head Speed (rpm)	Relative Rotation
1	SiC	P400/P600	Water	Until Plane/0:40	150	60	Comp
2	TexMet P	9 µm Metadi Supreme	N/A	5:00	150	60	Contra
3	TexMet P	3 µm Metadi Supreme	N/A	5:00	150	60	Comp
4	Trident	1 µm Metadi Supreme	N/A	3:00	150	60	Comp
5	ChemoMet	MasterMet Colloidal Silica	N/A	1:20	100	60	Contra

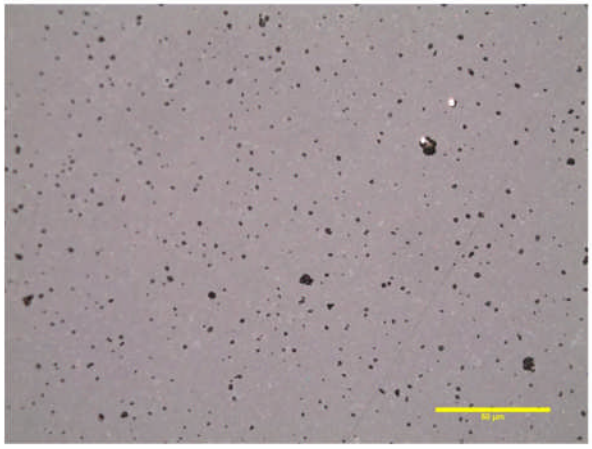

Figure 3-4. 1 µm polishing stage, 50x magnification

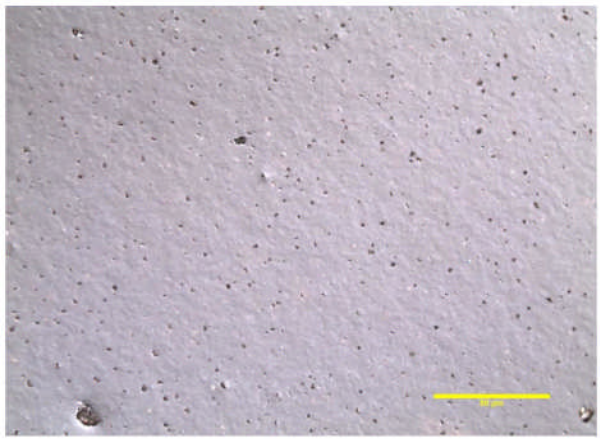

Figure 3-5. 0.02 µm polishing stage, 50x magnification

3.6.1 Scanning Electron Microscopy

Electron microscopy was performed on a LEO 1530 FEGSEM. The working distance was varied depending upon the sample and the accelerating voltages were between 5-8 kV. Magnifications were kept to a number of standard sizes for ease of comparison, typically 10 kX, 20 kX, 40 kX and 60 kX.

A number of sample forms were imaged, including fracture surfaces, powders and the aforementioned polished pellets all of which were placed on to carbon tape positioned on the sample stub and painted with carbon on the fringes of the sample and stub in order to prevent charging and allow current to pass. In addition a small layer (5 nm-20 nm) of platinum was sputtered on the surface of the sample to further prevent charging. Fracture surface images were prepared from broken pellets with the flattest shards used so that sample features could easily be imaged. Powders were pressed on to the SEM stubs and any loose powder was removed with a ‘gas duster’ as the sample must be able to withstand the forces within the evacuated sample chamber [209]. It is also possible to image ferroelectric domains in the SEM with the use of etching to create surface topography as domains that intersect the surface etch at different rates depending upon their polarization vector. It was found in $BaTiO_3$ that when etched with HCl the positive polarization vector etched rapidly whereas the negative polarization vector etched at an extremely slow rate [210]. A small etching study was carried out to determine the ideal etching rates for a wide range of compositions which will be presented in the results section.

3.6.2 Piezoresponse Force Microscopy

An Agilent Technologies 5420 SPM was used equipped with a series of lock-in amplifiers and function generators. The tip utilised was a NSC14/Ti-Pt probe with a tip radius of ~25 nm. The bottom electrode was established on the base of the sample with dry-on conductive silver paint attached to an aluminium sample stage. An AC voltage of 10 V and a frequency of 30 Hz was applied to the sample. Scanning speeds of 0.24 μm/s were used when imaging. The equipment was calibrated using a $LiNbO_3$ single crystal before use. Polished samples were prepared as previously outlined in Chapter 3.6.

4. Preparation and Characterisation of $BiFeO_3$-$(K_{0.5}Bi_{0.5})TiO_3$

4.1 Chapter Overview

The goal of this chapter is to outline the rationale during the development of the $BiFeO_3$-$(K_{0.5}Bi_{0.5})TiO_3$-$PbTiO_3$ system, beginning with the lead-free $BiFeO_3$-$(K_{0.5}Bi_{0.5})TiO_3$ family. This will allow for a greater understanding of the governing mechanisms. The objectives of the initial work into this system were to;

- Synthesise high-density bulk polycrystalline ceramics that are absent of secondary phases that are non-perovskite and non-piezoelectric.
- Fully characterise the structural and electrical properties using conventional laboratory techniques previously outlined.
- Evaluate their suitability as lead-free, high-temperature piezoelectric ceramics.

4.2 Background

The recently reported $x$$BiFeO_3$-$(1-x)(K_{0.5}Bi_{0.5})TiO_3$ system was discussed in Chapter 1.6.2.2, a number of researchers were simultaneously working on this system including the author of this thesis, however, a number of dissimilarities were discovered. Here, we present the entire compositional space and characterisation techniques that previous publications have not thus far addressed. The $BiFeO_3$-$(K_{0.5}Bi_{0.5})TiO_3$ family were all produced by ball milling as outlined in the Chapter 3.2.

The motivation for this research and the conclusions drawn must be first addressed before the $BiFeO_3$-$(K_{0.5}Bi_{0.5})TiO_3$-$PbTiO_3$ system is introduced. A simplified nomenclature will be used for brevity and clarity, the $x$$BiFeO_3$-$(1-x)(K_{0.5}Bi_{0.5})TiO_3$ will be suffixed by four numbers, the first two relate to the percentage content of $BiFeO_3$ with the last two referring to the percentage of $(K_{0.5}Bi_{0.5})TiO_3$ i.e. 8020 BF-KBT is equivalent to $x = 0.8$.

4.3 Sample Preparation

Sintered pellets were produced using the sintering route previously outlined in Chapter 3.3. Upon sintering geometrical density measurements were performed, the theoretical density was calculated by interpolating the densities of the end members, as reported in the literature of 8340 and 6244 kg/m^3 for $BiFeO_3$ [211] and $(K_{0.5}Bi_{0.5})TiO_3$ [212] respectively. The density recorded via the geometrical density method was found to be in excess of 90% of the theoretical density across the compositional space except at x = 0.1, shown in Figure 4-1. The density was found to significantly reduce at x = 0.1 owed to the reduction of $BiFeO_3$ content and the stabilising effect that this has upon the $(K_{0.5}Bi_{0.5})TiO_3$ compound, the volatilisation of potassium and bismuth is well documented [148]. For x = 0.1 a further increase in dwell temperature of 25 ºC led to melting of the sample, the use of attrition milling would aid in reducing the sintering temperature due to the reduction of particle size. These density values were similar to those found by Matsuo using standard milling techniques, the flash creation method was subsequently used to increase densification to in excess of 95% [144]. With reduction of $BiFeO_3$ content the appearance and hardness of the samples noticeably changed from grey at x = 1 to white at x = 0.

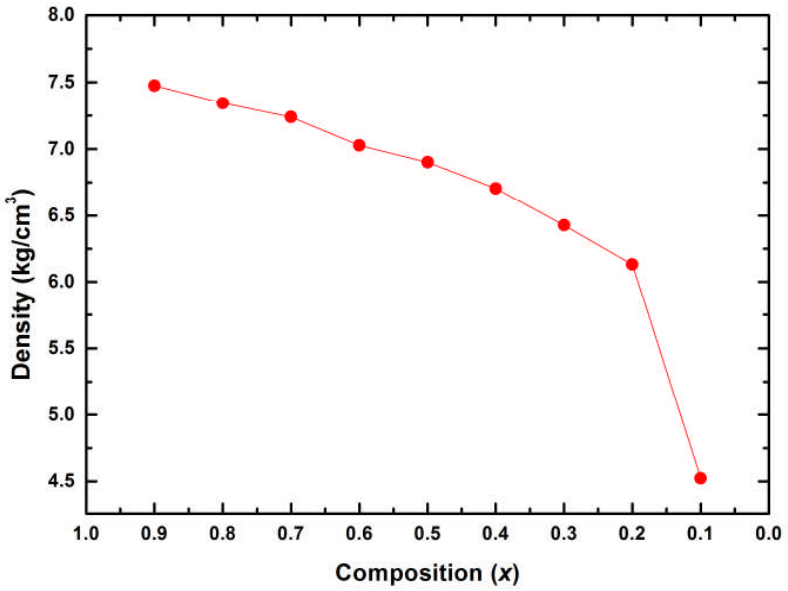

Figure 4-1. Geometrically measured density across the compositional space

4.4 Structural Phase Analysis

Laboratory X-ray analysis was used for phase identification on crushed and annealed pellets, the importance of the sample form will be discussed in more detail in Chapter 5.3.1. Examples of the diffraction patterns obtained are shown in Figure 4-2 with zoomed in patterns of the {111} and {200} family of planes shown in Figures 4-3 and 4-4 respectively. Single-phase ceramics belonging to the perovskite structure were produced across the entire compositional space. These were formed with no discernible secondary phases, as indicated by the absence of minor peaks between the major identified reflections. These compositions were scanned for considerably longer periods than normal (8 hours) as fluorescence was considerable and the background intensity was significant. Rietveld refinements were attempted although unsuccessful as isotropic negative temperature factors were generated and it was deemed beyond the scope of this study.

The $BiFeO_3$ rich compositions where x = 0.9 - 0.5 fit that of a rhomobohedrally distorted structure as typified by splitting of the {111} family, presented in Figure 4-3. Note that a small peak to the left of the {111} family, associated with oxygen octahedral tilting, was not observed using conventional XRD. From XRD, the relative intensity of the (111)/(-111) reflections in the $BiFeO_3$ rich compositions are ca. 1:3, as should be the case for unpoled rhombohedral materials. At x = 0.4, no obvious peak splitting was observed in the {111} family of planes although considerable broadening and asymmetry was observed in this data, in contrast to Morozov and Matsuo who noted this transition at x = 0.6. It has been suggested that the pseudocubic phase is characterized by nanodomain structures consisting of non-polar cubic and polar rhombohedral structures of the order of 10 nm identified using TEM, therefore explaining the absence of rhombohedral or tetragonal splitting using conventional laboratory X-rays. Morozov also noted tetragonal splitting at x = 0.75 in the {200} family, this was not observed in the diffraction patterns collected at the same $(K_{0.5}Bi_{0.5})TiO_3$ concentrations, although the {200} peak is broader at x = 0.2 as opposed to at x = 0.3. Peak broadening and minor peak splitting were observed in the (200) reflection for x = 0.1, this is indicative of the transition to the tetragonal phase

although these samples were under-sintered and grain size may be much reduced compared to $BiFeO_3$-rich compositions leading to peak broadening, this may explain the difficulty in observing this transition clearly.

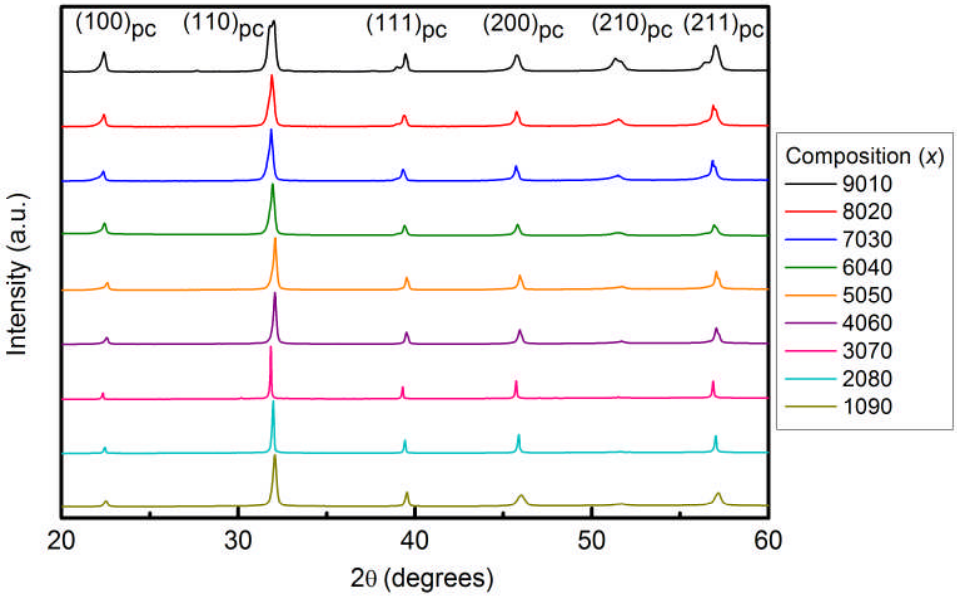

Figure 4-2. X-ray diffraction patterns taken from crushed annealed ceramics of $BiFeO_3$-$(K_{0.5}Bi_{0.5})TiO_3$

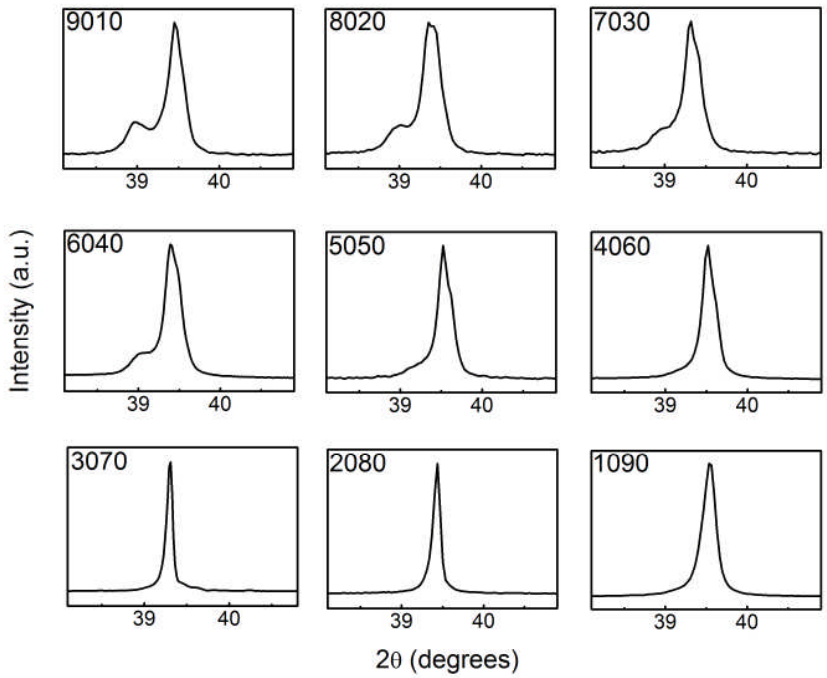

Figure 4-3. X-ray diffraction patterns of the 111 family *x*$BiFeO_3$-(1-*x*)$(K_{0.5}Bi_{0.5})TiO_3$ from 38 to 41°

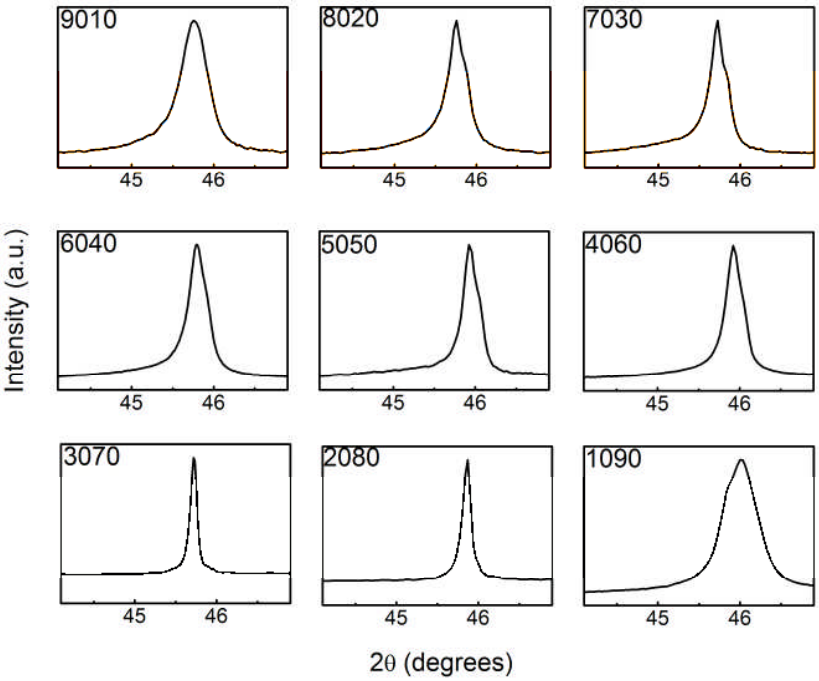

Figure 4-4. X-ray diffraction patterns of the 200 family belonging to xBiFeO$_3$-(1-x)(K$_{0.5}$Bi$_{0.5}$)TiO$_3$ from 44 to 47°

4.4.1 Neutron Diffraction

A limited amount of neutron diffraction time was awarded to investigate this system where x = 0.8, 0.7 and 0.6, the refinements were performed by Dr. T.P. Comyn, as the magnetic properties do not form a key component of this thesis they will largely be omitted. The magnetic structure was investigated using neutron diffraction data collected at room temperature from sintered ceramic samples on the GEM powder diffractometer at the ISIS pulsed neutron source (Rutherford Appleton Laboratory, UK). The nuclear and magnetic structures were refined by the Rietveld method using GSAS. The BiFeO$_3$ structure was used as the starting model and was modified to locate K and Ti on the Bi and Fe sites respectively. Neutron diffraction data are shown in Figure 4-5, as with XRD no secondary phases are evident and these compositions were refined to fit the R3c space group. The antiferromagnetic Bragg peak at ca. 4.6 Å (101) clearly reduces in magnitude with the dilution of the BiFeO$_3$ phase, as (K$_{0.5}$Bi$_{0.5}$)TiO$_3$ is added. The strongest correlation with composition is in the oxygen tilt angle. A tilt angle of 12.2° is reported in the literature for unmodified BiFeO$_3$ [117], in this system the angle reduces with x, to 10.26° (x=0.8), 8.84° (x = 0.7) and 7.07° (x = 0.6).

Oxygen tilting has been widely discussed in PZT and was found to inhibit domain wall mobility [17], the effects of which are discussed in Chapter 4.5.

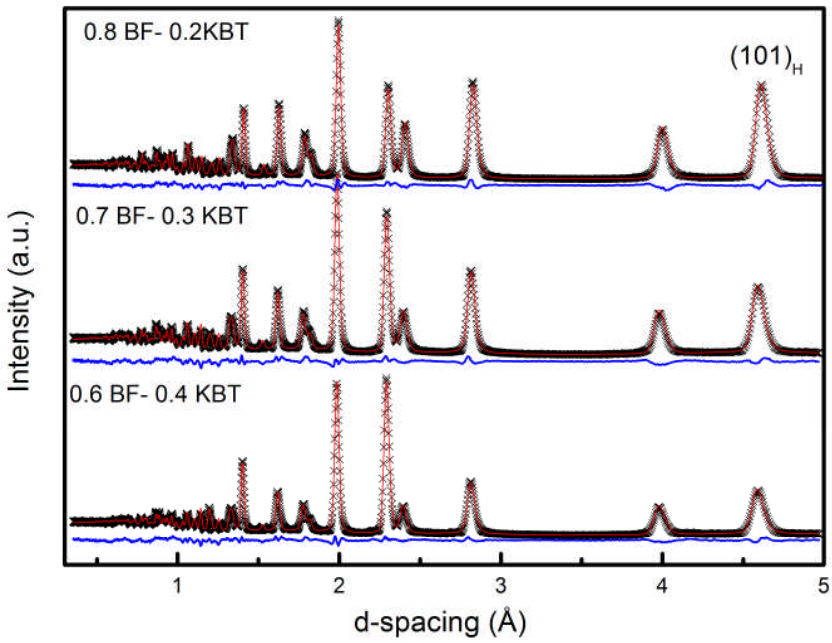

Figure 4-5. Neutron diffraction patterns with the associated structural and magnetic refinements for bulk ceramics collected at 296 K. The residual is shown underneath each scan.

4.5 Electrical Properties

The typical procedure after structural analysis would be to conduct basic electrical characterisation. Figure 4-6 demonstrates electric-field induced strain measurements across the compositional space. All measurements were collected at 8.5 kV/mm and 0.1 Hz to allow for useful comparison, although larger fields were used during the measurement cycle, especially in the $BiFeO_3$-rich compositions where up to 13 kV/mm was applied at x = 0.9 and 0.8, no behaviour was elucidated that cannot be explained at 8.5 kV/mm. The ability to apply large electric-fields is also an indicator as to the quality of the ceramics produced as samples absent of secondary phases can sustain greater fields during the measurement cycle than conductive non-perovskite secondary phases, porosity can also lead to dielectric breakdown.

Electric-field induced strain measurements, shown in Figure 4-6, indicate an increase in the strain response with the addition of $(K_{0.5}Bi_{0.5})TiO_3$, noticeably where x = 0.6 from 0.13% to 0.33% at x = 0.4. The values reported are sizeable although the application of large electric-fields is required, when compared to BFPT system it is apparent that much reduced electric fields are required to cause the onset of strain which is between 7-17 kV/mm in BFPT. Similarly to BFPT the electric-field induced strains observed appear to be largely electrostrictive although this can be owed to different origins. In BFPT, ferroelastic domains are pinned as a result of the c/a ratio of 1.18, as a consequence extraordinarily large fields (up to 20kV/mm) are required to exceed the coercive field and observe the piezoelectric effect in x-E measurements. However, the crystallography of the BF-KBT system would suggest that the electrostrictive response is dominant and piezoelectric effect is negligible in the 'pseudocubic' region where x <0.4 as little negative strain is observed in general and no negative strain observed at x = 0.3, a stipulation required for a material to defined as piezoelectric, this response is similar to that displayed by relaxor ferroelectrics.

The electric-field induced strain response, highlighted in Figure 4-7, is non-linear with some hysteretic behaviour, which is anticipated for a piezoelectric material as switching and movement of interfaces such as domain walls occurs when subjected to large electric-fields, especially for non-180 º domains which can be responsible for significant dimensional variations [213], however, this non-linearity does not correlate to low-signal measurements of the piezoelectric charge coefficient. As discussed in the literature review, other research groups have also observed this behaviour and the proposed origin is due to the presence of polar nanoregions which dominate the electromechanical response as an applied field easily aligns the PNRs but this behaviour is not spontaneous i.e. with the absence of an electric-field. Although not presented, the strain response was severely frequency dependent which is common in many lead-free and lead-based relaxor materials.

The reduction in coercive field correlates with the reduced oxygen tilt angle, which changes from 7.5 kV/mm in pure $BiFeO_3$, to 5.8 (x=0.8), 5.3 (x = 0.7) and 3.85 (x = 0.6) kV/mm. This is proposed to be due to the increased

domain wall mobility as a result of the antiphase tilt boundary suppression, as observed in $BiFeO_3$ and PZT [116].

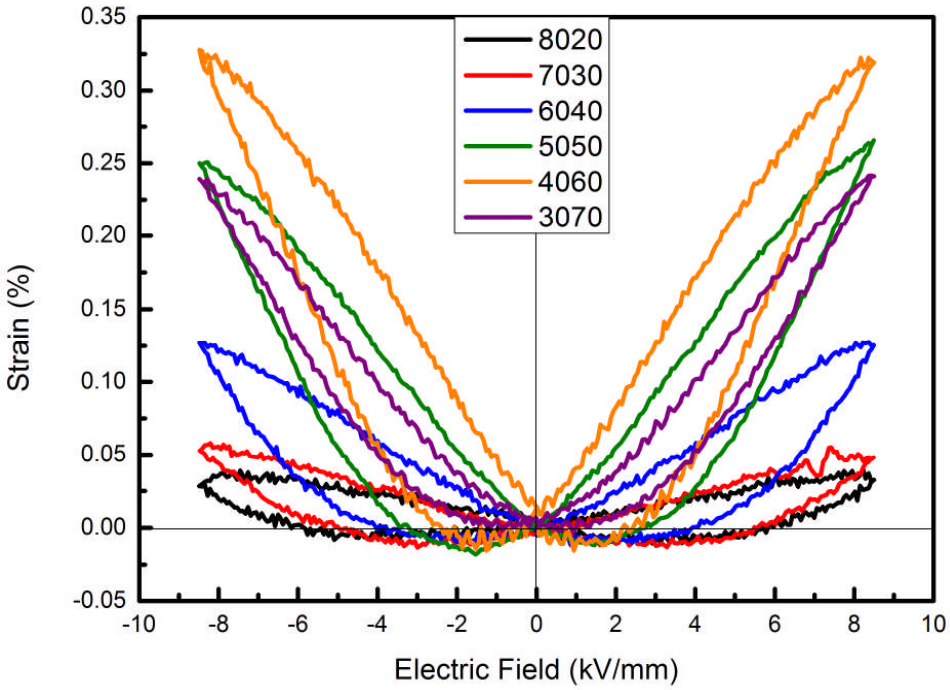

Figure 4-6. Bipolar electric field induced strain values for *x*$BiFeO_3$-($K_{0.5}Bi_{0.5}$)TiO3 at 8.5 kV/mm and a frequency of 0.1 Hz

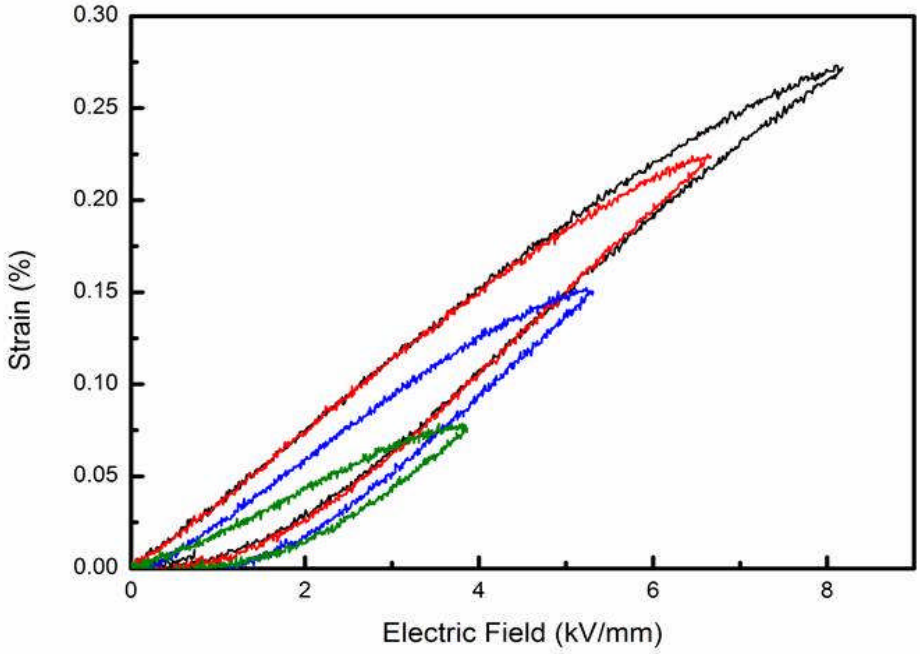

Figure 4-7. Unipolar electric field induced strain values for *x*$BiFeO_3$-($K_{0.5}Bi_{0.5}$)TiO_3 where *x* = 0.4 at 0.1 Hz

To highlight the effect of PNRs upon the piezoelectric response the d_{33} is presented in Figure 4-8 using two different measurement techniques, one utilising the direct effect with a conventional Berlincourt meter after poling and the other taken from the gradient of the electric-field induced strain values, S_{MAX}/E_{MAX}, which can be seen as the effective d_{33}^*. Relatively poor, compared to PZT, low-field piezoelectric charge coefficient d_{33} values were recorded across the compositional space with a maximum d_{33} of 45 pC/N observed at x = 0.6, however, the d_{33} values obtained in this study are an order of magnitude greater than in any undoped BFPT composition. The peak high-field d_{33}^* value identified was 386 pm/V at x = 0.4, this indicates that the behaviour observed in the electric-field induced strain measurements is dominated by electrostriction, as a result of PNRs, and the piezoelectric effect is actually limited. Another factor influencing the increasing d_{33}^* across the compositional space is the reducing coercive field as the electric-fields required to cause lattice or domain switching become reduced.

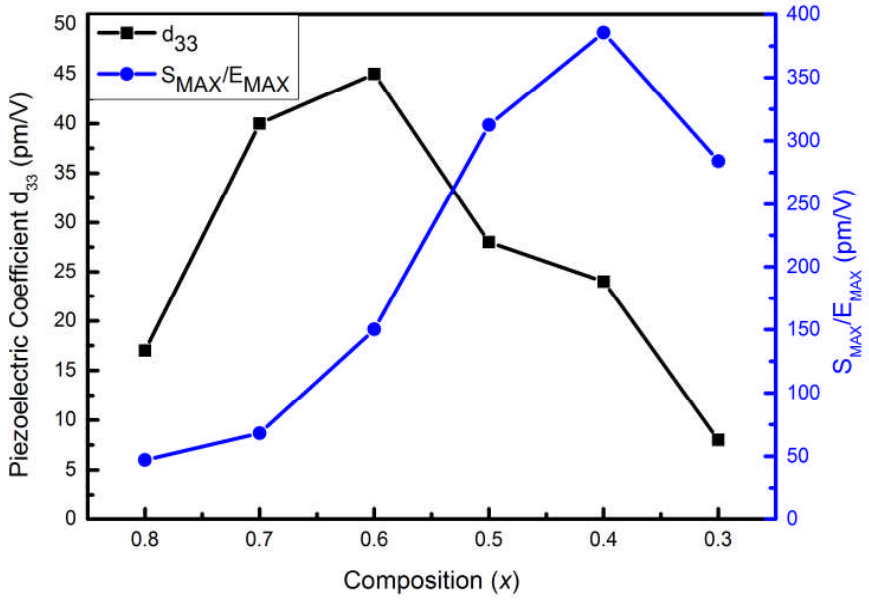

Figure 4-8. Piezoelectric coefficient obtained from a Berlincourt meter (110 Hz) and the effective d_{33} obtained from bipolar strain-field loops (0.1 Hz and 8.5 kV/mm) across the compositional range

A discrepancy is often observed between the d_{33} and d_{33}^* values, largely due to crystallography and domain structures [214], however, a disparity of this

scale is noteworthy. In the BF-KBT system the location of the peak d_{33} and d_{33}^* values do not correlate and the divergence increases with reduced $BiFeO_3$, this trend was also identified by Matsuo and in the pseudocubic region of the $BiFeO_3$-$BaTiO_3$ system [215], the origin of the discrepancy was suggested to be due to enhanced domain switching in high-field measurements with poor domain stability leading to reduced low-field coefficients. Future studies of novel piezoelectric ceramics should therefore not solely refer to the d_{33}^* as a means of identifying promising piezoelectric ceramics.

Electric-field induced polarization measurements correlate with the strain values collected. Well-defined ferroelectric or hysteretic behaviour cannot be deduced from these electric-field induced polarization measurements easily, especially at the $BiFeO_3$ rich end of the phase diagram where the materials exhibit behaviour consistent with that of a ferroelectric below saturation as observed in PZT [215]. At fields of 13 kV/mm for $x = 0.8$ the response is an open loop with no hysteresis as these samples are conductive at high fields owed potentially to the multivalent $Fe^{3+/2+}$ cation. The electric-field induced polarization measurement (calculated from an integration of current) becomes problematic when the electrical resistivity is low as conductive “football shaped” loops are often recorded, thus the measurement was performed at slightly higher frequencies (10 Hz) than the x-E measurements to negate the effects of electrical conduction which are much reduced as the frequency is increased.

P-E loops are exhibited for compositions where $x = 0.3$-0.6 in Figure 4-9 , concave loops were observed which is evidence of ferroelectric behaviour as endorsed by Scott [171]. The polarization values observed here are much lower in the active region (26-28 $\mu C/cm^2$) than those recorded by Matsuo of 52 $\mu C/cm^2$, which is attributed to the different processing techniques used. Whilst the maximum polarization value does not alter significantly where $x = 0.6 – 0.4$ the shape of the loop is increasingly linear; slim-loop type behaviour associated with certain classes of relaxor materials is observed. In conventional ferroelectrics, when $T < T_C$, hysteresis loops are square with $P_r \sim P_{SAT}$. As can be seen in Figure

4-10, the divergence between the P_{SAT} and P_R decreases up to x = 0.6 correlating with the piezoelectric activity, however, with further addition of $(K_{0.5}Bi_{0.5})TiO_3$ the divergence increases dramatically. The initial divergence between where x = 0.8 and 0.7 is proposed to be due to the relatively low electric fields applied. Therefore, PUND measurements were employed to confirm the time stability of the polarization.

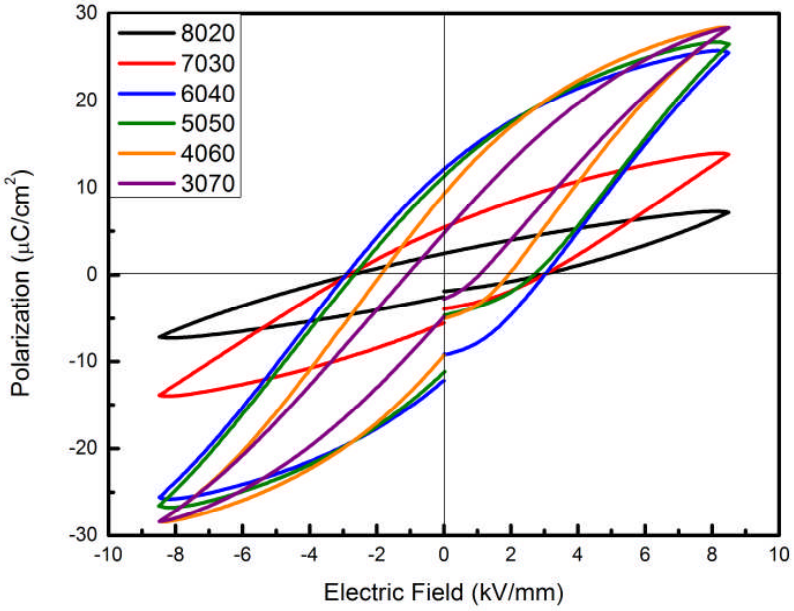

Figure 4-9. Bipolar electric-field induced polarization values for xBiFeO$_3$-(1-x)(K$_{0.5}$Bi$_{0.5}$)TiO$_3$ at 8.5 kV/mm and a frequency of 10Hz

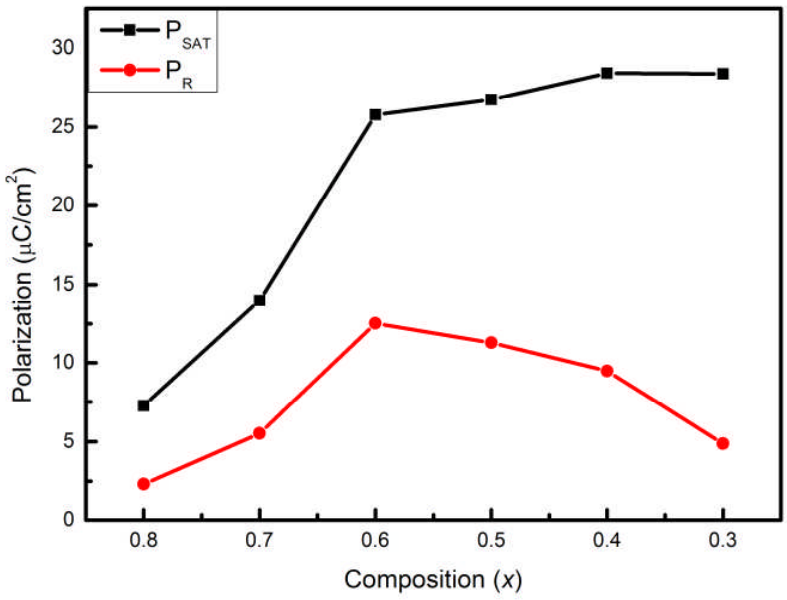

Figure 4-10. Saturation and remanent polarization values at 8.5 kV/mm across the compositional space

PUND analysis was carried out for x = 0.6 and 0.4, these compositions were chosen as the piezoelectric charge coefficient d_{33} was found to be highest at x = 0.6 and the largest d_{33}^* was observed at x = 0.4. This composition was proposed to be dominated by polar nanoregions which can be negated with this technique. The switchable polarization has been normalised to both the P_{SAT} and P_R to allow for suitable evaluation. It can be seen that the switchable polarization rises with increasing electric-fields as would be expected in typical ferroelectrics, both compositions appear to be at field amplitudes below saturation as the switchable polarization was not seen to level off. This linear behaviour in the PUND response has been observed in other lead-free $BiFeO_3$-based piezoelectric ceramics [46]. The switchable polarization at x = 0.6, shown in Figure 4-11, confirmed significant remanence with minor contributions from non-remanent polarization as $\Delta P/P_{SAT}$ and $\Delta P/P_R$ values of 0.83 and 0.4 respectively were identified. The coercive field can also be well defined at x = 0.6, in a typical ferroelectric material the switchable polarization would be expected to increase sharply beyond this point. The coercive field cannot easily be defined and a linear increase in the switchable polarization is observed where x = 0.4, shown in Figure 4-12, the magnitude of the remanence is lower with P_{SAT} and P_R values of 0.62 and 0.22 respectively, this reduction is due to suppression of long-range order by PNRs.

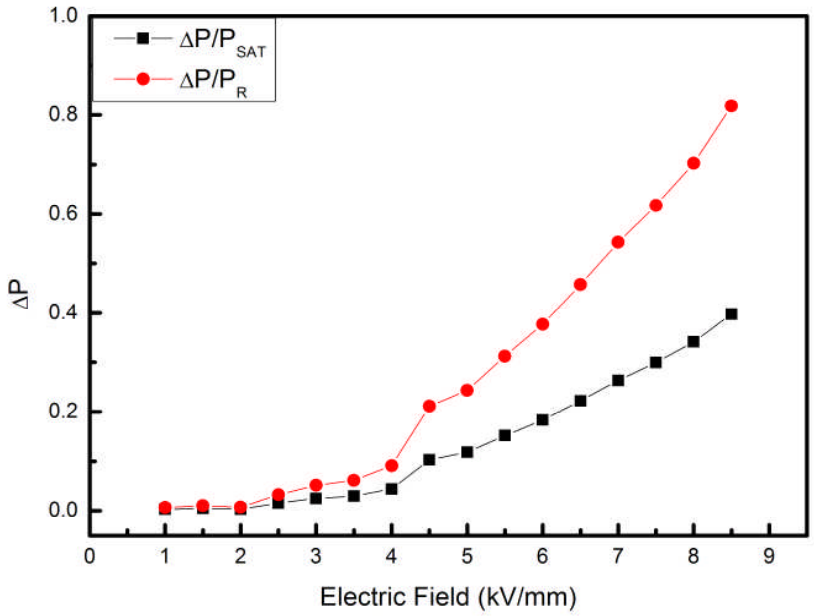

Figure 4-11. PUND data showing the switchable polarization of 6040 $BiFeO_3$-$(K_{0.5}Bi_{0.5})TiO_3$ normalised to both P_{SAT} and P_R at 8.5 kV/mm

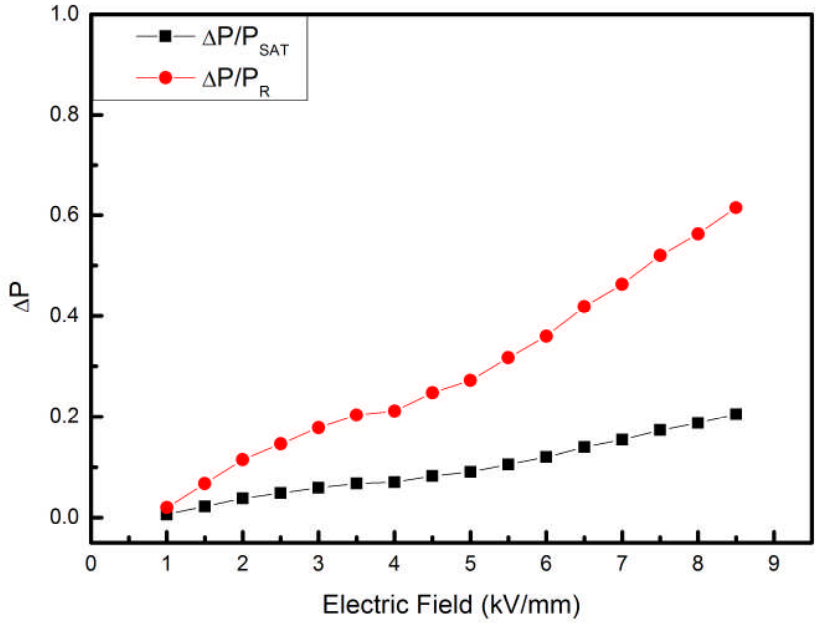

Figure 4-12. PUND data showing the switchable polarization of 40 $BiFeO_3$-$(K_{0.5}Bi_{0.5})TiO_3$ normalised to both P_{SAT} and P_R at 8.5 kV/mm

An explanation for the relatively low switchable polarization values obtained could be owed to leakage, however, the leakage was not found to be excessive, as shown in Figure 4-13 with values measured found to be typical for $BiFeO_3$-based piezoelectric ceramics. The leakage current density values measured are typically within the same order of magnitude albeit slightly higher than those documented by Matsuo [144], where x = 0.6 and 0.4 at 1 kV/mm J values were between 10^{-7}-10^{-8} A/cm^2, this can be explained by the different preparation methods utilised and the increased densification achieved by Matsuo.

The trend of the results correlated well to Matsuo's study in two respects, specifically with regard to the leakage as a function of electric field in each composition and with the leakage current values (measured at 8 kV/mm) as a function of composition. The $BiFeO_3$-rich composition where x = 0.8 exhibited lower leakage currents at low fields but upon application of large electric-fields was found to increase substantially, shown in Figure 4-14, due to enhanced charge carrier mobility under an applied electric field. The leakage current where x = 0.4 was comparatively linear with increasing electric-field amplitude. The leakage

current density measured under a high amplitude (measured at 8.5 kV/mm) across the compositional range reduced with increased $(K_{0.5}Bi_{0.5})TiO_3$.

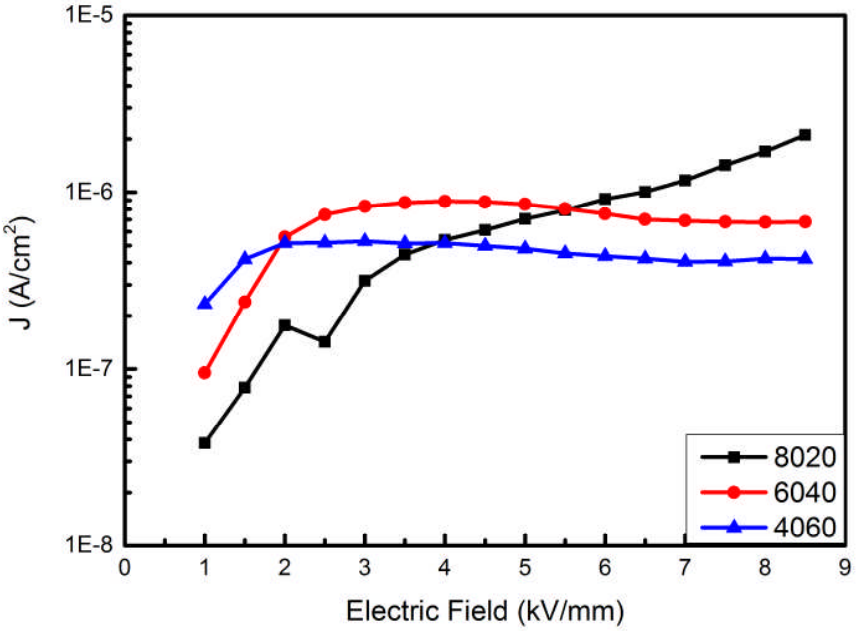

Figure 4-13. Leakage current density as a function of applied electric field strength for 8020, 6040 and 4060 $BiFeO_3$-$(K_{0.5}Bi_{0.5})TiO_3$ at ambient temperature

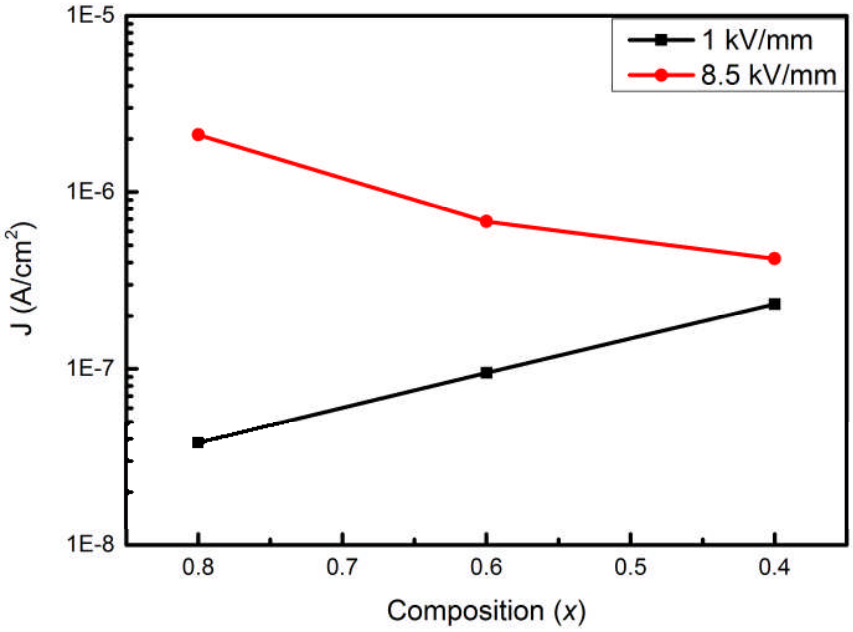

Figure 4-14. Leakage current density at 1kV/mm and 8.5 kV/mm for 8020, 6040 and 4060 $BiFeO_3$-$(K_{0.5}Bi_{0.5})TiO_3$ polycrystalline ceramics

4.6 Conclusions

The structural and electrical properties of $BiFeO_3$-$(K_{0.5}Bi_{0.5})TiO_3$ were investigated. Relatively dense ceramics, > 90%, were formed using ball-milling and conventional solid state processing. The perovskite structure was formed across the entire compositional space with the absence of secondary phases. The $BiFeO_3$-rich end of the phase diagram belonging to the rhombohedral phase where $x \leq 0.5$ was indexed to the R3c space group based upon diffraction experiments. A broad MPB was discovered between rhombohedral and pseudocubic phases at x = 0.4. A transition from the pseudocubic phase to the tetragonal phase was proposed to occur where x = 0.1, this is in disagreement with Morozov [145] who achieved a much higher densification although in agreement with Kim [143]. A phase-diagram has been included in Figure 4-15 to highlight the room-temperature structure and the phase transitions proposed by a number of authors. This phase diagram also highlights the transition temperature observed using permittivity as a function of temperature, although not presented in this thesis, as well as the low-field and high-field piezoelectric charge coefficients, which is discussed below. The transition temperature for the pseudocubic compositions is not immediately clear as this was often extremely broad and occurred over a wide temperature range, unlike in the $BiFeO_3$-rich compositions.

All compositions were found to exhibit piezoelectric coupling, the strength of this coupling varying significantly across the phase diagram. Across the rhombohedral phase the low-signal piezoelectric coefficient d_{33} values ranged from 17–45 pC/N where x = 0.8 and 0.6 respectively while in the pseudocubic region these ranged from 24-8 pC/N where x = 0.4 and 0.3. The compositions belonging to the $BiFeO_3$-rich region exhibited small negative strains during the electric-field induced strain measurements, the amplitude of this negative strain gradually reducing with the partial substitution of $(K_{0.5}Bi_{0.5})TiO_3$, until x = 0.3 where no negative strain was observed under an applied electric-field. An electric-field induced strain value was identified at x = 0.4 of 0.33%, compared to BFPT the addition of $(K_{0.5}Bi_{0.5})TiO_3$ serves to reduce the colossal coercive field and the onset field of piezoelectric strain substantially. The ferroelectric behaviour was closely aligned the piezoelectric response across the compositional space, to

further understand the origin of this behaviour PUND measurements were employed to gauge the switchable polarization, the value of which decreased with increased $(K_{0.5}Bi_{0.5})TiO_3$. The origin of these electrical properties is postulated to be due to the existence of polar nanoregions in the pseudocubic phase. Leakage current measurements confirmed the switching behaviour observed was authentic. Leakage was not the origin of the relatively low switchable polarization values obtained during the PUND measurements at x = 0.4. Based upon the evidence presented throughout this chapter it is apparent that the BF-KBT system does not satisfy the required criteria of a high-temperature piezoelectric ceramic as per the brief of the project.

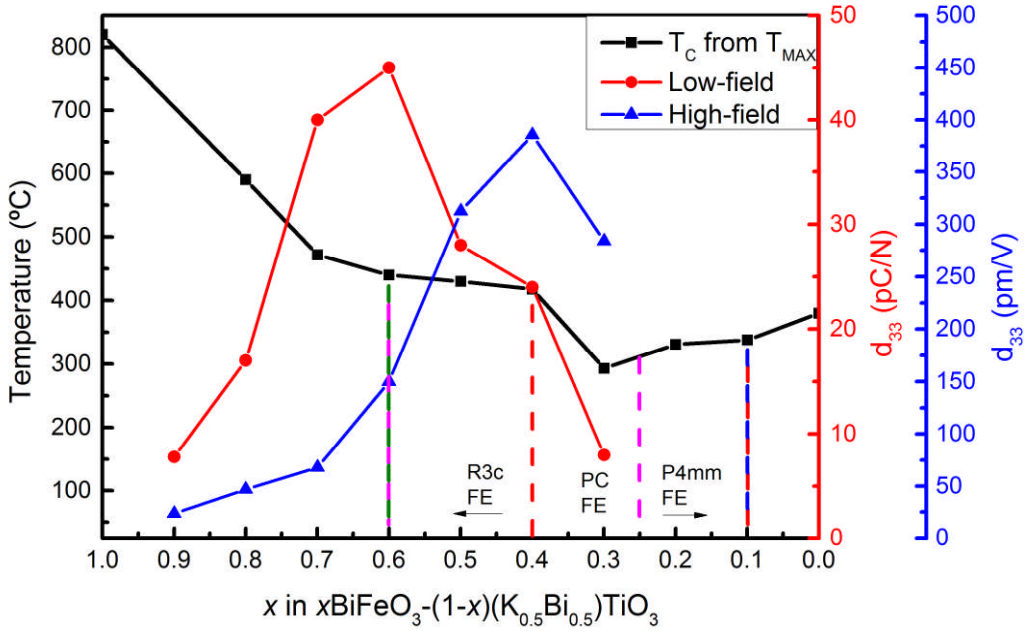

Figure 4-15. Phase diagram of the $BiFeO_3$-$(K_{0.5}Bi_{0.5})TiO_3$ system highlighting the low-field and high-field piezoelectric charge coefficients across the compositional space as well as the Curie temperature. The dashed lines represent the phase boundaries identified by Kim (blue), Matsuo (green) Morozov (pink) and Bennett (red), those at x = 0.1 (red and blue) represent the transition from pseudocubic to tetragonal.

5. Development of $BiFeO_3$-$(K_{0.5}Bi_{0.5})TiO_3$-$PbTiO_3$ piezoelectric ceramic system

This chapter focuses on the development of the (1-*x*-*y*)$BiFeO_3$-*x*$(K_{0.5}Bi_{0.5})TiO_3$-*y*$PbTiO_3$ (BF-KBT-PT) system. The major thrust of this thesis was to fully characterize the region between the well understood $BiFeO_3$-$PbTiO_3$ system and the recently identified $BiFeO_3$-$(K_{0.5}Bi_{0.5})TiO_3$ system. This initial development was centered on crystallographic phase, microstructural and basic electrical characterisation techniques similar to those discussed in the previous sections. The objectives of this segment are closely aligned with those from the previous chapter, however, the methodology used to identify the active region differed slightly as the development of materials belonging to a ternary system is more complex than for a binary system.

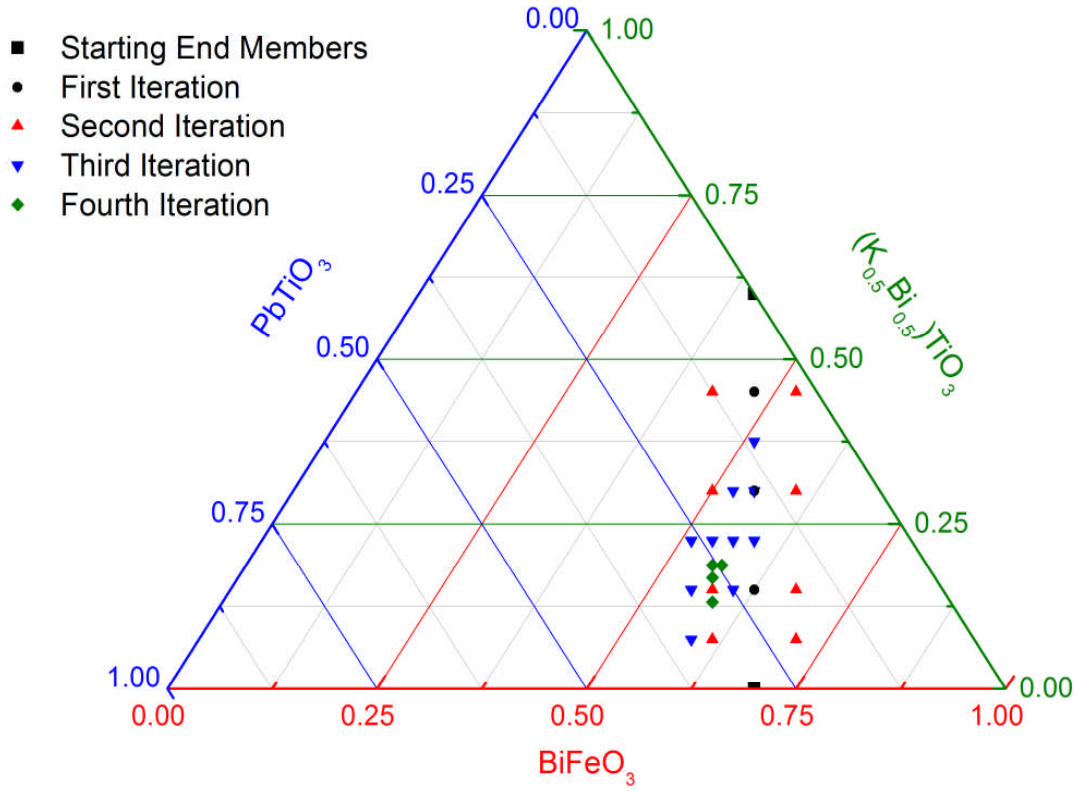

Figure 5-1. The ternary phase diagram of the $BiFeO_3$-$(K_{0.5}Bi_{0.5})TiO_3$-$PbTiO_3$ system with the strarting MPB end members highlighted and the iterations taken during the development of these ceramics. The first iteration of materials were ball milled, however, all subsequent compositions were attrition milled

Figure 5-1 shows the compositions that will be discussed at length in the following sections, they are shown here as it provides a basis for the introduction. Here, we used the active regions of binary end members as the root for determining the location of the two-phase region (MPB) in this system. The two end members display contrasting properties, the BFPT system is a true ferroelectric although the high coercive field inhibits its use in applications; BF-KBT exhibited relaxor-like properties at the MPB composition, this was also the composition that generated the largest electric-field induced strains.

A route was drawn between the two MPB regions and three points were marked equidistant with respect to the $(K_{0.5}Bi_{0.5})TiO_3$ content of the end members, between 0.6 and 0. The initial three compositions produced were ball-milled in line with the lead-free system, all other compositions belonging to this system were attrition milled. The active region was determined using the procedure demonstrated in the flow diagram, Figure 5-2. The region with the highest piezoelectric activity was identified on the basis of the crystal structure, piezoelectric coefficients such as k_p and d_{33}, and subsequent measurements that located the T_C. Once this procedure was complete, another iteration would follow in an attempt to identify the active region but also the area of the phase diagram where the favourable properties diminish in order to fully characterize the extents of the ternary phase diagram and understand the mechanisms governing the structural and electrical properties.

Figure 5-2. Flow-diagram of the typical procedure used when characterising the $BiFeO_3$-$(K_{0.5}Bi_{0.5})TiO_3$-$PbTiO_3$ system

5.1 Sample Appearance and Density

Bulk polycrystalline samples were similar in physical appearance to those belonging to the $BiFeO_3$-rich end of the lead-free system. When preparing samples for imaging using the polishing route provided by Buehler in Chapter 3.6, it was apparent that these ceramics were much harder than their lead-free counterparts. Despite the large tetragonality in the $PbTiO_3$-rich compositions, the fabrication of dense sintered ceramics was achieved which is not always possible such as in BFPT or $PbTiO_3$ where this is particularly problematic and appropriate processing is required such as a reduction in grain size [71], and appropriate cooling rates are necessary through the paraelectric phase transition. A large portion of the $BiScO_3$-$PbTiO_3$ phase diagram where the $PbTiO_3$ content reduces to <60 mol% cannot be fabricated due to the low solubility limit of Sc^{3+}, demonstrating the stabilising effect of $PbTiO_3$, this is vital when incorporating two compounds that can have substantial impurity phases.

The increase in hardness was coupled with an increase in the density of these ceramics that ranged from 7190 to 7761 kg/m^3 across the compositional space. This increase in density was due to two new variables in the processing of these ceramics, one being the partial substitution of $PbTiO_3$ for $(K_{0.5}Bi_{0.5})TiO_3$ as the density of the former is much larger. Also, the use of an attrition mill during processing of the BF-KBT-PT system led to a significant density increase as the average particle size was reduced and the energy required to cause necking due to an increase in surface area during sintering reduced.

5.2 Microstructure Analysis

The microstructures of samples were imaged at different stages of the processing route using secondary electrons (SE). Figure 5-3(a-d) displays the starting reagents, milled powders pre- and post-calcination and the fracture surface of a pellet of the same composition $(1-x-y)BiFeO_3$-$x(K_{0.5}Bi_{0.5})TiO_3$-$yPbTiO_3$ where x = 0.15 and y = 0.3. All of the images were recorded using an accelerating voltage of 5 kV, the scale bars are shown in each image.

The powders prior to calcination, Figure 5-3(b), can be seen to be a mix of the starting reagents with what appears to be little consistency of the particle size across the image, the large platelets are the bismuth oxide. Upon calcination the particle size is homogenous and the large bismuth oxide particles are indistinguishable, the irregularly shaped grains belong to the perovskite structure as evidenced by XRD which will be discussed in Chapter 5.3.1. The fracture surface is dense with no apparent porosity, no bright regions could be observed which evidence that secondary phases are certainly not widespread or discernible at all, solubility of all elements into the perovskite structure occurred and solid-solutions were produced.

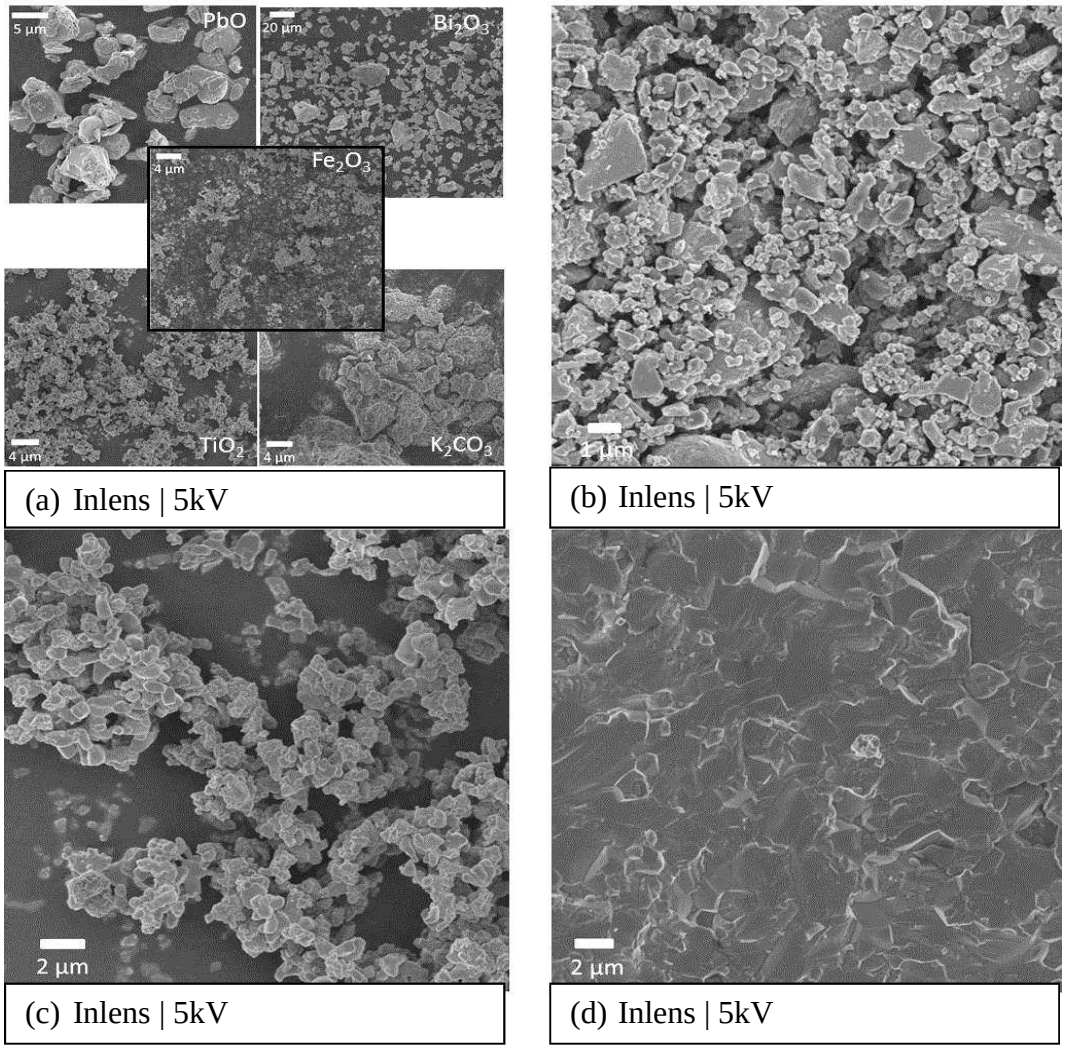

(a) Inlens | 5kV

(b) Inlens | 5kV

(c) Inlens | 5kV

(d) Inlens | 5kV

Figure 5-3. Scanning electron micrographs of (a) the starting reagents, (b) attrition milled powders pre-calcination, (c) calcined powders and (d) a fracture surface from a ceramic pellet of the composition where *x* = 0.15 and *y* = 0.3.

5.2.1 EDX Analysis

Energy dispersive x-ray analysis was performed to confirm compositional homogeneity within the sample. This allows a greater degree of certitude when discussing the structural and electrical ordering measured throughout this study as compositional inhomogeneity can be disregarded as an explanation of some phenomena. EDX is not used in this study to distinguish the true composition due to relative inaccuracy of the technique and the small compositional changes between each of the compositions, however, it is still a useful indicator. Samples were prepared by polishing as stated in Chapter 3-6.

Figure 5-4. EDX image of a polished surface highlighting (a) the mapped area (b-g) and individual elemental maps

The EDX analysis shown in Figure 5-4 belongs to the composition where $x = 0.15$ and $y = 0.3$. Individual elements can be mapped from the spectrum,

however, some overlapping may occur which can lead to obscuration of elements thus limiting the effectiveness of quantitative studies. Here, we provide evidence of sample homogeneity with no elemental segregation due to the homogenous distribution of the elements indicated by the coloured spots in each of the maps, the area mapped also contained a defect that on appearance was not consistent with the bulk of the material, this was found to match the compositional makeup of the surrounding mapped area.

5.3 Phase Analysis

5.3.1 Sample Form

The following discussion is intended to emphasise the consequence of the sample form, preparation and measurement technique used when acquiring diffraction patterns. Hence in this section, we quickly review sample preparation methodologies, which will be used herein for phase analysis. The data shown below is again for (1-*x*-*y*)$BiFeO_3$-*x*($K_{0.5}Bi_{0.5}$)TiO_3-*y*$PbTiO_3$ where $x = 0.15$ and $y = 0.3$ to ensure consistency with the microstructure data shown previously. A scanning time of 30 minutes was used for all of the diffraction patterns shown below except for Figure 5-5(f) which was scanned for 3 minutes. Mechanical lapping removed the sintered 'skin' from the as-sintered pellets shown in Figure 5-5(b-c).

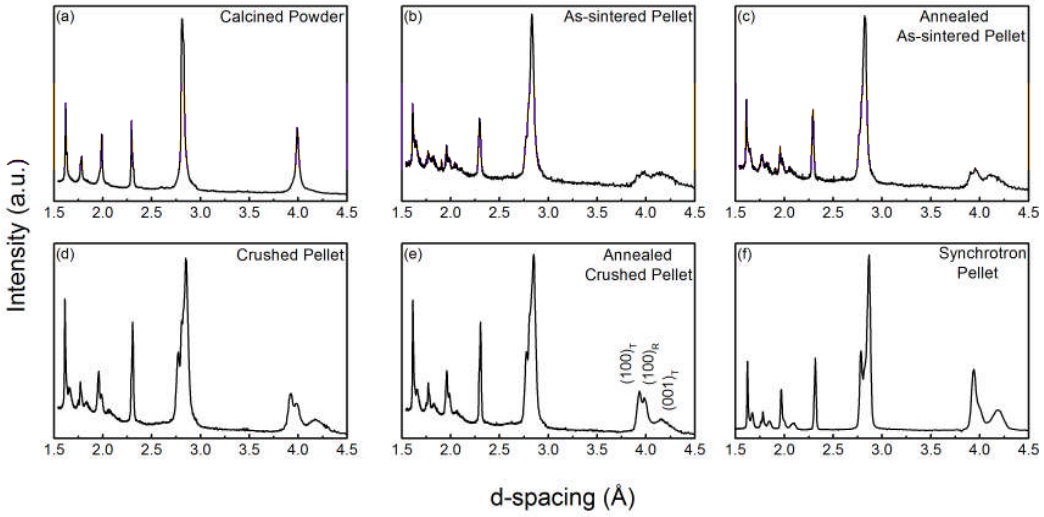

Figure 5-5.(a-f) Diffraction data collected using different sample forms and detection methods

Although not recommended as a method of phase identification it is useful to compare the plots of calcined powders to those of sintered powders, it is also a reasonable way of ensuring the milling and calcination process was completed successfully, the perovskite phase had formed and samples were fully sintered. The reflections in Figure 5-5(a) all correspond to the perovskite structure and no secondary phases or pyrochlore phase could be identified. Broad peaks were observed, notably in the {100} family of planes, although some splitting could be observed, specifically in the {111} and {200} reflections.

Ceramics in both as-sintered and annealed stress states were found to demonstrate peak splitting although refinement of these patterns using X'Pert Panalytical was challenging. The internal stresses in this particular specimen are also significant on account of its large c/a ratio and can lead to significant peak broadening. During XRD of these materials, the effect of microstrain on the surface morphology can lead to misleading results as reported by Seth in $BaTiO_3$ [206]. Post-sintering processing techniques such as mechanical grinding and polishing are known to affect the surface morphology. A surface layer may form that is entirely different to that of the bulk, in order to relieve stress at the surface a phase transformation may occur. With the composition analysed in Figure 5-5 as an example, using a mass absorption calculator built-in to the HighScore Plus software, lab X-rays only penetrate 15.5 μm (99% absorption), this is also dependent upon the angle of 2θ, therefore it is a possibility that a structure could be misrepresented by a diffraction pattern of a surface.

Pellets can be crushed to reduce the influence of a surface layer upon the XRD patterns, these powders may also be annealed to further relieve stress. Powders can also be used in conjunction with a spinning sample stage thus improving the statistics of the measurement. Clear peak splitting is observed in Figure 5-5(d-e) and coexistence between rhombohedral and tetragonal phases was identified. A transmissive technique was then applied using synchrotron x-rays in an attempt to remove the effect of surface modification as the energy of the X-rays allows for a sample to be penetrated and its bulk structure patterned, however, the sample is still in a clamped state and the sample may still retain

some inherent microstrain. Distinguishable peak splitting was observed although the intensity of some reflections differs slightly from lab X-rays. The $(001)_T$ reflection intensity is much greater in the bulk structure than for crushed annealed powders, Stevenson suggested this was due to the large lattice distortion and mismatch making the $(001)_T$ configuration extremely broad [135]. The detector used in Figure 5-5 was a Perkin Elmer flat panel 1621 EN, relatively short scanning periods were used, this was not a high-resolution detector and the pixel density would need to be increased for more distinct reflections. Based upon the results presented in Figure 5-5 it can be seen that sintered pellets which have subsequently been crushed and annealed, provide data in a reasonable time-scale that best matches the bulk structure confirmed using synchrotron x-rays, ergo, allowing for structure-property correlations.

5.3.2 Compositional Space

This section shall look in detail at the crystallography at differing points of the ternary phase diagram. 25 compositions were produced during this study, in the interests of brevity a number of selected outliers and exemplar compositions will be shown and discussed. The context of this discussion is extremely important with giant tetragonality at the MPB in BFPT and a pseudocubic structure with no long range crystallographic order noted in BF-KBT. Significantly in BFPT a phase coexistence of R3c and P4mm perovskite phases exists between $0.4 < x < 0.7$, which shall be defined as a broad mixed symmetry region (MSR).

The peak broadening observed in this system hinders structure refinement using the Rietveld method as discussed in the previous chapter, instead least squares peak fitting was performed using a combination of X'Pert Panalytical proprietary software or WinPlotR depending upon the measurement apparatus and techniques used. Profile fitting was undertaken until the most accurate fit was obtained. The weighted profile R-factor (R_{wp}) value was utilised to gauge the quality of the fit.

XRD analysis revealed that the perovskite structure was formed with no marked impurity phases, and unlike BSPT solid-solutions were formed across the entire compositional space. Figure 5-6 features the ternary diagram and the compositions produced corresponding to Figure 5-1, a broad mixed symmetry region featuring a coexistence of rhombohedral and tetragonal phases was observed in the circled territory. The compositions in the center of the MSR will be addressed in more detail later in this section, this stanza shall focus on the traces included in Figure 5-6, which were chosen as they are symbolic of the wider behaviour observed in this system. Moving from the lead-free MPB with Figure 5-6(d) belonging to the composition where $x = 0.375$ and $y = 0.1125$ it can be seen that sharp peaks were recorded with no distinguishable splitting of the reflections. Profile fitting produced the smallest R_{wp} values when fitted to a cubic symmetry. The partial substitution of $PbTiO_3$ did not result in the promotion of long-range non-centrosymmetric crystallographic order at these concentrations.

The pattern in Figure 5-6(c) where $x = 0.3$ and $y = 0.15$ displays much broader peaks, nevertheless no obvious peak splitting can be observed. This composition did not fit to a cubic model although an excellent fit was achieved with both tetragonal and a rhombohedral phase, as an Rwp value of 0.986% was recorded. Long-range non-centrosymmetric crystallographic order can be inferred in this and some of the previously discussed pseudocubic compositions, as low-signal piezoelectric charge coefficient d_{33} values were substantial, >100 pC/N, these will be presented in Chapter 5.4.2.

Figure 5-6(f) where $x = 0.075$ and $y = 0.2125$, surprisingly exhibits pseudocubic reflections that were relatively broad, there is no splitting of the {111} family which was not anticipated due to the high concentration of $BiFeO_3$ and the relatively low concentration of $(K_{0.5}Bi_{0.5})TiO_3$, this composition being the closest to the BFPT morphotropic phase boundary. The background intensity of this pattern is also the greatest relative to the strong {110} peak, this composition has the largest Fe^{3+} concentration which suggests fluorescence was influential.

Figure 5-6 (a)(b) and (e) are located inside the mixed symmetry region. Analysis of the diffraction patterns found that the compositions demonstrate peak splitting across all major reflections, indicative of a phase co-existence. This is clear from the {200} reflection. Tetragonal materials exhibit splitting in the {200} family while rhombohedral materials do not and three peaks signify a mixture of phases. Characteristic splitting of perovskite peaks belonging to the {111} family or the {100}, {110} and {200} family can identify rhombohedral or tetragonal structures respectively.

Figure 5-6(b) and (e) signifies the point where marked peak splitting is first observed with increasing $PbTiO_3$. Phase coexistence occurs in accordance with the above definition, a critical $PbTiO_3$ concentration was exceeded leading to the promotion of long-range non-centrosymmetric order that is detectable using laboratory X-rays. Extremely broad perovskite peaks are observed in inset Figure 5-6(a) belonging to the composition where x = 0.075 and y = 0.3375 which is symptomatic of the high levels of internal microstrain, still prevalent in crushed and annealed pellets. A large tetragonal distortion was recorded with a c/a-1 value of 12.2%, which is greater than for pure $PbTiO_3$. Enhanced tetragonality, whereby an increased c/a ratio is observed with partial substitution of alternative perovskite compounds for $PbTiO_3$ is unusual as most Pb or Bi based compounds reduce the tetragonality which subsequently aids in MPB formation [216] . The effect has however most notably been observed with the substitution of $BiFeO_3$, although $BiScO_3$, $Bi(Zn_{0.5}Ti_{0.5})O_3$ and $Bi(Zn_{0.75}W_{0.25})$ have resulted in sustained or enhanced tetragonality [14, 134, 216]. This behaviour is a manifestation of the strong coupling between Pb/Bi and ferroelectrically active displacive B-site cations such as Zn, Sc Ti and Fe [142]. Therefore, the addition of KBT in BFPT (or vice-versa) resulted in the migration of the MPB which occurs at ca. 70 mol% $BiFeO_3$ to lower lead-titanate concentrations or ca. 60 mol% $(K_{0.5}Bi_{0.5})TiO_3$. Such a shift is observed in other mixed phase systems, or as a result of doping.

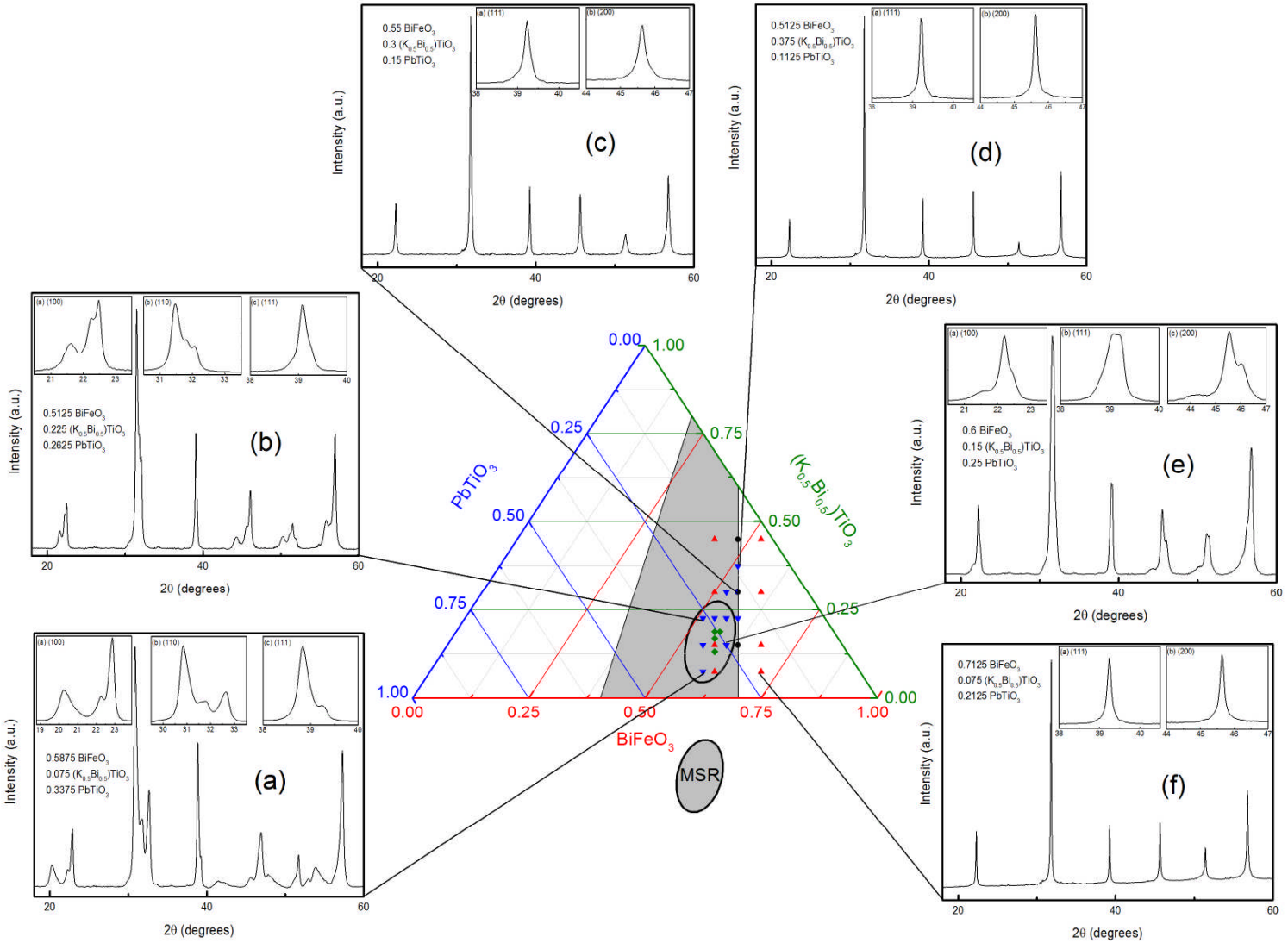

Figure 5-6. Ternary diagram highlighting the mixed symmetry region with selected compositions presented

Within the MSR a select number of compositions will be focused on pertaining to the compositions closest to the MPB shown in Figure 5-6, a simple labeling system is used for brevity and clarity and the key can be found in Table 10-1 in the appendix.

A broad $(002)_T$ tetragonal peak can be observed at 43.75º for composition A. The reduction in the intensity and increase in 2θ of the (002) peak is commensurate with a decrease in $PbTiO_3$ content, and can be seen to manifest as a broad shoulder in composition D2 at 44.92º and appears to be similar to those observed in the pseudocubic region in the BF-KBT system. The lack of substantial splitting across the {111} family confirms that the lattice distortion of the rhombohedral phase is very small, subsequently the tetragonal distortion would generally be expected to govern the piezoelectric properties as in lanthanum doped BFPT and this thesis follows this position. However, work by Kungl and Hoffman [217] illuminated the importance of the rhombohedral phase in allowing movement of non-180º domain walls, this is discussed in more detail in Chapter 6.7.

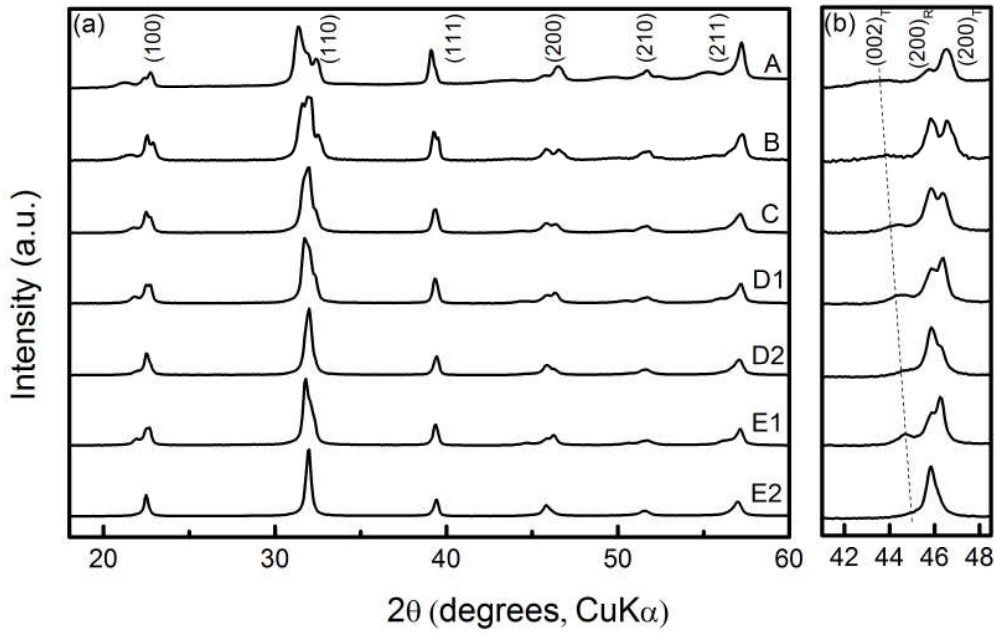

Figure 5-7. X-ray diffraction patterns of BF-KBT-PT ceramics in the 2θ range of 18°–60° and (b) from 41° to 48.5°

Figure 5-8. Lattice parameters and c/a ratio as a function of $PbTiO_3$ content

The lattice parameters and c/a ratio determined from the XRD patterns are shown in Figure 5-8, a strong correlation was found to exist between the tetragonality and the $PbTiO_3$ concentration. The a-lattice parameter does not change emphatically with increased $PbTiO_3$ content in contrast to the c-lattice parameter as anticipated.

One composition where $x = 0.15$ and $y = 0.275$ within the mixed symmetry region was found to not conform to type. Shown in Figure 5-9, in the unpoled state the sample appears to have a predominantly rhombohedral structure, as indicated by splitting in the {111} reflection with only a small tetragonal contribution at zero field. Manifested by the significant residual of the fit to the {200} peaks in the unpoled state, shown in Figure 5-9(b), the very broad peaks flanking the major R(200) reflection may indicate this. Note that no small peak to the left of the {111} family, normally associated with oxygen octahedral tilting, was observed. Upon poling, the sample appears to undergo a structural phase change, as shown in Figure 5-9(c) and (d). In the unpoled state the tetragonal contribution is almost zero, whereas in the poled state it is 17%, based on the relative area of R(200), T(002) and T(200) peaks, as shown in Figure 5-9(d). Both poled and unpoled materials were measured using the same diffractometer as used

throughout this study; in order to probe poled materials, electrodes were prepared with air-dry silver paint. After poling, the electrodes were carefully removed using acetone. After the measurement the sample was thermally depoled (600 °C) and re-measured, the pattern correlated with the original measurement in the unpoled state. This phase change may be explained due to the proximity to a compositional phase boundary.

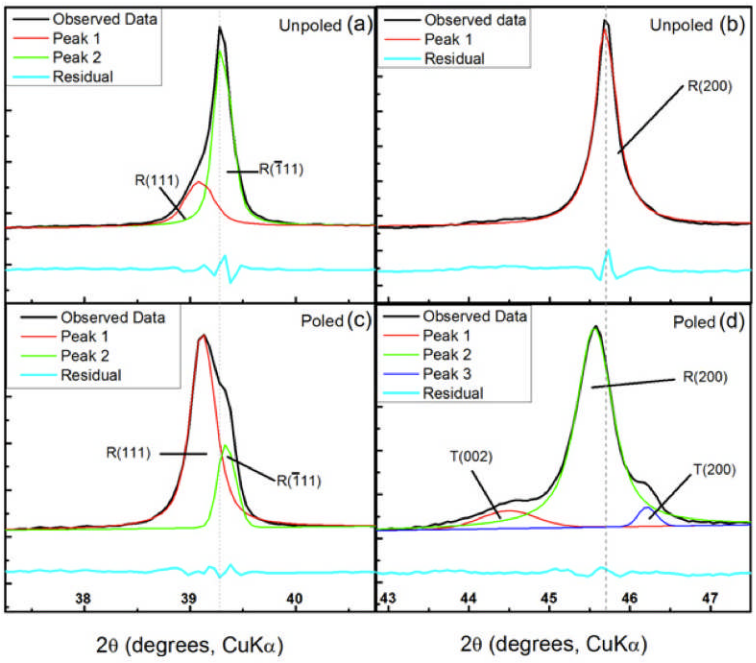

Figure 5-9. Diffraction patterns of poled and unpoled samples for the {111} peak (a) and (c) and the {200} peak (b) and (d) using lab x-rays

5.4 Basic Electrical Characterisation

5.4.1 Electric-field Induced Polarization and Strain

Electrical characterisation was undertaken on all compositions with a select number presented here. Ferroelectric and piezoelectric behaviour was noted across a wide compositional space. These measurements were performed at room temperature and at elevated temperatures to determine the temperature stability of the ferroelectric and piezoelectric response. Samples were measured at 7 kV/mm for ease of comparison, with strain-field loops at 0.1 Hz and polarization-field loops at 3.3 Hz.

Strain-field loops are presented below in Figure 5-10 for samples with decreasing $(K_{0.5}Bi_{0.5})TiO_3$ and increasing $PbTiO_3$. At room temperature in Figure 5-10(a) the piezoelectric switching amplitude is small with little negative strain observed, with the loops taking a similar shape to that of the lead-free system near to the MPB. This behaviour is to be expected as only small amounts of $PbTiO_3$ have been partially substituted. At elevated temperatures the loops become much slimmer and the negative strain diminishes, the electric-field induced strain response was entirely electrostrictive at 150 ºC.

Figure 5-10. Electrical-field induced strains for compositions where (a) *x* = 0.45 and *y* = 0.075, (b) *x* = 0.375 and *y* = 0.1125, (c) *x* = 0.225 and *y* = 0.1875 and (d) *x* = 0.15 and *y* = 0.25

Large strains (positive peak to negative peak) are observed in Figure 5-10(b), the magnitude of which is greater than for any sample across the $BiFeO_3$-$(K_{0.5}Bi_{0.5})TiO_3$ phase diagram. The origin of the strain response is inferred to be a combination of significant electrostrictive and piezoelectric behaviours at y = 0.1125 $PbTiO_3$. At increased temperatures the negative strain reduces although the total strain increases. The final two compositions, in Figure 5-10(c) and (d) are located inside the mixed symmetry region and outside respectively. The strain-field loops indicate obvious piezoelectric behaviour, again indicated by the negative strain response. The piezoelectric strains observed also increase as a function of temperature due to a 'softening' of both intrinsic and extrinsic contributions to the piezoelectric effect as widely reported in piezoelectric ceramic materials [218]. The onset of piezoelectric switching is much reduced compared to $BiFeO_3$-$PbTiO_3$ due to the reduction in the electrical coercive field.

Electric-field induced polarization measurements confirm the promotion of long-range polar order with the addition of $PbTiO_3$ and reduction of $(K_{0.5}Bi_{0.5})TiO_3$. Slim loops with a small concave region were observed in Figure 5-11(a) although evidence for large scale ferroelectric switching is not extensive. An increase in temperature leads to slimming of the P-E loops and a small increase in polarization, at 150 ºC conductivity is assumed to contribute. Ferroelectric switching can clearly be distinguished in Figure 5-11(b), this corresponds to the piezoelectric switching identified. The ferroelectric loops remain slim and cannot be described as a classical 'square' hysteresis loops. Figures 5-11(c) and (d) demonstrate behaviour consistent with classical ferroelectric materials. The P-E loops observed here are widely representative of the mixed symmetry region, some of which will be shown in more detail in Chapter 6-4. The measurement at 150 ºC, Figure 5-11(c), has been omitted due to the high levels of conductivity, these measurements were performed at 3.3 Hz and it is conceivable that faster measurement frequencies may reduce this effect as observed widely in the literature. Although not presented measurements were performed at higher electric fields, the P-E loops remained square and saturation fields were realised. The appendix features a P-E loop from the region close to the $BiFeO_3$-$PbTiO_3$ MPB, shown in Figure 10-1, it can be seen that at 8 kV/mm P-E

loops were consistent with a ferroelectric material beneath the saturation field, however, at 13 kV/mm a concave region is observed even with the high levels of conductivity in this sample. The E_C of this composition is ~7 kV/mm which is relatively high and is proportionate with the c/a ratio of 1.122 identified in this composition.

Figure 5-11. Electrical-field induced polarization for compositions where (a) *x* = 0.45 and *y* = 0.075, (b) *x* = 0.375 and *y* = 0.1125, (c) *x* = 0.225 and *y* = 0.1875 and (d) *x* = 0.15 and *y* = 0.25

5.4.2 Poling Study

The poling results across the compositional space are presented in this section, giving a tangible insight as to the low-signal piezoelectric response at room temperature. A thorough poling study was undertaken, this was vital for two reasons. The first being that the d_{33} value is a fundamental material property that is a useful gauge as to the suitability in strain-dependent applications. The second being that a number of measurements require samples that are fully poled such as PRAP or Rayleigh analysis, as domain wall mechanics cannot be fully evaluated in samples in which domains are not saturated as unrepresentative behaviour may be elucidated [219].

Table 5-1 shows the results of a typical poling study. These measurements were carried out at the Pennsylvania State University and the optimal poling regime identified was used throughout the remainder of this study. The poling field and temperature were varied while the poling time remained constant at 10 minutes unless a dielectric breakdown event occurred. Elevated temperatures are usually preferred as there is a marked increase domain wall mobility, however, the sample must be resistive at high temperatures otherwise dielectric breakdown can occur. The maximum temperature available to the author was 150 ºC due to the safe operating limit of the dielectric oil although the maximum temperature used was 125 ºC as dielectric breakdown was common at elevated temperatures and fields, 8 kV/mm was only successfully applied to this sample at 50 ºC. This study found that in composition D1 an optimal poling temperature and field of 125 ºC and 6 kV/mm respectively. An increase of 49 pC/N from the initial observation at 50 ºC and 4 kV/mm, emphasising the importance of a thorough poling study.

Table 5-1. Typical poling study data obtained for this system, the data shown below belongs to Composition D1

BD=Breakdown	**4 kV/mm**	**5 kV/mm**	**6 kV/mm**	**7 kV/mm**	**8 kV/mm**
50 °C	179	188	194	199	203
75 °C	196	202	212	218	BD
100 °C	210	216	220	BD	-
125 °C	216	222	228	-	-

A contour plot has been used to symbolise the piezoelectric d_{33} coefficient across the compositional space, shown in Figure 5-12. The colour of the points corresponds to the order of fabrication, as shown in Figure 5-1. The yellow points situated on the peripheries correspond to values from the literature for the starting end members and $BiFeO_3$-$PbTiO_3$ across the compositional space while the values corresponding to the $BiFeO_3$-$(K_{0.5}Bi_{0.5})TiO_3$ system are a result of the authors own work. The navy blue region symbolises where the compositional space has not been mapped in line with the smoothing formulation used in the Origin

graphical software. As mentioned previously, the most piezoelectrically active composition was found to have a d_{33} of 228 pC/N at room temperature, this value is similar to that of an undoped PZT which demonstrates a d_{33} of 223 pC/N at the MPB [77]. This region is indicated in the contour plot of d_{33} across the compositional space by the red region, the d_{33} values identified near this region where relatively similar highlighting the broad region of phase coexistence and the wide window of elevated piezoelectric activity.

Figure 5-12. Contour plot showing the low-signal piezoelectric charge coefficient d_{33} as a function of composition, the colour of the markers corresponding to those represented in Figure 5-1. Values from the literature have also been included (indicated by the yellow markers) where possible in order to map a greater compositional space

As expected, with compositions near to the BFPT or BF-KBT MPB a sharp drop in piezoelectric activity is noted in agreement with the gigantic tetragonality and pseudocubic crystallographic distortions. The tetragonality close to the BFPT MPB was found to be 1.122 in the composition where $x = 0.075$ and $y = 0.3375$, this was coupled with a d_{33} of 58 pC/N, although relatively low it is a sharp increase when compared to the d_{33} values recorded in the $BiFeO_3$-$PbTiO_3$

system. In selected compositions in the region where pseudocubic peaks were observed in the diffraction patterns it can be seen that d_{33} coefficients exceeded 100 pC/N.

The crystallography of this system is no longer a barrier as the tetragonality has been reduced significantly compared to the BFPT MPB, whilst the pseudocubic patterns observed using XRD for BF-KBT are no longer observed as long-range crystallographic ordering is present that supports piezoelectricity. One further iteration flanking the $PbTiO_3$-rich and $(K_{0.5}Bi_{0.5})TiO_3$-reduced compositional space of the ternary diagram may have been beneficial as the critical point where wholly tetragonal symmetry is observed in parallel with a reduction in piezoelectric properties was not identified. Phase coexistence was observed in all of the $PbTiO_3$-rich compositions as well as reasonably high piezoelectric d_{33} coefficients.

5.6 Conclusions

The data reported in this chapter belonging to the $BiFeO_3$-$(K_{0.5}Bi_{0.5})TiO_3$-$PbTiO_3$ system demonstrates some results that have a potentially great impact. The perovskite structure was identified across the entire compositional space studied, the partial substitution of $PbTiO_3$ did not lead to impurity phases. Pseudocubic reflections with no peak splitting was observed in compositions with low $PbTiO_3$-concentrations, a critical concentration where y = 0.1125 $PbTiO_3$ was exceeded which led to the long-range non-centrosymmetric crystallographic order. The tetragonal distortion of the $BiFeO_3$-$PbTiO_3$ and $BiFeO_3$-$(K_{0.5}Bi_{0.5})TiO_3$ end members is 18% and 0% respectively, the tetragonal distortion observed in this system was found to lie within these parameters and a relatively continuous increase in the c/a ratio correlated with increased $PbTiO_3$ content. A broad mixed symmetry region was observed that consisted of rhombohedral and tetragonal symmetries, similar to the $x$$BiFeO_3$-(1-$x$)$PbTiO_3$ family where $0.4 < x < 0.7$. A number of compositions exhibited enhanced tetragonality relative to the $PbTiO_3$ end member, a c/a-1 of 12.2% was measured where x = 0.075 and y = 0.3375. Enhanced tetragonality, whereby an increased c/a ratio is observed with partial substitution of alternative perovskite compounds for

$PbTiO_3$ is unusual as most Pb or Bi based compounds reduce the tetragonality which subsequently aids in MPB formation, this may explain the formation of the broad mixed symmetry region as the tetragonality is enhanced, therefore, a fraction of the tetragonal phase may transform to the rhombohedral phase as a stress relief mechanism.

It was found that piezoelectric charge coefficient d_{33} values greatly increased in the mixed symmetry region. The most piezoelectrically active composition was found to have a d_{33} of 228 pC/N at room temperature, all of the active compositions (205-228 pC/N) had c/a ratios of >1.045. Electric-field induced polarization and strain values as a function of temperature confirmed that the partial substitution of $PbTiO_3$ increased polar order, as significant negative strains and square ferroelectric hysteresis loops respectively were detected, these were stable at temperatures up to 150 ºC although conductivity was an issue.

The room temperature tetragonal x_s, T_C and piezoelectric d_{33} were found to correlate strongly with the $PbTiO_3$ concentration across the mixed symmetry region. A small number of compositions across the MSR were selected for further investigation, shown in the following chapter.

6. Origins of the Piezoelectric Behaviour and High Temperature Characterisation

In this chapter, a number of techniques will be used to determine the temperature stability of the structural and electrical properties. The intrinsic and extrinsic contributions to the piezoelectric effect will be investigated and the long-range non-centrosymmetric crystallographic and polar order will be evaluated.

6.1 Narrowing the Compositional Space

In the interests of brevity and clarity, the compositional space previously discussed will be narrowed and a limited number of compositions, shown in Figure 6-1, will be characterised in more detail as strong ferroelectric behaviour has been exhibited across a remarkably broad region, the narrowing of the compositional space was based upon crystallographic and basic electrical characterisation. Occasionally compositions may be referred to that lie outside the region shown in Figure 6-1, in this instance the stoichiometric composition will be stated clearly in the text using "where x = and y =" descriptors. This will be necessary when discussing the onset of long range structural and electrical ordering in the $PbTiO_3$-deficient compositions that do not occupy the mixed symmetry region.

Figure 6-1. This region of the ternary phase diagram was characterised in detail due to the correlation between structural properties and $PbTiO_3$ concentration

Figure 6-2. Electric field induced strains for Compositions A-E2 as a function of temperature

The strain-field loops, shown in Figure 6-2, belonging to the mixed symmetry region compositions demonstrate large electric-field induced strain values, these are greater than the $PbTiO_3$-rich compositions discussed in the previous chapter in Figure 5-10. A significant step change occurs in compositions A and B as the electric-field induced strains are significantly reduced compared to their mixed symmetry region counterparts, corresponding to a lower d_{33} in these two compositions of 140 and 152 pC/N respectively compared to the other compositions highlighted in Figure 6-1, this also corresponds to a significant step

change in the tetragonality with the c/a ratio in excess of 1.06 in A and B, however, it is below 1.045 in the remaining compositions. Room temperature strains were in the region of 0.225-0.417 % at 7 kV/mm. Measurements were also performed at -50, -25 and 0 ºC in a number of compositions, although not presented, to see if the origin of these high strains was due to a structural phase transition just below room temperature that may be detected in the strain-field and polarization-field response, for example Composition C which is shown in Figure 10-2 of the Appendix, the total electric-field induced strain at -50 ºC was found to be 0.369 % compared to 0.417 % at room temperature, this reduction is not significant and no obvious fluctuations were observed indicative of a phase transition.

As anticipated there is a reduction in the electrical coercive field amplitude as a function of temperature, shown in Figure 6-3 as taken from the averaging of positive and negative deviations in the strain response and the E_C is defined as the point where the strain intercepts the *x*-axis. These samples were studied at 7 kV/mm to allow reasonable comparison, however, composition A was measured at 8 kV/mm, this is due to composition A displaying limited piezoelectric and ferroelectric (to be discussed) hysteresis at 7 kV/mm. The coercive field for compositions A and B is larger than for the other compositions, linked to their high c/a ratio, this could also partly account for the reduced strains observed as larger electric-fields are required to cause an equivalent electric-field induced strain response. Throughout this chapter the term c/a ratio will be used interchangeably with the tetragonal spontaneous strain, x_s, as the tetragonal distortion appears to dominate a number of structural and electrical properties. The coercive field and c/a ratio reduces with temperature largely due to increased ferroelectric domain wall motion. Unfortunately the saturation electric-field was not achieved in composition B at low temperatures and has led to a perturbation in the coercive field at elevated temperatures, here the coercive field can be seen to behave erroneously as to the behaviour anticipated.

It would be reasonable to assume that the high strains observed in this system are related to the long-range non-centrosymmetric crystallographic

ordering that facilitates piezoelectricity as opposed to the large electrostrictive effect seen in the lead-free system as both the intrinsic and extrinsic contributions are related to the spontaneous strain. From classical phenomenology, the intrinsic piezoelectric coefficient is proportional to the spontaneous polarization and hence to the square root of the spontaneous strain, whilst the extrinsic contribution due to the interchange in a- and c-axes for the tetragonal phase during domain wall translation should be directly proportional to spontaneous strain [220]. However, low ferroelastic domain wall mobility can also limit the extrinsic contribution as seen in $BiFeO_3$-$PbTiO_3$. Hence a high c/a ratio can make non-180° domain wall motion more difficult, increasing the electrical coercive field and ultimately the fields required to achieve high strains, which would therefore make the low field d_{33} lower than in, for example, doped PZT which has a reduced c/a ratio.

Figure 6-3. Temperature dependence of the coercive field for Compositions A-E2, taken from high-field x-E measurements

A great detail of information can be gathered from hysteresis loops for a given material, in simple terms the above materials display ferroelectric switching which is reversible manifested in the extensive concave regions. In correlation with the strain-field measurements the P_R and P_{SAT} are reduced in compositions A and B, which relates to the high tetragonal distortion and the high coercive field.

Again a distinct step change can be observed between the behaviour of these two compositions in comparison to the other mixed symmetry region compositions.

Figure 6-4. Electric field induced polarization values for compositions A-E2 as a function of temperature

The P_R and P_{SAT} can generally be seen to increase in the compositions with reduced c/a ratios, shown in Figure 6-5, the polarization was typically between 30-40 $\mu C/cm^2$ across the mixed symmetry region. All samples demonstrated an increase in P_R and P_{SAT} with temperature, providing evidence of the existence of ferroelectric ordering up to at least 150 ºC.

Figure 6-5. P_{SAT} and P_R as a function of the tetragonal distortion across the MSR

The sharpness of the loop at the maximum applied field can relate to a number of variables, one being the magnitude of the applied electric-field being inadequate, another is due to poor electrical resistivity. Haertling suggested sharp tips were found in samples in which resistivity was high, $>10^9$ Ω.cm [7], at room temperature. In a number of compositions at elevated temperatures the hysteresis loops can be seen to have P_R values that exceed the P_{SAT} values, and a distinct rounding at the top of the loop with 'blunt' tips recorded. This effect becomes amplified with increased temperature, notably in compositions A and B. This low resistivity also meant that measurements at high electric-fields and temperatures would often result in dielectric breakdown. This low resistivity is not uncommon for $BiFeO_3$-based piezoelectric ceramics.

Composition A and B also exhibited some minor asymmetry in their hysteresis loops believed to be related to the generation of an internal bias field, conceivably due to the addition of an extra cation (K^+ on the A-site for Pb^{2+} or Bi^{3+}) which leads to oxygen vacancy defect dipoles [91] which align parallel to the polarization vector when the field is applied resulting in an internal electrical bias, thus increasing the coercive field.

6.2 High Temperature X-ray Diffraction

High temperature XRD was used as a method to determine the T_C of a number of materials belonging to the mixed symmetry region, the results are presented in this section for selected compositions as well as an evaluation of this technique for determining T_C. The {111} and {200} reflections were scanned at room temperature, at every century up to 300ºC and then in 10 ºC steps thereafter up to a maximum of 600 ºC. The {111} and {200} reflections were chosen as they exhibit 'characteristic' peak splitting that allow the transition to a paraelectric cubic phase to be observed and any other transitions that may occur before this point. Peak fitting was then used to calculate the tetragonal distortion of the mixed symmetry samples as a function of temperature upon heating.

Composition A, presented in Figure 6-6, exhibits a large c/a ratio of 1.068, one of the largest observed across the MSR in this system. The magnitude of both the *c* and *a*-lattice parameter reduces with an increase in temperature as expected. The reduction in the relative size of the lattice parameters occurs rapidly with increased temperature compared to work by Sai Sunder who presented the tetragonal distortion of $PbTiO_3$ and a number of $BiFeO_3$-$PbTiO_3$ compositions as a function of temperature, at 6040 BFPT a reduction of 1% in the lattice parameters is observed between room temperature and 230 ºC contrasted to Composition A which demonstrates a decrease of ~30% [70]. A sharp transition was also observed to the cubic phase in 6040 BFPT, although Burnett notes how a small 'beak' was identified prior to the transformation to the cubic phase which while unusual is consistent across a number of compositions [221]. It can be seen that this 'beak' is also present in these materials. The transition to a cubic phase was identified as being the point where the fit of a singular peak provided a smaller R_{wp} than for alternative peak fits, in Composition A this was between 550-560 ºC, the addition of 15 mol% of $(K_{0.5}Bi_{0.5})TiO_3$ had led to a reduction in the T_C compared to the BFPT MPB composition, however, the paraelectric phase transition is still much improved compared to PZT. A plot of the same measurement is shown for Composition E1 in Figure 6-7, with the reduction in the paraelectric phase transition commensurate with reduced $PbTiO_3$ content. Peak fitting near to the transition temperature was much more problematic in the

compositions with a reduced c/a ratio. Due to the time taken to interpret the results and the errors associated with the peak fitting an alternative method of determining the paraelectric phase transition was required i.e. ε_r-Temperature. Anton *et al* also suggested that this technique was the least accurate of a number of common structural and electrical techniques in determining the transition temperature [186].

Figure 6-6. Temperature dependence of the {200} lattice parameters for Composition A

Figure 6-7. Temperature dependence of the {200} lattice parameters for Composition E1

6.3 Permittivity-Temperature

The temperature dependence of the permittivity was evaluated across compositions A-E2 of the mixed symmetry region principally to identify the Curie point. An additional plot has been included in the Appendix in order to widen the discussion. This section should be prefixed by stating that in the mixed symmetry region a number of compositions display relaxor-like properties. It is proposed that the maximum in permittivity may not relate to a structural phenomenon and hence the divergence from T_C as determined via XRD, however, for consistency and the purposes of this thesis the T_{MAX} will be referred to as the T_C as the extent of the divergence will change in each composition and is also difficult to approximate. This is due to a number of counteracting phenomena, when the material is in excess of T_C the paraelectric phase obeys Curie-Weiss behaviour, as the ceramic is cooled dynamic PNRs arise which can be easily aligned with even minor electric-fields leading to local P_s, this temperature is often called the Burns temperature and at this point the permittivity no longer obeys Curie-Weiss law. As it is cooled further the energy well for reorientation of the PNRs deepens and the contribution to the relative permittivity is lessened, however, the P_S increases as the material cools therefore increasing ε_r.

The permittivity as a function of temperature over a relatively narrow range of frequencies (1 kHz-100 kHz) is plotted in Figure 6-8. A number of interesting conclusions can be deduced from the plots. At 1 kHz the T_C in Composition A was located at 542 ºC, the highest reported in the narrowed compositional range, this correlates with the largest c/a ratio of the seven compositions of 1.068. To emphasise this relationship, Figure 10-3 shows the permittivity-temperature plot for where x = 0.075 and y = 0.3375, the T_C was located at ~590 ºC coupled with a c/a ratio of 1.122 as well as a reduced d_{33} of 58 pC/N compared to the mixed symmetry region. A reduction in $PbTiO_3$ therefore leads to a general increase in room temperature permittivity and a decrease in T_{MAX} occurs as the thermal barrier required to produce the paraelectric cubic phase is reduced from 542 ºC to 410 ºC between compositions A-E2 respectively, significantly higher than in PZT. The increase in Curie temperature with increased $PbTiO_3$ may be a result of considerable covalence between the Pb and O ions. No

intermediate transitions were found across the mixed symmetry region between room temperature and the ferroelectric-paraelectric phase transition except for where $x = 0.15$ and $y = 0.275$, the composition in which the electric-field induced phase changing behaviour was discussed in Chapter 5-3-2.

Figure 6-8. Permittivity and loss as a function of temperature for Compositions A - E2 highlighting the transition to the paraelectric phase

With decreasing $PbTiO_3$, significant peak broadening of the permittivity peaks with an increasing bias frequency occurred. This was accompanied with a shift in the T_{MAX} toward higher temperatures and the suppression of permittivity with increasing frequency, the origin of this relaxor-like behaviour is hitherto unknown, however, a possible explanation may be due to frustration of long-range

structural order as a result of cationic disorder. This may be due to B-site disorder although A-site disorder is more likely due to the difference in ionic radii between K^{+}, Pb^{2+} and Bi^{3+} of 1.64, 1.49 and 1.36 Å respectively.

Canonical ferroelectrics that are compositionally ordered macroscopically have the same forces acting upon the cationic bonds, in disordered materials a number of ions can be located on the same site, the bonding between the cations is disturbed and the long-range order is frustrated. It is proposed that this disorder gives rise to random local strain fields that result in the formation of polar nanoregions, as the polar nanoregions endure with a wide range of relatively small sizes each with its own characteristic relaxation temperature. Further investigation would be required to ascertain the origin of the behaviour in this system [42].

Figure 6-9. The relationship between the $PbTiO_3$ content and T_C & the room temperature low-field piezoelectric coefficient d_{33}

Figure 6-9 illustrates the relationship between the $PbTiO_3$ content, the Curie temperature and room temperature piezoelectric d_{33}. The correlation between the tetragonal lattice distortion and the Curie temperature has been widely discussed in the literature review with respect to La-doped BFPT piezoelectric ceramics [138], here we show that an increase in room temperature tetragonal spontaneous strain is coupled with an increased Curie temperature which is consistent with the thermodynamic models of ferroelectricity [222]. This

is of note in the BFPT system as the c/a ratio is found to be ~1.18 at the MPB where La-doping leads to significant reduction in the c/a ratio and a threshold c/a ratio was identified at 1.045, above which the coercive field is elevated and limited domain switching occurs in conjunction with an inferred reduction in the domain wall density.

6.4 High Temperature Piezoelectric Coefficients

The T_C in conventional lead-based piezoelectric ceramics is usually commensurate with the depolarization temperature, T_d. However, in certain classes of materials this is often not the case, particularly in $(Bi_{0.5}Na_{0.5})TiO_3$-based piezoelectric ceramics as the piezoelectric properties diminish long before the paraelectric phase transition. A macroscopic distortion in the crystallographic properties can also be difficult to observe in these pseudocubic materials. Piezoelectric resonance data was therefore collected and analysed at elevated temperatures to determine the T_d while also elucidating some key piezoelectric and elastic coefficients such as d_{31}, k_p and S_E^{11}. These coefficients were selected as they can easily be determined on bulk ceramic discs which require minimal sample preparation compared to complicated bar and plate geometries. The T_d was defined by fitting a linear plot to the sharp reduction in d_{31} and k_p and extrapolating this back to 0, although resonance peaks may have revealed relatively minor piezoelectric behaviour above the T_d temperature as defined previously, this definition was used across all compositions to ensure consistency.

The room temperature piezoelectric coefficient d_{31} values, shown in Figure 6-10, were found to range between -23.4 pC/N and -60.8 pC/N, all compositions demonstrated an increase in the magnitude of the d_{31} coefficient with increased temperature in accordance with Landau theory, this was shown in Equation 1-11. The polarization and permittivity demonstrate strong temperature dependence as shown in Figure 6-4 and Figure 6-8 which leads to an increase in the piezoelectric properties. The T_d was found to be broadly commensurate with the T_C across the compositional space, a T_d that was 15-39 ºC below the T_C was observed in compositions A, B and D1, here the loss of piezoelectric properties was more abrupt, while a small ‘lip’ was observed in the remaining compositions.

The lowest d_{31} value of -23.4 pC/N was observed composition A in agreement with the structural effects previously discussed, this increased to 100 pC/N at 490 ºC before a reduction in d_{31} occurred as the T_d was approached. The highest d_{31} value of -188.9 pC/N was found in composition E2 at 320 ºC.

Figure 6-10. -d_{31} as a function of temperature for Compositions A-E2

The k_p, presented in Figure 6-11, of these materials was found to range from 0.16 to 0.4 at room temperature and this was relatively stable in all materials until the onset of depolarization. This temperature stability has been also observed in La-doped BFPT where $(1-x)(Bi_{0.9}La_{0.1})FeO_3$-$x$$PbTiO_3$ where x = 0.4, although a reduced k_p of 0.2 was recorded. The planar coupling coefficient values reported

here are lower than for PZT (~0.529) [77], unlike PZT which displays a gradual dampening of the response from room temperature up to 200 ºC and then reduces significantly as it approaches the T_d, in the BF-KBT-PT system the response actually remains stable or increases slightly up to a maximum just before the T_d. This relative temperature stability is owed to the strong interdependence of the contributing coefficients, namely piezoelectric charge constant, permittivity and compliance.

Figure 6-11. Temperature dependence of the electromechanical planar coupling coefficient, k_p, for Compositions A-E2

The variation with temperature of the elastic compliance belonging to compositions A-E2 has also been measured and is shown in the Appendix, Figure 10-4. Here, it was observed that the ceramics became softer with increasing

temperature, this effect often occurs in electrically ‘soft’ materials as domain walls are subject to temperature effects. The values observed here are well within the normal bounds for a commercial PZT [223]. This softening is not observed across all systems with increased temperature, such is the case in tetragonal $BiScO_3$-$PbTiO_3$ although it is observed at the MPB composition [224]. The stiffening observed, indicated by a reduction in the magnitude of elastic compliance, is due to temperature induced depoling, as would be expected near to the T_d and T_c.

The behaviour of a select number of material properties has been presented with respect to the elastic, piezoelectric and dielectric properties of the $BiFeO_3$-$(K_{0.5}Bi_{0.5})TiO_3$-$PbTiO_3$ system. The T_C of these materials was confirmed using both permittivity and x-ray diffraction at elevated temperatures. Piezoelectric resonance peak analysis evidenced that the T_d was broadly commensurate with the T_C across the mixed symmetry region. While this section has reported on the effects of temperature upon the piezoelectric effect the origin of the phenomenon has not been discussed in great detail, the remainder of this chapter aims to elucidate the origin of the piezoelectric effect in this system.

6.5 Piezoelectric Nonlinearity

The background relating to the intrinsic and extrinsic effects in piezoelectric ceramics has already been discussed in the literature review and experimental chapters. The following aside will discuss the motivation for performing Rayleigh analysis. The effect of the $PbTiO_3$ concentration upon the tetragonal distortion and Curie temperature across the MSR has been previously discussed, this relationship is demonstrated graphically in Figure 6-12, noticeably the piezoelectric charge coefficient d_{33} did not scale with the $PbTiO_3$ concentration. The origins of this relationship were not fully understood, thus the Rayleigh technique was used to augment understanding of this system. These measurements were performed while the author was seconded to the Pennsylvania State University, unfortunately, due to time constraints not all of the samples belonging to the mixed symmetry region could be analysed, therefore this section shall focus on compositions B-E2.

Figure 6-12. The c/a ratio, Curie temperature and piezoelectric charge coefficient of the compositions examined in this section

All the compositions studied demonstrated a linear relationship between the d_{33} as a function of the amplitude of the electric-field between $0.2<E_0<1$ kV/mm, the data collected is showcased in Figure 6-13. The piezoelectric charge coefficient d_{33} of each composition increased with electric-field and temperature which is consistent with the literature [17]. The d_{33} observed remained linear up to 150 °C which signifies adherence to the Rayleigh model as it is only applicable in the linear region [150]. The maximum applied field was generally ~1/4 of the coercive field at 25 °C, this threshold field reduces with increased temperature and is ~1/3 of the coercive field at 150 °C, identified from electric-field induced strain measurements at 7 kV/mm and 0.1 Hz shown previously. Figure 6-14 illustrates the measured and calculated electric-field induced strain loops at 25 °C and 150 °C in order to verify that the Rayleigh model was applicable to this system within the MSR at both room and high temperatures. Reasonable agreement was found across all compositions between the measured and calculated loops at both 25 °C and 150 °C. Opening' of the loops is evident at high temperature which is typical, and no major asymmetric hysteresis was observed that is characteristically associated with hard materials and a deviation from the 'Rayleigh' region. Composition E2 shows the greatest divergence from the calculated strain and the amount of loss had been undervalued possibly due to

the existence of other hysteretic mechanisms, such as a linear viscoelastic response [225], however, the divergence was relatively small. Certain piezoelectric materials sucPage 141Ph as ‘hard’ PZTs deviate from the Rayleigh model as pinning centres are not randomly distributed and an internal bias field forms upon poling [138].

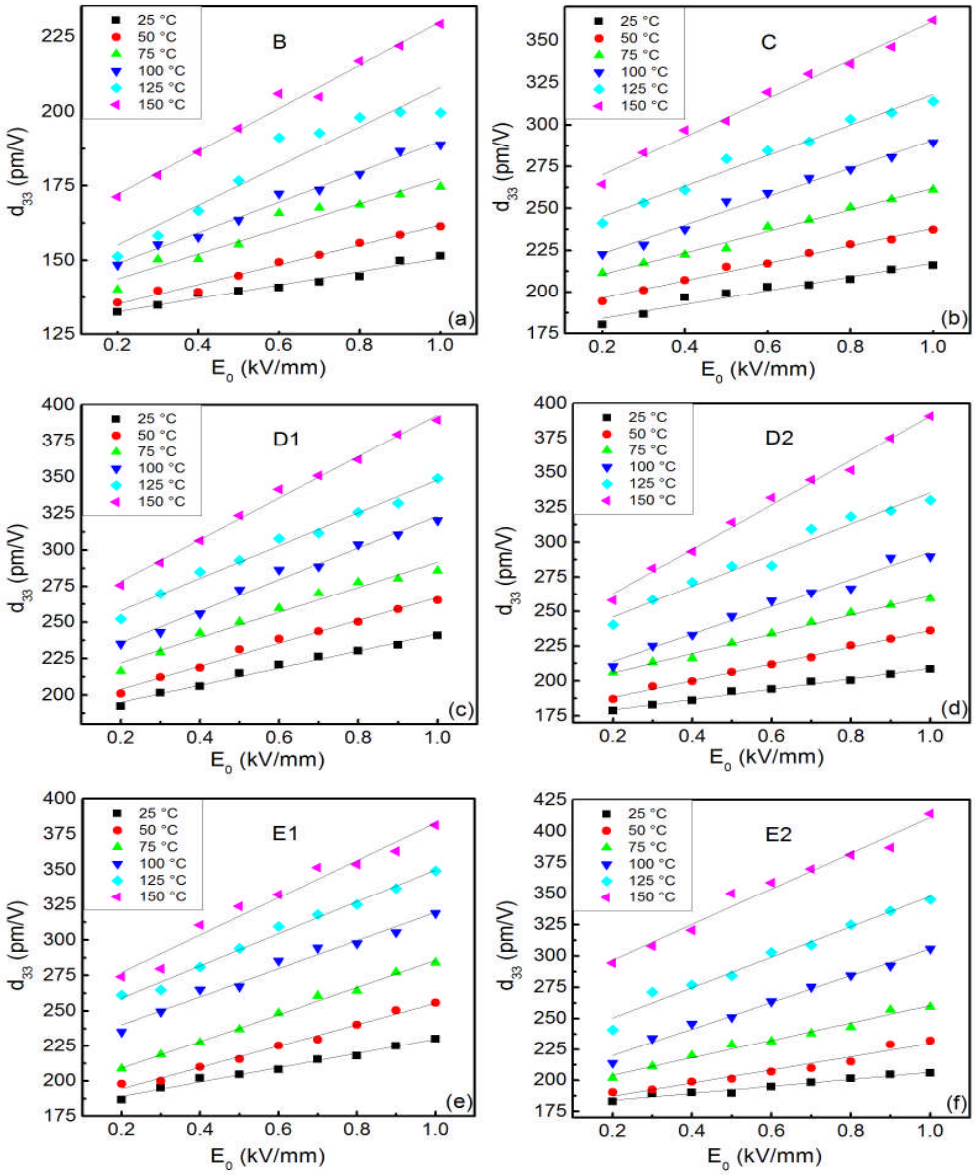

Figure 6-13. (a-f) d_{33} vs. E_0 at varying temperatures for various compositions belonging to the $BiFeO_3$-$(K_{0.5}Bi_{0.5})TiO_3$-$PbTiO_3$ system

Figure 6-14. (a-f) Measured and calculated electric-field induced strain loops using the Rayleigh model at 25 °C and 150 °C at 1 kV/mm

6.5.1 The Effect of Tetragonal Distortion on the Room-Temperature Intrinsic/Extrinsic Effects

In this section, only the room temperature intrinsic/extrinsic piezoelectric response shall be considered, this will be correlated with the tetragonal distortion across the compositional space. The d_{init} was found to be highest in composition D1, the intrinsic component to the piezoelectric effect was found to be 183 x 10^{-12} (m/V), the lowest value observed was found in composition B which displayed the largest tetragonality across the compositional space studied. The largest room temperature Rayleigh coefficient recorded in this study also belonged to composition D1, a value of 59 x10^{-18} m^2/V^2 was measured, this was commensurate with the largest piezoelectric coefficient d_{33} of 228 pC/N, with a general decrease in both d_{init} and α_d noted flanking this composition. Whilst the

Rayleigh coefficient may be at a maximum in composition D1, this trend is mirrored for the E_C, with the lowest value of 3.64 kV/mm observed in composition D1 and this increased gradually in the flanking compositions with the largest value being found for composition B, 4.21 kV/mm, commensurate with the tetragonality, demonstrating the importance of domain wall mobility. A general decrease in both d_{init} and α_d was noted either side of this composition, a discrepancy was observed in composition D2, as a α_d of 36.9 $x10^{-18}$ m^2/V^2 was observed, shown by ♦ in Figure 6-15.

Figure 6-15. Room temperature values of the (a) d_{init}, (b) Rayleigh coefficient, α_d and (c) extrinsic contributions as a function of the tetragonal distortion. The lines are drawn as a guide for the eye.

The d_{init}, α_d, and fractional irreversible extrinsic contribution values as a function of the c/a ratio are presented in Figure 6-15(a-c). A clear trend exists between the room temperature d_{init} and the c/a ratio, this correlation holds for the Rayleigh coefficient and total extrinsic contributions although the significance is reduced. An optimum c/a ratio of 1.041 exists in the mixed symmetry region belonging to composition D1, where both the intrinsic and d_{init} and α_d are optimized, with the fractional contribution to the extrinsic piezoelectric effect also

enhanced in this composition. This enhancement may be due to proximity to the location of the MPB, as observed in BSPT and PZT as the domain wall density and mobility increases due to the increased number of polarization vectors. When this system is compared to similar piezoelectric compounds such as La-doped BFPT it is apparent that both the intrinsic and extrinsic contributions have been greatly enhanced as evidenced by the d_{33}, d_{init}, and α_d coefficients. For composition D1, the Rayleigh coefficient increased by more than one order of magnitude while the intrinsic contribution more than doubled, summarized in Table 6-1. Stresses that arise during the paraelectric phase transition to the tetragonal phase in La-BFPT ceramics, especially those with a high c/a ratio have been shown to dominate the domain switching behaviour as ferroelastic domain walls are pinned. A threshold c/a ratio of 1.045 was suggested with which our findings concur [138], above this domain switching is largely inhibited, this was demonstrated by piezoelectric and electromechanical coupling coefficients in as a function of temperature previously in this chapter.

As stated previously, the intrinsic effect is dominated by distortions of the lattice and a contribution from domain wall vibrations is also possible, these are reversible and relatively non-lossy at room temperature [150]. The temperature dependence of the intrinsic piezoelectric response can be approximated using Landau theory [225-226] in single crystal, bulk polycrystalline and thin films using the following equation;

$$\boldsymbol{d = 2\varepsilon_r\varepsilon_0\sqrt{Q.x_s}}$$

Equation 6-1

where ε_r and ε_0 are the relative permittivity and free-space permittivity respectively, Q is the electrostrictive coefficient, and x_s is the tetragonal spontaneous strain, which can be related to the spontaneous polarization;

$$P_S = \sqrt{\frac{x_s}{Q}}$$

Equation 6-2

Q is assumed to be largely temperature independent [63].

The explanation for an optimum c/a ratio can therefore be related appropriately to Equations 6-1 and 6-2, an assumption is made that the electrostriction coefficient is generally independent of perovskite symmetry and the degree of ferroelectric ordering across the compositional space and is largely dependent on cation disorder [63]. Firstly, it has been observed using *ab initio* studies [227] that increased polarization values correlate strongly with higher experimentally observed *c/a*-1 values for a large number of $PbTiO_3$-derived perovskite solutions, shown in Figure 6-16. Polarization is therefore often reduced in compositions with reduced tetragonal distortions. This behaviour is closely associated with B-site displacement as opposed to A-site displacement in the unit cell, hence, solid solutions with large B-site cations such as $BiInO_3$ can generate enhanced tetragonality when partially substituted with $PbTiO_3$. Compositions with a high c/a ratio often suffer from relatively low relative permittivity values, composition B (c/a = 1.061) has a relative permittivity at room temperature ε_r = 635. Conversely, compositions with a low c/a ratio demonstrate a considerable increase in the relative permittivity, composition E2 with a c/a = 1.025 has a relative permittivity ε_r = 941. This is also shown in La-BFPT with a significant increase in compositions with a reduced *c/a* ratio [138].

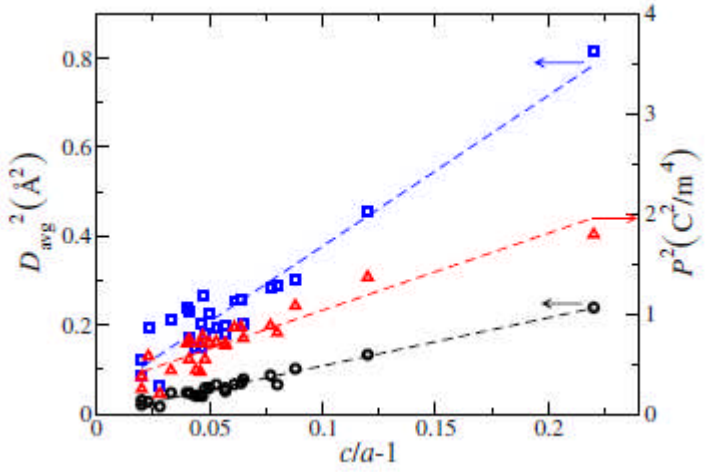

Figure 6-16. The red triangles show the experimentally observed c/a-1 correlated with the calculated P^2 values (From Qi [227])

The Rayleigh response displays a weaker correlation although behaves similarly to d_{init} with an optimum response observed in the same composition, this is not always the case such as in the $Li_x(Na_{0.5}K_{0.5})_{1-x}NbO_3$ system, the

orthorhombic (A*mm*2) and monoclinic (P*m*) phase exhibited the largest extrinsic contributions while the largest intrinsic contributions were found at the polymorphic phase boundary between the monoclinic and tetragonal (P4*mm*) phase [183], as stated previously domain switching can be limited in the tetragonal phase due to the internal mechanical stress.

Additional influencing factors to consider with the reduction of $PbTiO_3$ content may be due to an increase in localized effects associated with the partial substitution of $(K_{0.5}Bi_{0.5})TiO_3$ which leads to the frustration of the tetragonal ordering due to the reduced tetragonal distortion. Due to the volatility of both the K and Bi cation, vacancies may also lead to pinning of the domains thus limiting switching. It has also been suggested in the lead-free $BiFeO_3$-$(K_{0.5}Bi_{0.5})TiO_3$ system that polar nanoregions may exist, in the BF-KBT-PT system it is possible that with reduced $PbTiO_3$ and increased $(K_{0.5}Bi_{0.5})TiO_3$ that an increase in the lattice disorder occurs which reduces the long-range polar order, thus reducing domain wall energy and resulting in the existence of polar nanoregions.

It has therefore been shown that an optimum c/a ratio exists and a trade-off between the lattice polarization and permittivity occurs for the intrinsic effect, this trend is also recorded for the extrinsic effect although the trade-off exists here between potential for domain switching of the respective phases and the saturation of the piezoelectric effect when subjected to an applied electric-field during poling.

6.5.2 The Intrinsic/Extrinsic Response at Elevated Temperatures

Figure 6-17 (a-f) demonstrates the temperature dependence of the d_{init} and Rayleigh coefficient as extracted from Figure 6-13, both the α_d and d_{init} increase in magnitude as a function of temperature, this is due to a softening of both reversible intrinsic and irreversible extrinsic contributions, the thermodynamic origin of the enhancement can be owed to the flattening of a free energy profile [228], as the energy required to cause local atomic displacements is lowered and the process of domain switching is thermally activated [17]. d_{init} values demonstrated an approximately linear increase with temperature although the

significance of this was much reduced across the compositional space with reduced $PbTiO_3$. The lowest d_{init} values observed belonged to composition B, which also demonstrated the lowest increase as a function of temperature from 128 to 157 x 10^{-12} m/V, this material possesses the largest tetragonal distortion of all the compositions. It is noteworthy that composition E2 exhibited the largest observable d_{33} at 150°C, while also exhibiting the largest d_{init} value of 268 x10^{-12} m/V, the Rayleigh coefficient was modest at 143 x10^{-18} m^2/V^2 suggesting that the intrinsic response is critical to an enhanced d_{33} not just in this composition but across the BF-KBT-PT system, thus the large piezoelectric coefficient in composition E2 is predominantly due to the displacement of the unit cell, this was the case for all of the compositions studied.

Figure 6-17.(a-f) d_{init}, α_d and (g-l) extrinsic contributions as a function of temperature for various compositions

Results indicate that generally an increase was found for the Rayleigh coefficient as a function of temperature across all compositions with some discontinuities observed. The Rayleigh coefficient identified for composition B demonstrated the greatest temperature stability, however, this was also the composition with the lowest Rayleigh coefficients of 23 and 73 $x10^{-18}$ m^2/V^2 at 25°C and 150°C respectively. This composition has the highest $PbTiO_3$ content and tetragonality of the compositions presented as well as the lowest room temperature piezoelectric coefficients. The divergence from a linear trend of the Rayleigh coefficient as a function of temperature became more significant with reduced $PbTiO_3$, and at elevated temperatures in excess of 100°C. The significant increase in the d_{init} and Rayleigh coefficients in the $PbTiO_3$-reduced compositions is owed to the lower ferroelectric transition temperatures, T_C, of these compositions.

The fractional irreversible extrinsic contributions to the piezoelectric effect as a function of temperature were calculated using Equation 2-8, and are shown in Figure 6-17(g-l). The fractional irreversible extrinsic contributions were found to increase in magnitude as a function of temperature across all of the compositions. This behaviour was also relatively linear in compositions B-D1, however, compositions E1 and E2 displayed decreasing linearity of the extrinsic contributions, largely due to reduction in the increase in the Rayleigh coefficient, thus confirming that larger tetragonal distortion is associated with greater temperature stability. A greater range of extrinsic contributions was found at room temperature, 15.1-24.3%, compared to at 150 ºC, 31.8-39.6%.

6.5.3 Reconstructing the Temperature Dependence of the Intrinsic/Extrinsic Effects

In order to fully understand the enhancement of the intrinsic and extrinsic contributions to the piezoelectric effect as a function of temperature shown previously in Figure 6-17, a number of experiments were performed to satisfy the terms presented in Equations 6-1 and 6-2, to describe the behaviour shown in Figure 6-17(c) for composition D1. Permittivity, polarization and x-ray diffraction responses, shown in Figure 6-18, were measured as a function of temperature. The

electrostriction coefficient was measured at room temperature and was assumed to be temperature independent as observed elsewhere [63].

All of these measurements were performed on poled samples in order to closely replicate the Rayleigh measurements presented in Figure 6-17(a-l). Relative permittivity was measured at 1 kHz as a function of temperature using an Agilent 4192A, with a non-inductively wound furnace upon heating using a ramp rate of 2 ºC/min. Thermally stimulated depolarization current (TSDC) measurements were performed using a Keithley 6430 to measure current as a function of time, a constant heating rate dT/dt of 2 ºC/min was used following Anton *et al* [186]. X-ray diffraction (Cu Ka_1) was performed on highly polished samples, this was achieved using up to 1 micron diamond suspensions with proprietary polishing cloths (Buehler, UK) in order to reduce the significance of surface effects, discussed in Chapter 3.6.

The composition D1 exhibited the largest room temperature piezoelectric charge coefficient, d_{33} = 228 pC/N, and was selected for further examination. The derivation of the intrinsic piezoelectric response based upon the coupling between the relative permittivity, electrostrictive coefficient and spontaneous polarization has already been discussed with respect to the tetragonal distortion in this thesis.

The first point to consider is that while the relative permittivity can display an intrinsic and extrinsic component, the applied fields used during this measurement (0.0005 kV/mm) are not significant enough to result in the measurement of the irreversible extrinsic response, Hall suggested that 0.01 kV/mm and 0.3 kV/mm were required to exceed the threshold field, E_t, in a soft and well-aged hard PZT respectively, below which the permittivity is independent of the field amplitude, E_0 [60]. A measurement frequency of 1 kHz was selected as conductivity is reduced compared to much lower measuring frequencies. One method that can qualify the intrinsic and extrinsic components of the dielectric nonlinearity is by ‘freezing out’ domain wall contributions by measuring the permittivity at close to 0K or at extremely high frequencies where the effects of domains are negligible, however, neither of these techniques were available to the

author. The relative permittivity displayed significant temperature dependence, this behaviour was linear up to ~100 ºC, at which point a slight divergence was found. The polarization (although this was not the intrinsic polarization) determined by TSDC was found to decrease slightly in the temperature range examined as anticipated, shown in Figure 5(b). In contradiction to the electric-field induced polarization as a function of temperature data often reported in the literature. As shown in Figure 6-2, for D1 of the BF-KBT-PT system, at 1 and 7 kV/mm respectively, an increase was also found in the large-signal polarization response, this response is partly attributable to conductivity, while conductivity does not influence the TSDC result. The room temperature effective electrostrictive coefficient, Q_{33}, was derived from the slope of x-P^2 profiles. An average room temperature electrostrictive coefficient, Q_{33}, of 0.0305 m^4/C^2 was calculated for composition C. Although not presented, the product of the permittivity and polarization increases up to 150 °C highlighting the dominating effect of the permittivity thus endorsing the measured d_{init} values presented in Figure 6-17(c)

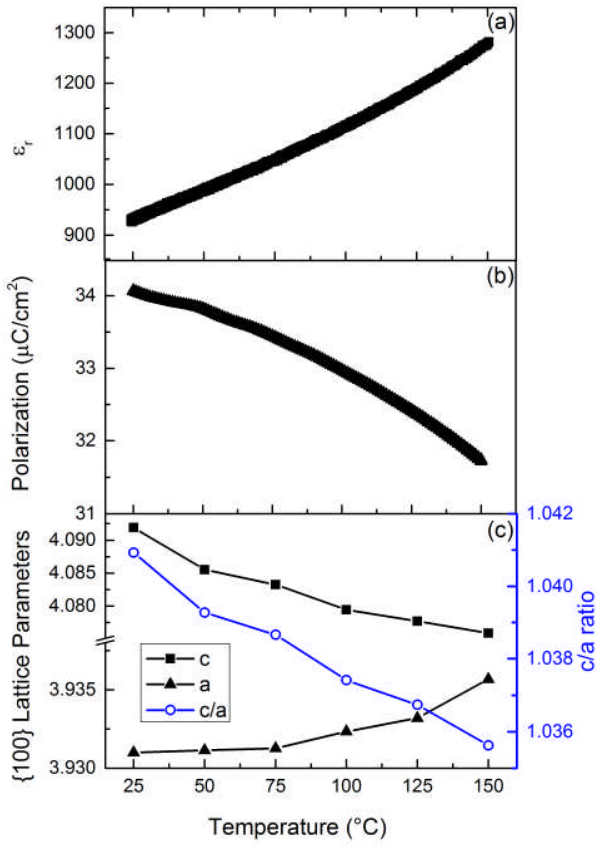

Figure 6-18.(a) Relative permittivity, (b) polarization and (c) lattice parameters of a poled sample of composition D1

The data presented in Figure 6-18(c) demonstrates that with increasing temperature a relatively small shift is observed in the a-lattice parameter in contrast to the c-lattice parameter which experiences a significant reduction, hence a reduction in the tetragonality (c/a) is observed, accordingly demonstrating the potential for enhanced domain wall mobility. A relatively minor increase (5.5%) in the tetragonal phase volume fraction was observed across the temperature range, this is less significant in the enhancement of piezoelectric properties. The reduction of the tetragonal lattice distortion is commensurate with an associated decrease in internal stress levels [138]. The linear decrease in the c/a ratio corresponds to the linear increase in the extrinsic response at these temperatures although there is no reason to suggest that this should be the case across different systems or even different compositions of the same system. At high temperatures the domain wall energy is reduced and domain wall mobility is enhanced, evidenced by the reduction in the electrical coercive-field measured using the converse effect at high-fields (7 kV/mm), this was found to decrease across all compositions as a function of temperature [229]. As stated previously, the applied electric-field during the Rayleigh measurement was kept at reduced levels well below the coercive field in order to avoid the depolarization of the sample and nucleation of new domains. The enhancement in both the intrinsic and extrinsic contributions to the piezoelectric coefficient d_{31} has been shown in a previous section using resonance analysis therefore confirming this effect at low and moderate excitation levels [230].

It was therefore possible to calculate the d_{init} and contrast this to the measured d_{init} values. The reversible extrinsic component was calculated by deducting the calculated from the measured values, the results of this are shown in Figure 6-19. A general increase in the reversible extrinsic contributions was identified with increasing temperature from 9.2 pm/V to 30.2 pm/V at room temperature and 150 °C respectively. An increase in the reversible Rayleigh coefficients has also been demonstrated at the MPB in lead-free piezoelectric ceramics [231] and as a function of temperature in $PbTiO_3$-derived thin films [232].

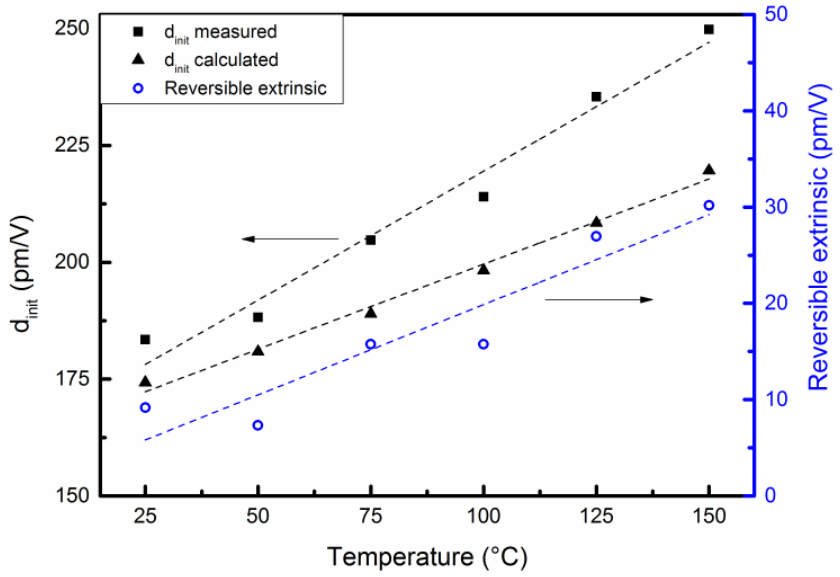

Figure 6-19. The measured d_{init}, calculated d_{init} values and the reversible extrinsic component as a function of temperature for composition D1.

The reversible extrinsic component from domain wall switching that is independent of the applied electric-field strength is often assumed to be relatively minor compared to the reversible intrinsic due to atomic displacements and irreversible extrinsic contributions [233]. However, it has been suggested that in hard PZTs reversible domain wall movement is the dominant mechanism at room temperature as the material response does not adhere to Rayleigh law [234]. As the Rayleigh law is closely obeyed in the BF-KBT-PT system it is can be inferred that this system behaves more similarly to a soft PZT although driven at much higher excitation levels where lossy processes could become more prevalent, hence an increase in the contribution from reversible domain wall processes.

An increase in the reversible extrinsic components is anticipated with an increase in temperature and can be explained succinctly in terms of the potential energy profile. At room temperature there is not sufficient thermal energy for extensive polarization rotation and the reversible motion of interfaces. The potential energy barrier at room temperature is significant enough to prevent irreversible domain wall switching as the activation energy required is greater than the thermal energy of the system, kT, required to enable irreversible domain

wall switching. As the temperature is increased the thermal energy increases thus allowing a greater contribution from irreversible and reversible extrinsic domain wall effects, (as they are thermally activated). The energy barrier also reduces (i.e. the energy potential wells reduce in magnitude and broaden) therefore for the same excitation levels an increase in both irreversible and reversible domain wall motion is observed (hence the increase in d_{33} here and d_{31} as a function of temperature shown in a previous contribution [230]). The caveat being that the tetragonal spontaneous strain, x_s, lessens as temperature increases therefore reducing the magnitude of these effects. However, the increase in thermal energy and reduction in the energy barrier are dominant in the temperature range discussed.

Table 6-1. Summary of electrical properties and Rayleigh parameters at room temperature for BF-KBT-PT, La-BFPT [137] and PZT ceramics [25] [166], d_{33} values were measured with a Berlincourt meter, E_C was taken from x-E data at 7 kV/mm.

Composition	B	C	D1	D2	E1	E2	La-BFPT	PZT
d_{33} (pC/N)	152	206	228	208	220	203	120	180
E_C (kV/mm)	4.21	3.93	3.64	3.82	3.98	4.01	10	-
T_C	514	442	427	422	419	410	450	386
Tetragonality (c/a)	1.061	1.045	1.041	1.034	1.034	1.25	-	-
α_d x 10^{-18} (m^2/V^2)	23.39	42.40	58.83	36.9	51.49	38.47	4.2	130
d_{init} x 10^{-12} (m/V)	128.25	175.77	183.43	171.93	178.82	170.12	82.4	242.4
Extrinsic cont. (%)	15.11	19.43	24.28	18.21	22.23	18.4	4.8	~25

6.6 PUND

A series of PUND measurements were recorded, for brevity only a select number are shown, these were found to be representative for the BF-KBT-PT system across the compositional space. The PUND data was normalised against P_{SAT} values taken from P-E loops displayed in Figure 6-20, these were obtained from the same sample and measured prior to the PUND measurement as it is an

aggressive technique due to the rapid switching of samples that frequently resulted in dielectric breakdown and destruction of samples. As shown in previous chapters the lead-free compositions display little indication of widespread domain switching, upon addition of the $PbTiO_3$ a clearly distinguishable electrical coercive field emerges and typical hysteresis loops were recorded across the MSR typified in composition C, shown in Figure 6-20. A number of compositions that lie outside of the mixed symmetry region have been included as they show the graduation from the largely electrostrictive and minor ferro/piezoelectric response (>45 pC/N) behaviour observed in the lead-free system to the classical ferroelectric material that also displays enhanced piezoelectric charge coefficients d_{33} (140-228 pC/N). Varying electrical fields have been used although these should have been significant enough to demonstrate representative behaviour, the necessity for this change is due to the variation in coercive field across the compositional space.

Figure 6-20. P-E loops measured pre-PUND analysis

The PUND measurements normalised to P_{SAT} are shown in Figure 6-21. The PUND technique has been discussed earlier in the literature review and is utilised to separate ferroelectric switching from non-switching parasitics such as leakage current, relaxation processes and polar nanoregions, the value measured is

the true ferroelectric switching of the sample, as P-E loops can often be misrepresentative as discussed by Scott [171]. The PUND measurement gives two key values, the total switchable polarization and the non-switchable polarization. $\Delta P/P_{SAT}$ shows that the lead-free compositions demonstrate limited ferroelectric switching as discussed in Chapter 4-5. The lack of an obvious electrical coercive field with this measurement shows that switching occurs gradually and not at a distinct electric-field especially in the lead-free 4060 BF-KBT composition and the coercive field garnered from electric-field induced strain measurements is rather an average from a very broad set of values.

Figure 6-21. $\Delta P/P_{SAT}$ for selected compositions

In stark contrast, a large region of the BF-KBT-PT compositional space, even at relatively low $PbTiO_3$ values as shown in the compositions where x = 0.375 0.3, and y = 0.1125 and 0.175 respectively, demonstrated a clearly defined threshold field where ferroelectric switching increases sharply. The magnitude of ferroelectric switching also increases with further partial substitution of $PbTiO_3$ providing substantial evidence of the increase in long-range polar order. For the composition where x = 0.15 and y = 0.3 located near to the BFPT MPB, ferroelectric switching occurs over a broad range of excitation levels, proposed to be due to the large c/a ratio of 1.068 and the significant electrical coercive field of

~6 kV/mm. The ferroelectric switching has not fully saturated which would suggest that with larger electric-fields a greater degree of switching would occur, this is contradictory to other compositions belonging to MSR in the BF-KBT-PT which exhibit behaviour consistent with saturation, manifested by flattening of the switchable polarization at a number of different excitation levels. Composition C with a d_{33} of 208 pC/N displays a $\Delta P/P_{SAT}$ value of 0.81 which shows that some parasitics are present.

PUND measurements cannot discriminate between individual parasitic components which led to the measurement of leakage current, shown in Figure 6-22, to confirm that the reduction in ferroelectric switching in the lead-free compositions was not singularly attributable to increased leakage. The soak and measure period was set to 1 second to correlate with the P-E loop measurements frequency and the pulse and delay period used for the PUND measurements. A pronounced enhancement in the leakage current was observed as the electrical coercive field is exceeded and then reduces with increased fields, this data shows that leakage values of the BF-KBT-PT system are not excessive compared to their lead-free counterparts and this is not the origin of the reduced ferroelectric switching and in some cases leakage is more pronounced in the $PbTiO_3$-derived compounds.

Figure 6-22. Leakage Current as a function of electric field

6.7 Structural Analysis

The previous subchapters have demonstrated the temperature dependence of a number of dielectric, piezoelectric and elastic coefficients up to the Curie temperature as well as the nature of the intrinsic/extrinsic contributions of a narrowed compositional space belonging to the MSR. The remaining sections aim to broadly discuss the structural ordering across the entire BF-KBT-PT system and how this affects the polar order, a particular focus is paid to the effect of $PbTiO_3$ congruent with the previous sections.

Analysis of the {200} family across the compositional space elucidates a great deal of information regarding the influence of $PbTiO_3$. The lattice parameters, c/a ratio and tetragonal volume phase fraction all show a strong correlation with the $PbTiO_3$ content not only across the narrowed mixed symmetry region but also toward the $BiFeO_3$-$(K_{0.5}Bi_{0.5})TiO_3$ end member, shown in Figure 6-23.

Across the entire system no significant change is observed in the a-lattice, however, the c-lattice parameter changes markedly and displays enhanced tetragonality as previously discussed a c/a ratio of 1.122 was observed with a $PbTiO_3$ concentration of 0.3375 which exceeds the $PbTiO_3$ content at the MPB of the BFPT end member, the partial substitution of 0.075 mol% $(K_{0.5}Bi_{0.5})TiO_3$ therefore leads to a migration of the MPB. As the $PbTiO_3$ is reduced the c/a ratio decreases, at <0.2 $PbTiO_3$ the tetragonality lessens markedly with peak fitting increasingly difficult. At x = 0.375 and y = 0.1125 the lowest R_{wp} values were achieved when fitted to a cubic model, although a d_{33} of 100 pC/N is achieved in this composition, signifying that electrical ordering is still prevalent, believed to be due to the presence of PNRs, as the directions of PNR dipole moments are random the spatial coherence length is not significant enough that average structure determination techniques such as XRD are useful.

The intensity of the tetragonal (002) and (200) peaks, I_T, has been considered as a function of $PbTiO_3$ concentration in Figure 6-23, calculated according to;

$$I_T = \frac{I(200)_T + I(002)_T}{I(200)_T + I(002)_T + I(200)_R}$$

Equation 6-3

where $I(002)_T$, $I(200)_T$, and $I(200)_R$ represent the intensities of the respective peaks.

A general increase in the tetragonal phase can be observed with increased $PbTiO_3$. At contrasting ends of the scale where x = 0.075 and y = 0.3375, the tetragonal phase volume accounts for 85.5% while where x = 0.3 and y = 0.15 the tetragonal contribution is 13.7%. Several perturbations from the trend occurs in the compositions belonging to the mixed symmetry region, this may be due to proximity to the MPB as the ratio between the $BiFeO_3$, $(K_{0.5}Bi_{0.5})TiO_3$ and $PbTiO_3$ varies throughout. The composition that sits closest to the MPB is composition D1 as the tetragonal intensity was found to be ~51%, this composition also exhibited the largest room temperature d_{33}.

A general region has been marked in Figure 6-23 where piezoelectric properties are enhanced, Kungl and Hoffman highlight the importance of a balance between lattice distortion and the phase composition [217], specifically with regard to non-180° domain switching and their contribution towards the electric-field induced strain response. Whilst a large lattice distortion and volume phase fraction of the tetragonal phase in mixed symmetry materials may be indicative of a large potential for extrinsic contributions, however, in a pure tetragonal material for example, the actual response is reduced due to mechanical stress induced upon actuation, as there is a considerable energy barrier preventing non-180º domain switching. In order to fully exploit the potential piezoelectric properties of materials with a large tetragonal lattice distortion, an increase in the rhombohedral phase volume fraction is often useful in order to promote domain switching as the barrier to domain switching is therefore reduced. In PZT the lattice distortion of the tetragonal phase is reduced which allows a greater degree of poling. Therefore a significant rhombohedral phase is desired in allowing the movement of non-180° domain walls. Kungl suggested that in PZT, a 25–40% rhombohedral phase is optimum [217], whilst in the BF-KBT-PT system, where the c/a ratio (=1.025-1.061) is generally far larger in the mixed symmetry region

(cf c/a for La-doped PZT = 1.028) [235], a higher rhombohedral content is advantageous, the rhombohedral phase fraction in compositions B-E2 is between 44-71% while it is 51.2% in composition B which exhibits a c/a ratio of 1.061, thus increasing domain switching compared to the closely related BFPT system. For composition A, the rhombohedral phase volume fraction is ~24%, resulting in limited electric-field induced strains observed at both room temperature and high temperature. In this system the rhombohedral phase volume fraction is significantly larger than in PZT as this counters the larger c/a ratio of the MSR.

Figure 6-23. {200} Lattice Parameters, c/a ratio and tetragonal intensity ratio as a function of $PbTiO_3$ content

6.7.1 Synchrotron Study

The piezoelectric response observed via electric-field induced strain measurements is often attributed to both to displacements of atoms in the unit cell and non-180° domain switching. Rayleigh analysis quantified these effects, an alternative technique that can augment this understanding is the use of *in-situ* and *ex-situ* electric-field synchrotron powder diffraction. In an ideal structure, domain switching can be inferred from variations in the peak intensities, and lattice displacements are usually represented by modifications in the location of the peaks. In rhombohedral materials a reduction in the (-111) and heightening of the

(111) peak accompanied with a shift to lower 2θ angles in the (200) family indicative of an increase in lattice strain as the macroscopic polarization direction aligns with the electric field. While in tetragonal materials a reduction in the intensity of the (200) and increase in the (002) peak accompanied with a shift of the (111) peaks to lower 2θ angles would be anticipated. The separation of the strains attributed to the lattice and domains is challenging, as domain switching can alter the stress state of the lattice, this is especially true in mixed symmetry ceramics as the obscuration of the effects can occur, this technique has frequently been used to observe the intrinsic and electromechanical contributions to the piezolectric effect in PZT [233-234] and lead-free compounds [101], [202].

Measurement of the lead-free 4060 $BiFeO_3$-$(K_{0.5}Bi_{0.5})TiO_3$ composition was performed with an applied electric-field *in-situ*. The resulting diffraction patterns have been normalised to allow for ease-of-comparison and to account for experimental deficiencies such as attenuation of the x-rays as the electric-field was applied, this can occur due to the oil becoming polarized as the electric-field is increased. As the 4060 BF-KBT composition is pseudocubic, conventional peak position shifting and peak intensity analysis is limited in the amount of information that can be inferred from this data.

Figure 6-24 (a-d) demonstrates the diffraction patterns of the {111} and {200} family of peaks, in their unpoled state, with an applied field of 6 kV/mm and after removal of the electric-field. The diffraction patterns were caked in order to allow for the observation of texturing, the patterns are presented for φ = 0 ° and 90 °. As this composition lies on the rhombohedral/pseudocubic transition it is feasible that an electromechanical response synonomous with rhombohedral switching would be observed. The {111} family before the application of an electric-field demonstrates no peak splitting that is indicative of a rhombohedral phase, pseudocubic peaks were observed that were relatively broad, upon application of the electric-field a shift to higher d-spacings is observed parallel (φ = 0°) to the applied electric-field, the shift is predominantly reversible and not significant in magnitude. For the {200} family a change in the lattice dimensions also to higher d-spacings upon application of an electric-field is shown to be

noteworthy although practically reversible for both φ = 0° and 90°. This modification in lattice parameters, however, is similar to that offered in the literature for a canonical rhombohedral PZT as the shift suggests the {200} increases in size upon application of an electric-field although in a piezoelectric material this would not be entirely reversible. The relatively large effect observed in the {200} compared to the {111} family may however explain the large electric-field induced strains reported in this composition and also the relatively low piezoelectric coefficients measured using a Berlincourt meter as it is largely reversible and the domains do not stabilise once the field is removed. The behaviour observed across both reflections φ = 0° and 90° is similar (although contradictory as anticipated) with no great deal of texturing observed upon application of the electric-field which suggests neither tetragonal or rhombohedral phases exist over a long-range in the bulk average structure. No electric-field induced phase changes were observed as in other $(K_{0.5}Bi_{0.5})TiO_3$-derived systems [101], although a time-dependent transformation cannot be ruled out.

Figure 6-24. *In-situ* synchrotron diffraction patterns of the 111 family where φ = 0° (a) and 90° (c) and the 200 family where φ = 0° (b) and 90° (d) for BF-KBT 4060 before, during and after application of 6 kV/mm

The BF-KBT-PT system was examined during a separate cycle at Diamond on the I15 beamline. It was decided that the samples would not be measured *in-situ* due to time constraints as it removed the possibility of dielectric breakdown of the samples during application of the electric-field and accelerated turnaround times between measurements. Samples were prepared by the author and the measurement was performed by Dr. T.P. Comyn, data reduction and analysis was also completed by the author. As alluded to previously, a phase change (or significant change in phase volume fraction) was observed in this system using conventional laboratory XRD with an applied electric-field *ex-situ*, this led to an assumption that the phase-changing behaviour may be the origin of the large electric-field induced strains and piezoelectric charge coefficients as the tetragonal:rhombohedral proportion changes during actuation, similar to behaviour observed in PZT [217].

Diffraction patterns, shown in Figure 6-25, were normalised to the maximum peak intensity as a number of factors may influence peak intensity such as the beam current at the time of measurement and the sample width (the thickness was identical as samples were cut from the same pellet), this normalisation removes the possibility of quantifying the domain switching behaviour, however, it can provide significant qualitative details. This measurement was performed on the 7 BF-KBT-PT compositions that have been focused on throughout this chapter.

Due to the coexistence of rhombohedral and tetragonal symmetries a number of different effects can often compete against each other. Additional contributions may be observed due to intergranular strain effects. It is immediately clear that the diffraction patterns support the existence of ferroelectricity, which has already been confirmed using an assortment of techniques. Generally, all of the compositions demonstrated significant variations in either peak height or peak position between the unpoled and poled samples for both $\varphi = 0°$ and $90°$. As stated previously, the rhombohedral phase volume fraction is significant in these materials in spite of the large c/a ratio of the tetragonal phase, as a result most of the {200} family of peaks are normalised to

the $(200)_R$ which allows for a useful comparison of the tetragonal peaks which are believed to dominate the electrical properties.

In terms of lattice strain in the unpoled and poled samples a significant shift of the peak position can be seen for compositions C-E2 that is irreversible although this is not as apparent in compositions A and B, these two compositions display the lowest piezoelectric charge coefficients and composition B was also shown to display the lowest intrinsic effect of compositions B-E2. The decreasing tetragonality (c/a) with a reduction of $PbTiO_3$ is clearly manifested in the decreasing $(002)_T$ reflection location, especially in poled samples for $\varphi = 0°$. The peak splitting demonstrated in Figure 6-25(n) in composition E2 is not immediately clear due to the reduced tetragonal splitting, however, upon poling this structure is plainly elucidated, particularly with respect to the $\varphi = 0$ ° bank. Elongation of the unit cell, as indicated by a shift in the {111} family to higher d-spacings similar to previous reports in tetragonal materials was found to occur in alignment with the macroscopic polarization direction along the c-axis for $\varphi = 0°$ in poled samples, while $\varphi = 90°$ displayed a relatively stable lattice constant. A small shift in the $\{200\}_R$ reflection to higher d-spacings also occurs in poled samples and is commensurate with the increase in size in the {111} family for $\varphi = 0°$ while a decrease in the lattice spacing occurs for $\varphi = 90°$ demonstrating significant texturing.

The changing relative intensities of the {200} family exhibits generally conventional behaviour, for a tetragonal material as stated earlier an enhancement of the $(002)_T$ peak for $\varphi = 0°$ would be anticipated as the domains reorient to the direction closest to the polarization vector, in poled samples, the $(002)_T$ reflections display an enhancement for $\varphi = 0°$ across the entire compositional space except in composition B which displays a negligible decrease in the $(002)_T$ peak. Composition A has the largest tetragonal phase volume fraction of the compositions studied, and displays the most conventional tetragonal peak splitting with an enhancement in intensity of the $(002)_T$ reflection although the shift was relatively minor, this coresponds to the low extrinsic contributions confirmed using Rayleigh analysis and also inferred from the high c/a ratio of 1.068. Poling

of compositions A and B led to a decrease in the relative intensity in the $(-1-11)_R$ reflection for φ = 0°, in agreement with anticipated behaviour for a rhombohedral material. The extent to which the domains reorient and the polarization vector aligns to the electric-field is dependent upon the phase and this may differ with proximity to the MPB, as these compositions do not lie along a pseudobinary line it is also difficult to identify where the MPB is located.

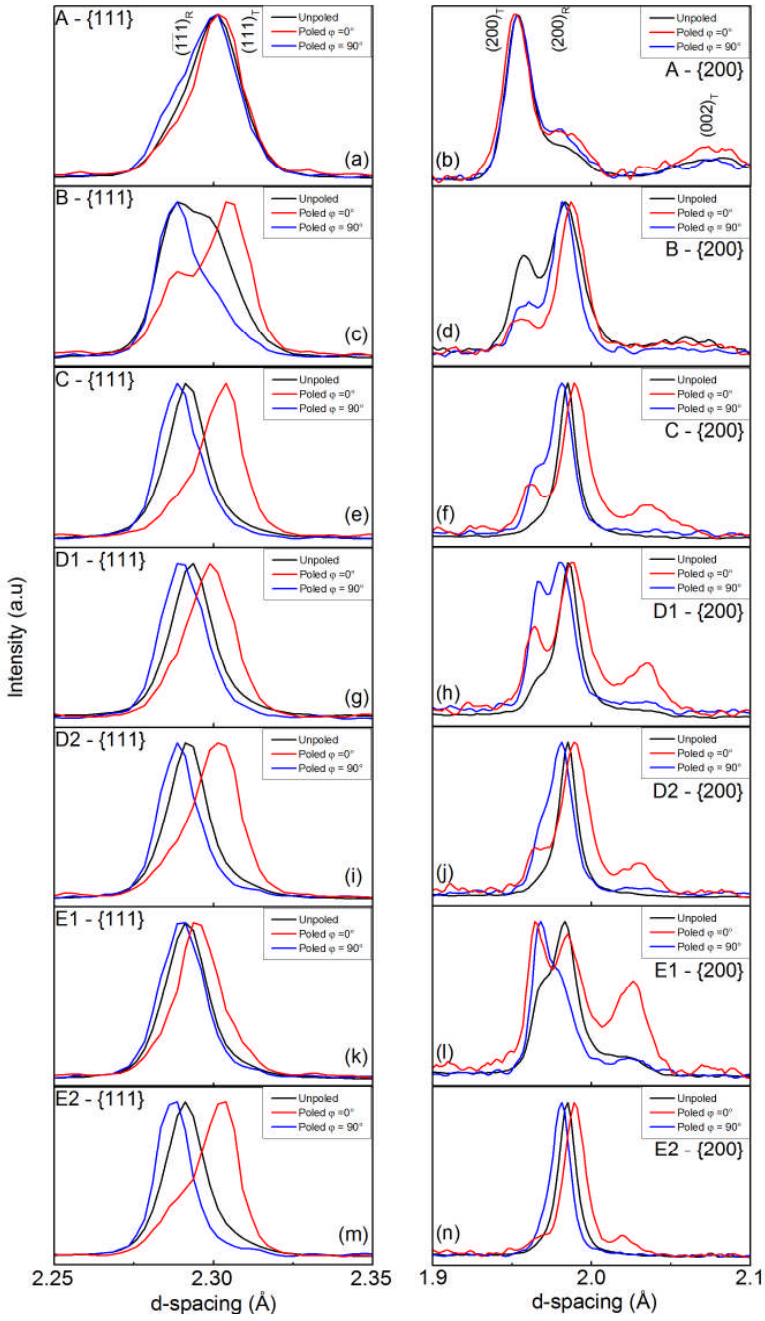

Figure 6-25.(a-n) Diffraction patterns of unpoled and *ex-situ* poled samples from the same pellet at φ = 0° and 90° for BF-KBT-PT

In summary, the most compelling argument made in this section is that for the lead-free system in the pseudocubic region, while displaying an enhancement in the electric-field induced strains it is not due to significant piezoelectric coupling and is largely electrostrictive in origin. Here we have shown with an electric-field *in-situ* that this behaviour is almost entirely reversible and no obvious texturing occurs during or upon removal of the field up to 6 kV/mm, while this applied field is below 8.5 kV/mm that was used to record the electric-field induced strains it is still in excess of the coercive field so irreversible behaviour was expected. This is in stark contrast to the BF-KBT-PT system that demonstrates behaviour consistent with canonical ferroelectric materials and the behaviour is spontaneous unlike that of the BF-KBT system. Peak splitting is progressively obscured with reduction of $PbTiO_3$ and an increase in $(K_{0.5}Bi_{0.5})TiO_3$, attributed to the reduced c/a ratio and reduction of the lattice spacing leading to overlapping of the peaks that are gradually indistinguishable. Irreversible domain switching is evident in the poled samples, indicated by the change in peak intensities and position as well as divergences between $\varphi = 0^o$ and 90^o. Phase switching behaviour was not observed but rather a change in the tetragonal:rhombohedral phase volume fraction.

6.8 Scanning Electron Microscopy

Scanning electron microscopy was used to confirm the existence of ferroelectric domains and to elucidate information regarding the phase coexistence observed by x-ray diffraction. Before imaging could occur across a wide range of compositions an etching study was required. This was not a detailed study in itself, rather a study that simply enabled the author to produce comparable images across the compositional space. The etchant used was 100 mL water, 5 mL HCl and 5 drops HF, this was formulated by Professor Bell during his own thesis, and was used by Burnett for his study of BFPT single crystals and was therefore deemed suitable [238]. Samples belonging to the same composition, D1, and produced in the same batch were etched for varying times of 0, 5, 10, 30, 60, 600 and 1800 seconds. The results shown in Figure 6-26 are those for 0, 10, 30 and 600 second etching times as these are widely representative.

Figure 6-26(a) displays an unetched surface belonging to composition D1, it is apparent that no features can be observed belonging to structural defects, grain boundaries or domains within the grains. The sample is extremely dense with very few pores, some of the features that can be observed in the micrographs across all etching times are due to pull-out during processing which can be prevalent in brittle or hard materials such as these ceramics. Pull-out is reduced with careful control of pressure, grinding cloths and diamond suspension size. The lack of any obvious features is the result of the sample being relatively flat, the topography is 20 nm peak-to-trough as observed using PFM, the white speckles that can be seen are owed to the colloidal silica used during the final polishing stage, this is also confirmed using PFM as these were approximately 20 nm in height and diameter. An etching time of 5 seconds showed little difference to the polished unetched sample, however, the 10 second etch shows some signs of topographical contrast as a small trace of a grain can be observed as indicated inside the white rectangle, this is due to the different polarization vectors that intersect the surface etching at different rates. A longer etching time, shown in Figure 6-26(c), can be seen to fully elucidate the grain structure and domains are revealed for 30 seconds and 1 minute. Etching for 10 minutes resulted in over-etching of the sample, shown in Figure 6-26(d), allowing the outline of each grain to be identified more easily, largely due to the pores becoming greater in size and density. Eventually obliteration of the sample after etching for 30 minutes occurred with destruction to the sample observable with the naked eye. As a result of this study an etching time of 30 seconds was used for all of the compositions studied including for the BF-KBT system.

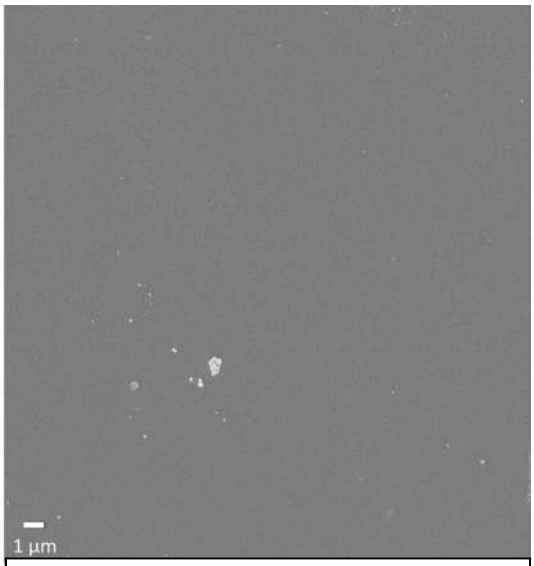

(a) Inlens, 5kV | Unetched

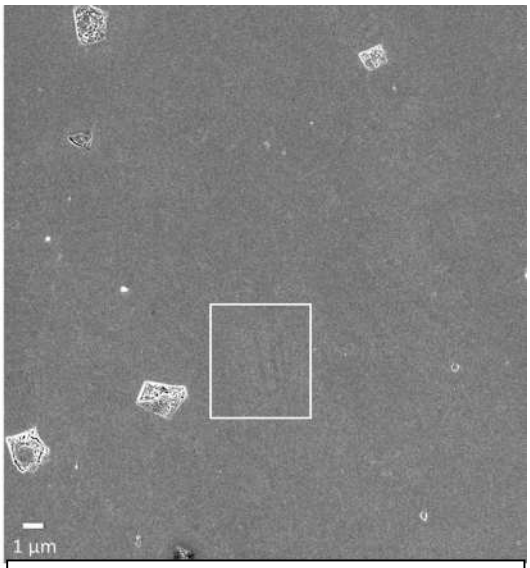

(b) Inlens, 5kV | 10 second

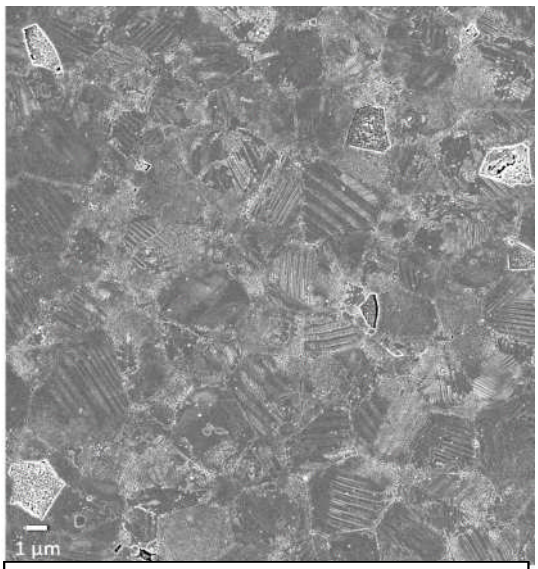

(c) Inlens, 6kV | 30 second

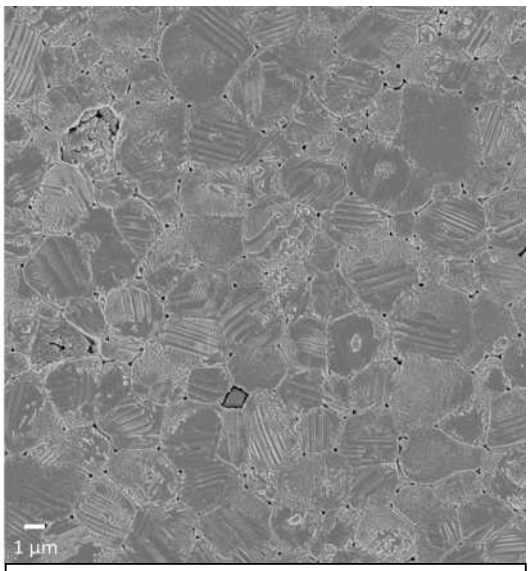

(d) Inlens, 6kV | 10 minute

Figure 6-26.(a-d) Scanning electron micrographs of Composition D1 as a function of etching time in a HF and HCl based solution

The origin behind domain formation was described in the literature review with 180° and non-180° domains forming to reduce the energy associated with electrostatic charge and mechanical stresses. Extensive studies have previously been performed on the canonical $BaTiO_3$ regarding domain patterns [239] and a number of other materials although it is not an overly used technique, the imaging of domains alone cannot be used to confirm ferroelectricity but rather as a useful

supporting technique, for instance WO_3 demonstrates room temperature domain structures but remains unperturbed by an applied electric-field [25].

An SEM image of composition A is shown in Figure 6-27, the average grain size was found to be 2.42 μm using the line intercept technique, and a uniform equiaxed microstructure was found. However, not all compositions demonstrated this uniform behaviour with compositions D2 and E1 (shown in the Appendix, Figures 10-8 and 10-9) exhibiting sporadic core-shell type domains. The porosity of composition A and all other compositions belonging to this system was low while some minor pull-out was observed. Individual grain boundaries can be difficult although not impossible to differentiate, it is clear that ferroelectric domains can be observed across the entire sample area, the inset image which was taken from a different area of the sample shows the classical 'herringbone' structure, furthermore α-type domains are in effect, these are free of polarization charge and like 90° domains are seen to exhibit the correspondence of the same polarization state. The herringbone-type domains are known as 90° domains and are associated with mechanical stresses upon cooling, while they are commonly referred to as 90° domains this is in fact a misleading notion as the tetragonal strain affects the 90° rotation at the domain boundaries and there are usually subtle divergences from exactly 90º. This is due to the difference in the c- and a-lattice parameters and lattice matching at interfaces [240], resulting in a small deviation, this deviation can be estimated using the following equation;

$$90 - \delta = 2\tan^{-1}(\frac{a}{c})$$

Equation 6-4

where δ is the nonconformity to the ideal 90° domain boundary

Therefore, an increased tetragonal distortion leads to greater the deviation from an ideal 90° domain boundary. An angle of 88.4° was observed by Maclaren for $Pb(Zr_{0.45}Ti_{0.55})O_3$ which exhibited a *c/a* ratio of 1.03. The tetragonal distortion for composition A is 1.068 which results in a significant estimated deviation of 86.2°.

This deviation cannot be confirmed easily in polycrystalline ceramics as the images are not taken from a zone axis perpendicular to the domains.

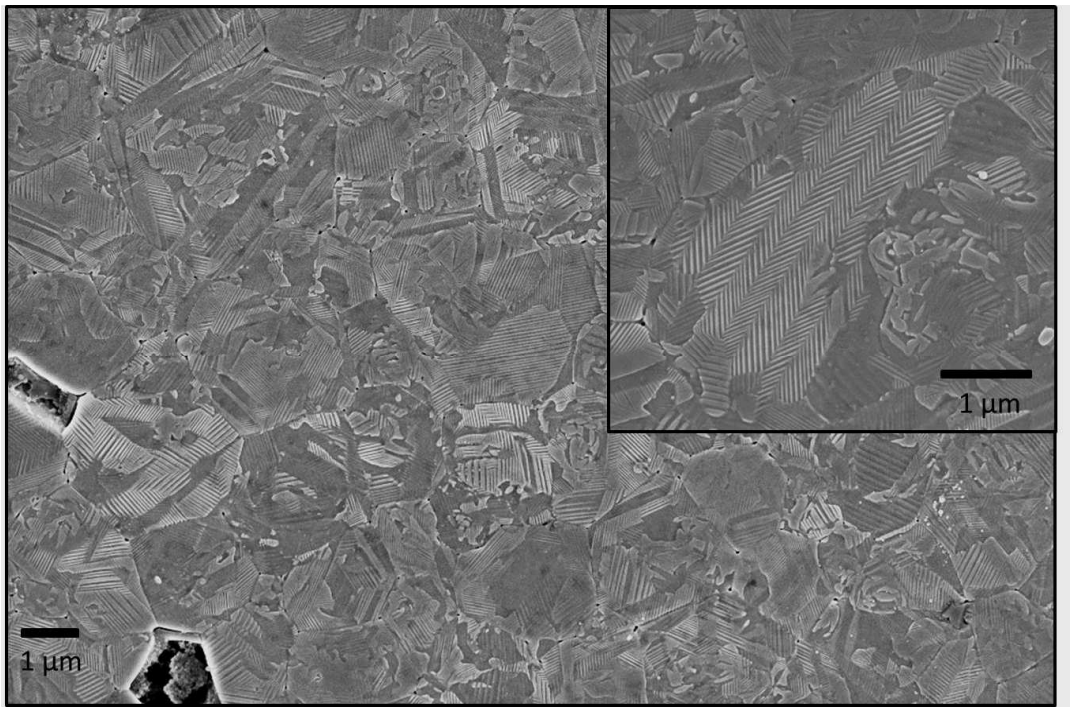

Figure 6-27. Scanning electron micrograph of Composition A that has been optically polished and chemically etched. The inset image is of a highly magnified grain belonging to a different region

A number of other interesting features are also present. Surprisingly the existence of rhombohedral domains appears to be minimal, while this is commensurate with the low rhombohedral phase volume fraction it would be expected that some rhombohedral-type domains could be observed. The white box marks what appear to be rhombohedral domains although it is difficult to confirm, in the Appendix for composition D1, shown in Figure 10-7, rhombohedral domains can clearly be observed although this is not the case for a number of other compositions belonging to the A-E2 series. For composition A, 90º and 180º domains can be seen in both the inset and the wider image, another feature that exists is highlighted in the green box, these seemingly irregular random domains are known as watermarks which are180º domains intersecting the surface and form in an attempt to reduce the electrostatic energy upon cooling exactly like conventional 180º domains.

In contrast to the BF-KBT-PT system across the entire compositional space where ferroelectric domains are clearly visible as well as a number of interesting features, the lead-free 4060 BF-KBT composition shown in Figure 6-28, polished and etched using the same routine offers a largely featureless canvass. Grain boundaries are almost indistinguishable in the BF-KBT system, and the porosity is also increased which can attributed to the use of ball milling rather than attrition milling. The inset shows a region subject to a higher magnification, even in this instance it is difficult to observe grain boundaries, the white box highlights one grain that is distinguishable. It is apparent that no obvious ferroelectric domains are present in this sample, while ferroelectric behaviour is much-reduced at the BF-KBT MPB there is still some limited ferroelectric switching as indicated by electric-field induced polarization and PUND measurements. Distinctive regions can be observed, often at the centre of the grains, that could be commensurate with core-shell type behaviour with ferroelectric regions located in the centre of the grain, although this is unconfirmed. The possibility of chemical segregation has also not yet been disqualified with the use of techniques such as EDX or TEM, although XRD and SEM of fracture surfaces did not exhibit any indication of this.

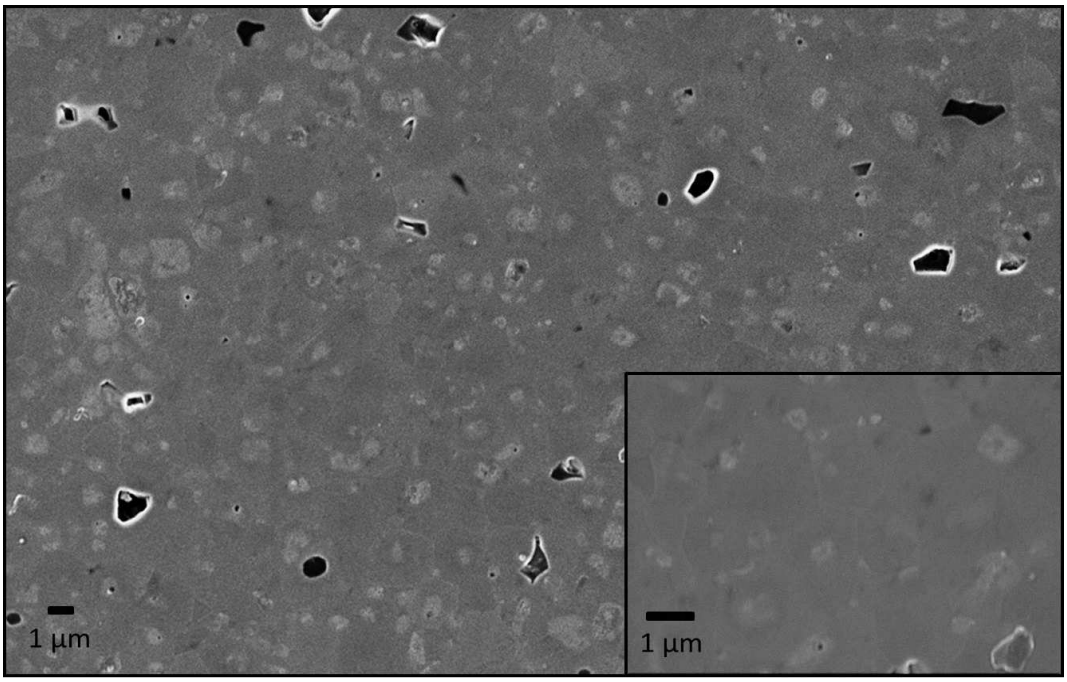

Figure 6-28. Scanning electron micrograph of 4060 $BiFeO_3$-$(K_{0.5}Bi_{0.5})TiO_3$, sample prepared as above

6.7 Piezoresponse Force Microscopy

Piezoresponse force microscopy was used to further investigate the domain structure, particularly for the lead-free BF-KBT system as SEM did not elicit any recognisable domain patterns for the pseudocubic composition. The following section will firstly show one set of images providing an overview of the sample and another set magnifying any interesting or exemplar features. To prevent repetition in the figure captions, each sub-figure presented corresponds to (a) surface topography, (b) deflection error, (c) vertical amplitude, (d) vertical phase, (e) lateral amplitude and (f) lateral phase response of the sample. As domains had previously been observed with the use of SEM in composition A it was decided that it would be imaged (along with a reference $LiNbO_3$) in order to confirm the techniques applicability. Samples were polished flat commensurate with the SEM preparation although not etched. Peak-to-trough sample topography was found to typically be 20 nm although if the tip scanned above holes due to either porosity or pull-out as a result of processing this would increase substantially and lead to poor images as the tip drags across the sample surface.

Composition A is presented in Figure 6-29, typical domain structures are observed, an obvious piezoelectric response can be confirmed which is not always the case with PFM as it can be prone to artefacts. Domain patterns show no correlation with topography in this area and a number of other areas scanned, thus confirming the topography signal is independent to the (vertical) out-of-plane response associated with piezoelectric ordering. The amplitude can provide information regarding the piezoelectric displacement and the phase provides information regarding domain orientation, it is clear that both of these contributions demonstrate significant effects. The topography of the magnified grain can be observed much more clearly in the more heavily magnified image, this is shown in Figure 6-30. The piezoresponse within the grain itself demonstrates both 180º domains and 90º domains although these are much less obvious. The polarization vector of the 180º domains in the vertical phase figure displays alignment of the *c*-axis in both up and down directions. A watermark can be observed in the bottom right-hand side of the grain and the polarization vector can be seen to switch that is commensurate with 180º domain walls.

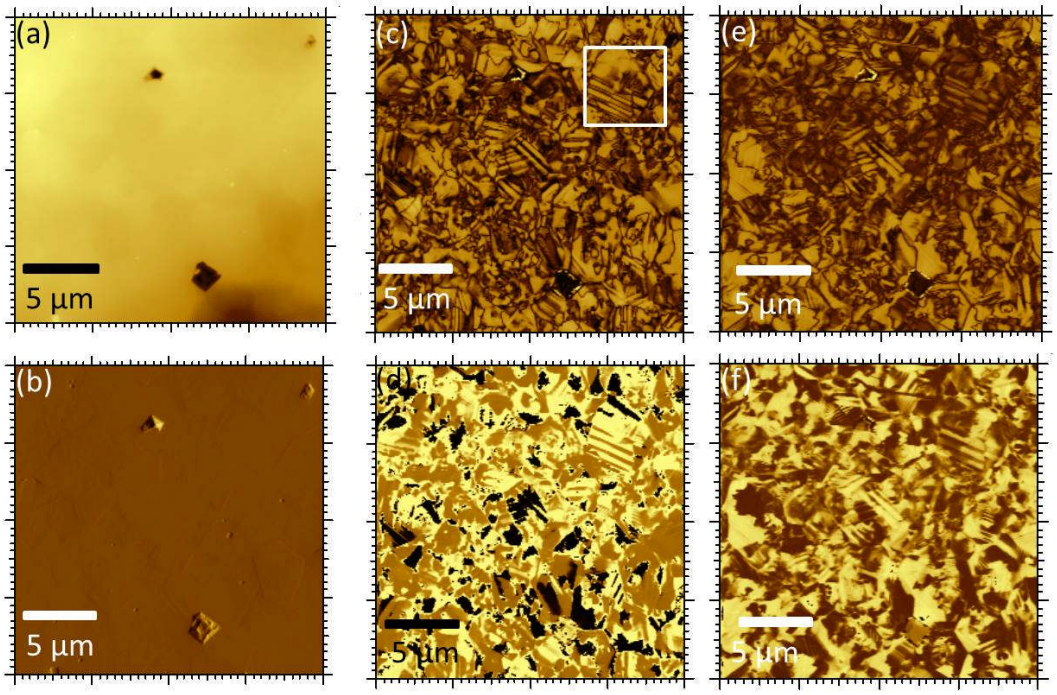

Figure 6-29. PFM images of a 400 µm^2 area of a polished sample of Composition A with (a)topography, (b)deflection error, (c)vertical amplitude, (d)vertical phase, (e)lateral amplitude and (f)lateral phase

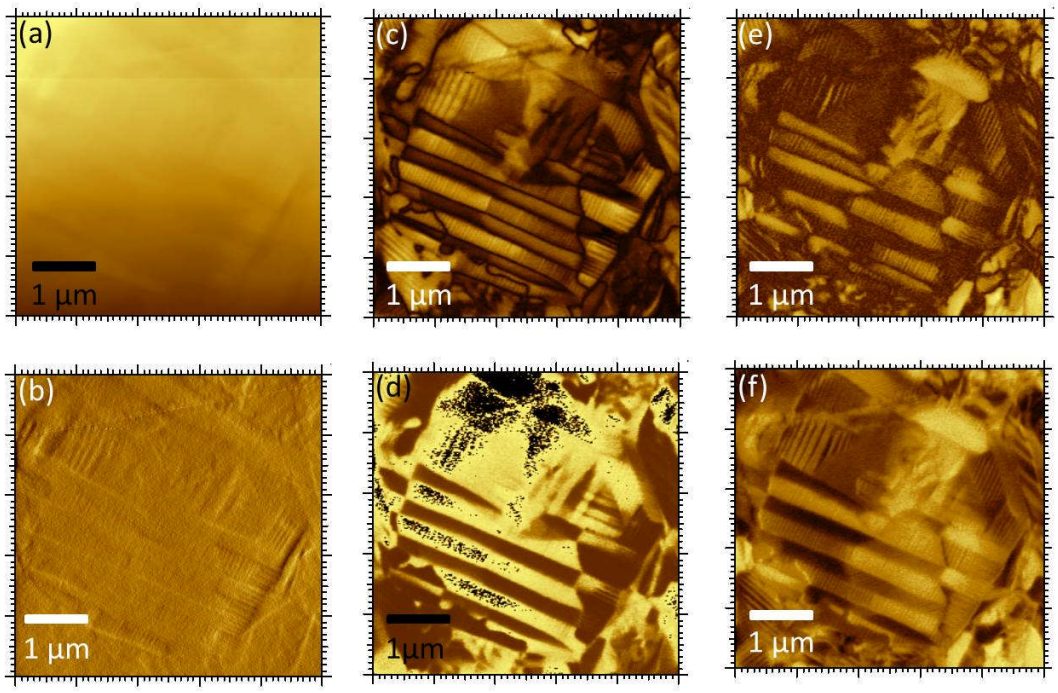

Figure 6-30. PFM images of a 25 µm^2 area of a polished sample of Composition A

The other compositions belonging to the mixed symmetry region are shown in the Appendix, domain switching is widespread and clearly visible in most compositions, except in composition D2 although some domains are visible that are consistent with core-shell type behaviour, this is also commensurate with the images collected using SEM. The PFM response of composition B was typical, domains were easily identified which confirms the SEM images that displayed clear herringbone type structures. The remaining compositions responses were similar to those shown in composition A.

The next composition to be discussed belonged to a region outside of the MSR of the BF-KBT-PT system that has been the focus throughout this chapter. This is shown in Figure 6-31 and belongs to the composition where $x = 0.3$ and $y = 0.15$. The $PbTiO_3$ content is much reduced in this composition although a relatively large room temperature d_{33} was still measured in this composition using a berlincourt meter of 180 pC/N, however, pseudocubic peaks (that can be fitted to mixed symmetry rhombohedral and tetragonal phases with the lowest residual) are elucidated with the use of XRD. The topographical image demonstrates some scratching although these can clearly be identified, as the striations are linear. Here, the domains can be characterized as “labyrinthe”-type domains [241], which have been observed in both lead-free and lead-based relaxor ferroelectrics whereby polar regions with a seemingly random trace similar to watermarks are observed, these are suggested to also correspond to 180º domain walls, those observed here are much larger than those observed in $Pb_{0.9125}La_{0.0975}(Zr_{0.65}Ti_{0.35})_{0.976}O_3$ (PLZT) which are ~50 nm in size but similar to those observed in $0.9Pb(Mg_{1/3}Nb_{2/3})O_3$-$0.1PbTiO_3$ [242], and are suggested to be due to the formation of a glassy state where random fields destroy long-range ferroelectric order, it is also stated that local poling with a dc bias resulted in the growth of micron sized domains in PLZT, a similar process may occur under the application of an electric-field in the lead-reduced compositions of the BF-KBT-PT system that display relaxor-like behaviour. The domains observed in this system are ~200-500 nm in size and therefore much larger than the hypothesised polar nanoregions. Kalinin suggested that domains of this type are due to the

presence of static PNR's, they are defined as static as the imaging timescale, typically a few minutes, allows for their observation.

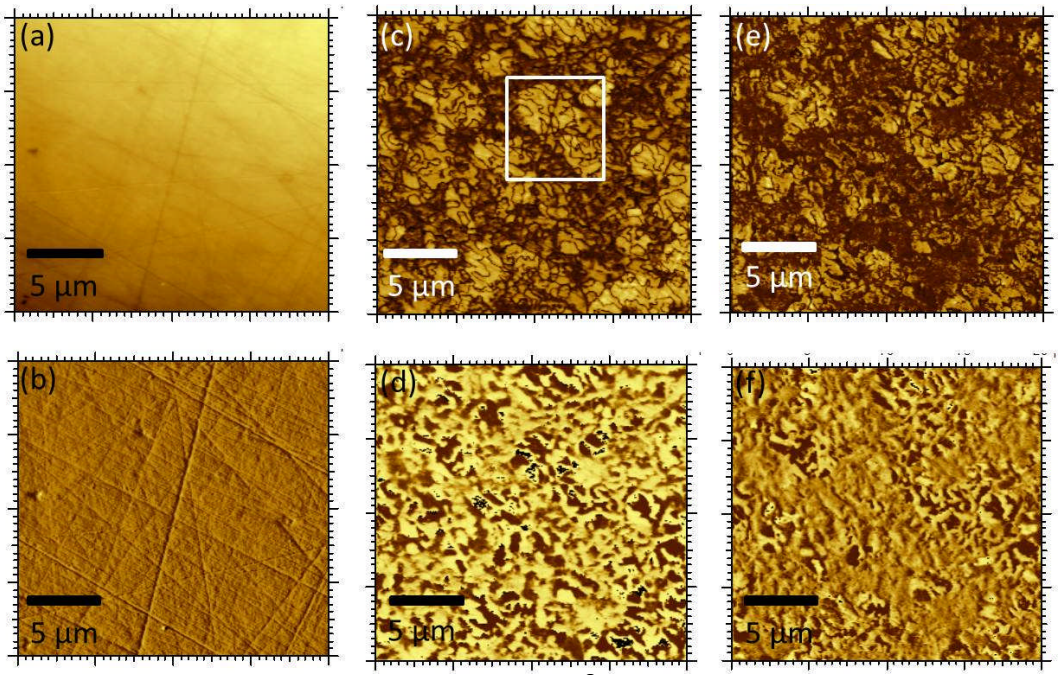

Figure 6-31. PFM images of a 400 µm^2 area of a polished sample of (1-*x*-*y*)BiFeO$_3$-*x*(K$_{0.5}$Bi$_{0.5}$)TiO$_3$-*y*PbTiO$_3$ where *x* = 0.3 and *y* = 0.15

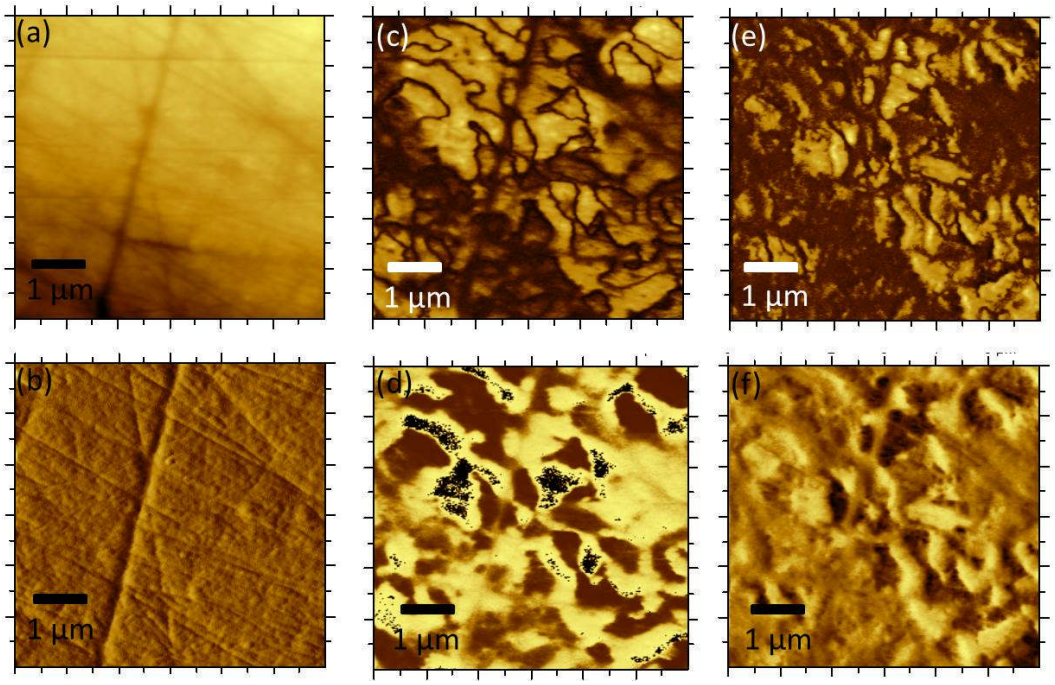

Figure 6-32. PFM images of a 36 µm^2 area of a polished ceramic disc of (1-*x*-*y*)BiFeO$_3$-*x*(K$_{0.5}$Bi$_{0.5}$)TiO$_3$-*y*PbTiO$_3$ where *x* = 0.3 and *y* = 0.15

The following section will focus on the BF-KBT system and the contrast compared to the BF-KBT-PT system. These measurements were performed to see if any long-range ferroelectric banding could be observed similar to the BF-KBT-PT system, the resolution of PFM was suggested to be sufficient enough to observe effects of tens of nanometres although the temporal resolution of this technique in the set-up used is not enough to confirm dynamic PNRs and the scan speed is not fast enough to measure *in-situ* which means that information regarding nucleation and growth of domains cannot be elucidated, this technique is used to rule out long-range ferroelectric order and to support previously obtained data.

The first composition shown in Figure 6-33 is the 8020 BF-KBT composition which has been shown to belong to the R3c space group using XRD and neutron diffraction. The piezoresponse is shown to not correlate with the topographical image thus confirming piezoelectric ordering. The domains shown are not consistent with fractal domains that have been widely observed in $BiFeO_3$-derived ultrathin films, these are typically much smaller in size although similar in morphology [243]. This system generally displayed limited piezoelectric switching as gauged by electric-field induced strain measurements and low piezoelectric charge coefficients measured using a Berlincourt meter. However, the electrostrictive effect in this composition was present and this behaviour has to some extent been confirmed by the PFM responses as some piezoelectric responses have been observed in these isolated piezoelectric ‘islands’. It is possible that piezoelectric regions could exist within a matrix that behaves as an electrostrictor, similar to some relaxor systems that are thought to contain PNR’s in a cubic matrix, elemental segregation has not been excluded as a possible explanation although it is not thought to be probable. The contrast observed in the vertical and lateral amplitude responses, which are indicative of the electromechanical contribution, are substantial while the contrast observed in the phase response is reduced. The density of the domains is substantial and the size of the domains is not irregular, demonstrated in Figure 6-34 more plainly. Therefore, the size of these domains is indicative of long-range ordering in the 8020 composition, the majority of the features observed are spherical with no

obvious ferroelectric domain patterns such as 109º and 71º domains as would be anticipated in a rhombohedral symmetry composition.

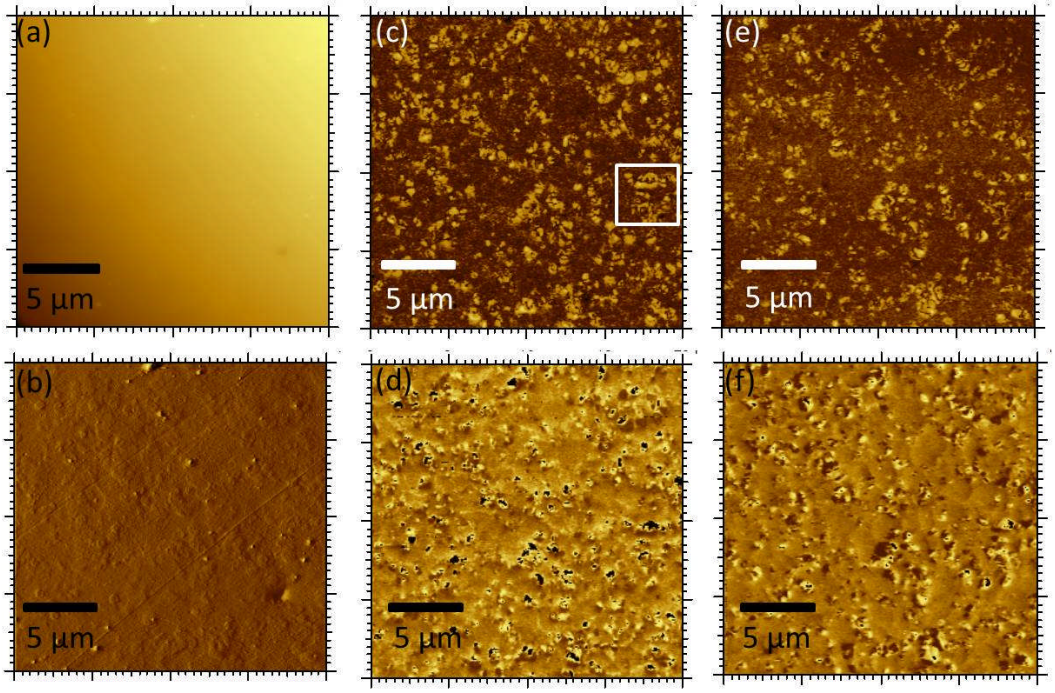

Figure 6-33. PFM images of a 400 µm^2 area of a polished ceramic disc of xBiFeO$_3$-(1-x)(K$_{0.5}$Bi$_{0.5}$)TiO$_3$ where x = 0.8

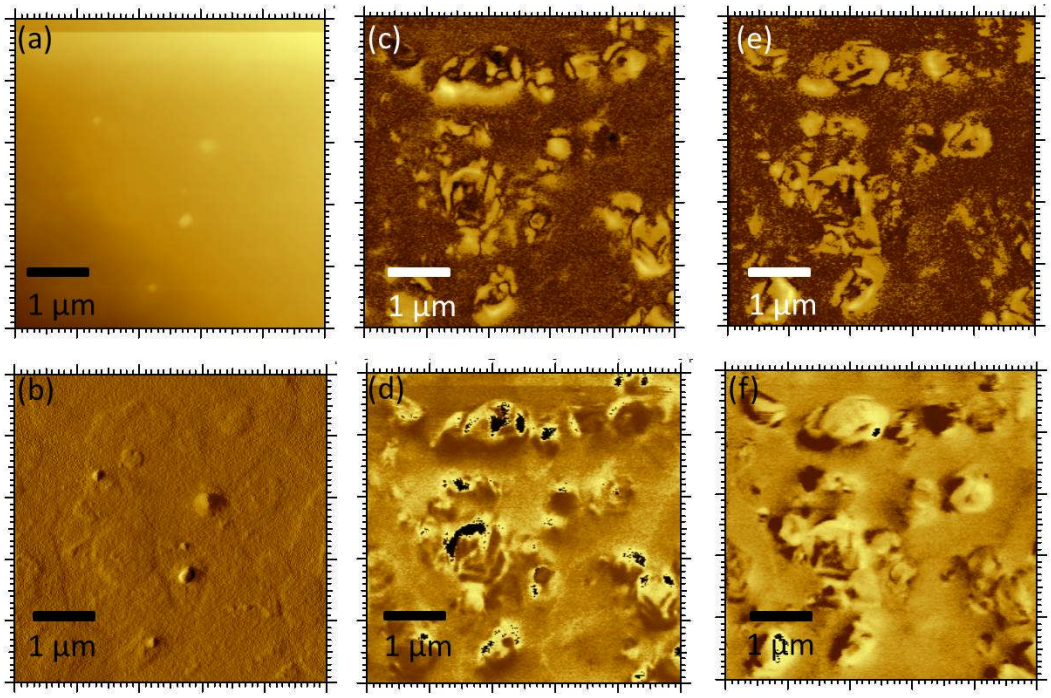

Figure 6-34. PFM images of a 25 µm^2 area of a polished ceramic disc of xBiFeO$_3$-(1-x)(K$_{0.5}$Bi$_{0.5}$)TiO$_3$ where x = 0.8

As the $BiFeO_3$ content is reduced by the partial substitution of $(K_{0.5}Bi_{0.5})TiO_3$ the domain density and piezoresponse decreases as does the size of the domains in general, presented in Figure 6-35 and Figure 6-36. The largest low-signal piezoelectric charge coefficient d_{33} of this system was also measured in this composition which is a result of reduced oxygen tilt angle as the coercive field is reduced and domain wall mobility increased compared to 8020 BF-KBT.

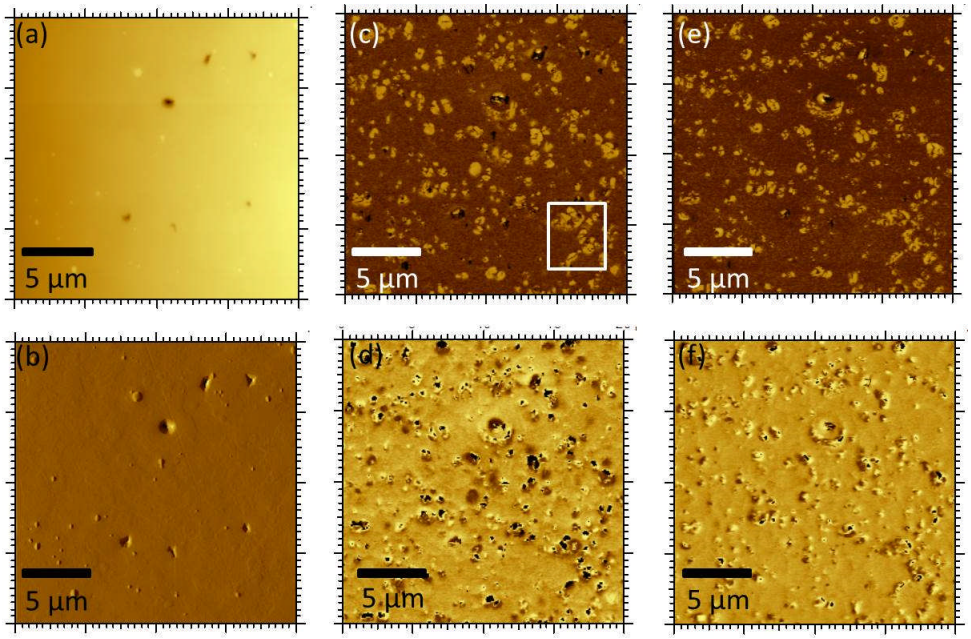

Figure 6-35. PFM images of a 400 µm^2 area of a polished ceramic disc of xBiFeO$_3$-(1-x)(K$_{0.5}$Bi$_{0.5}$)TiO$_3$ where x = 0.6

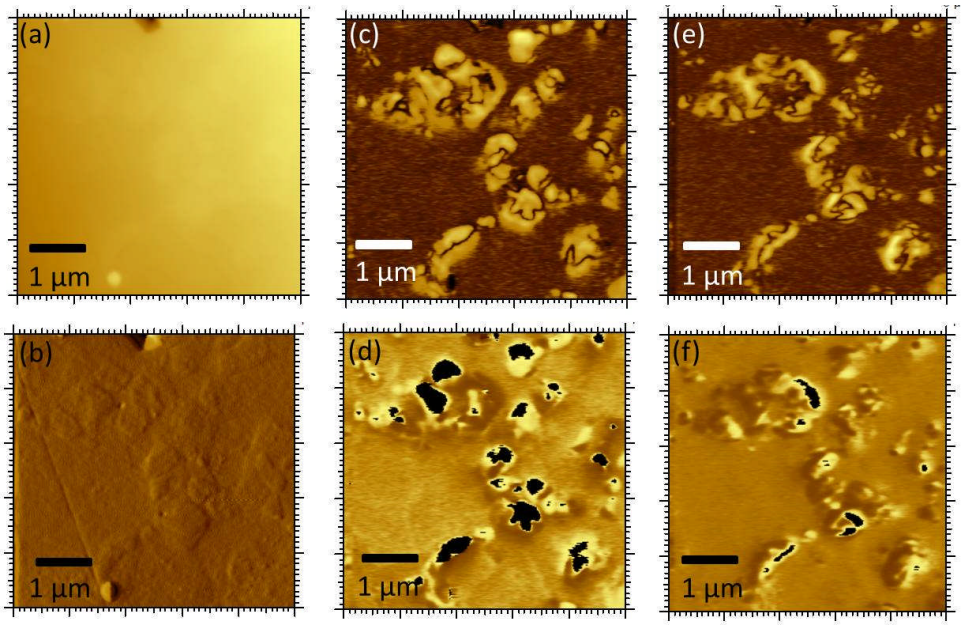

Figure 6-36. PFM images of a 25 µm^2 area of a polished ceramic disc of xBiFeO$_3$-(1-x)(K$_{0.5}$Bi$_{0.5}$)TiO$_3$ where x = 0.6

The reduction in the density and magnitude of the piezoresponse is more evident in the 4060 BF-KBT composition belonging to the pseudocubic region which revealed the largest electric-field induced strain values although reduced piezoelectric coefficients compared to the 6040 BF-KBT composition. These images, shown in Figure 6-37 and Figure 6-38, confirm a barren piezoelectric response with no evidence of ferroelectric domains on the scales examined. An additional image belonging to this region with a higher magnification is included in the Appendix, Figure 10-16, at increased magnifications only very minor piezoelectric responses can be observed in the out-of-plane response that is independent from the topography signal.

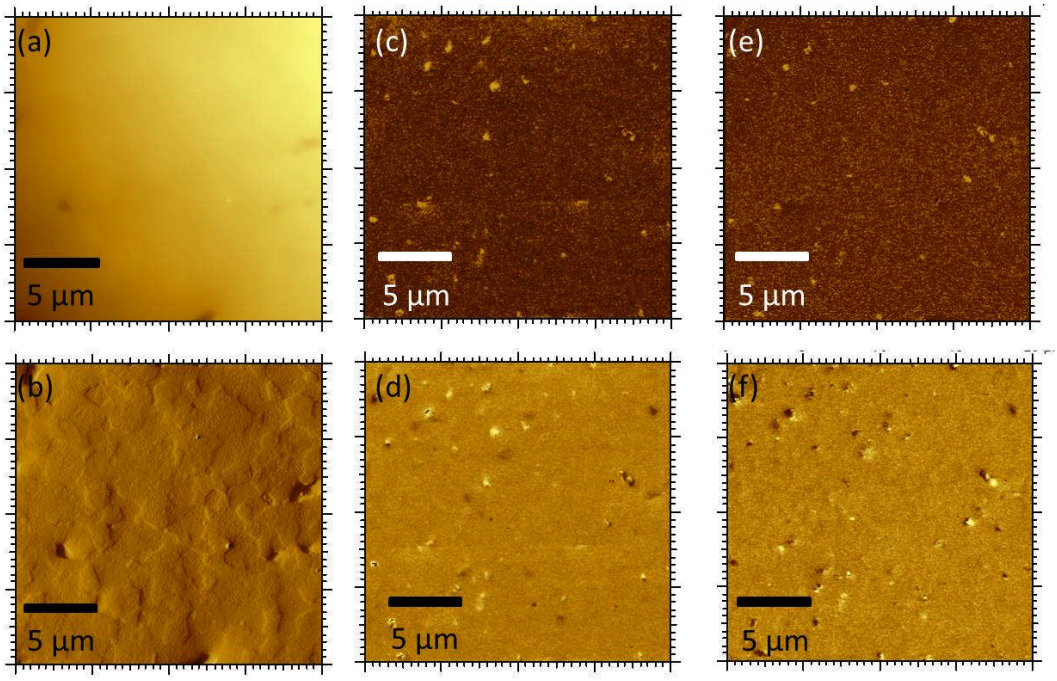

Figure 6-37. PFM images of a 400 µm^2 area of a polished ceramic disc of xBiFeO$_3$-(1-x)(K$_{0.5}$Bi$_{0.5}$)TiO$_3$ where x = 0.4

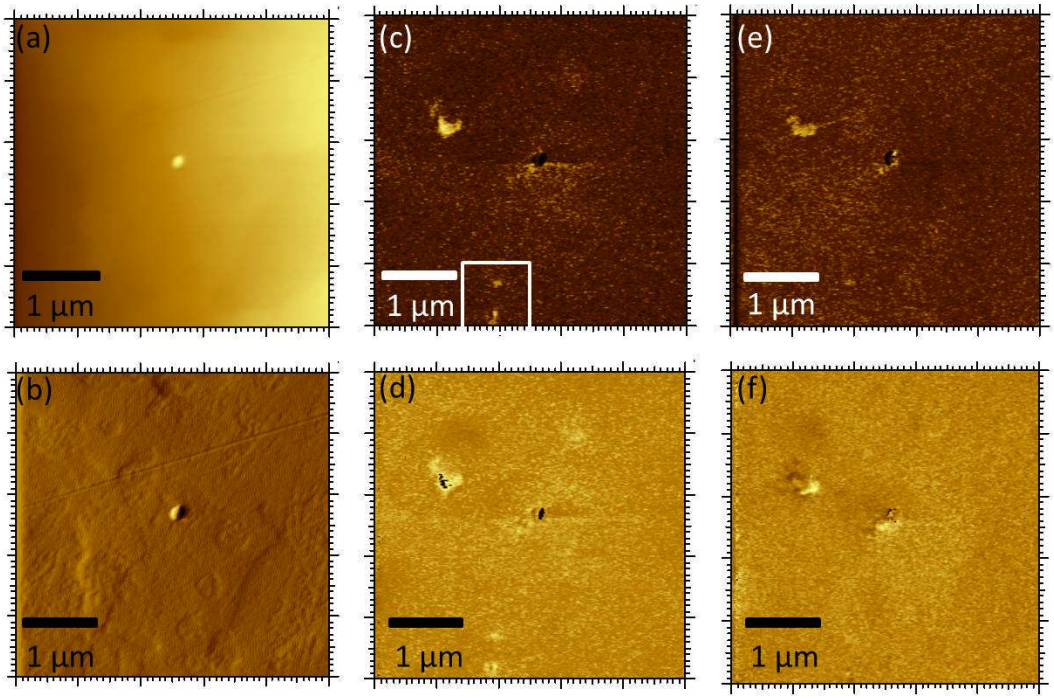

Figure 6-38. PFM images of a 25 µm^2 area of a polished ceramic disc of xBiFeO$_3$-(1-x)(K$_{0.5}$Bi$_{0.5}$)TiO$_3$ where x = 0.4

This technique does not provide evidence for the existence of polar nanoregions that are anticipated to be a handful of unit cells in size, however, long-range ferroelectric order manifested in the piezoresponse can be ruled out. If the PNRs were spatially ordered then it is anticipated that lab XRD or synchrotron x-rays would allow detection due to the cumulative effect of these regions. This technique does not rule out the possibility of these PNRs being temporally ordered. Due to the limitations of the temporal resolution of the equipment, which scans over the course of minutes, it is not be possible to observe PNRs. It does confirm ferroelectric switching in the lead-based compositions across a broad compositional space while the origin of the behaviour in the lead-free system is hitherto unconfirmed.

6.8 Summary and Discussion

The piezoelectric response of a ceramic body is a combination of a number of effects namely; intrinsic lattice distortion, polarization rotation, domain wall translation, domain-lattice coupling, domain wall broadening and polar nanoregions. Several of these components have been examined during this thesis. These will be discussed comparatively between the xBiFeO$_3$-(1-x)(K$_{0.5}$Bi$_{0.5}$)TiO$_3$ system which displayed limited piezoelectric properties and relaxor-like behaviour across the compositional space principally where x = 0.4 (4060 BF-KBT) and the (1-x-y)BiFeO$_3$-x(K$_{0.5}$Bi$_{0.5}$)TiO$_3$-yPbTiO$_3$ system which across the mixed symmetry region demonstrated conventional ferroelectric and piezoelectric behaviour that was stable to temperatures largely unmatched in perovskite compounds.

The effect of partial substitution of PbTiO$_3$ upon the crystallographic properties is significant. It is clear that by using PbTiO$_3$ we have increased the crystallographic strain that supports long-range structural and electrical order, this is not the case in the BF-KBT system which is a pseudocubic ferroelectric at the MPB. Often a larger distortion of the lattice (either rhombohedral or tetragonal) can lead to an enhanced ferroelectric Curie temperature, this relationship holds for the BF-KBT-PT system. The greater the crystallographic strain the greater the potential for a large extrinsic piezoelectric response although the barrier required to achieve the full potential is extremely large such as in the case of the BFPT MPB (c/a = 1.18 and E_C ~18 kV/mm) [70]. Alternate symmetry end members often reduce the large c/a ratio of the PbTiO$_3$ phase to facilitate the formation of an MPB [216], the BF-KBT-PT system sustains and enhances the tetragonal spontaneous strain, x_S, in a number of compositions and leads to a mixed symmetry region rather than well-defined rhombohedral and tetragonal phases either side of a clearly defined MPB.

Polarization rotation is an important mechanism for generating large piezoelectric coefficients, often with the monoclinic phase acting as a link between tetragonal and rhombohedral symmetries in PZT, typically as the polarization vector and electric-field induced strain follow the direction of the

applied field thus maximising the piezoelectric effect. *Ex-situ* diffraction measurements have shown a shift in the rhombohedral/tetragonal phase volume fraction which can be viewed as a form of polarization rotation, however, due to the coexistence of rhombohedral and tetragonal phases it is difficult to distinguish between the two contributions making quantification problematic. There is no suggestion that a monoclinic phase exists in this system although it is possible that monoclinic regions can be obscured by the bulk average crystallographic structure of the surrounding matrix using laboratory x-rays such as in PZT.

This study has found widespread evidence of ferroelectric domains in the BF-KBT-PT system and the rhombohedral phase of the BF-KBT system. Domain wall motion was widely evidenced using the Rayleigh relations, although this method can only distinguish between non-180º domain wall motion based upon electric-field induced strain responses as 180º domain wall motion does not result in modification of the electric-field induced strain. Piezoelectric properties across the mixed symmetry region are dominated by the tetragonal distortion, although the rhombohedral phase is key to enabling the rotation of non-180º domains leading to enhanced piezoelectric coefficients. The rhombohedral phase volume fraction is between 44-71% for compositions B-E2, this is greater than the 25-40% suggested by Kungl for PZT [217], however, for these materials that have a larger tetragonal distortion a greater rhombohedral phase volume fraction is required to relieve internal stresses that enable domain wall motion and reduce pinning centres. As domain wall mobility is inversely related to the tetragonal x_S, it is anticipated that domain translation would peak as a function of spontaneous strain which was confirmed for the composition where $x = 0.188$ and $y = 0.256$ with the caveat that the maximum domain wall mobility permissible lessens with reduced tetragonal x_S.

It is assumed that the lattice strain is coupled to the domain wall motion via grain-to-grain interaction as shown by Pramanick in PZT [207]. Under an applied electric-field a single grain will change dimensions in the direction of the applied-field as a result of a combination of both intrinsic distortion of the unit-cell and non-180º domain wall motion, thus each grain must work cooperatively.

Domain wall broadening in $BaTiO_3$ has been widely discussed by Wada. No direct experimental observation of domain wall enlargement was discovered in either the lead-free or lead-based compounds. Domain wall broadening is however a potential explanation for the enhanced piezoelectric properties. It is also possible that domain walls may form that belong to a different symmetry, thus a different polar axis than the domains it separates [244], and is a possible explanation for the increased intensity measured along non-polar axes during *ex-situ* measurements on poled and unpoled samples in composition B.

PUND measurements have been used to provide evidence of polar nanoregions in the BF-KBT system, while no evidence can be found in the BF-KBT-PT system although it can possibly be inferred in $PbTiO_3$-reduced relaxor-like compositions. PUND cannot discriminate between individual parasitics, the reduced ferroelectric switching of the BF-KBT system in the pseudocubic region coupled with the significant electric-field induced strain responses, d_{33}^*, and non-stable piezoelectric charge coefficients, d_{33}, frequency dependence and lack of long-range crystallographic strain, coupled with similar leakage current densities in the lead-free and lead-based system, is indicative of the existence of electrostrictive polar nanoregions. While SEM and PFM did not observe these features directly it also did not rule out their existence.

All of the effects discussed above can contribute to the piezoelectric effect, Table 6-2, summarises some of the key properties across the entire compositional spectrum in the BF-KBT and BF-KBT-PT systems. PNR's are dominant in the electrical response of Bi-based solutions and can mimic a number of seemingly ferroelectric behaviours. The partial substitution of $PbTiO_3$ into BF-KBT therefore leads to enhanced polar order. Future development of ternary piezoelectric compounds should aim to harness the above mechanisms for the development of long-range structural and therefore polar order, as $PbTiO_3$ is dominant in enabling these mechanisms, it is suggested that it is an essential compound for the development of high-temperature piezoelectric systems.

Table 6-2. Summary of structural and electrical properties across the BF-KBT and BF-KBT-PT compositional space

Composition	d_{33} (pC/N)	d_{33}^* (pm/V)	k_p	T_C/T_d (ºC)	x_S	E_C (kV/mm)	P_{SAT} ($\mu C/cm^2$)	P_R ($\mu C/cm^2$)	α_d x 10^{-18} (m^2/V^2)	d_{init} x 10^{-12} (m/V)	Domains (SEM/PFM)
BF-KBT 8020	17	47	-	590/-	1.0048 (R)	5.8	7.26	2.31	-	-	(-/Y)
BF-KBT 6040	45	150	-	441/-	1.0039 (R)	5.3	25.77	12.52	-	-	(-/Y)
BF-KBT 4060	24	385	-	418/ -	~ 1 (PC)	3.85	28.42	9.47	-	-	(N/N)
BF-KBT-PT 0.15 PT	180	568	0.23	465/ ~300	1.004 (T)	4.15	41.02	29.35	-	-	(Y/Y)
BF-KBT-PT E2	203	196 (*)	0.29	410/ 395	1.025 (T)	4.01	45.04	38.44	38	170	(Y/Y)
BF-KBT-PT D1	228	249 (*)	0.29	417/ 409	1.041 (T)	3.64	42.04	34.03	59	183	(Y/Y)
BF-KBT-PT B	152	104 (*)	0.31	517/ 489	1.061 (T)	4.21	34.89	29.04	23	128	(Y/Y)
BF-KBT-PT A	140	154 (*)	0.16	542/ 523	1.068 (T)	5.99	28.49	21.30	-	-	(Y/Y)

* Calculated from the positive strain of a bipolar loop

7. Concluding Remarks

The overall aim of this research was to develop bismuth-ferrite derived ceramics for high temperature applications with the original focus upon lead-free materials. Initially $BiFeO_3$-$(K_{0.5}Bi_{0.5})TiO_3$ was fabricated across the compositional space with the intention of replicating the MPB observed in PZT and as a lead-free alternative to the closely related $BiFeO_3$-$PbTiO_3$ system. Relatively dense ceramics, >90%, were formed using ball-milling and conventional solid state processing. The perovskite structure was formed across the entire compositional space with the absence of secondary phases. The $BiFeO_3$-rich end of the phase diagram belonging to the rhombohedral phase where $x \leq 0.5$ was indexed to the R3c space group, based upon x-ray and neutron diffraction experiments. A broad region devoid of long-range structural ordering was observed and pseudocubic perovskite reflections were recorded.

Ferroelectric and piezoelectric behaviour was not clearly elucidated from electric-field induced polarization and strain measurements due to the lack of polarization hysteresis and negative-strain switching in the respective measurements. Ferroelectric P-E loops were largely linear as a function of the applied-field although in the $BiFeO_3$-rich compositions this was a result of the large electrical coercive-field which reduced in conjunction with the reduced oxygen tilt angle. PUND measurements did confirm limited ferroelectric switching which lessened with increased $(K_{0.5}Bi_{0.5})TiO_3$. Leakage current measurements confirmed the switching behaviour observed was not associated with the leakage current density across the compositional space. Poling studies also revealed that all compositions were found to exhibit piezoelectric coupling, the strength of this coupling varied significantly across the phase diagram. The low-signal piezoelectric charge coefficient d_{33} measured using a Berlincourt meter was enhanced in the rhombohedral phase with values ranging from 17–45 pC/N where x = 0.8 and 0.6 respectively while in the pseudocubic region these ranged from 24-8 pC/N where x = 0.4 and 0.3 respectively.

The pseudocubic region demonstrated relaxor-like properties as giant electric-field induced electrostrictive strains of 0.33% were observed as well as a

broad plot of the maximum permittivity as a function of temperature, although not presented, that confirmed a significant suppression and shift of the relative permittivity to higher temperatures with increasing frequency. The origin of these electrical properties was postulated to be due to the existence of polar nanoregions in the pseudocubic phase, this theory was not discredited with PFM and SEM imaging although it could not confirm this as the origin of the relaxor-like behaviour. High power synchrotron diffraction for $x = 0.4$ with an applied electric-field *in-situ* did not reveal any irreversible lattice or domain behaviour and was almost entirely reversible. Therefore, this system did not satisfy the objective of the project to develop a high-temperature piezoelectric.

Based upon this preliminary research into the $BiFeO_3$-$(K_{0.5}Bi_{0.5})TiO_3$ system it was hypothesised that the partial substitution of $PbTiO_3$ may induce long-range non-centrosymmetric structural order and enhanced piezoelectric performance. It was anticipated that this would also reduce the giant tetragonality of 1.18 and electrical coercive-field of the $BiFeO_3$-$PbTiO_3$ system at the MPB which prevents its use in applications.

Samples of the $(1-x-y)BiFeO_3$-$x(K_{0.5}Bi_{0.5})TiO_3$-$yPbTiO_3$ ternary solid solution were fabricated using the conventional solid-state reaction method. Structural analysis using x-ray and synchrotron diffraction established that long-range non-centrosymmetric crystallographic order was no longer inhibited above a critical $PbTiO_3$ concentration where $y \leq 0.1125$ as indicated by peak fitting of the Bragg reflections. A phase coexistence was also observed between rhombohedral and tetragonal symmetries across a broad range of compositions with the tetragonality closely related to the $PbTiO_3$ content across the mixed symmetry region, the c/a ratio in a number of compositions was found to be in excess of that measured in pure $PbTiO_3$, this was also the origin of the phase coexistence over a broad region rather than a narrow compositional line.

Conventional ferroelectric and piezoelectric switching was observed using standard electric-field induced polarization and strain measurements up to 150 ºC although conductivity was significant at high temperatures. The origin of the

piezoelectric response was also measured up to 150ºC using the Rayleigh technique which allowed quantification of the intrinsic and extrinsic contributions to the piezoelectric response, a critical c/a ratio was identified at 1.045 with domain mobility limited above this. Synchrotron x-rays with *ex-situ* electric-fields allowed for a more detailed structural analysis, with selected compositions demonstrating significant changes of the rhombohedral:tetragonal phase volume fraction. SEM and PFM images exhibited further evidence of the long-range structural and electrical order which was commensurate with reduced $PbTiO_3$ content in the BF-KBT-PT system and reduced $BiFeO_3$ in the BF-KBT system respectively.

The ferroelectric Curie temperature was between 410-590 ºC across the mixed symmetry region, the depolarization temperature was also largely commensurate with the Curie temperature. High temperature stability is recorded for k_p until 20–100 ºC below T_C. The highest temperature member of this family that is most viable for applications exhibits a T_C of 542 ºC with a d_{33} of 140 pC/N; this is considerably higher than any other material with a similar T_C. This high temperature system has been developed without the use of prohibitively expensive Sc_2O_3, and with an operating ceiling in excess of PZT. As the T_C and tetragonal spontaneous strain correlate strongly with the $PbTiO_3$ concentration, this enables tailoring of the structural and piezoelectric properties making this system an excellent candidate for use in high temperature piezoelectric applications.

The operating window of this system coupled with respectable piezoelectric coefficients far exceeds any comparable materials as shown in Figure 7-1 which was introduced previously in the literature review, this is adapted from Zhang's review of high temperature sensors [95]. This figure contrasts relaxor-$PbTiO_3$ compositions, doped PZT, Mn-doped BSPT, BLSF, and perovskite layer structures with the compositions discussed in this contribution. The only materials which can rival compositions A and B are not classical perovskite structures and offer much reduced piezoelectric coefficients and performance.

This work demonstrates a number of important results that have wider implications. The search for novel high-temperature piezoelectric ceramics can continue to exploit the accommodating nature of the perovskite family, which allows significant variance in chemical and physical character in the exploration of new solid-solutions. Often unsuccessfully, the search for high-temperature piezoelectric systems has centred on the $BiFeO_3$-$PbTiO_3$ compound and historically, doping of $BiFeO_3$-$PbTiO_3$ has largely been ineffective in the search for high-temperature materials that offer satisfactory piezoelectric properties. However, the $BiFeO_3$-$(K_{0.5}Bi_{0.5})TiO_3$-$PbTiO_3$ system demonstrates that the partial substitution of alternative end-members can be an efficacious method. Although ternary and pseudoquaternary systems have recently been subject to large amounts of research as many of the possible binary systems have been exhausted, a raft of materials with high-strains and large high-field piezoelectric charge coefficients have been reported, these are often electrostrictive or have limited operating temperatures. The partial substitution of the dominant $PbTiO_3$ compound into $BiFeO_3$-$(K_{0.5}Bi_{0.5})TiO_3$ enables long-range non-centrosymmetric crystallographic order, resulting in increased polar order and T_C.

Figure 7-1. d_{33} as a function of T_C for a range of piezoelectric compounds with the purple rectangle highlighting the mixed symmetry region of the BF-KBT-PT system [95].

8. Future Work

As anticipated with the development of two novel piezoelectric systems there is an enormous potential for further work. The overarching feature of this thesis was to develop novel $BiFeO_3$-derived compounds for high temperature applications. The first issue to address is to further augment understanding in both the lead-free and lead-based compounds. The second issue relates to the practicality of these materials for high-temperature applications, as there is significant room for improvement in terms of compositional optimisation in order to reduce conductivity by means such as doping or adjusting the processing conditions as well as thermally accelerated aging for prolonged periods to examine how these materials perform *in-situ*.

This study has shown the importance of $PbTiO_3$ in generating long-range crystallographic order in order to increase piezoelectric properties although it has largely not paid focus as to how this occurs. Therefore, a number of methods can be used to investigate this belonging to both theoretical and experimental branches. Modelling can be undertaken to observe the effect of $PbTiO_3$ on alternative systems. Studies into the bonding mechanisms are important as significant covalence between the Pb and O ions is suggested to lead to a high T_C while the Pb lone pair greatly influences the lattice distortion. An in-depth investigation of the structural order of BF-KBT at the MPB should be explored, and the existence of PNR's should be confirmed or dismissed, a number of techniques can elucidate this behaviour including pair distribution function measurements using synchrotron or neutron diffraction at the MPB. To further elucidate electrical properties of the BF-KBT system PFM would be utilised using a different set-up, the piezoresponse of the composition belonging to the pseudocubic region appeared to demonstrate significant areas that showed no piezoelectric response, the switching dynamics of these regions can be diagnosed using the response of the second harmonic which can confirm if these regions are purely electrostrictive or piezoelectric.

Rayleigh analysis can be used in conjunction with a DC-bias field to observe the response in a number of compositions, those belonging to the

pseudocubic region and those that are rhombohedral to provide a useful contrast as has been performed on $BiFeO_3$-$BaTiO_3$+0.1 wt% MnO [215]. This system developed by Leontsev is pseudocubic in the 33 mol% $BaTiO_3$ composition and exhibits a disordered pseudocubic structure with a low-field d_{33} of 70 pC/N and a high-field d_{33} of 327 pm/V which is extremely similar to the properties in the pseudocubic $x$$BiFeO_3$-(1-$x$)($K_{0.5}Bi_{0.5}$)$TiO_3$ where x = 0.4. It also displays a large unipolar electric-field induced strain response of 0.16% at 5 kV/mm with some hysteresis that is suggestive of enhanced domain switching but this does not translate into a stable piezoelectric response measured at low-fields. Rayleigh analysis of this sample under an applied DC bias of 0, 2 and 4 kV/mm on PZT showed that domain switching is suppressed by the DC bias while in the lead-free $BiFeO_3$-$BaTiO_3$ system in the pseudocubic region a DC-bias increases both the intrinsic and extrinsic response, thus generating a stable ordered ferroelectric [215]. The $BiFeO_3$-rich rhombohedral phase of this system also did not show any enhancement of the intrinsic or extrinsic contributions under a DC-bias, therefore it would be of academic and industrial significance if this can be shown in this system also. The generation of a stable ferroelectric phase was confirmed using TEM in this system as ferroelectric banding could be observed post-poling while not in the virgin state [215]. A similar procedure was attempted although not accomplished successfully during this study by performing piezoelectric resonance analysis under a DC-bias using the Agilent 4192A although it was difficult to obtain samples thin enough to generate a large enough field to demonstrate any significant change in the piezoelectric response as the equipment was limited to a 40 V bias.

Rayleigh analysis could also be measured *in-situ* at a synchrotron source as detailed by Pramanick [207] on the BF-KBT-PT system, crucially it could also be measured as a function of temperature to replicate and correlate with the data obtained using electric-field induced strain responses. This would augment the already significant understanding of this system.

The second issue regarding further work would be solely focussed on the BF-KBT-PT system, as this system is understood more than it’s lead-free

counterpart and is a much more attractive candidate for high-temperature devices, this would encapsulate all optimisation of the system for use in applications.

Conductivity especially at elevated temperatures has been shown to be problematic in $BiFeO_3$ and $BiFeO_3$-derived compounds [116]. Morozov demonstrated that annealing samples in Nitrogen at 580 ºC increases the activation energy thus supressing conductivity allowing regular strain-field loops to be obtained with applied electric-fields in excess of 13 kV/mm in BF-KBT ceramics where $x = 0.7$ [245]. Rojac also demonstrated that quenching of $BiFeO_3$ prevents defects becoming ordered and prevents oxygen defects becoming dominant [116]. These are all relatively simple techniques that can be implemented easily.

Manganese doping is a frequently used method of reducing conductivity and thus increasing the RC time constant which makes integration into sensing devices more feasible, this has been utilised in both $BiScO_3$-$PbTiO_3$ and $BiFeO_3$-$PbTiO_3$ [59, 196]. Manganese is also proposed as a viable dopant as the reducing impact upon the Curie temperature is relatively minor compared to alternative dopants such as lanthanum.

A thermal ageing study is also appropriate as in applications these materials would be expected to operate at elevated temperatures for prolonged periods of time. This measurement was tentatively performed in composition B as a test, the results are shown in the appendix in Figure 10-17. In a more rigorous study a number of compositions and temperatures would be selected and measured. Rayleigh analysis could also be integrated into this approach as shown by Eitel's group in $BiScO_3$-$PbTiO_3$ polycrystalline ceramics [182] at sub-coercive fields are required and it is assumed that no domain nucleation occurs so samples can be re-measured.

9. References

[1] C. Hammond, *The Basics of Crystallography and Diffraction*, 2nd ed. Oxford: Oxford University Press, 2001.

[2] W. B. Jensen, *Holleman-Wiberg's Inorganic Chemistry (edited by Wiberg, Nils)*, vol. 79, no. 8. 2002, p. 944.

[3] J. J. Burckhardt, "The correspondence fedorov-schoenflies: The groups Pm, Pc, Cm, Cc," *Struct. Chem.*, vol. 2, no. 7, pp. 645–649, 1991.

[4] S. C. Abrahams, H. J. Levinstein, and J. M. Reddy, "Ferroelectric lithium niobate. 5. Polycrystal X-ray diffraction study between 24°C and 1200°C," *J. Phys. Chem. Solids*, vol. 27, no. 6–7, pp. 1019–1026, Jun. 1966.

[5] R. E. Cohen, "Origin of ferroelectricity in perovskite oxides," *Nature*, vol. 358, no. 6382, pp. 136–138, 1992.

[6] B. Raveau, "The perovskite history: More than 60 years of research from the discovery of ferroelectricity to colossal magnetoresistance via high TC superconductivity," *Prog. Solid State Chem.*, vol. 35, no. 2, pp. 171–173, 2007.

[7] G. H. Haertling, "Ferroelectric Ceramics: History and Technology," *J. Am. Ceram. Soc.*, vol. 82, no. 4, pp. 797–818, 1999.

[8] C. B. Carter and M. G. Norton, *Ceramic Materials: Science and Engineering* . New York: Springer, 2007.

[9] D. Damjanovic, "Ferroelectric, dielectric and piezoelectric properties of ferroelectric thin films and ceramics," *Reports Prog. Phys.*, vol. 61, no. 9, p. 1267, 1999.

[10] W. Kinase, K. Nakamura, and K. Harada, "Origin of ferroelectricity in the perovskite ABO_3 crystals," *Ferroelectrics*, vol. 259, no. 1, pp. 175–180, 2001.

[11] C. M. Yagnik, R. Gerson, and W. J. James, “Mossbauer Studies of $BiFeO_3$-$PbTiO_3$ Perovskite-Type Solid Solutions,” *J. Appl. Phys.*, vol. 42, no. 1, pp. 395–399, 1971.

[12] V. M. Goldschmidt, “Die Gesetze der Krystallochemie,” *Naturwissenschaften*, vol. 14, no. 21, pp. 477–485, 1926.

[13] Y. Kuroiwa, S. Aoyagi, A. Sawada, J. Harada, E. Nishibori, M. Takata, and M. Sakata, “Evidence for Pb-O Covalency in Tetragonal $PbTiO_3$,” *Phys. Rev. Lett.*, vol. 87, no. 21, p. 217601, 2001.

[14] R. E. Eitel, C. A. Randall, T. R. Shrout, and S. E. Park, “Preparation and characterization of high temperature perovskite ferroelectrics in the solid-solution (1-x)$BiScO_3$-x$PbTiO_3$,” *Jpn. J. Appl. Phys.*, vol. 41, no. 4A, pp. 2099–2104, 2002.

[15] R. E. Eitel, C. A. Randall, T. R. Shrout, P. W. Rehrig, W. Hackenberger, and S. E. Park, “New High Temperature Morphotropic Phase Boundary Piezoelectrics,” *Jpn. J. Appl. Phys.*, vol. 40, no. 10, pp. 5999–6002, 2001.

[16] M. A. Glazer, “The classification of tilted octahedra in perovskites,” *Acta Crystallogr.*, vol. B28, pp. 3384–3392, 1972.

[17] R. E. Eitel and C. A. Randall, “Octahedral tilt-suppression of ferroelectric domain wall dynamics and the associated piezoelectric activity in $Pb(Zr,Ti)O_3$,” *Phys. Rev. B*, vol. 75, no. 9, p. 94106, 2007.

[18] A. J. Moulson and J. M. Herbert, *Electroceramics: materials, properties, applications*. Wiley, 2003.

[19] J. C. Anderson, *Dielectrics*. London: Chapman and Hall , 1964.

[20] A. Chelkowski, *Dielectric Physics*. Amsterdam: Elseiver, 1980.

[21] P. J. Harrop, *Dielectrics*. London: Butterworth, 1972.

[22] R. C. Buchanan, *Ceramic materials for electronics*, vol. 25. Boca Raton: CRC Press, 2004.

[23] M. E. Lines and A. M. Glass, *Principles and applications of ferroelectrics and related materials*. Oxford University Press, 1977.

[24] L. E. Cross and R. E. Newnham, “History of ferroelectrics,” *J Am Ceram*, vol. 11, pp. 289–305, 1987.

[25] B. Jaffe and W. R. Cook, *Piezoelectric Ceramics*, no. 3. London: Academic Press, 1971.

[26] J. Valasek, “Piezo-electric and allied phenomena in Rochelle salt,” *Phys. Rev.*, vol. 17, no. 4, pp. 475–481, 1921.

[27] A. I. Frenkel, D. M. Pease, J. Giniewicz, E. A. Stern, D. L. Brewe, M. Daniel, and J. Budnick, “Concentration-dependent short-range order in the relaxor ferroelectric $(1-x)Pb(Sc,Ta)O_3$-$xPbTiO_3$,” *Phys.l Rev. B*, vol. 70, no. 1, p. 14106, 2004.

[28] L. E. Cross, “Relaxorferroelectrics: An overview,” *Ferroelectrics*, vol. 151, no. 1, pp. 305–320, 1994.

[29] L. E. Cross, “Relaxor ferroelectrics,” *Ferroelectrics*, vol. 76, no. 1, pp. 241–267, 1987.

[30] V. A. Isupov, “Some problems of diffuse ferroelectric phase transitions,” *Ferroelectrics*, vol. 90, no. 1, pp. 113–118, 1989.

[31] V. A. Isupov, “Phenomena at transformation from sharp to diffuse ferroelectric phase transition,” *Ferroelectrics*, vol. 143, no. 1, pp. 109–115, 1993.

[32] G. A. Smolenskii, V. A. Isupov, and A. I. Agranovskaya, “Ferroelectric Substitutional-Defect Solid Solutions,” *Sov. Phys.-Solid State*, vol. 1, no. 10, pp. 1438–1445, 1959.

[33] G. A. Smolenskii, “Physical phenomena in ferroelectrics with diffused phase transition,” *J. Phys. Soc. Jpn*, vol. 28, no. Suppl, pp. 26–37, 1970.

[34] S. B. Vakhrushev and S. M. Shapiro, “Direct evidence of soft mode behavior near the Burns temperature in the $Pb(Mg_{1/3}Nb_{2/3})O_3$ relaxor ferroelectric,” *Phys. Rev. B*, vol. 66, no. 21, p. 214101, 2002.

[35] Y. Liu, R. L. Withers, X. Wei, and J. D. Fitz Gerald, “Structured diffuse scattering and polar nano-regions in the $Ba(Ti_{1-x}Sn_x)O_3$ relaxor ferroelectric system,” *J. Solid State Chem.*, vol. 180, no. 3, pp. 858–865, 2007.

[36] J. Macutkevic, J. Banys, A. Bussmann-Holder, and A. R. Bishop, “Origin of polar nanoregions in relaxor ferroelectrics: Nonlinearity, discrete breather formation, and charge transfer,” *Phys. Rev. B*, vol. 83, no. 18, p. 184301, 2011.

[37] Y. L. Li, L. Xie, and J. Zhu, “Polar nanoregion in relaxor ferroelectrics studied by analytical electron microscopy,” *J. Adv. Dielectr.*, vol. 02, no. 02, p. 1241008, 2012.

[38] J. Yao, L. Yan, W. Ge, L. Luo, J. Li, D. Viehland, Q. Zhang, and H. Luo, “Evolution of domain structures in $(Na_{1/2}Bi_{1/2})TiO_3$ single crystals with BaTiO3,” *Phys. Rev. B*, vol. 83, no. 5, p. 54107, 2011.

[39] S. J. L. Billinge and M. G. Kanatzidis, “Beyond crystallography: the study of disorder, nanocrystallinity and crystallographically challenged materials with pair distribution functions,” *Chem. Commun.*, no. 7, pp. 749–760, 2004.

[40] S. J. L. Billinge and I. Levin, “The Problem with Determining Atomic Structure at the Nanoscale,” *Science (80-.).*, vol. 316, no. 5824, pp. 561–565, 2007.

[41] V. V Shvartsman and D. C. Lupascu, “Lead-Free Relaxor Ferroelectrics,” *J. Am. Ceram. Soc.*, vol. 95, no. 1, pp. 1–26, Jan. 2012.

[42] A. A. Bokov and Z. G. Ye, “Recent progress in relaxor ferroelectrics with perovskite structure,” *J. Mater. Sci.*, vol. 41, no. 1, pp. 31–52, 2006.

[43] S. V Kalinin, B. J. Rodriguez, J. D. Budai, S. Jesse, A. N. Morozovska, A. A. Bokov, and Z. G. Ye, “Direct evidence of mesoscopic dynamic heterogeneities at the surfaces of ergodic ferroelectric relaxors,” *Phys. Rev. B*, vol. 81, no. 6, p. 64107, 2010.

[44] Y. P. Shi and A. K. Soh, “Effects of volume evolution of static and dynamic polar nanoregions on the dielectric behavior of relaxors,” *Appl. Phys. Lett.*, vol. 99, no. 9, p. 092908, 2011.

[45] S. V Kalinin and A. Gruverman, *Scanning Probe Microscop: Nanoscale Imaging and Spectroscopy*. New York: Springer, 2010.

[46] M. Dolgos, U. Adem, X. Wan, Z. Xu, A. J. Bell, T. P. Comyn, T. Stevenson, J. Bennett, J. B. Claridge, and M. J. Rosseinsky, “Chemical control of octahedral tilting and off-axis A cation displacement allows ferroelectric switching in a bismuth-based perovskite,” *Chem. Sci.*, no. 3, pp. 1426–1435, 2012.

[47] G. A. Samara and E. L. Venturini, “Ferroelectric/relaxor crossover in compositionally disordered perovskites,” *Phase transitions*, vol. 79, no. 1–2, pp. 21–40, 2006.

[48] W. G. Cady, *Piezoelectricity: an introduction to the theory and applications of electromechanical phenomena in crystals*, vol. 1. New York: Dover Publications, 1964.

[49] N. Setter, *Piezoelectric materials in devices*. Lausanne: Setter, N., 2002.

[50] J. Curie and P. Curie, “Développement, par pression, de l’électricité polaire dans les cristaux hémièdres à faces inclinées,” *Comptes rendus l’Académie des Sci.*, vol. 91, pp. 294–295, 1880.

[51] W. P. Mason, “Piezoelectricity, its history and applications,” *J. Acoust. Soc. Am.*, vol. 70, no. 6, pp. 1561–1566, 1981.

[52] R. B. Gray, “Transducer and method of making the same.” Google Patents, 1949.

[53] W. P. Mason, “Barium-titanate ceramic as an electromechanical transducer,” *Phys. Rev.*, vol. 74, no. 9, p. 1134, 1948.

[54] J. P. Arndt, “Piezoelectric transducer.” Google Patents, 1947.

[55] R. E. Eitel and T. Shrout R., “Novel Piezoelectric Ceramics: Development of High Temperature, High Performance Piezoelectrics on the Basis of Structure,” Pennsylvania State University, State College, 2003.

[56] S. Zhang, R. Xia, C. A. Randall, T. R. Shrout, R. Duan, and R. F. Speyer, “Dielectric and piezoelectric properties of niobium-modified $BiInO_3$-$PbTiO_3$ perovskite ceramics with high Curie temperatures,” *J. Mater. Res.*, vol. 20, no. 8, pp. 2067–2071, 2005.

[57] A. J. Bell, A. X. Levander, S. L. Turner, and T. P. Comyn, “Internal Stress and Phase Coexistence in Bismuth Ferrite-Lead Titanate Ceramics,” in *Applications of Ferroelectrics, 2007. ISAF 2007. Sixteenth IEEE International Symposium on*, 2007, pp. 406–409.

[58] S. Zhang, L. Lebrun, D. Anderson, and T. R. Shrout, “Piezoelectric materials for high power, high temperature applications,” *Mater. Lett.*, vol. 59, no. 27, pp. 3471–3475, 2005.

[59] S. Zhang, R. E. Eitel, C. A. Randall, T. R. Shrout, and E. F. Alberta, “Manganese-modified $BiScO_3$-$PbTiO_3$ piezoelectric ceramic for high-temperature shear mode sensor,” *Appl. Phys. Lett.*, vol. 86, no. 26, pp. 262903–262904, 2005.

[60] D. A. Hall, “Nonlinearity in piezoelectric ceramics,” *J. Mater. Sci.*, vol. 36, no. 3, p. 26, 2001.

[61] S.-T. Zhang, A. B. Kounga, W. Jo, C. Jamin, K. Seifert, T. Granzow, J. Rödel, and D. Damjanovic, “High-Strain Lead-free Antiferroelectric Electrostrictors,” *Adv. Mater.*, vol. 21, no. 46, pp. 4716–4720, 2009.

[62] J. Kuwata, K. Uchino, and S. Nomura, “Electrostrictive Coefficients of $Pb(Mg_{1/3}Nb_{2/3})O_3$ Ceramics,” *Japan Soc. Appl. Phys.*, vol. 19, no. 11, pp. 2099–2103, 1980.

[63] K. Uchino, S. Nomura, L. E. Cross, R. E. Newnham, and S. J. Jang, “Electrostrictive effect in perovskites and its transducer applications,” *J. Mater. Sci.*, vol. 16, no. 3, pp. 569–578, 1981.

[64] Q. M. Zhang and J. Zhao, “Polarization responses in lead magnesium niobate based relaxor ferroelectrics,” *Appl. Phys. Lett.*, vol. 71, no. 12, pp. 1649–1651, 1997.

[65] R. E. Eitel, “Rayleigh Law Response in Ferroelectric Ceramics: Quantifying Domain Wall Dynamics and Structural Relationships,” *16th IEEE Int. Symp. Appl. Ferroelectr.*, vol. vols 1–2, pp. 319–323, 2007.

[66] A. Y. Belov and W. S. Kreher, “Micromechanics of ferroelectrics: from domain walls to piezoceramic devices,” *Ferroelectrics*, vol. 351, no. 1, p. 79, 2007.

[67] S. A. Mabud, “The morphotropic phase boundary in PZT solid solutions,” *J. Appl. Crystallogr.*, vol. 13, no. 3, pp. 211–216, 1980.

[68] M. Ahart, M. Somayazulu, R. E. Cohen, P. Ganesh, P. Dera, H. Mao, R. J. Hemley, Y. Ren, P. Liermann, and Z. Wu, “Origin of morphotropic phase boundaries in ferroelectrics,” *Nature*, vol. 451, no. 7178, pp. 545–548, 2008.

[69] G. Shirane, R. Pepinsky, and B. C. Frazer, “X-ray and neutron diffraction study of ferroelectric $PbTiO_3$,” *Acta Crystallogr.*, vol. 9, no. 2, pp. 131–140, 1956.

[70] V. V. S. S. Sai Sunder, A. Halliyal, and A. M. Umarji, “Investigation of tetragonal distortion in the ($PbTiO_3$)-($BiFeO_3$) system by high-temperature x-ray diffraction,” *J. Mater. Res.*, vol. 10, pp. 1301–1306, 1995.

[71] Y. Matsuo and H. Sasaki, “Effect of Grain Size on Microcracking in Lead Titanate Ceramics,” *J. Am. Ceram. Soc.*, vol. 49, no. 4, pp. 229–230, 1966.

[72] G. Shirane and A. Takeda, “Phase Transitions in Solid Solutions of $PbZrO_3$ and $PbTiO_3$ (I) Small Concentrations of $PbTiO_3$” *J. Phys. Soc. Jpn.*, vol. 7, no. 1, p. 5, 1952.

[73] G. Shirane, K. Suzuki, and A. Takeda, “Phase transitions in solid solutions of $PbZrO_3$ and $PbTiO_3$ (II) X-ray study” *J. Phys. Soc. Japan*, vol. 7, p. 12, 1952.

[74] E. Sawaguchi, “Ferroelectricity versus antiferroelectricity in the solid solutions of $PbZrO_3$ and $PbTiO_3$” *J. Phys. Soc. Japan*, vol. 8, p. 615, 1953.

[75] B. Jaffe, R. S. Roth, and S. Marzullo, “Piezoelectric Properties of Lead Zirconate-Lead Titanate Solid-Solution Ceramics,” *J. Appl. Phys.*, vol. 25, no. 6, pp. 809–810, 1954.

[76] S. Zhang, R. Xia, and T. R. Shrout, “Lead-free piezoelectric ceramics vs. PZT?,” *J. Electroceramics*, vol. 19, no. 4, pp. 251–257, 2007.

[77] D. A. Berlincourt, C. Cmolik, and H. Jaffe, “Piezoelectric Properties of Polycrystalline Lead Titanate Zirconate Compositions,” *Proc. IRE*, vol. 48, no. 2, pp. 220–229, 1960.

[78] B. Noheda, D. E. Cox, G. Shirane, J. A. Gonzalo, L. E. Cross, and S.-E. Park, “A monoclinic ferroelectric phase in the $Pb(Zr_{1-x}Ti_x)O_3$ solid solution,” *Appl. Phys. Lett.*, vol. 74, no. 14, pp. 2059–2061, 1999.

[79] D. I. Woodward, J. Knudsen, and I. M. Reaney, “Review of crystal and domain structures in the $PbZr_xTi_{1-x}O_3$ solid solution,” *Phys. Rev. B*, vol. 72, no. 10, p. 104110, 2005.

[80] L. Bellaiche, A. García, and D. Vanderbilt, “Finite-Temperature Properties of $Pb(Zr_{1-x}Ti_x)O_3$ Alloys from First Principles,” *Phys. Rev. Lett.*, vol. 84, no. 23, pp. 5427–5430, 2000.

[81] R. S. Solanki, S. K. Mishra, A. Senyshyn, S. Yoon, S. Baik, N. Shin, and D. Pandey, “Confirmation of the monoclinic Cc space group for the ground state phase of $Pb(Zr_{0.525}Ti_{0.475})O_3$: A combined synchrotron X-ray and neutron powder diffraction study,” *Appl. Phys. Lett.*, vol. 102, no. 5, p. 52903, 2013.

[82] N. Zhang, H. Yokota, A. M. Glazer, and P. A. Thomas, “Neutron powder diffraction refinement of $PbZr_{1-x}TixO_3$,” *Acta Crystallogr. Sect. B*, vol. 67, no. 5, pp. 386–398, 2011.

[83] F. Cordero, F. Trequattrini, F. Craciun, and C. Galassi, “Octahedral tilting, monoclinic phase and the phase diagram of PZT,” *J. Phys. Condens. Matter*, vol. 23, no. 41, p. 415901, 2011.

[84] R. Schierholz and H. Fuess, “Ferroelectric domains in PZT ceramics at the morphotropic phase boundary. Can the splitting of reflections in SAED patterns be used for the distinction of different pseudo-cubic phases?,” *J. Appl. Crystallogr.*, vol. 45, no. 4, pp. 766–777, 2012.

[85] J. Frantti, “Notes of the Recent Structural Studies on Lead Zirconate Titanate,” *J. Phys. Chem. B*, vol. 112, no. 21, pp. 6521–6535, 2008.

[86] R. Guo, L. E. Cross, S. E. Park, B. Noheda, D. E. Cox, and G. Shirane, “Origin of the High Piezoelectric Response in $PbZr_{1-x}Ti_xO_3$,” *Phys. Rev. Lett.*, vol. 84, no. 23, p. 5423, 2000.

[87] A. J. Bell, “Factors influencing the piezoelectric behaviour of PZT and other ‘morphotropic phase boundary’ ferroelectrics,” *J. Mater. Sci.*, vol. 41, no. 1, pp. 13–25, 2006.

[88] D. A. Berlincourt, “Piezoelectric ceramic compositional development,” *J. Acoust. Soc. Am.*, vol. 91, no. 5, pp. 3034–3040, 1992.

[89] T. R. Shrout and S. J. Zhang, “Lead-free piezoelectric ceramics: Alternatives for PZT?,” *J. Electroceramics*, vol. 19, no. 1, pp. 113–126, 2007.

[90] J. B. Lim, S. Zhang, J.-H. Jeon, and T. R. Shrout, “(K,Na)NbO_3-Based Ceramics for Piezoelectric ‘Hard’Lead-Free Materials,” *J. Am. Ceram. Soc.*, vol. 93, no. 5, pp. 1218–1220, 2010.

[91] S. Zhang, J. B. Lim, J.-L. Hyeong, and T. R. Shrout, “Characterization of Hard Piezoelectric Lead-Free Ceramics,” *Ultrason. Ferroelectr. Freq. Control. IEEE Trans.*, vol. 56, no. 8, pp. 1523–1527, 2009.

[92] R. H. Bishop, *The Mechatronics Handbook*. CRC Press, 2002.

[93] M. R. Kermani, M. Moallem, and R. V Patel, *Applied Vibration Suppression Using Piezoelectric Materials*. Nova Publishers, 2008.

[94] R. C. Turner, P. A. Fuierer, R. E. Newnham, and T. R. Shrout, “Materials for high temperature acoustic and vibration sensors: A review,” *Appl. Acoust.*, vol. 41, no. 4, pp. 299–324, 1994.

[95] S. Zhang and F. Yu, “Piezoelectric Materials for High Temperature Sensors,” *J. Am. Ceram. Soc.*, vol. 94, no. 10, pp. 3153–3170, 2011.

[96] T. Takenaka, H. Nagata, and Y. Hiruma, “Current developments and prospective of lead-free piezoelectric ceramics,” *Jpn. J. Appl. Phys.*, vol. 47, no. Compendex, pp. 3787–3801, 2008.

[97] C. F. Buhrer, “Some Properties of Bismuth Perovskites,” *J. Chem. Phys.*, vol. 36, no. 3, pp. 798–803, 1962.

[98] J. F. Carroll, *Potassium Sodium Bismuth Titanate Ceramics: Processing and Property Relationships for Higher-temperature Electromechanical Actuation*. ProQuest, 2008.

[99] Y.-R. Zhang, J.-F. Li, and B.-P. Zhang, “Enhancing Electrical Properties in NBT–KBT Lead-Free Piezoelectric Ceramics by Optimizing Sintering Temperature,” *J. Am. Ceram. Soc.*, vol. 91, no. 8, pp. 2716–2719, 2008.

[100] Y. Hiruma, H. Nagata, and T. Takenaka, “Phase diagrams and electrical properties of $(Bi_{1/2}Na_{1/2})TiO_3$-based solid solutions,” *J. Appl. Phys.*, vol. 104, no. 12, p. 124106, 2008.

[101] A. J. Royles, A. J. Bell, A. P. Jephcoat, A. K. Kleppe, S. J. Milne, and T. P. Comyn, “Electric-field-induced phase switching in the lead free piezoelectric potassium sodium bismuth titanate,” *Appl. Phys. Lett*, vol. 97, no. 13, p. 132909, 2010.

[102] L. Egerton and D. M. Dillon, “Piezoelectric and dielectric properties of ceramics in the system potassium—sodium niobate,” *J. Am. Ceram. Soc.*, vol. 42, no. 9, pp. 438–442, 1959.

[103] R. E. Jaeger and L. Egerton, “Hot Pressing of Potassium-Sodium Niobates,” *J. Am. Ceram. Soc.*, vol. 45, no. 5, pp. 209–213, 1962.

[104] J.-F. Li, K. Wang, B.-P. Zhang, and L.-M. Zhang, “Ferroelectric and Piezoelectric Properties of Fine-Grained $Na_{0.5}K_{0.5}NbO_3$ Lead-Free Piezoelectric Ceramics Prepared by Spark Plasma Sintering,” *J. Am. Ceram. Soc.*, vol. 89, no. 2, pp. 706–709, 2006.

[105] S. O. Leontsev and R. E. Eitel, “Progress in engineering high strain lead-free piezoelectric ceramics,” *Sci. Technol. Adv. Mater.*, vol. 11, no. 4, p. 44302, 2010.

[106] E. Hollenstein, M. Davis, D. Damjanovic, and N. Setter, “Piezoelectric properties of Li- and Ta-modified $(K_{0.5}Na_{0.5})NbO_3$ ceramics,” *Appl. Phys. Lett.*, vol. 87, no. 18, pp. 182903–182905, 2005.

[107] Y. Saito, H. Takao, T. Tani, T. Nonoyama, K. Takatori, T. Homma, T. Nagaya, and M. Nakamura, “Lead-free piezoceramics,” *Nature*, vol. 432, no. 7013, pp. 84–87, 2004.

[108] P. Zhao, B.-P. Zhang, R. Tu, and T. Goto, “High Piezoelectric d_{33} Coefficient in Li/Ta/Sb-Codoped Lead-Free (Na,K)NbO_3 Ceramics Sintered at Optimal Temperature,” *J. Am. Ceram. Soc.*, vol. 91, no. 11, p. 3824, 2008.

[109] K. Wang, J.-F. Li, and N. Liu, “Piezoelectric properties of low-temperature sintered Li-modified (Na,K)NbO_3 lead-free ceramics,” *Appl. Phys. Lett.*, vol. 93, no. 9, pp. 92903–92904, 2008.

[110] P. Royen and K. Swars, “Das System Wismutoxyd-Eisenoxyd im Bereich von 0 bis 55 Mol% Eisenoxyd,” *Angew. Chemie*, vol. 69, no. 24, p. 779, 1957.

[111] A. A. Belik, H. Yusa, N. Hirao, Y. Ohishi, and E. Takayama-Muromachi, “Structural Properties of Multiferroic $BiFeO_3$ under Hydrostatic Pressure,” *Chem. Mater.*, vol. 21, no. 14, pp. 3400–3405, 2009.

[112] G. A. Smolenskii, V. M. Yudin, E. Sher, and Y. E. Stolypin, “Weak Ferromagnetism of Some $BiFeO_3$-Pb($Fe_{0.5}Nb_{0.5}$)O_3 Perovskites,” *Sov. Phys.-Solid State*, vol. 6, pp. 2936–2942, 1965.

[113] J. R. Teague, R. Gerson, and W. J. James, “Dielectric hysteresis in single crystal $BiFeO_3$,” *Solid State Commun.*, vol. 8, no. 13, pp. 1073–1074, 1970.

[114] C. Michel, J. M. Moreau, G. D. Achenbach, R. Gerson, and W. J. James, “The atomic structure of $BiFeO_3$,” *Solid State Commun.*, vol. 7, no. 9, pp. 701–704, 1969.

[115] L. W. Martin, “Engineering functionality in the multiferroic $BiFeO_3$-controlling chemistry to enable advanced applications,” *Dalt. Trans.*, vol. 39, no. 45, pp. 10813–10826, 2010.

[116] T. Rojac, B. Budic, N. Setter, and D. Damjanovic, “Strong ferroelectric domain-wall pinning in $BiFeO_3$ ceramics,” *J. Appl. Phys.*, vol. 108, no. 7, pp. 74107–74108, 2010.

[117] P. Fischer, M. Polomska, I. Sosnowska, and M. Szymanski, “Temperature dependence of the crystal and magnetic structures of $BiFeO_3$,” *J. Phys. C Solid State Phys.*, vol. 13, no. 10, p. 1931, 1980.

[118] I. Sosnowska, T. P. Neumaier, and E. Steichele, “Spiral magnetic ordering in bismuth ferrite,” *J. Phys. C Sol. Stat. Phys.*, vol. 15, no. 23, p. 4835, 1982.

[119] F. Azough, R. Freer, M. Thrall, R. Cernik, F. Tuna, and D. Collison, “Microstructure and properties of Co-, Ni-, Zn-, Nb- and W-modified multiferroic $BiFeO_3$ ceramics,” *J. Eur. Ceram. Soc.*, vol. 30, no. 3, pp. 727–736, 2010.

[120] M. Azuma, H. Kanda, A. A. Belik, Y. Shimakawa, and M. Takano, “Magnetic and structural properties of $BiFe_{1-x}Mn_xO_3$,” *J. Magn. Magn. Mat.*, vol. 310, no. 2, Part 2, pp. 1177–1179, 2007.

[121] M. S. Bernardo, T. Jardiel, M. Peiteado, A. C. Caballero, and M. Villegas, “Sintering and microstuctural characterization of W^{6+}, Nb^{5+} and Ti^{4+} iron-substituted $BiFeO_3$,” *J. All. Comp.*, vol. 509, no. 26, pp. 7290–7296, 2011.

[122] V. A. Khomchenko, D. A. Kiselev, J. M. Vieira, A. L. Kholkin, M. A. Sa, and Y. G. Pogorelov, “Synthesis and multiferroic properties of $Bi_{0.8}A_{0.2}FeO_3$ (A = Ca,Sr,Pb) ceramics,” *App. Phys. Lett.*, vol. 90, no. 24, pp. 242901–242903, 2007.

[123] I. Sosnowska, W. Schäfer, W. Kockelmann, K. H. Andersen, and I. O. Troyanchuk, “Crystal structure and spiral magnetic ordering of $BiFeO_3$ doped with manganese,” *App. Phys. A Mat Sci Proc.*, vol. 74, no. 0, pp. s1040–s1042, 2002.

[124] W. Kaczmarek, Z. Pająk, and M. Połomska, “Differential thermal analysis of phase transitions in $(Bi_{1-x}La_x)FeO_3$ solid solution,” *Sol. Stat. Comm.*, vol. 17, no. 7, pp. 807–810, 1975.

[125] V. A. Khomchenko, D. A. Kiselev, I. K. Bdikin, V. V Shvartsman, P. Borisov, W. Kleemann, J. M. Vieira, and A. L. Kholkin, “Crystal structure and multiferroic properties of Gd-substituted $BiFeO_3$,” *App. Phys. Lett.*, vol. 93, no. 26, pp. 262903–262905, 2008.

[126] I. Levin, S. Karimi, V. Provenzano, C. L. Dennis, H. Wu, T. P. Comyn, T. J. Stevenson, R. I. Smith, and I. M. Reaney, “Reorientation of magnetic dipoles at the antiferroelectric-paraelectric phase transition of $Bi_{1-x}Nd_xFeO_3$ ($0.15 \leq x \leq 0.25$),” *Phys. Rev. B*, vol. 81, no. 2, p. 20103, 2010.

[127] K. S. Nalwa and A. Garg, “Phase evolution, magnetic and electrical properties in Sm-doped bismuth ferrite,” *J. App. Phys.*, vol. 103, no. 4, pp. 44101–44106, 2008.

[128] P. Uniyal and K. L. Yadav, “Observation of the room temperature magnetoelectric effect in Dy doped $BiFeO_3$,” *J. Phys Cond. Matt.*, vol. 21, no. 1, p. 12205, 2009.

[129] Y. N. Venevstev, “No Title,” *Sov. Phys. Crystallogr.*, vol. 5, no. 594, 1960.

[130] S. A. Fedulov, P. B. Ladyzhinskii, I. L. Pyatigorskaya, and Y. N. Venevtsev, “Complete Phase Diagram of the $PbTiO_3$-$BiFeO_3$ System,” *Sov. Physics-Solid State*, vol. 6, no. 2, pp. 375–378, 1964.

[131] W. M. Zhu, H. Y. Guo, and Z. G. Ye, “Structural and magnetic characterization of multiferroic $(BiFeO_3)_{\{1-x\}}(PbTiO_3)_{\{x\}}$ solid solutions,” *Phys. Rev. B*, vol. 78, no. 1, p. 14401, 2008.

[132] D. I. Woodward, I. M. Reaney, R. E. Eitel, and C. A. Randall, “Crystal and domain structure of the $BiFeO_3$-$PbTiO_3$ solid solution,” *J. Appl. Phys.*, vol. 94, no. 5, pp. 3313–3318, 2003.

[133] S. Bhattacharjee, S. Tripathi, and D. Pandey, “Morphotropic phase boundary in (1-x)$BiFeO_3$-x$PbTiO_3$: phase coexistence region and unusually large tetragonality,” *Appl. Phys. Lett.*, vol. 91, no. 4, p. 42903, 2007.

[134] M. R. Suchomel and P. K. Davies, “Enhanced tetragonality in (x)$PbTiO_3$-(1− x)$Bi(Zn_{0.5}Ti_{0.5})O_3$ and related solid solution systems,” *Appl. Phys. Lett.*, vol. 86, p. 262905, 2005.

[135] T. Stevenson, T. P. Comyn, A. Daoud-Aladine, and A. J. Bell, “Change in periodicity of the incommensurate magnetic order towards commensurate order in bismuth ferrite lead titanate,” *J. Magn. Magn. Mater.*, vol. 322, no. 22, pp. L64–L67, 2010.

[136] L. F. Cotica, V. F. Freitas, I. B. Catellani, I. A. Santos, D. Garcia, and J. A. Eiras, “High-resolution structural studies and covalent bond interactions in $BiFeO_3$-$PbTiO_3$ compounds: The role of ferroism,” *Appl. Phys. Lett.*, vol. 101, no. 17, pp. 172903–172904, 2012.

[137] T. P. Comyn and A. J. Bell, “Study of intrinsic / extrinsic piezoelectric contributions in La-doped $BiFeO_3$-$PbTiO_3$ ceramics using the Rayleigh method,” *16th IEEE Int. Symp. Appl. Ferroelectr.*, vol. vols 1–2, pp. 402–403, 2007.

[138] T. Leist, T. Granzow, W. Jo, and J. Rodel, “Effect of tetragonal distortion on ferroelectric domain switching: A case study on La-doped $BiFeO_3$-$PbTiO_3$ ceramics,” *J. Appl. Phys.*, vol. 108, no. 1, pp. 14103–14106, 2010.

[139] R. T. Smith, G. D. Achenbach, R. Gerson, and W. J. James, “Dielectric Properties of Solid Solutions of $BiFeO_3$ with $Pb(Ti,Zr)O_3$ at High Temperature and High Frequency,” *J. Appl. Phys.*, vol. 39, no. 1, pp. 70–74, 1968.

[140] T. P. Comyn, T. Stevenson, and A. J. Bell, “Piezoelectric properties of $BiFeO_3$-$PbTiO_3$ ceramics,” *Applications of Ferroelectrics, 2004. ISAF-04. 2004 14th IEEE International Symposium on*. pp. 122–125, 2004.

[141] T. P. Comyn, T. Stevenson, and A. J. Bell, “Piezoelectric properties of $BiFeO_3$ – $PbTiO_3$ ceramics,” *J. Phys. IV Proc.*, vol. 128, no. c, pp. 13–17, 2005.

[142] J. Chen, C. Jinrong, Y. Shengwen, J. Dengren, and Z. Meng, “Effects of La concentration on the structural and dielectric properties of $0.57BiFeO_3$-$0.43PbTiO_3$ crystalline solutions,” *Ultrason. Ferroelectr. Freq. Control. IEEE Trans.*, vol. 54, no. 12, pp. 2637–2640, 2007.

[143] J. M. Kim, Y. S. Sung, J. H. Cho, T. K. Song, M. H. Kim, H. H. Chong, T. G. Park, D. Do, and S. S. Kim, “Piezoelectric and Dielectric Properties of Lead-Free $(1-x)(Bi_{0.5}K_{0.5})TiO_3$-$xBiFeO_3$ Ceramics,” *Ferroelectrics*, vol. 404, no. 1, pp. 88–92, Oct. 2010.

[144] H. Matsuo, Y. Noguchi, M. Miyayama, M. Suzuki, A. Watanabe, S. Sasabe, T. Ozaki, S. Mori, S. Torii, and T. Kamiyama, “Structural and piezoelectric properties of high-density $(Bi_{0.5}K_{0.5})TiO_3$-$BiFeO_3$ ceramics,” *J. Appl. Phys.*, vol. 108, no. 10, pp. 104103–104106, 2010.

[145] M. I. Morozov, M. A. Einarsrud, and T. Grande, “Polarization and strain response in $(Bi_{0.5}K_{0.5})TiO_3$-$BiFeO_3$ ceramics,” *Appl. Phys. Lett.*, vol. 101, no. 25, p. 252904, 2012.

[146] M. I. Morozov, M. A. Einarsrud, T. Grande, and D. Damjanovic, “Lead-Free Relaxor-Like $0.75Bi_{0.5}K_{0.5}TiO_3$-$0.25BiFeO_3$ Ceramics with Large Electric Field-Induced Strain,” *Ferroelectrics*, vol. 439, no. 1, pp. 88–94, 2012.

[147] T. Ozaki, H. Matsuo, Y. Noguchi, M. Miyayama, and S. Mori, “Microstructures Related to Ferroelectric Properties in $(Bi_{0.5}K_{0.5})TiO_3$–$BiFeO_3$,” *Jpn. J. Appl. Phys.*, vol. 49, no. 9, 2010.

[148] O. N. Razumovskaya, T. B. Kuleshova, and L. M. Rudkovskaya, “Formation Reactions of $BiFeO_3$, $(K_{0.5}Bi_{0.5})TiO_3$ and $(Na_{0.5}Bi_{0.5})TiO_3$,” *Inorg. Mater.*, vol. 19, no. 1, pp. 96–99, 1983.

[149] Sigma-Aldrich, “Scandium(III) oxide,” 2013. [Online]. Available: http://www.sigmaaldrich.com/catalog/product/aldrich/307874?lang=en&region=GB.

[150] R. E. Eitel, T. R. Shrout, and C. A. Randall, “Nonlinear contributions to the dielectric permittivity and converse piezoelectric coefficient in piezoelectric ceramics,” *J. Appl. Phys.*, vol. 99, no. 12, pp. 124110–124117, 2006.

[151] G. Feng, H. Rongzi, L. Jiaji, L. Zhen, C. Lihong, and T. Changsheng, “Phase formation and characterization of high Curie temperature $xBiYbO_3$–$(1-x)PbTiO_3$ piezoelectric ceramics,” *J. Eur. Ceram. Soc.*, vol. 29, no. 9, pp. 1687–1693, 2009.

[152] R. Duan, R. F. Speyer, E. Alberta, and T. R. Shrout, “High curie temperature perovskite $BiInO_3$-$PbTiO_3$ ceramics,” *J. Mater. Res.*, vol. 19, no. 7, pp. 2185–2193, 2004.

[153] J. R. Cheng, W. M. Zhu, N. Li, and L. E. Cross, “Fabrication and characterization of $xBiGaO_3$–$(1-x)PbTiO_3$: a high temperature reduced Pb-content piezoelectric ceramic,” *Mater. Lett.*, vol. 57, no. 13, pp. 2090–2094, 2003.

[154] H. Yu, W. Ren, and Z.-G. Ye, “Structural, dielectric, and ferroelectric properties of the (1-x)PbTiO3-xBiAlO3 solid solution.,” *IEEE Trans. Ultrason. Ferroelectr. Freq. Control*, vol. 57, no. 10, pp. 2177–81, Oct. 2010.

[155] R. S. Weiss. and T. K. Gaylord., “Lithium Niobate: Summary of Physical Properties and Crystal Structure,” *Appl. Phys. A*, vol. 37, pp. 191–203, 1985.

[156] D. Damjanovic, “Materials for high temperature piezoelectric transducers,” *Curr. Opin. Solid State Mater. Sci.*, vol. 3, no. 5, pp. 469–473, 1998.

[157] H. Fritze and H. L. Tuller, “Langasite for high-temperature bulk acoustic wave applications,” *Appl. Phys. Lett.*, vol. 78, no. 7, pp. 976–977, 2001.

[158] J. Bohm, E. Chilla, C. Flannery, H. J. Fröhlich, T. Hauke, R. B. Heimann, M. Hengst, and U. Straube, “Czochralski growth and characterization of

piezoelectric single crystals with langasite structure: $La_3Ga_5SiO_{14}$ (LGS), $La_3Ga_{5.5}Nb_{0.5}O_{14}$ (LGN) and $La_3Ga_{5.5}Ta_{0.5}O_{14}$ (LGT) II. Piezoelectric and elastic properties," *J. Cryst. Growth*, vol. 216, no. 1–4, pp. 293–298, 2000.

[159] B. D. Cullity and S. R. Stock, *Elements of X-Ray Diffraction*, 3rd ed. London: Prentice-Hall, 2001.

[160] W. Massa, *Crystal structure determination*. Springer, 2011.

[161] C. B. Carter and D. B. Williams, *Transmission electron microscopy*. Springer-Verlag US, 2009.

[162] J. P. Blewett, "Synchrotron radiation-early history," *J. Synchrotron Radiat.*, vol. 5, no. 3, pp. 135–139, 1998.

[163] Diamond, "About Diamond," 2010. [Online]. Available: http://www.diamond.ac.uk/Home/About/FAQs/Background.html.

[164] R. P. Walker, "Overview of the Status of the Diamond Project," in *Proceedings of EPAC,(Edinburgh)*, 2006, pp. 2718–2722.

[165] A. Pramanick, D. Damjanovic, J. C. Nino, and J. L. Jones, "Subcoercive Cyclic Electrical Loading of Lead Zirconate Titanate Ceramics I: Nonlinearities and Losses in the Converse Piezoelectric Effect," *J. Amer. Ceram. Soc.*, vol. 92, no. 10, pp. 2291–2299, 2009.

[166] A. Pramanick, J. E. Daniels, and J. L. Jones, "Subcoercive Cyclic Electrical Loading of Lead Zirconate Titanate Ceramics II: Time-Resolved X-Ray Diffraction," *J. Amer. Ceram. Soc.*, vol. 92, no. 10, pp. 2300–2310, 2009.

[167] MTI, "Fibre Optic Measurement System," 2009. .

[168] C. B. Sawyer and C. H. Tower, "Rochelle Salt as a Dielectric," *Phys. Rev.*, vol. 35, no. 3, p. 269, 1930.

[169] B. Ando and S. Graziani, “Basic measurements for the characterization of ferroelectric devices,” *Instrum. Meas. IEEE Trans.*, vol. 54, no. 3, pp. 1054–1060, 2005.

[170] L. Pintilie and M. Alexe, “Ferroelectric-like hysteresis loop in nonferroelectric systems,” *Appl. Phys. Lett.*, vol. 87, no. 11, p. 112903, 2005.

[171] J. F. Scott, “Ferroelectrics go bananas,” *J. Phys. Condens. Matter*, vol. 20, no. 2, p. 21001, 2008.

[172] M. Dawber, N. Stucki, C. Lichtensteiger, S. Gariglio, P. Ghosez, and J. M. Triscone, “Tailoring the Properties of Artificially Layered Ferroelectric Superlattices,” *Adv. Mater.*, vol. 19, no. 23, pp. 4153–4159, 2007.

[173] R. Ranjith, B. Kundys, and W. Prellier, “Periodicity dependence of the ferroelectric properties in $BiFeO_3/SrTiO_3$ multiferroic superlattices,” *Appl. Phys. Lett.*, vol. 91, no. 22, pp. 222903–222904, 2007.

[174] D. Shindo, T. Yoshimura, and N. Fujimura, “Dielectric properties of ferroelectric/DMS heterointerface using $YMnO_3$ and Ce doped Si,” *Appl. Surf. Sci.*, vol. 254, no. 19, pp. 6218–6221, 2008.

[175] T. Lehnert, J. Adam, and M. Veith, “Ferroelectric characterization of nondensified particle-based structures,” *J. Appl. Phys.*, vol. 106, no. 6, pp. 64105–64108, 2009.

[176] S. Li, W. Cao, and L. E. Cross, “The extrinsic nature of nonlinear behavior observed in lead zirconate titanate ferroelectric ceramic,” *J. Appl. Phys.*, vol. 69, no. 10, pp. 7219–7224, 1991.

[177] L. Rayleigh, “On the behaviour of iron and steel under the operation of feeble magnetic forces,” *Phil. Mag.*, vol. 1, no. 23, pp. 225–245, 1887.

[178] D. Damjanovic and M. Demartin, “The Rayleigh law in piezoelectric ceramics,” *J. Phys. D. Appl. Phys.*, vol. 29, no. 7, p. 2057, 1996.

[179] D. Damjanovic and M. Demartin, “Contribution of the irreversible displacement of domain walls to the piezoelectric effect in barium titanate and lead zirconate titanate ceramics,” *J. Phys Cond. Mat.*, vol. 9, no. 23, p. 4943, 1997.

[180] A. Petošić, M. Budimir, and N. Pavlović, “Comparison between piezoelectric material properties obtained by using low-voltage magnitude frequency sweeping and high-level short impulse signals,” *Ultrasonics*, vol. 53, no. 6, pp. 1192–1199, 2013.

[181] K. H. Gilchrist, D. E. Dausch, and S. Grego, “Electromechanical performance of piezoelectric scanning mirrors for medical endoscopy,” *Sensors Actuators A Phys.*, vol. 178, no. 0, pp. 193–201, 2012.

[182] S. W. Gotmare, S. O. Leontsev, and R. E. Eitel, “Thermal Degradation and Aging of High-Temperature Piezoelectric Ceramics,” *J. Am. Ceram. Soc.*, vol. 93, no. 7, pp. 1965–1969, 2010.

[183] K. Kobayashi, Y. Mizuno, K. Hatano, and C. A. Randall, “Rayleigh Behavior in the Lead Free Piezoelectric $Li_x(Na_{0.5}K_{0.5})_{1-x}NbO_3$ Ceramic,” *Appl. Phys. Express*, vol. 5, no. 3, p. 31501, 2012.

[184] B. Peng, Z. Yue, and L. Li, “Evaluation of domain wall motion during polymorphic phase transition in (K, Na)NbO_3-based piezoelectric ceramics by nonlinear response measurements,” *J. Appl. Phys.*, vol. 109, no. 5, pp. 54106–54107, 2011.

[185] H. A. Kunkel, S. Locke, and B. Pikeroen, “Finite-element analysis of vibrational modes in piezoelectric ceramic disks,” *Ultrason. Ferroelectr. Freq. Control. IEEE Trans.*, vol. 37, no. 4, pp. 316–328, 1990.

[186] E.-M. Anton, W. Jo, D. Damjanovic, and J. Rodel, “Determination of depolarization temperature of $(Bi_{1/2}Na_{1/2})TiO_3$-based lead-free piezoceramics,” *J. Appl. Phys.*, vol. 110, no. 9, pp. 94108–94114, 2011.

[187] S. Zhang, C. A. Randall, and T. R. Shrout, “Dielectric, piezoelectric and elastic properties of tetragonal $BiScO_3$-$PbTiO_3$ single crystal with single domain,” *Solid State Commun.*, vol. 131, no. 1, pp. 41–45, 2004.

[188] P. W. Hawkes, *Science of microscopy*. Springer Science+ Business Media, 2007.

[189] L. Rayleigh, “XXXI. Investigations in optics, with special reference to the spectroscope,” *London, Edinburgh, Dublin Philos. Mag. J. Sci.*, vol. 8, no. 49, pp. 261–274, 1879.

[190] R. W. Kelsall, I. W. Hamley, M. Geoghegan, and J. Wiley, *Nanoscale science and technology*. Wiley Online Library, 2005.

[191] P. Guthner and K. Dransfeld, “Local poling of ferroelectric polymers by scanning force microscopy,” *Appl. Phys. Lett.*, vol. 61, no. 9, pp. 1137–1139, 1992.

[192] S. Kalinin and A. Gruverman, *Scanning probe microscopy*. New York: Springer, 2007.

[193] S. Kalinin, A. N. Morozovska, L. Q. Chen, and B. J. Rodriguez, “Local polarization dynamics in ferroelectric materials,” *Reports Prog. Phys.*, vol. 73, no. 5, p. 56502, 2010.

[194] A. Gruverman and S. V Kalinin, “Piezoresponse force microscopy and recent advances in nanoscale studies of ferroelectrics,” in *Frontiers of Ferroelectricity*, Springer US, 2007, pp. 107–116.

[195] C. Miclea, C. Tanasoiu, A. Gheorghiu, C. F. Midea, and V. Tanasoiu, “Sintering behaviour of piezoceramic powders prepared by conventional, ceramic and mechanical activation process,” in *Semiconductor Conference, 2001. CAS 2001 Proceedings. International*, 2001, vol. 2, pp. 297–300.

[196] A. J. Bell, T. Schlegel, M. Alduraibi, M. A. Khan, T. P. Comyn, and J. Rodel, “Impedance Spectroscopy of Mn-Doped $BiFeO_3$-$PbTiO_3$

Ceramics," in *15th IEEE Symposium on the Applications of Ferroelectrics, 2006.*, 2006, pp. 1–4.

[197] J. Bennett, A. J. Bell, T. J. Stevenson, and T. P. Comyn, "Exceptionally large piezoelectric strains in $BiFeO_3$–$(K_{0.5}Bi_{0.5})TiO_3$–$PbTiO_3$ ceramics," *Scr. Mater.*, vol. 68, no. 7, pp. 491–494, 2013.

[198] T. P. Comyn, S. P. McBride, and A. J. Bell, "Processing and electrical properties of $BiFeO_3$-$PbTiO_3$ ceramics," *Mat. Lett.*, vol. 58, no. 30, pp. 3844–3846, 2004.

[199] T. P. Comyn, T. Stevenson, M. Al-Jawad, G. André, A. J. Bell, and R. Cywinski, "Antiferromagnetic order in tetragonal bismuth ferrite–lead titanate," *J. Magn. Magn. Mater.*, vol. 323, no. 21, pp. 2533–2535, 2011.

[200] T. P. Comyn, T.J.Stevenson, M.Al-Jawad, S. L. Turner, R. I. Smith, W. G. Marshall, A. J. Bell, and R. Cywinski, "Phase-specific magnetic ordering in $BiFeO_3$ - $PbTiO_3$," *Appl. Phys. Lett.*, vol. 93, no. 23, p. 232901, 2008.

[201] A. J. Royles, A. J. Bell, J. E. Daniels, S. J. Milne, and T. P. Comyn, "Observation of a time-dependent structural phase transition in potassium sodium bismuth titanate," *Appl. Phys. Lett*, vol. 98, no. 18, p. 182904, 2011.

[202] J. E. Daniels, W. Jo, J. Rodel, and J. L. Jones, "Electric-field-induced phase transformation at a lead-free morphotropic phase boundary: Case study in a 93%$(Bi_{0.5}Na_{0.5})TiO_3$-7%$BaTiO_3$ piezoelectric ceramic," *App. Phys. Lett.*, vol. 95, no. 3, pp. 32903–32904, 2009.

[203] Y. Hiruma, H. Nagata, and T. Takenaka, "Phase Transition Temperatures and Piezoelectric Properties of $(Bi_{1/2}Na_{1/2})TiO_3$–$(Bi_{1/2}K_{1/2})TiO_3$–$BaTiO_3$ Lead-Free Piezoelectric Ceramics," *Jpn. J. Appl. Phys.*, vol. 45, no. 9B, p. 74097412, 2006.

[204] S. T. Zhang, A. B. Kounga, E. Aulbach, H. Ehrenberg, and J. Rodel, “Giant strain in lead-free piezoceramics $(Bi_{0.5}Na_{0.5})TiO_3$-$BaTiO_3$-$(K_{0.5}Na_{0.5})NbO_3$ system,” *App. Phys. Lett.*, vol. 91, no. 11, pp. 112903–112906, 2007.

[205] S. T. Zhang, A. B. Kounga, E. Aulbach, T. Granzow, W. Jo, H. J. Kleebe, and J. Rodel, “Lead-free piezoceramics with giant strain in the system $(Bi_{0.5}Na_{0.5})TiO_3$-$BaTiO_3$-$(K_{0.5}Na_{0.5})NbO_3$. I. Structure and room temperature properties,” *J. Appl. Phys.*, vol. 103, no. 3, pp. 34107–34108, 2008.

[206] V. K. Seth, G. J. Gatins, and W. A. Schulze, “Comparison of surface and bulk room temperature domain structure of barium titanate ceramics using x-ray diffraction,” *Ferroelectrics*, vol. 87, no. 1, pp. 243–253, 1988.

[207] A. Pramanick, D. Damjanovic, J. E. Daniels, J. C. Nino, and J. L. Jones, “Origins of Electro-Mechanical Coupling in Polycrystalline Ferroelectrics During Subcoercive Electrical Loading,” *J. Am. Ceram. Soc.*, vol. 94, no. 2, pp. 293–309, 2011.

[208] K. Kin Wing, H. L. W. Chan, and C. L. Choy, “Evaluation of the material parameters of piezoelectric materials by various methods,” *Ultrason. Ferroelectr. Freq. Control. IEEE Trans.*, vol. 44, no. 4, pp. 733–742, 1997.

[209] P. Echlin, *Handbook of sample preparation for scanning electron microscopy and x-ray microanalysis*. Springer, 2009.

[210] J. A. Hooton and W. J. Merz, “Etch Patterns and Ferroelectric Domains in $BaTiO_3$ Single Crystals,” *Phys. Rev.*, vol. 98, no. 2, pp. 409–413, 1955.

[211] S. M. Selbach, M.-A. Einarsrud, T. Tybell, and T. Grande, “Synthesis of $BiFeO_3$ by Wet Chemical Methods,” *J. Am. Ceram. Soc.*, vol. 90, no. 11, pp. 3430–3434, 2007.

[212] P. V. B. Rao, E. V Ramana, and T. B. Sankaram, “Electrical properties of $(K_{0.5}Bi_{0.5})TiO_3$,” *J. Alloys Compd.*, vol. 467, no. 1–2, pp. 293–298, 2009.

[213] T. Rojac, M. Kosec, and D. Damjanovic, “Large Electric-Field Induced Strain in $BiFeO_3$ Ceramics,” *J. Am. Ceram. Soc.*, vol. 94, no. 12, pp. 4108–4111, 2011.

[214] K. Uchino, “Advanced Piezoelectric Materials: Science And Technology.” Woodhead Publishing, Cambridge, 2010.

[215] S. O. Leontsev and R. E. Eitel, “Origin and magnitude of the large piezoelectric response in the lead-free $(1–x)BiFeO_3–xBaTiO_3$ solid solution,” *J. Mater. Res.*, vol. 26, no. 01, pp. 9–17, 2011.

[216] D. M. Stein, M. R. Suchomel, and P. K. Davies, “Enhanced tetragonality in $(x)PbTiO_3$-$(1-x)Bi(B'B'')O_3$ systems: $Bi(Zn_{3/4}W_{1/4})O_3$,” *Appl. Phys. Lett.*, vol. 89, no. 13, pp. 132903–132907, 2006.

[217] H. Kungl and M. J. Hoffmann, “Temperature dependence of poling strain and strain under high electric fields in LaSr-doped morphotropic PZT and its relation to changes in structural characteristics,” *Acta Mater.*, vol. 55, no. 17, pp. 5780–5791, 2007.

[218] T. Sebastian, I. Sterianou, I. M. Reaney, T. Leist, W. Jo, and J. Rödel, “Piezoelectric activity of $(1-x)[0.35Bi(Mg_{1/2}Ti_{1/2})O_3$-$0.3BiFeO_3$-$0.35BiScO_3]$-$xPbTiO_3$ ceramics as a function of temperature,” *J. Electroceramics*, vol. 28, no. 2–3, pp. 95–100, 2012.

[219] A. D. Prewitt and J. L. Jones, “Effects of the Poling Process on Piezoelectric Properties in Lead Zirconate Titanate Ceramics,” *Ferroelectrics*, vol. 419, no. 1, pp. 39–45, 2011.

[220] Q. M. Zhang, H. Wang, N. Kim, and L. E. Cross, “Direct evaluation of domain‐wall and intrinsic contributions to the dielectric and piezoelectric response and their temperature dependence on lead zirconate‐titanate ceramics,” *J. Appl. Phys.*, vol. 75, no. 1, pp. 454–459, 1994.

[221] T. L. Burnett and A. J. Bell, “Growth and characterisation of bismuth ferrite lead titanate single crystals,” University of Leeds, Leeds, 2008.

[222] A. F. Devonshire, “Theory of Ferroelectrics” *Adv. Phys.*, vol. 3, no. 10, pp. 85–130, 1954.

[223] R. G. Sabat, W. Ren, G. Yang, and B. K. Mukherjee, “Temperature Dependence of the Dielectric, Elastic and Piezoelectric Material Coefficients of Soft and Hard Lead Zirconate Titanate (PZT) Ceramics,” in *Applications of Ferroelectrics, 2007. ISAF 2007. Sixteenth IEEE International Symposium on*, 2007, pp. 612–615.

[224] J. Chen, H. Shi, G. Liu, J. R. Cheng, and S. Dong, “Temperature dependence of dielectric, piezoelectric and elastic properties of $BiScO_3$–$PbTiO_3$ high temperature ceramics with morphotropic phase boundary (MPB) composition,” *J. Alloys Compd.*, vol. 537, no. 0, pp. 280–285, 2012.

[225] F. Li, S. Zhang, Z. Xu, X. Wei, J. Luo, and T. R. Shrout, “Composition and phase dependence of the intrinsic and extrinsic piezoelectric activity of domain engineered $(1-x)Pb(Mg_{1/3}Nb_{2/3})O_3-xPbTiO_3$ crystals,” *J. Appl. Phys.*, vol. 108, no. 3, p. 034106, 2010.

[226] A. L. Kholkin, E. L. Colla, A. K. Tagantsev, D. V Taylor, and N. Setter, “Fatigue of piezoelectric properties in $Pb(Zr,Ti)O_3$ films,” *Appl. Phys. Lett.*, vol. 68, no. 18, pp. 2577–2579, 1996.

[227] T. Qi, I. Grinberg, and A. M. Rappe, “Correlations between tetragonality, polarization, and ionic displacement in $PbTiO_3$-derived ferroelectric perovskite solid solutions,” *Phys. Rev. B*, vol. 82, no. 13, p. 134113, 2010.

[228] M. Budimir, D. Damjanovic, and N. Setter, “Qualitative distinction in enhancement of the piezoelectric response in $PbTiO_3$ in proximity of coercive fields: 90° versus 180° switching,” *J. Appl. Phys.*, vol. 101, no. 10, p. 104119, 2007.

[229] D. Wang, Y. Fotinich, and G. P. Carman, “Influence of temperature on the electromechanical and fatigue behavior of piezoelectric ceramics,” *J. Appl. Phys.*, vol. 83, no. 10, pp. 5342–5350, 1998.

[230] J. Bennett, A. J. Bell, T. J. Stevenson, and T. P. Comyn, “Tailoring the structure and piezoelectric properties of $BiFeO_3$-$(K_{0.5}Bi_{0.5})TiO_3$–$PbTiO_3$ ceramics for high temperature applications,” *Appl. Phys. Lett.*, vol. 103, no. 15, p. -, 2013.

[231] J. Gao, X. Hu, L. Zhang, F. Li, L. Zhang, Y. Wang, Y. Hao, L. Zhong, and X. Ren, “Major contributor to the large piezoelectric response in $(1-x)Ba(Zr_{0.2}Ti_{0.8})O_3-x(Ba_{0.7}Ca_{0.3})TiO_3$ ceramics: Domain wall motion,” *Appl. Phys. Lett.*, vol. 104, no. 25, p. -, 2014.

[232] N. Bassiri-Gharb, I. Fujii, E. Hong, S. Trolier-McKinstry, D. Taylor, and D. Damjanovic, “Domain wall contributions to the properties of piezoelectric thin films,” *J. Electroceramics*, vol. 19,no. 1,pp. 49–67, 2007.

[233] M. Davis, D. Damjanovic, and N. Setter, “Temperature dependence of the direct piezoelectric effect in relaxor-ferroelectric single crystals: Intrinsic and extrinsic contributions,” *J. Appl. Phys.*, vol. 100, no. 8,p.084103, 2006.

[234] J. E. Garcia, D. A. Ochoa, V. Gomis, J. A. Eiras, and R. Pérez, “Evidence of temperature dependent domain wall dynamics in hard lead zirconate titanate piezoceramics,” *J. Appl. Phys.*, vol. 112, no. 1, p. -, 2012.

[235] M. Hammer, C. Monty, A. Endriss, and M. J. Hoffmann, “Correlation between Surface Texture and Chemical Composition in Undoped, Hard, and Soft Piezoelectric PZT Ceramics,” *J. Amer. Ceram. Soc.*, vol. 81, no. 3, pp. 721–724, 1998.

[236] D. A. Hall, A. Steuwer, B. Cherdhirunkorn, T. Mori, and P. J. Withers, “A high energy synchrotron x-ray study of crystallographic texture and lattice strain in soft lead zirconate titanate ceramics,” *J. Appl. Phys.*, vol. 96, no. 8, pp. 4245–4252, 2004.

[237] K. A. Schönau, M. Knapp, H. Kungl, M. J. Hoffmann, and H. Fuess, “In situ synchrotron diffraction investigation of morphotropic $Pb[Zr_{1-x}Ti_x]O_3$ under an applied electric field,” *Phys. Rev. B*, vol.76,no.14,p.144112, 2007.

[238] M. U. Farooq, R. Villaurrutia, I. MacLaren, T. L. Burnett, T. P. Comyn, A. J. Bell, H. Kungl, and M. J. Hoffmann, “Electron backscatter diffraction mapping of herringbone domain structures in tetragonal piezoelectrics,” *J. Appl. Phys.*, vol. 104, no. 2, p. 024111, 2008.

[239] G. Arlt and P. Sasko, “Domain configuration and equilibrium size of domains in $BaTiO_3$ ceramics,” *J. Appl. Phys.*,vol.51,no.9,pp.495660, 1980.

[240] I. MacLaren, L. A. Schmitt, H. Fuess, H. Kungl, and M. J. Hoffmann, “Experimental measurement of stress at a four-domain junction in lead zirconate titanate,” *J. Appl. Phys.*, vol. 97, no. 9, p. 094102, 2005.

[241] V. V Shvartsman, A. L. Kholkin, A. Orlova, D. Kiselev, A. A. Bogomolov, and A. Sternberg, “Polar nanodomains and local ferroelectric phenomena in relaxor lead lanthanum zirconate titanate ceramics,” *Appl. Phys. Lett.*, vol. 86, no. 20, p. 094102, 2005.

[242] A. A. Bokov, B. J. Rodriguez, X. Zhao, J.-H. Ko, S. Jesse, X. Long, W. Qu, T. H. Kim, J. D. Budai, and A. N. Morozovska, “Compositional disorder, polar nanoregions and dipole dynamics in $Pb(Mg_{1/3}Nb_{2/3})O_3$-based relaxor ferroelectrics,” *Zeitschrift für Krist. Cryst. Mater.*, vol. 226, no. 2, pp. 99–107, 2011.

[243] R. Ranjith, R. V. K. Mangalam, P. Boullay, A. David, M. B. Lepetit, U. Lüders, W. Prellier, A. Da Costa, A. Ferri, R. Desfeux, G. Vincze, Z. Radi, and C. Aruta, “Constrained ferroelectric domain orientation in $(BiFeO_3)$m$(SrTiO_3)$n superlattice,” *Appl. Phys. Lett.*, vol. 96, no. 2, p. 022902, 2010.

[244] S. Wada, K. Yako, K. Yokoo, H. Kakemoto, and T. Tsurumi, “Domain Wall Engineering in Barium Titanate Single Crystals for Enhanced Piezoelectric Properties,” *Ferroelectrics*, vol. 334, no. 1, pp. 17–27, 2006.

[245] M. I. Morozov, M.-A. Einarsrud, and T. Grande, “Control of conductivity and electric field induced strain in bulk $Bi_{0.5}K_{0.5}TiO_3$–$BiFeO_3$ ceramics,” *Appl. Phys. Lett.*, vol. 104, no. 12, p. 122905, 2014.

10. Appendix

10.1 Supplementary Data

Table 10-1. Key of the labelling system and the corresponding stoichiometric ratios

Label	$(1-x-y)BiFeO_3$	$x(K_{0.5}Bi_{0.5})TiO_3$	$yPbTiO_3$
A	$(1-x-y) = 0.55$	$x = 0.15$	$y = 0.3$
B	$(1-x-y) = 0.584$	$x = 0.131$	$y = 0.285$
C	$(1-x-y) = 0.566$	$x = 0.169$	$y = 0.265$
D1	$(1-x-y) = 0.566$	$x = 0.188$	$y = 0.256$
D2	$(1-x-y) = 0.567$	$x = 0.188$	$y = 0.245$
E1	$(1-x-y) = 0.537$	$x = 0.225$	$y = 0.238$
E2	$(1-x-y) = 0.562$	$x = 0.225$	$y = 0.213$

10.2 Electrical and Resonance Measurements

Figure 10-1. P-E loop for $(1-x-y)BiFeO_3$-$x(K_{0.5}Bi_{0.5})TiO_3$-$yPbTiO_3$ where $x = 0.375$ and $y = 0.075$ at 8 kV/mm and 13 kV/mm

Figure 10-2. (a) Electric-field induced strain, (b) coercive-field and (c) S_{MAX}/E_{MAX} as a function of temperature for composition C

Figure 10-3. Permittivity and loss as a function of temperature for 1-*x*-*y*)$BiFeO_3$-*x*($K_{0.5}Bi_{0.5}$)TiO_3-*y*$PbTiO_3$ where *x* = 0.375 and *y* = 0.075

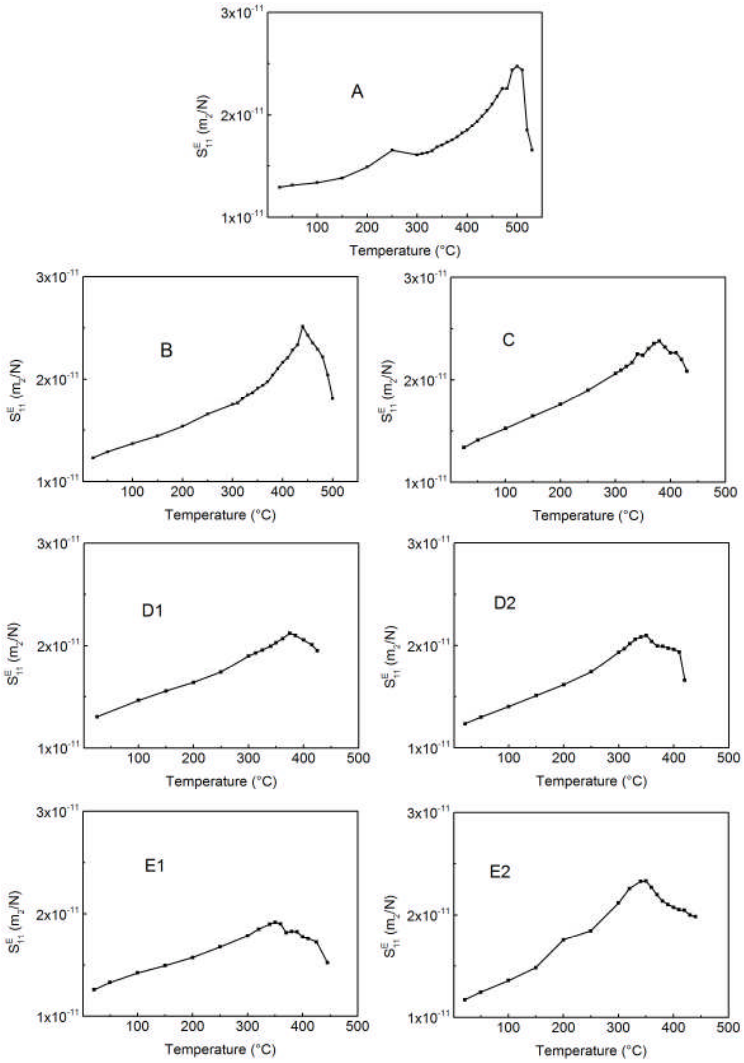

Figure 10-4. Elastic compliance as a function of temperature for Compositions A-E2

Figure 10-5. Room temperature (a) d_{init}, (b) α_d and (c) extrinsic contributions as a function of the $PbTiO_3$ concentration across the MSR

10.3 SEM

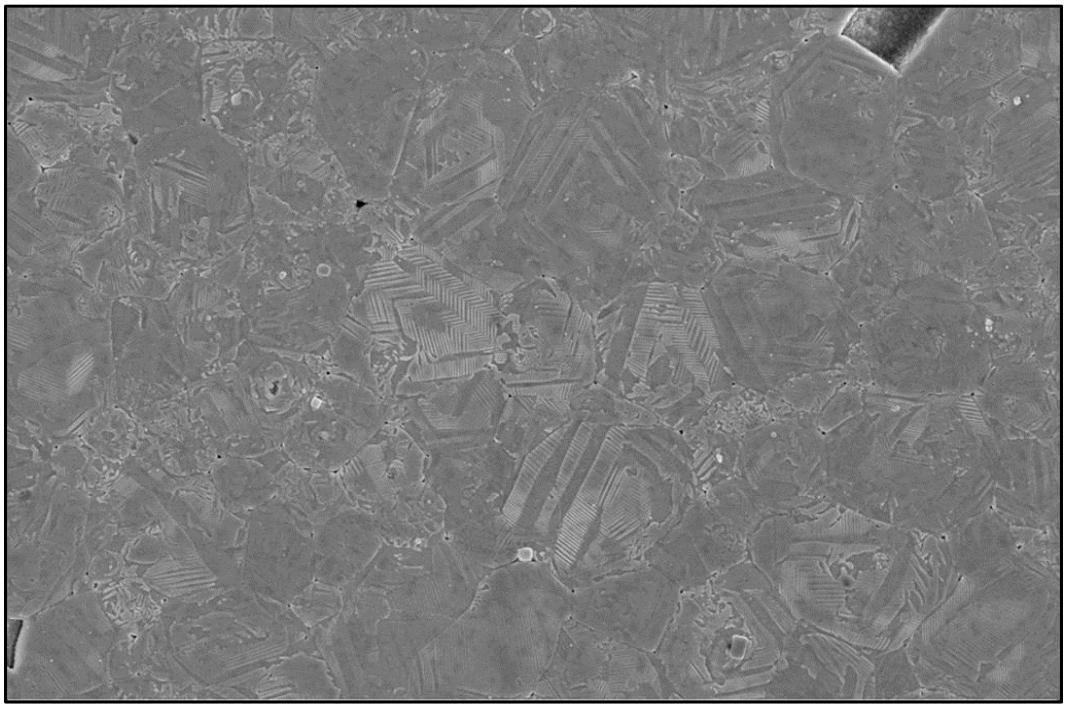

Figure 10-6. Scanning electron micrograph of Composition B

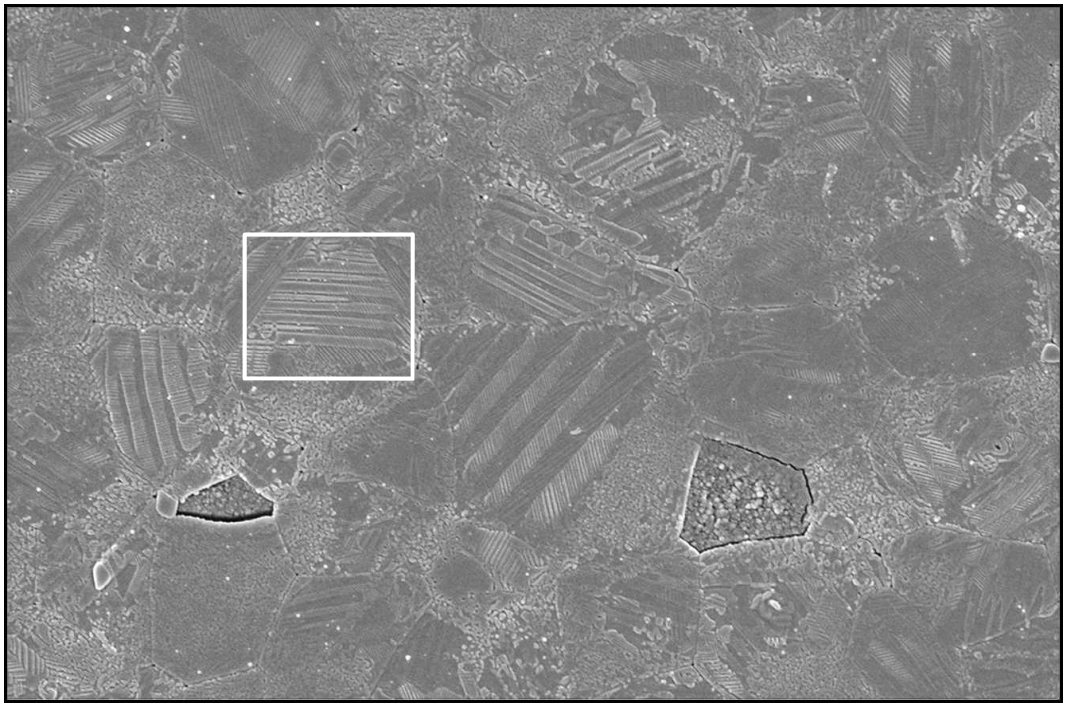

Figure 10-7. Scanning electron micrograph of Composition D1

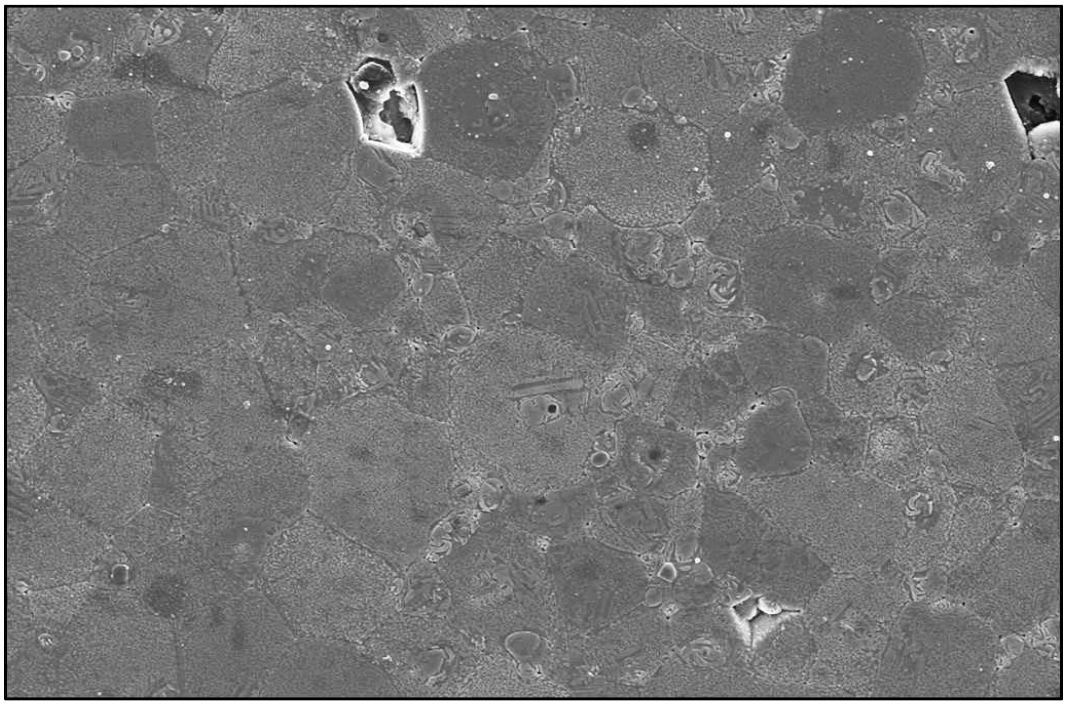

Figure 10-8. Scanning electron micrograph of Composition D2

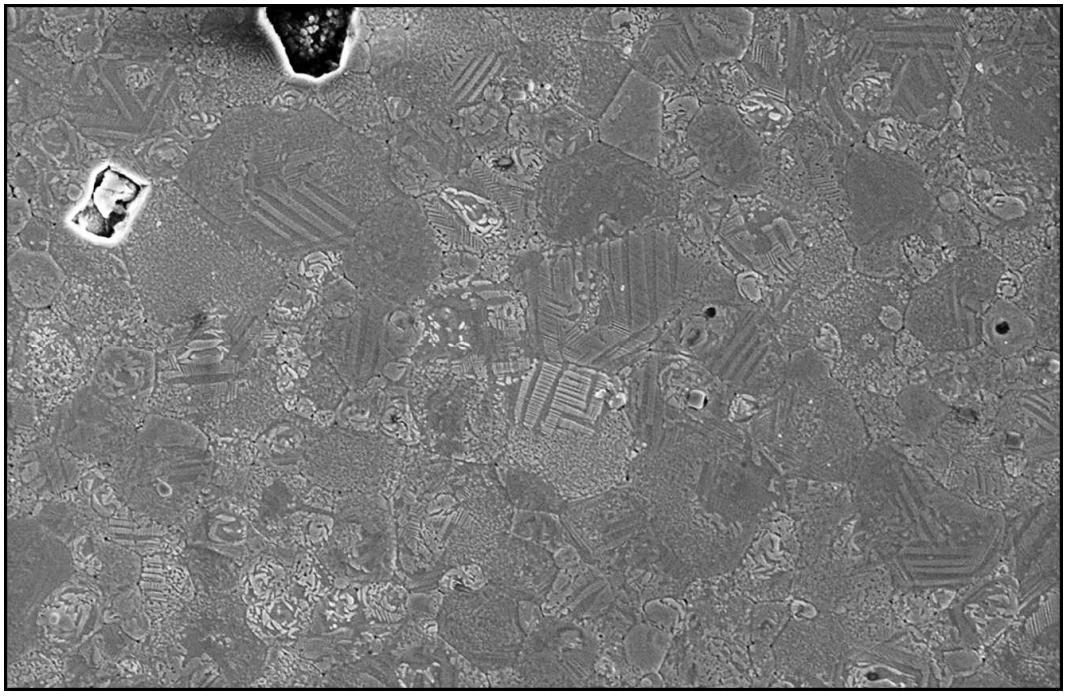

Figure 10-9. Scanning electron micrograph of Composition E1

10.4 PFM

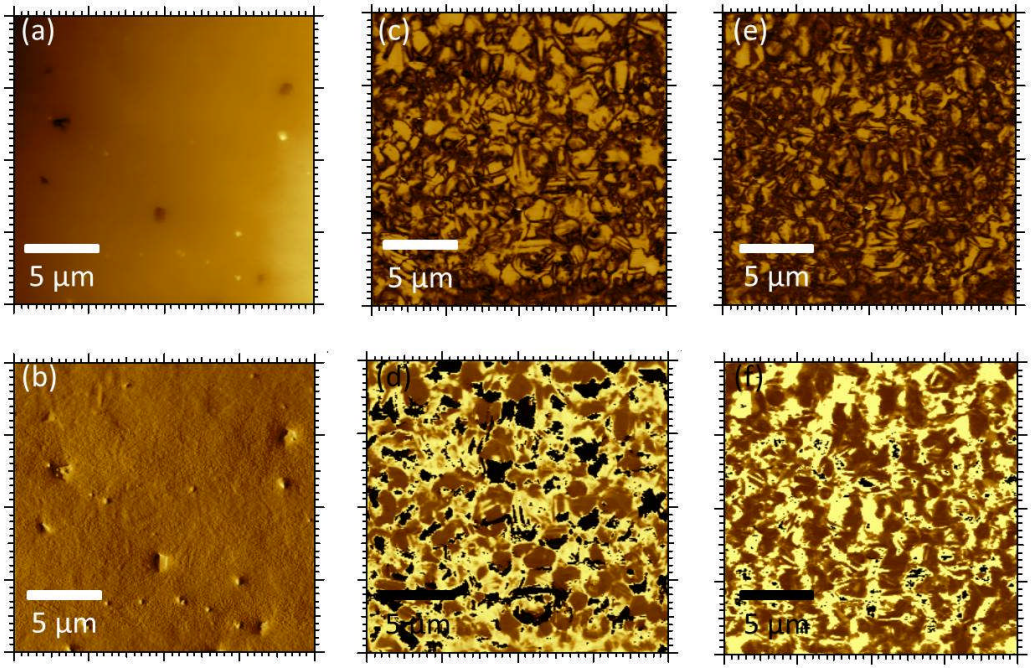

Figure 10-10. PFM images of a 400 µm^2 area of a polished sample of Composition B

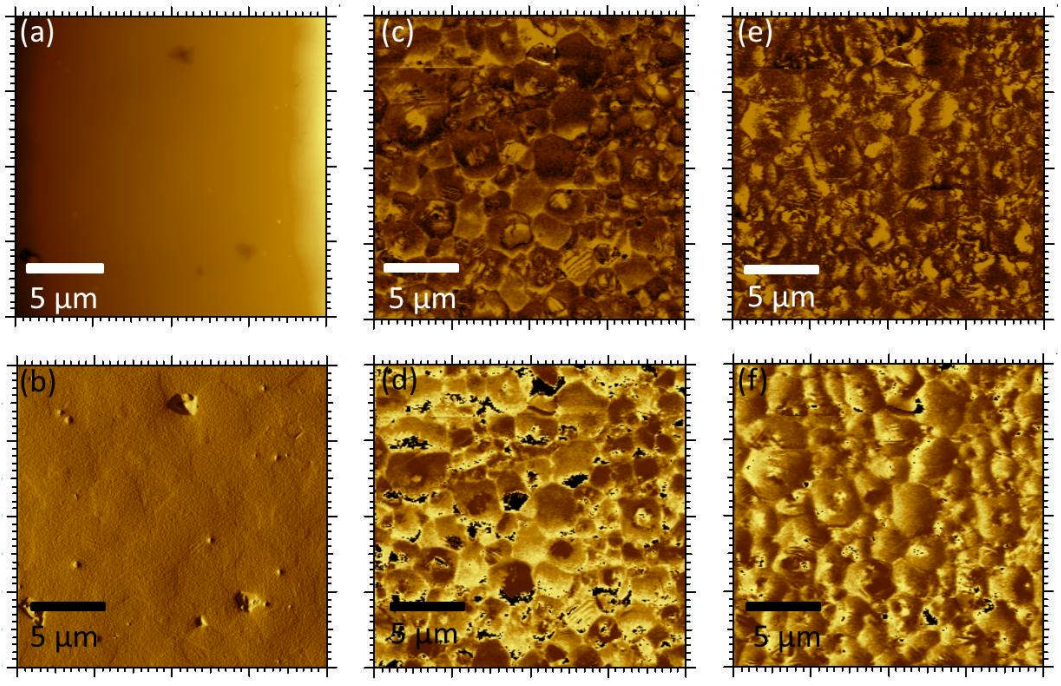

Figure 10-11. PFM images of a 400 µm^2 area of a polished sample of Composition C

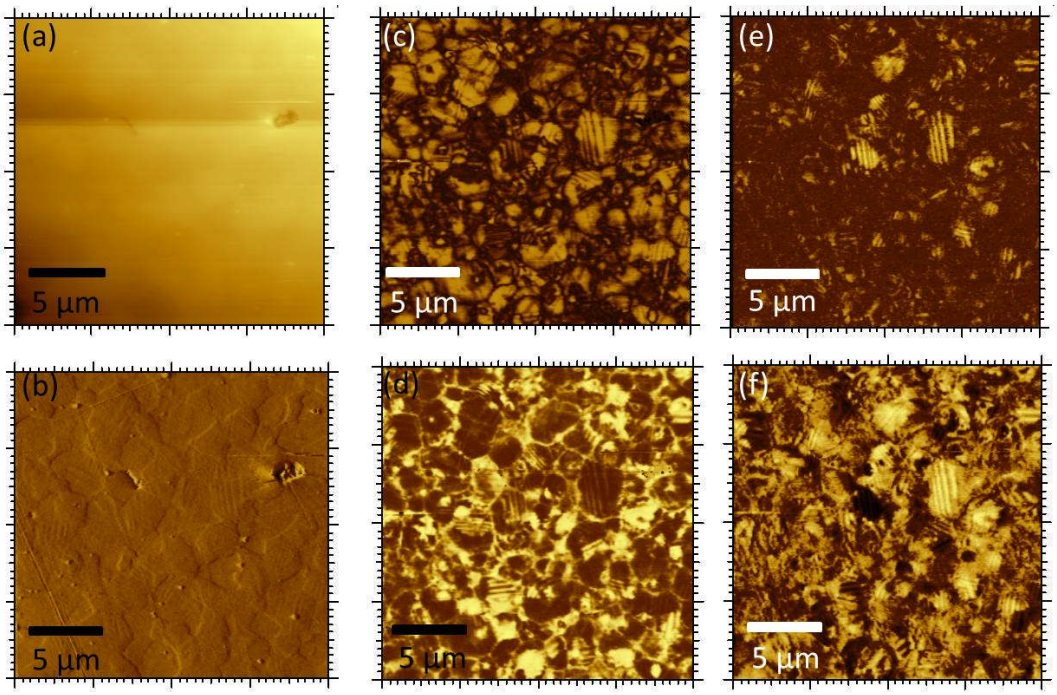

Figure 10-12. PFM images of a 400 µm^2 area of a polished sample of Composition D1

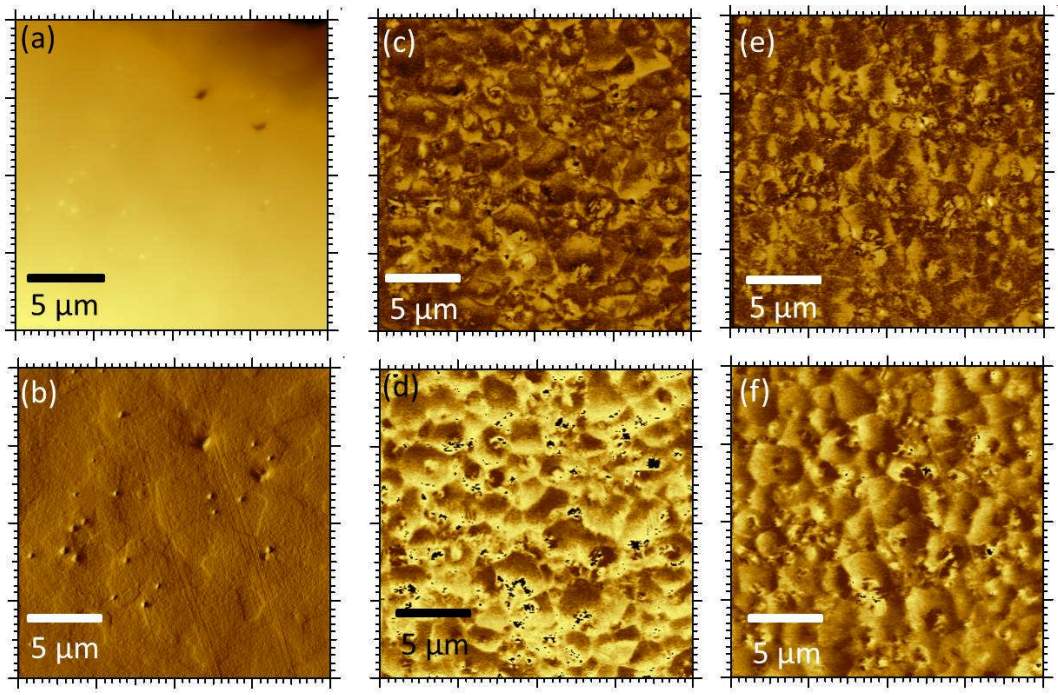

Figure 10-13. PFM images of a 400 µm^2 area of a polished sample of Composition D2

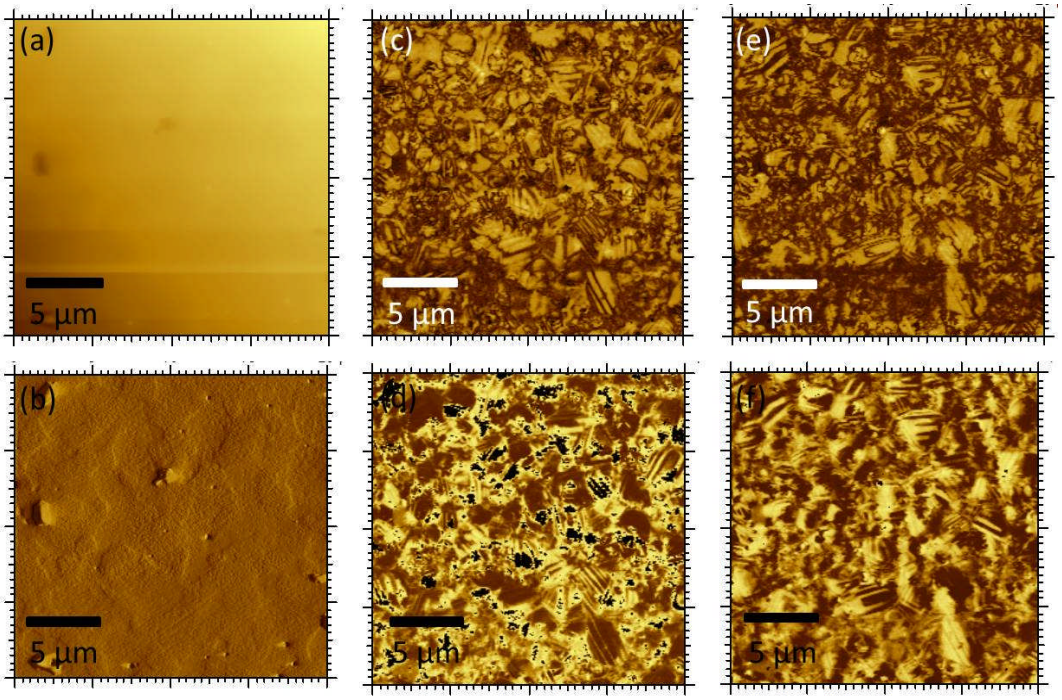

Figure 10-14. PFM images of a 400 µm^2 area of a polished sample of Composition E1

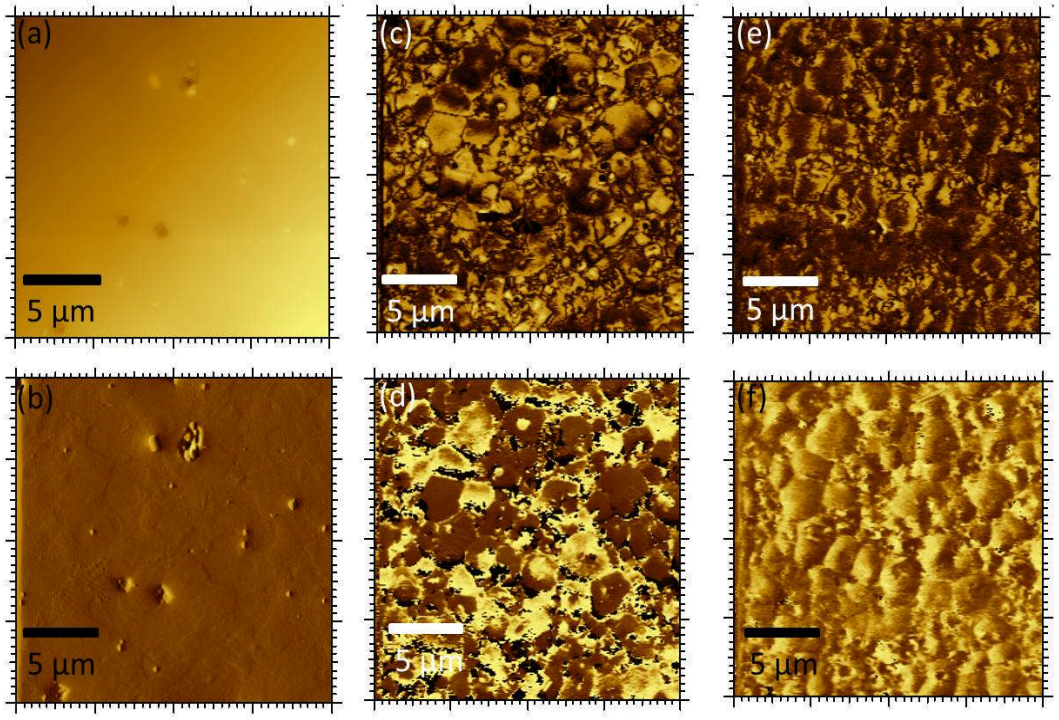

Figure 10-15. PFM images of a 400 µm^2 area of a polished sample of Composition E2

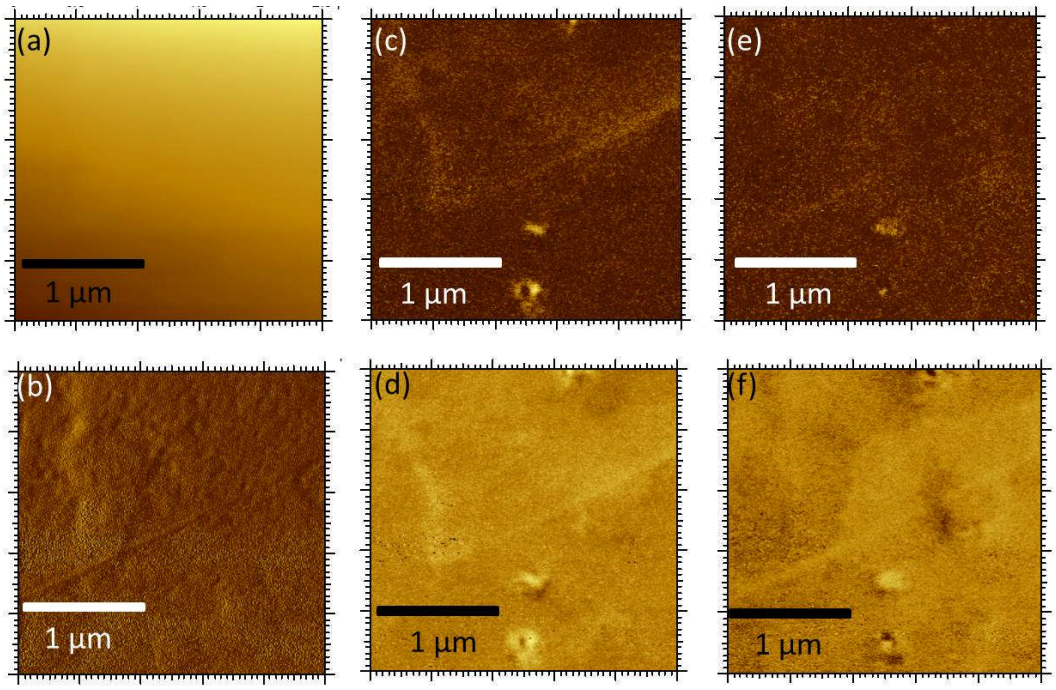

Figure 10-16. PFM images of a 6.25 µm^2 area of a polished ceramic disc of xBiFeO$_3$-(1-x)(K$_{0.5}$Bi$_{0.5}$)TiO$_3$ where x = 0.4

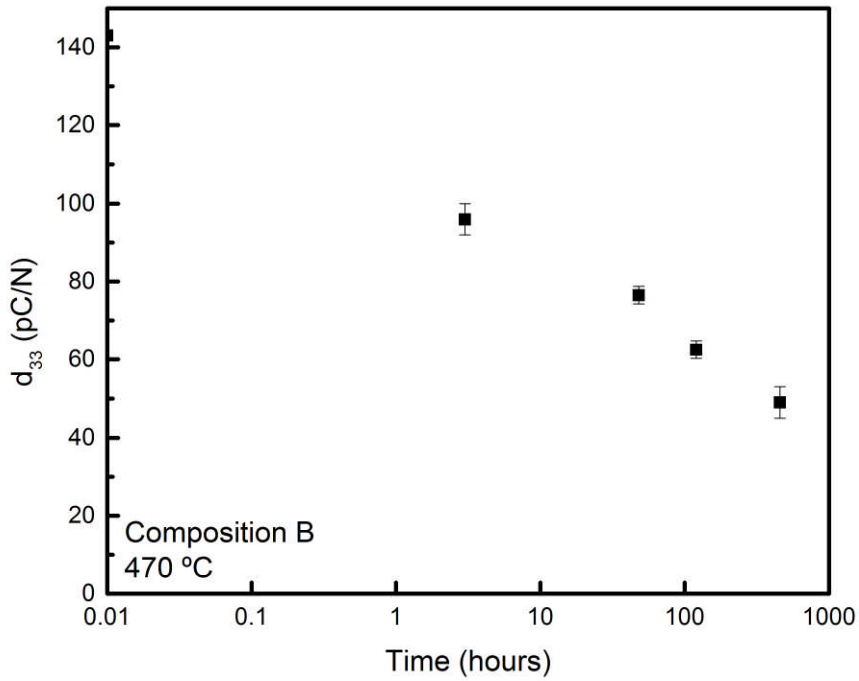

Figure 10-17. Thermal degradation study of composition B at 470 ºC

11. Publications

J. Bennett, T. R. Shrout, S. J. Zhang, H. E. Owston, T. J.Stevenson, F. Esat, A. J. Bell and T. P. Comyn. (Accepted October 2014) *Variation of piezoelectric properties and mechanisms across the relaxor-like/ferroelectric continuum in $BiFeO_3$-$(K_{0.5}Bi_{0.5})TiO_3$-$PbTiO_3$ ceramics*. Special Issue IEEE TUFFC.

J. Bennett, T.R. Shrout, S.J. Zhang, P. Mandal, A.J. Bell, T.J. Stevenson and T.P Comyn. (2014) *Temperature dependence of the intrinsic and extrinsic contributions in $BiFeO_3$-$(K_{0.5}Bi_{0.5})TiO_3$-PbTiO3 piezoelectric ceramics*. Journal of Applied Physics, **116**, 094102 DOI: 10.1063/1.4894443

J. Bennett, A.J. Bell, T.J. Stevenson, T.P. Comyn. (2013) *Tailoring the structure and piezoelectric properties of $BiFeO_3$-$(K_{0.5}Bi_{0.5})TiO_3$-$PbTiO_3$ ceramics*. Applied Physics Letters. **103**, pp.152901-1-152901-5 DOI: 10.1063/1.4824652

J. Bennett, A.J. Bell, T.J. Stevenson, T.P Comyn. (2013) *Exceptionally large piezoelectric strains in $BiFeO_3$-$(K_{0.5}Bi_{0.5})TiO_3$-$PbTiO_3$ ceramics*. Scripta Materialia. **68**, pp 491-494. DOI: 10.1016/j.scriptamat.2012.11.029

J. Bennett, A.J. Bell, T.J. Stevenson, R.I. Smith, I. Sterianou, I.M. Reaney, T.P Comyn. (2013) *Multiferroic properties of $BiFeO_3$-$(K_{0.5}Bi_{0.5})TiO_3$ ceramics*. Materials Letters. **94**, pp.172-175. DOI: 10.1016/j.matlet.2012.12.053

T. Stevenson, **J. Bennett**, A. P. Brown, T. Wines, A. J. Bell, R. I. Smith and T. P. Comyn. (2014) *Reversible piezomagnetoelectric switching in bulk polycrystalline ceramics*. APL Materials. **2**, 086105 DOI: 10.1063/1.4894070

M. Dolgos, U. Adem, X. Wan, Z. Xu, A.J. Bell, T.P. Comyn, T. Stevenson, **J. Bennett**, J.B. Claridge, and M.J. Rosseinsky. (2012) *Chemical control of octahedral tilting and off-axis A cation displacement allows ferroelectric switching in a bismuth-based perovskite*. Journal of Chemical Science. 3, pp.1426-1435. DOI: 10.1039/c2sc01115h

M. Dolgos, U. Adem, A.Manjon-Sanz, X. Wan, T.P. Comyn, T.Stevenson, **J. Bennett**, A. J. Bell, T. T.Tran, P. S.Halasyamani, J. B. Claridge,* and M. J. Rosseinsky. (2012) *Perovskite B-Site Compositional Control of [110]p Polar Displacement Coupling in an Ambient-Pressure-Stable Bismuth-based Ferroelectric*. Angewandte. Chem. Int. Ed. 2012, 51, pp.10771-10775. DOI: 10.1002/anie.201203884

11.1 Conference Proceedings

T.P. Comyn, T.J. Stevenson, S.A. Qaisar, **J.Bennett**, A.J. Bell. (2012) *High performance piezoelectric materials*. Actuator 12:Bremen. 2012

12. Conferences and Travel

(Poster) 19th International Symposium on the Applications of Ferroelectrics (2010) Edinburgh, United Kingdom.

(Poster) SET for Britain hosted by the Parliamentary Scientific Committee (2011) London, United Kingdom.

Piezo Technology Course (2011) Helsingør, Denmark.

(Oral Presentation) Piezo Conference: Electroceramics for End users VI (2011) Sestriere, Italy.

(Poster) 20th International Symposium on the Applications of Ferroelectrics (2011) Vancouver, Canada.

World Universities Network (WUN) Research Mobility Program. Hosted by Professors Thomas Shrout and Shujun Zhang. (2012) Pennsylvania State University, United States of America.

(Oral Presentation) Ferroelectrics UK (2013) Sheffield, United Kingdom.

(Oral Presentation) Piezo Conference: Electroceramics for End users VII (2013) Les Arcs, France.

(Oral Presentation) 22nd International Symposium on the Applications of Ferroelectrics (2013) Prague, Czech Republic. Presented in absentia by A.J. Bell

(Oral Presentation) 23rd International Symposium on the Applications of Ferroelectrics (2014) State College, United States of America.

Made in Merseyside